

In-vivo MRI study of the effects of low-intensity rTMS on brain activity, chemistry, and structure in rats

Bhedita Jaya Seewoo (BSc. Hons.)



This thesis is presented for the degree of Doctor of Philosophy of Neuroscience of The
University of Western Australia
School of Biological Sciences
Experimental and Regenerative Neurosciences
September 2021

(Page intentionally left blank)

Thesis Declaration

I, Bhedita Jaya Seewoo, certify that:

This thesis has been substantially accomplished during enrolment in this degree.

This thesis does not contain material which has been submitted for the award of any other degree or diploma in my name, in any university or other tertiary institution.

In the future, no part of this thesis will be used in a submission in my name, for any other degree or diploma in any university or other tertiary institution without the prior approval of The University of Western Australia and where applicable, any partner institution responsible for the joint-award of this degree.

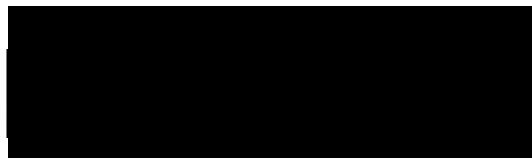
This thesis does not contain any material previously published or written by another person, except where due reference has been made in the text and, where relevant, in the Authorship Declaration that follows.

This thesis does not violate or infringe any copyright, trademark, patent, or other rights whatsoever of any person in the text.

The research involving animal data reported in this thesis was assessed and approved by The University of Western Australia Animal Ethics Committee. Approval #: RA/3/100/1430, RA/3/100/1599 and RA/3/100/1640. The research involving animals reported in this thesis followed The University of Western Australia and national standards for the care and use of laboratory animals.

This thesis contains published work and/or work prepared for publication, some of which has been co-authored.

Signature:

A large black rectangular box redacting the signature of the author.

Date: 08/09/2021

Abstract

Repetitive transcranial magnetic stimulation (rTMS) is a non-invasive neuromodulation technique that has shown therapeutic potential in many neuropsychiatric conditions and is approved by the United States Food and Drug Administration for treatment of medication-resistant depression. However, the mechanisms underlying the therapeutic effects of rTMS remain poorly understood. Animal models have been useful in elucidating some of the cellular, molecular, and genetic mechanisms of rTMS. Nevertheless, the invasive nature of these studies limits the clinical translatability of the findings. Magnetic resonance imaging (MRI) is one of only a few analytical methods that can assay *in-vivo* and longitudinal brain changes associated with rTMS treatment, with the added advantage of being a technique that can be utilized in both preclinical and clinical studies. This thesis aimed to characterise the effects of low-intensity (LI) rTMS on brain function, chemistry, and structure using MRI in healthy rats and a rat model of depression, and link these results to behaviour and gut microbiome composition.

I first investigated the effects of LI-rTMS in healthy animals. Resting-state functional MRI (rs-fMRI) data was acquired immediately before and after a single 10 min session of LI-rTMS (1 Hz, continuous theta burst stimulation, 10 Hz, biomimetic high frequency stimulation). LI-rTMS induced frequency-specific effects on functional links within the resting-state brain networks and these effects were similar to those described in humans following rTMS. After assessing the immediate effect of one stimulation session, I performed a longitudinal multimodal MRI (rs-fMRI, proton magnetic resonance spectroscopy (MRS) and diffusion MRI) study in which healthy rats received

daily 10 min of 10 Hz or 1 Hz LI-rTMS for two weeks. 10 Hz LI-rTMS increased resting-state connectivity and GABA, glutamine, and glutamate levels in healthy rats while 1 Hz stimulation decreased connectivity and glutamine levels. 10 Hz and 1 Hz stimulation induced similar changes in diffusion MRI metrics, although the changes in the 10 Hz group were detectable earlier than in the 1 Hz group, and only 10 Hz stimulation increased axial and mean kurtosis within the external capsule. Overall, 1 Hz stimulation had subtler and opposite effects to 10 Hz stimulation, showing that the two stimulation protocols may have different underlying mechanisms. Following stimulation cessation, the induced functional and chemical changes decreased to baseline levels within three weeks in the 10 Hz group but were sustained in the 1 Hz group. This study confirmed the frequency-specific effects of LI-rTMS and further suggests that effects of 1 Hz stimulation, although milder, may persist longer after cessation of treatment compared to those of 10 Hz stimulation.

I then investigated the effects of LI-rTMS in a chronic restraint stress (CRS) model of depression. CRS involved placing the animals in individual transparent tubes for 2.5 h daily for 13 days, following which: 1) elevated plus-maze and forced swim tests revealed increased anxiety and depression-related behaviours; 2) multimodal MRI revealed hypo- and hyper-connectivity within several resting-state networks, decreased sensorimotor cortical glutamate, glutamine, and combined glutamate-glutamine levels, decreased hippocampal volume, microstructural disruption in the white matter, and delayed brain maturation-related changes in the white matter; and 3) analysis of the gut microbiota revealed gut microbial dysbiosis. Importantly, these CRS-induced changes are similar to anomalies found in human depression. An

accelerated protocol of 10 Hz LI-rTMS (10 min three times daily, five days/week for two weeks) successfully restored several of these changes. Additionally, immunohistochemistry data revealed higher myelination in restrained animals which received active LI-rTMS compared to those which received sham or no stimulation.

Effective development of new therapies based on rTMS will require a cyclical from bench-to bedside-to-bench approach. Overall, the results of this thesis reveal the ability of LI-rTMS to elicit changes in brain function, chemistry, and structure as well as in behaviour and gut microbiome. These correlational measures may be used to suggest how to improve personalised rTMS treatment protocols by optimising the treatment effects.

Acknowledgements

My PhD would not have been as pleasing and rewarding if it was not for the exceptional group of people who have supported me throughout the years.

First and foremost, I would like to thank my supervisors A/Prof Jennifer Rodger, Dr Kirk Feindel and Dr Sarah Etherington for their continued support and exceptional guidance. It has been an extremely rewarding experience to be your student and develop as a scientist. Jenny, I feel really lucky to have you as my supervisor and I cannot imagine going through this with anyone else. I am extremely grateful for the support, research mentorship, and opportunities you have provided. Kirk, thank you for your enthusiastic and encouraging supervision and patience with my numerous questions during our scientific discussions. Your consistent support greatly strengthened my research efforts and developed my scientific skills. Your critical perspective and exceptional scope of knowledge is inspirational, and I am constantly saying how much I want to be more like you. Sarah, I immensely appreciate your analytical approach and invaluable feedback. Your assistance constantly improved and refined my perspective. I genuinely look up to you as a scientist and as a person.

I also wish to acknowledge technical assistance provided during my PhD, especially Marissa Penrose-Menz, Kerry Leggett and the team at UWA M Block Animal Care Services. Thank you to everyone at Experimental and Regenerative Neurosciences, who were always generous in their offers of assistance with any matters. Lauren and Jess, thank you for your genuine friendship and for always being there for me when needed you. Prof Paul Croarkin, I am grateful for your unwavering encouragement and for all the research advice and collaborative opportunities you provided me with during my PhD.

I am deeply grateful and appreciative of the unyielding support of my family, specially, my younger sisters, Deepty and Dishty Seewoo, for their encouragements to “hang in there”, and my parents, Tookraj and Bharatee Seewoo, for always being there for me and for keeping me motivated. Rizky, I wish to express my sincere gratitude for your endless love and support.

Additionally, my PhD would not have been feasible without the financial support from the Forrest Research Foundation Scholarship. Special thanks to Andrew and Nicola Forrest for creating such a conducive research environment for Forrest Scholars. This research is supported by an Australian Government Research Training Program (RTP) Scholarship and University Postgraduate Award.

Authorship Declaration: Co-authored Publications

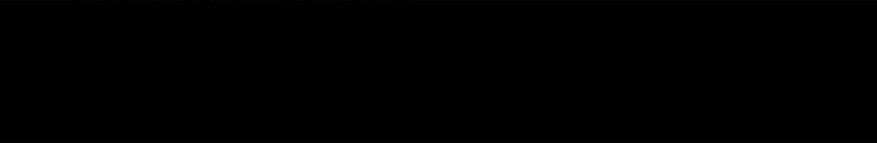
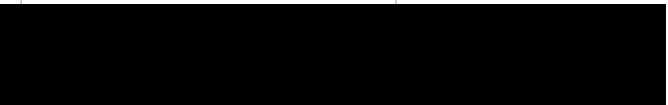
This thesis contains work that has been published and prepared for publication. The published work is co-authored, and my contributions to each paper are detailed below.

This thesis is composed of seven published research papers (Chapters 1-6), one published conference abstract (Chapter 7), one manuscript which has been prepared for publication (Chapter 7), one accepted manuscript (Chapter 8), and one manuscript under review (Chapter 9). Supervisors reviewed and edited drafts.

1. Details of the work: Seewoo, B.J. , Etherington, S.J., Feindel, K.W. & Rodger, J., 2018. Combined rTMS/fMRI studies: An overlooked resource in animal models. <i>Front Neurosci.</i> 12, 180. doi: 10.3389/fnins.2018.00180		
Location in thesis: Chapter 1: General Introduction		
Student contribution to work: I was the primary author and major contributor to all components of the work. I conducted the literature search, wrote the first draft of the review article, and worked with the co-authors to refine it for publication and respond to reviewers' comments.		
Co-author signatures and dates:		
		
Sarah J Etherington Date: 10/08/2021	Kirk W Feindel Date: 12/08/2021	Jennifer Rodger Date: 09/08/2021

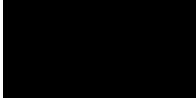
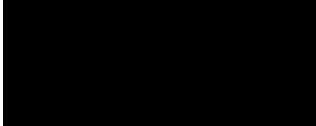
2. Details of the work: Seewoo, B.J. , Etherington, S.J. & Rodger, J., 2019a. Transcranial Magnetic Stimulation eLS. John Wiley & Sons, Ltd, pp. 1-8. doi: 10.1002/9780470015902.a0028620	
Location in thesis: Chapter 1: General Introduction	
Student contribution to work: I was the primary author and major contributor to all components of the work. I conducted the literature search, wrote the first draft of the book chapter, and worked with the co-authors to refine it for publication and respond to reviewers' comments.	
Co-author signatures and dates:	
	
Sarah J Etherington Date: 10/08/2021	Jennifer Rodger Date: 09/08/2021

3. Details of the work: Kint, L.T., Seewoo, B.J. , Hyndman, T.H., Clarke, M.W., Edwards, S.H., Rodger, J., Feindel, K.W. & Musk, G.C., 2020. The pharmacokinetics of medetomidine administered subcutaneously during isoflurane anaesthesia in Sprague-Dawley rats. <i>Animals.</i> 10, 1050. doi: 10.3390/ani10061050
--

Location in thesis: Chapter 2: Methods Development: The pharmacokinetics of medetomidine administered subcutaneously during isoflurane anaesthesia in Sprague-Dawley rats			
Student contribution to work: I was the second author. K.W.F., G.C.M and I designed the research. L.T.K, G.C.M. and I carried out all animal experiments, wrote the first draft of the manuscript, and worked with the co-authors to refine it for publication and respond to reviewers' comments.			
Co-author signatures and dates:			
			
Leila T Kint Date: 9/08/2021	Timothy H Hyndman Date: 09/08/2021	Michael W Clarke Date: 09/08/2021	Scott H. Edwards Date:
			
Jennifer Rodger Date: 09/08/2021	Kirk W Feindel Date: 12/08/2021	Gabrielle C Musk Date: 09/08/2021	

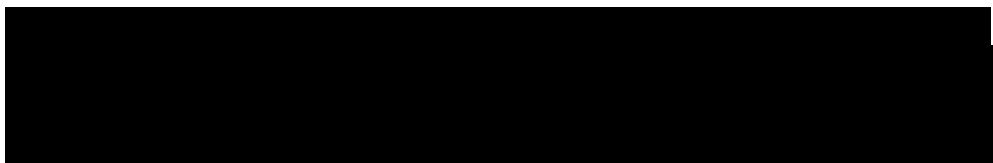
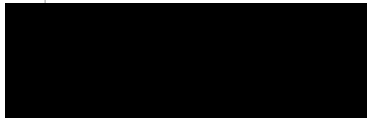
4. Details of the work: Seewoo, B.J. , Joos, A.C. & Feindel, K.W., 2020. An analytical workflow for seed-based correlation and independent component analysis in interventional resting-state state fMRI studies. 165: 26–37. <i>Neuroscience Research</i> . doi: 10.1016/j.neures.2020.05.006	
Location in thesis: Chapter 3: Methods Development: An analytical workflow for seed-based correlation and independent component analysis in interventional resting-state fMRI studies	
Student contribution to work: I was the primary author and major contributor to all components of the work. I developed, designed, and planned the study and carried out all experiments. I conducted data analysis and wrote the first version of the manuscript with assistance from A.C.J. I worked with the co-authors to refine it for publication and respond to reviewers' comments.	
Co-author signatures and dates:	
	
Alexander C Joos Date: 11/08/2021	 Kirk W Feindel Date: 12/08/2021

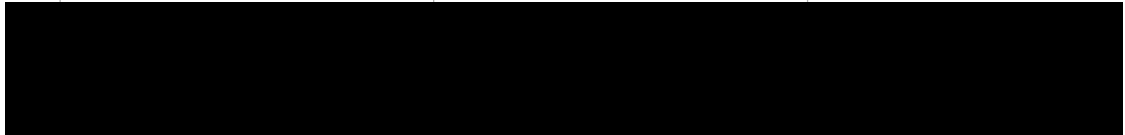
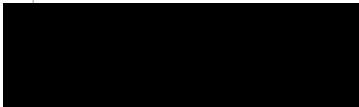
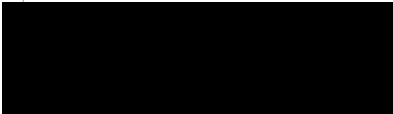
5. Details of the work: Seewoo, B.J. , Feindel, K.W., Etherington, S.J. & Rodger, J., 2018. Resting-state fMRI study of brain activation using low-intensity repetitive transcranial magnetic stimulation in rats. <i>Sci Rep.</i> 8, 6706. doi: 10.1038/s41598-018-24951-6
Location in thesis: Chapter 4: Immediate effects of low-intensity repetitive transcranial magnetic stimulation on brain activity in healthy rats

<p>Student contribution to work: I was the primary author and major contributor to all components of the work. I conducted all data collection and analysis with assistance from K.W.F. I wrote the first version of the manuscript and worked with the co-authors to refine it for publication and respond to reviewers' comments.</p>		
<p>Co-author signatures and dates:</p>		
 Kirk W Feindel Date: 12/08/2021	 Sarah J Etherington Date: 10/08/2021	 Jennifer Rodger Date: 09/08/2021

<p>6. Details of the work: Seewoo, B.J., Feindel, K.W., Etherington, S.J. & Rodger, J., 2019. Frequency-specific effects of low-intensity rTMS can persist for up to 2 weeks post-stimulation: A longitudinal rs-fMRI/MRS study in rats. <i>Brain Stimul.</i> 12, 1526–1536. doi: 10.1016/j.brs.2019.06.028</p>		
<p>Location in thesis: Chapter 5: Long-term effects of repeated low-intensity repetitive transcranial magnetic stimulation on brain activity and chemistry in healthy rats</p>		
<p>Student contribution to work: I was the primary author and major contributor to all components of the work. I developed, designed and planned the study, conducted all data collection and analysis and wrote the first version of the manuscript. I worked with the co-authors to refine it for publication and respond to reviewers' comments.</p>		
<p>Co-author signatures and dates:</p>		
 Kirk W Feindel Date: 12/08/2021	 Sarah J Etherington Date: 10/08/2021	 Jennifer Rodger Date: 09/08/2021

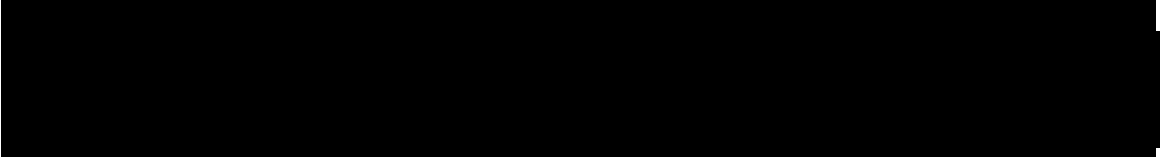
<p>7. Details of the work: Seewoo, B.J., Hennessy, L.A., Feindel, K.W., Etherington, S.J., Croarkin, P.E. & Rodger, J., 2020. Validation of chronic restraint stress model in young adult rats for the study of depression using longitudinal multimodal MR imaging. <i>eneuro</i>. 7. doi: 10.1523/eneuro.0113-20.2020</p>		
<p>Location in thesis: Chapter 6: Depression model: Validation of chronic restraint stress model of depression in rats using multimodal MRI</p>		
<p>Student contribution to work: I was the primary author and major contributor to all components of the work. I developed, designed and planned the study. I carried out all experiments with assistance from L.A.H. I analysed all MRI data and two out of three behavioural data. I wrote the first version of the manuscript and worked with the co-authors to refine it for publication and respond to reviewers' comments.</p>		
<p>Co-author signatures and dates:</p>		
		

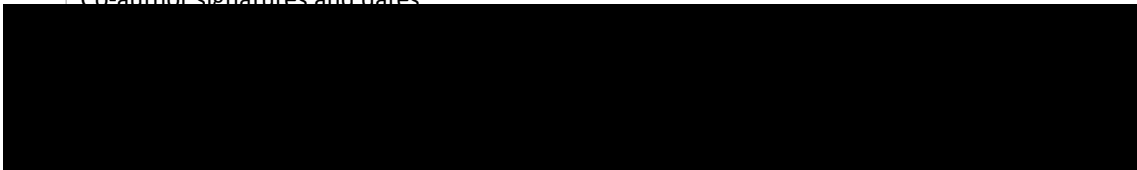
		
Lauren A Hennessy Date: 09/08/2021	Date: 12/08/2021	Sarah J Etherington Date: 10/08/2021
		Jennifer Rodger Date: 09/08/2021
Paul E Croarkin Date: 09/08/2021		

8. Details of the work: Seewoo, B.J. , Feindel, K.W., Etherington, S.J., Hennessy, L.A., Croarkin, P.E., Rodger, J., 2019. M85. Validation of the chronic restraint stress model of depression in rats and investigation of standard vs accelerated rTMS treatment. <i>Neuropsychopharmacology</i> 44:122–123. doi: 10.1038/s41386-019-0545-y		
Location in thesis: Chapter 7: Depression model: Long-term effects of repeated 10 Hz LI-rTMS on chronic restraint stress model of depression		
Student contribution to work: I was the primary author and major contributor to all components of the work. I developed, designed and planned the study. I carried out all experiments with assistance from L.A.H. I analysed all MRI data and two out of three behavioural data. I wrote the first version of the manuscript and worked with the co-authors to refine it for publication and respond to reviewers' comments.		
Co-author signatures and dates:		
		
Kirk W Feindel Date: 12/08/2021	Sarah J Etherington Date: 10/08/2021	Lauren A Hennessy Date: 09/08/2021
		Jennifer Rodger Date: 09/08/2021
Paul E Croarkin Date: 09/08/2021		

9. Details of the work: Seewoo, B.J. , Hennessy, L.A., Jaeschke-Angi, L.A., Mackie, L.A., Etherington, S.J., Dunlop, S.A., Croarkin, P.E. & Rodger, J., 2021. A preclinical study of standard versus accelerated transcranial magnetic stimulation for depression in adolescents. <i>Journal of Child and Adolescent Psychopharmacology</i> . doi: 10.1089/cap.2021.0100		
Hennessy, L.A.*, Seewoo, B.J.* , Jaeschke-Angi, L.A., Mackie, L.A., Etherington, S.J., Dunlop, S.A., Croarkin, P.E. & Rodger, J., 2022. Accelerated low-intensity rTMS does not rescue anxiety behaviour or abnormal connectivity in young adult rats following chronic restraint stress. <i>Submitted</i> .		

Location in thesis: Chapter 7: Depression model: Long-term effects of repeated 10 Hz LI-rTMS on chronic restraint stress model of depression			
Student contribution to work: I am co-first author with L.A.H and I am a major contributor to all components of the work. L.A.H and I carried out all experiments with assistance from L.A.J and L.A.M. I analysed all MRI data and wrote the MRI methods and results section of the manuscript. I worked with the co-authors to refine the manuscript for publication.			
Co-author signatures and dates:			
			
Date: 09/08/2021	Liz A. Jaeschke-Angi Date: 10/08/2021	Date:10/08/2021	
			
Sarah J Etherington Date: 10/08/2021	Sarah A. Dunlop Date: 09/08/2021	Paul E Croarkin Date: 09/08/2021	Jennifer Rodger Date: 09/08/2021

10. Details of the work: Seewoo, B.J. , Feindel, K.W., Won, Y., Joos, A.C., Figliomeni, A., Hennessy, L.A. & Rodger, J., 2021 White matter changes following chronic restraint stress and neuromodulation: a diffusion magnetic resonance imaging study in young male rats. <i>Under review.</i>			
Location in thesis: Chapter 8: Changes in the white matter of young male Sprague Dawley rats following chronic restraint stress and following low-intensity rTMS: a diffusion MRI study			
Student contribution to work: I was the primary author and major contributor to all components of the work. I developed, designed and planned the study. I carried out all experiments with assistance from K.W.F., Y.W., A.C.J., A.F., and L.A.H. I conducted all data analysis with assistance from K.W.F. and Y.W. I wrote the first version of the manuscript and worked with the co-authors to refine it for publication and respond to reviewers' comments.			
Co-author signatures and dates:			
			
Date: 12/08/2021		Date: 11/08/2021	
			
Date: 09/08/2021	Lauren A Hennessy Date: 09/08/2021	Date: 09/08/2021	

<p>11. Details of the work: Seewoo, B.J., Arena-Foster, Y., Hennessy, L.A., Gorecki, A.M., Anderton, R. & Rodger, J., 2021 Changes in the rodent gut microbiome following chronic restraint stress and low-intensity rTMS. <i>Under review.</i></p>		
<p>Location in thesis: Chapter 9: Changes in the rodent gut microbiome following chronic restraint stress and low-intensity rTMS</p>		
<p>Student contribution to work: I was the primary author and major contributor to all components of the work. I developed, designed and planned the study. I carried out all experiments with assistance from Y.A., and L.A.H. I conducted all microbiome, MRI and correlational analyses. I wrote the first version of the manuscript and worked with the co-authors to refine it for publication and respond to reviewers' comments.</p>		
<p>Co-author signatures and dates:</p>		
		
<p>Date: 10/08/2021</p>	<p>Lauren A Hennessy Date: 09/08/2021</p>	<p>Date: 9/8/21</p>
 <p>Ryan Anderton Date: 09/08/2021</p>	 <p>Date: 09/08/2021</p>	

<p>Student signature: </p> <p>Date: 08/09/2021</p>
<p>I, A/Prof Jennifer Rodger, certify that the student statements regarding their contribution to each of the works listed above are correct</p> <p>As all co-authors' signatures could not be obtained, I hereby authorise inclusion of the co-authored work in the thesis.</p> <p>Coordinating supervisor signature: </p> <p>Date: 08/09/2021</p>

Table of Contents

Thesis Declaration	<i>i</i>
Abstract	<i>ii</i>
Acknowledgements	<i>v</i>
Authorship Declaration: Co-authored Publications	<i>vi</i>
Table of Contents	<i>xii</i>
List of Figures	<i>xviii</i>
List of Tables	<i>xxii</i>
Chapter 1: General Introduction	<i>1</i>
1.1. Overview	<i>1</i>
1.2. The principle underlying TMS	<i>4</i>
1.3. TMS Protocols	<i>5</i>
1.4. Monitoring the effects of TMS	<i>10</i>
1.4.1. Changes in functional connectivity: fMRI	<i>12</i>
1.4.2. Changes in neurometabolic levels: MRS	<i>18</i>
1.4.3. Changes in structure: structural MRI and diffusion MRI	<i>20</i>
1.5. Biological mechanisms of TMS	<i>22</i>
1.6. rTMS frequencies and their specific effects in human functional connectivity studies	<i>24</i>
1.6.1. Simple stimulation protocols.....	<i>24</i>
1.6.2. Complex stimulation patterns	<i>27</i>
1.7. Potential applications of combined rTMS/fMRI studies in human diseases	<i>29</i>
1.7.1. Change in connectivity post rTMS linked to improvement in symptoms.....	<i>29</i>
1.7.2. Predicting susceptibility to rTMS therapy	<i>30</i>
1.7.3. Other outcomes.....	<i>31</i>
1.8. Depression	<i>32</i>
1.8.1. Depression and the brain functional connectivity.....	<i>33</i>
1.8.2. Depression and the gut microbiome	<i>34</i>
1.9. Need for animal rTMS/MRI studies	<i>36</i>
1.9.1. Potential for linking functional connectivity changes post rTMS to genetic/molecular changes	<i>39</i>
1.9.2. Potential for linking functional connectivity changes post rTMS to structural changes	<i>40</i>
1.9.3. Combined rTMS/fMRI studies using depression models.....	<i>41</i>
1.10. Challenges associated with rTMS/fMRI studies in animals	<i>43</i>
1.10.1. Choice of animal model and development of rTMS coils	<i>43</i>
1.10.2. Use of anesthetics in animal fMRI studies.....	<i>47</i>
1.10.3. Rs-fMRI studies in rodents — challenges in data analysis.....	<i>49</i>
1.11. Summary	<i>51</i>
1.12. Thesis scope and aims	<i>52</i>

Chapter 2	56
2.1. Introduction	58
2.2. Materials and Methods	63
2.2.1. Animals	63
2.2.2. Experimental procedure.....	64
2.2.3. Blood sampling	66
2.2.4. Serum analysis	67
2.2.5. Pharmacokinetic and pharmacodynamic calculations	68
2.2.6. Trial of results	68
2.2.7. Statistical analyses.....	69
2.3. Results	69
2.3.1. Group T	69
2.3.2. Group IV.....	71
2.3.3. Group SC.....	71
2.3.4. Pharmacokinetic calculations	72
2.3.5. Trial of results	73
2.4. Discussion	73
2.5. Conclusion	78
Chapter 3	79
3.1. Introduction	81
3.2. Materials and Methods	84
3.2.1. Resting-state fMRI data	84
3.2.2. Common image pre-processing steps for ICA and SCA	87
3.2.3. Independent component analysis	89
3.2.4. Seed-based correlation analysis	93
3.3. Results	97
3.3.1. Choice of template for independent component analysis	97
3.3.2. Considerations for using seed-based correlation analysis	98
3.4. Discussion	103
3.4.1. Choice of RSN template for dual regression analysis	104
3.4.2. Considerations for using seed-based correlation analysis	106
3.4.3. Study limitations.....	108
3.5. Conclusion	108
3.6. Supplementary Figures	110
Chapter 4	114
4.1. Introduction	116
4.2. Methods	118
4.2.1. Ethics statement	118
4.2.3. Animals	118
4.2.4. Experimental Protocol	118
4.2.4. Animal preparation for MRI.....	120
4.2.5. rTMS procedure.....	120
4.2.6. Magnetic field measurements.....	120
4.2.7. MRI data acquisition.....	121

4.2.8. Image processing	122
4.2.9. Image analysis	123
4.3. Results and Discussion	124
4.3.1. Identification of resting-state brain networks	125
4.3.2. Reproducibility over time and between subjects	130
4.3.3. Effects of LI-rTMS on resting-state brain activity	132
4.3.4. Use of anaesthetics in rs-fMRI and rTMS studies in rodents	140
4.4. Conclusion	142
4.5 Supplementary Figures and Tables	143
Chapter 5	145
5.1. Introduction	147
5.2. Materials and Methods	150
5.2.1. Animals	150
5.2.2. Experimental Protocol	150
5.2.3. Data acquisition	151
5.2.4. Image processing and analysis	152
5.2.5. MRS data analysis and presentation	153
5.3. Results	154
5.3.1. Template RSNs identified by group-ICA	154
5.3.2. Functional connectivity changes	156
5.3.3. Changes in metabolite ratios	159
5.4. Discussion	162
5.4.1. Functional connectivity changes in 10 Hz group	163
5.4.2. Functional connectivity changes in 1 Hz group	164
5.4.3. Changes in neurometabolite concentrations induced by 10 Hz and 1 Hz stimulation	167
5.5. Conclusion	170
5.6. Supplementary Methods	171
5.6.1. Animal preparation for MRI	171
5.6.2. Data acquisition	171
5.6.3. Image processing	173
5.6.4. Image analysis	174
5.7. Supplementary Figures and Tables	175
Chapter 6	183
6.1. Introduction	185
6.2. Materials and Methods	187
6.2.1. Ethics statement	187
6.2.2. Animals	187
6.2.3. Chronic restraint stress procedure	187
6.2.4. Behavioural tests	188
6.2.5. MRI data acquisition	192
6.2.6. Analysis steps	195
6.3. Results	200
6.3.1. Increase in anxiety and depression-like behaviours	200
6.3.2. Changes in resting-state functional connectivity	214

6.3.3. Changes in neurometabolite levels as detected by ¹ H-MRS	217
6.3.4. Change in hippocampal volume	220
6.3.5. Correlations	221
6.4. Discussion.....	223
6.4.1. Aberrant resting-state functional connectivity following chronic restraint stress.....	223
6.4.2. Decrease in glutamate and glutamine levels following chronic restraint stress	227
6.4.3. Decrease in hippocampal volume	229
6.4.4. Study limitations.....	230
6.5. Conclusion	231
Chapter 7.....	233
7.1. Introduction	235
7.2. Materials and Methods.....	236
7.2.1. Animals	236
7.2.2. Study Overview.....	237
7.2.3. Chronic restraint stress.....	239
7.2.4. Repetitive Transcranial Magnetic Stimulation	239
7.2.5. Behavioural testing.....	240
7.2.6. Magnetic Resonance Imaging.....	241
7.3. Results.....	245
7.3.1. Short-term Pilot Study: Standard vs Accelerated Treatment	245
7.3.2. Main Study – extended longitudinal study of accelerated LI-rTMS following chronic restraint stress	248
7.4. Discussion.....	260
7.4.1. Decreased functional connectivity and behavioural response following Chronic Restraint Stress	260
7.4.2. Accelerated LI-rTMS did not affect connectivity, hippocampal volume, metabolites or behaviour	262
7.4.3. Conclusion	264
7.5. Supplementary Material	265
7.5.1. Full Behavioural Methods.....	265
7.5.2. Summary tables for pilot study	268
7.5.2. Summary tables and figures for main study.....	271
7.5.3. Resting-state fMRI: Independent component analysis methods and results	279
Chapter 8.....	283
8.1. Introduction	285
8.2. Materials and Methods.....	286
8.2.1. Animals	286
8.2.2. MRI data acquisition.....	288
8.2.3. dMRI data analysis.....	289
8.2.4 Brain immunohistochemistry	292
8.3. Results.....	293
8.3.1. White matter changes following 10 Hz and 1 Hz LI-rTMS in healthy rats	293
8.3.2. Rat model of depression: white matter changes following CRS	296
8.3.3. Rat model of depression and treatment: white matter changes following CRS and accelerated 10 Hz LI-rTMS.....	300

8.4. Discussion	305
8.4.1 High-frequency LI-rTMS induces greater and faster changes in the white matter of healthy rats than low-frequency LI-rTMS	305
8.4.2 Compromised brain maturation-related changes following CRS	307
8.4.3 Accelerated 10 Hz LI-rTMS rescued brain maturation-related changes	308
8.4.4 Study limitations and future directions	310
8.4.5 Conclusion	311
8.5. Supplementary Methods	311
8.5.1. LI-rTMS procedure	311
Animal preparation for MRI	313
8.5.2. MRI data acquisition	313
8.5.3. dMRI data analysis	315
8.5.2. Brain immunohistochemistry	318
8.6. Supplementary Figures	320
Chapter 9	322
9.1. Introduction	324
9.2. Methods	326
9.2.1. Animals	326
9.2.2. Sample preparation and sequencing	328
9.2.3. 16S data processing	329
9.2.4. Statistical analysis	331
9.3. Results	332
9.3.1. Effect of CRS on the gut microbiome	332
9.3.2. Effect of LI-rTMS on the gut microbiome	333
9.3.3. Correlation between the gut microbiome and brain and behavioural measures	337
9.4. Discussion	340
9.4.1. Diversity and volatility	340
9.4.2. CRS and LI-rTMS increase abundance of Firmicutes	342
9.4.3. Functional and pathway implications of microbiome changes	344
9.4.4. Correlations of microbiome with behaviour and MRI	345
9.4.5. Study limitations and future directions	346
9.4.6. Conclusion	347
9.5. Supplementary Figures	348
Chapter 10: General Discussion	356
10.1. Effect of LI-rTMS in healthy animals	356
10.1.1. Immediate effects of one LI-rTMS session	356
10.1.2. Immediate and long-term effects of repeated LI-rTMS delivery	357
10.2. Animal model of depression: using the HPA axis and glucocorticoids as a unifying theory	359
10.2.1. Glucocorticoids and myelination	361
10.2.2. Glucocorticoids and the hippocampus	362
10.3. Effect of LI-rTMS on animal model of depression	364
10.4. Limitations and future directions	367
10.5. Conclusion	370

References.....	371
Appendices.....	419
Appendix A	422
Appendix B.....	439
Appendix C.....	447
Appendix D	461
Appendix E	488
Appendix F	501
Appendix G	512
Appendix H	534
Appendix I	537
Appendix J	544
Appendix K	558

List of Figures

Chapter 1

Figure 1.1. Neuronal activation by TMS using a "figure-of-eight" coil.

Figure 1.2. Repetitive Transcranial Magnetic Stimulation (rTMS) protocols.

Figure 1.3. Human fMRI data showing whole-brain effects of (left) high-intensity rTMS at 110% resting motor threshold (RMT), and (right) low-intensity rTMS at 90% active motor threshold (AMT).

Figure 1.4. Evidence of functional connectivity abnormalities in patients with dystonia and changes following rTMS.

Figure 1.5. Evidence of correlation between behavioural improvements and functional connectivity before and after rTMS treatment.

Figure 1.6. Evidence of translatability of fMRI studies: similar brain regions forming part of the default mode network (DMN) in the rat (Paxino's atlas coordinates indicated) and human (Talairach coordinates indicated) brains.

Figure 1.7. rTMS coil size with respect to brain sizes of humans, macaque and rodents.

Chapter 2

Figure 2.1. Time course of mean (\pm standard deviation) blood glucose concentration during anaesthesia of Sprague-Dawley rats in Group T (0.05 mg/kg medetomidine subcutaneous (SC) followed by a continuous infusion of 0.15 mg/kg/h SC with 0.5% isoflurane; squares) and Group SC (0.05 mg/kg medetomidine SC; triangles).

Figure 2.2. Time course of mean (\pm standard deviation) serum medetomidine concentration after subcutaneous administration of 0.05 mg/kg medetomidine in six Sprague-Dawley rats.

Chapter 3

Figure 3.1. Data analysis pipeline.

Figure 3.2. Atlas-based regions of interest positioning within the retrosplenial cortex.

Figure 3.3. Resting-state networks resulting from group-ICA.

Figure 3.4. Interoceptive network (C1) and default mode network (C2) identified from group-ICA and SCA using baseline rs-fMRI data.

Figure 3.5. Comparison of SCA results when using atlas-based seeds vs individualised seeds on ICA-cleaned data.

Chapter 4

Figure 4.1. Experimental protocol.

Figure 4.2. Independent component maps of pre-stimulation rs-fMRI group overlaid on 3D-rendered standard Sprague Dawley brain atlas.

Figure 4.3. Thresholded independent component spatial maps showing the resting-state network in the pre-stimulation rs-fMRI group-ICA dataset.

Figure 4.4. Reproducibility between sessions and between subjects of a representative group-ICA component.

Figure 4.5. Coil position and magnetic field.

Figure 4.6. Homologous group-ICA components showing synchronised resting-state neuronal activity of isoflurane-anaesthetized rats before and after LI-rTMS at four frequencies: 10 Hz, BHFS, 1 Hz and cTBS.

Chapter 5

Figure 5.1. Timeline of an experiment for one rat.

Figure 5.2. Volume of interest (VOI) positioning.

Figure 5.3. Template resting-state networks from baseline rs-fMRI scans.

Figure 5.4. Functional connectivity changes within the (A) interoceptive/default mode network, (B) cortico-striatal-thalamic network and (C) basal ganglial network induced by 10 Hz LI-rTMS.

Figure 5.5. Functional connectivity changes within the (A) cortico-striatal-thalamic network, (B) basal ganglial network and (C) the salience network induced by 1 Hz LI-rTMS.

Figure 5.6. Longitudinal changes in metabolite ratios at the different timepoints in rat sensorimotor cortex following 10 Hz and 1 Hz LI-rTMS.

Chapter 6

Figure 6.1. Experimental timeline.

Figure 6.2. Voxel position for proton magnetic resonance spectroscopy.

Figure 6.3. Effect of chronic restraint stress on exploration in open (A) and closed (B) arms and on stress-response behaviours (C-D) displayed during elevated plus maze test.

Figure 6.4. Effect of chronic restraint stress on behaviours displayed during forced swim test.

Figure 6.5. Decreased functional connectivity within the salience and interoceptive networks following chronic restraint stress as detected by dual regression (A & B) and corresponding Cumming estimation plots (C & D).

Figure 6.6. Increased functional connectivity to the cingulate cortex following chronic restraint stress as detected by seed based analysis (A) and corresponding Cumming estimation plots (B).

Figure 6.7. Representative spectra obtained from LCModel for proton magnetic resonance spectroscopy data at baseline (A) and restraint timepoints (B) for the CRS group and effect of restraint on glutamine (C), glutamate (D) and combined glutamine and glutamate (E).

Figure 6.8. Correlation between weight of animals and whole-brain volume at baseline (A) and percentage hippocampal volume before and after chronic restraint stress (B).

Figure 6.9. Correlations between behavioural tests and MRI measures.

Chapter 7

Figure 7.1. Experimental timeline and study design.

Figure 7.2. Comparisons of depression and anxiety-related behaviours during forced swim test (A-B) and elevated plus maze test (C-F) between active and sham groups of the accelerated (A, C, E) and standard (B, D, F) LI-TMS protocols.

Figure 7.3. Comparisons of functional connectivity to the cingulate cortex between baseline and post-CRS timepoints assessed via seed based analysis (A) and Cumming estimation plot (B).

Figure 7.4. Comparisons of depression-related behaviours at baseline and post-CRS timepoints from the Elevated Plus Maze (A-B) and Forced Swim Test (C-E).

Figure 7.5. Comparisons of functional connectivity to the cingulate cortex across all timepoints for active treatment (A), sham treatment (B) and depression control (C) conditions.

Figure 7.6. Comparisons of total hippocampal volume across all timepoints for active treatment (A), sham treatment (B) and depression control (C) conditions.

Figure 7.7. Concentration levels across all timepoints for Glutamate (Glu) (A-C) and GABA (D-F).

Figure 7.8. Behaviours with significant interactions from the Elevated Plus Maze (A-D) and Forced Swim Test (E-H) displayed across all timepoints.

Chapter 8

Figure 8.1. Timeline of an experiment.

Figure 8.2. TBSS analysis shows significant changes in diffusion and kurtosis parameters following 10 Hz or 1 Hz LI-rTMS in healthy rats ($P_{\text{Bonferroni}} < 0.006$).

Figure 8.3. Significant changes in DTI and DKI measures within the internal and external capsules and fimbria in healthy animals receiving 10 Hz or 1 Hz LI-rTMS ($p_{\text{FDR}} < 0.006$).

Figure 8.4. Chronic restraint stress (CRS) results in significant changes in the white matter ($P_{\text{Bonferroni}} < 0.025$).

Figure 8.5. Chronic restraint stress (CRS) results in significant changes in (A) DTI measures and (B) fibre cross-section (FC), combination of apparent fibre density and FC (FDC), and (C) average pathlength mapping (APM) within white matter regions.

Figure 8.6. Increase in (A) DTI/DKI FA and (B) fibre cross-section following restraint in animals receiving active (CRS⁺/10Hz⁺), sham (CRS⁺/0Hz⁺), and no stimulation (CRS⁺/0Hz⁻).

Figure 8.7. Significant changes in (A) DKI RD and (B) DTI RD within the corpus callosum and fimbria in animals receiving active (CRS⁺/10Hz⁺), sham (CRS⁺/0Hz⁺), and no stimulation (CRS⁺/0Hz⁻).

Figure 8.8. Myelin Basic Protein (MBP) immunostaining in CRS animals receiving active (CRS⁺/10Hz⁺), sham (CRS⁺/0Hz⁺), and no stimulation (CRS⁺/0Hz⁻).

Chapter 9

Figure 9.1. Experimental timeline.

Figure 9.2. Effect of chronic restraint stress on abundance of Deltaproteobacteria class (a), and its corresponding Desulfovibrionales order (b), and *Anaerostipes* (c), and *Frisingicoccus* (d) genera of the Clostridia class.

Figure 9.3. Changes in abundance of taxa between timepoints within the active, sham and depression control groups.

Figure 9.4. Changes in KEGG pathways between timepoints within the active, sham and depression control groups.

Figure 9.5. Correlations between microbiome data and MRI and behavioural measures.

Chapter 10

Figure 10.1. Simplified schematic representation of the potential effects of rTMS on the elements involved in the pathogenesis of depression.

List of Tables

Chapter 2

Table 2.1. Mean (\pm standard deviation) concentration of expired isoflurane during administration of isoflurane after an initial dose of medetomidine of 0.05 mg/kg SC followed by a continuous medetomidine infusion of 0.15 mg/kg/h SC (Group T) or a medetomidine dose of 0.05 mg/kg SC (Group SC).

Table 2.2. Individual and mean (\pm standard deviation) pharmacokinetic (PK) and pharmacodynamic parameters after administration of 0.05 mg/kg SC medetomidine in seven Sprague-Dawley rats.

Chapter 3

Table 3.1. ICA templates and group comparisons.

Table 3.2. Functional connectivity changes within the interoceptive/default mode networks using different ROIs within the retrosplenial cortex for seed-based correlation analysis of ICA-cleaned rs-fMRI data.

Chapter 5

Table 5.1. Summary of brain regions within the four components identified by group-ICA.

Table 5.2. Summary of results from repeated-measures ANOVA of neurometabolite levels to test for main effect of timepoint.

Chapter 6

Table 6.1. Weight of animals and size of restraints.

Table 6.2. Statistical table indicating the results of all analyses.

Table 6.3. Summary of changes in functional connectivity within the interoceptive and salience networks when using all rs-fMRI data from post-restraint timepoint vs using a subset of animals showing greatest behavioural changes in forced swim test (FST).

Chapter 8

Table 8.1. Statistical table indicating the results of MBP analyses.

Chapter 9

Table 9.1. Summary of changes in abundance for KEGG functional pathways following chronic restraint stress (CRS) and between timepoints within the active, sham and depression control groups.

Chapter 10

Table 10.1. Summary of the frequency-specific effects of LI-rTMS on healthy rats from Chapters 4, 5 and 8.

Table 10.2. Summary of the effects of CRS on rats from Chapters 7-9.

Table 10.3. Summary of the effects of LI-rTMS on CRS rats from Chapters 7-9.

(Page intentionally left blank)

Chapter 1: General Introduction

Published as:

1. Seewoo, B.J., Etherington, S.J., Feindel, K.W. & Rodger, J., 2018. Combined rTMS/fMRI studies: An overlooked resource in animal models. *Frontiers in Neuroscience*. 12, 180. doi: 10.3389/fnins.2018.00180 (Appendix A)
2. Seewoo, B.J., Etherington, S.J. & Rodger, J., 2019. Transcranial Magnetic Stimulation. *eLS*. John Wiley & Sons, Ltd, pp. 1–8. doi: 10.1002/9780470015902.a0028620 (Appendix B)

1.1. Overview

An exciting approach for the treatment of neuropsychiatric conditions is to use neuronal activity itself to encourage repair and improve brain function. This method can be used as an adjuvant with other interventions and might prove to be more effective and specific than a pharmacological approach, which often has side-effects and might not induce lasting changes. Transcranial magnetic stimulation (TMS) is a neuromodulation technique that uses magnetic fields to induce electrical currents in the brain, thereby modulating neuronal activity and networks (Barker and Freeston, 2007; Wassermann and Zimmermann, 2012).

This technique has advantages over direct electrical stimulation of nerves by application of external current (e.g., electroconvulsive therapy, ECT) which has been widely used in the treatment of several psychiatric conditions (Fujiki and Steward, 1997; Barker and Freeston, 2007). Unlike ECT which involves the delivery of electrical signals via implanted electrodes, TMS is entirely non-invasive and does not require the use of anaesthesia. TMS is able to stimulate the human brain and deep peripheral nerves without causing pain as there is no induced current that passes through the skin, where most of the pain fibre nerve endings are located (Barker and Freeston,

2007). TMS also very rarely causes seizures compared to other techniques for electrical or pharmacological modulation of brain function (Wassermann and Zimmermann, 2012). This safety and lack of discomfort enable the technique to be readily used on patients and volunteers for therapeutic and research purposes. TMS can modulate brain function both locally (directly under the stimulating coil) and in distant brain regions by driving existing neural networks (Bohning et al., 1999).

Repetitive transcranial magnetic stimulation (rTMS) delivers trains of closely spaced pulses to the brain to induce transient modulation of neural excitability and brain function. The modulation induced by rTMS can outlast the stimulation period leading to long-term changes in synaptic plasticity and behaviour (for review, see Lenz and Vlachos, 2016). rTMS has been shown to have therapeutic potential for a range of neurological and psychiatric disorders, including depression (O'Reardon et al., 2007), Parkinson's disease (Arias-Carrion, 2008), obsessive-compulsive disorder (Jaafari et al., 2012), and stroke (Corti et al., 2012). To improve the safety and efficacy of rTMS in a clinical setting, a better understanding of the mechanism of action of rTMS is required (Muller-Dahlhaus and Vlachos, 2013). Improving understanding of the underlying mechanism of rTMS in health and in depression is the focus of this thesis.

Animal models have been useful in elucidating some of the mechanisms of rTMS as they allow us to perform invasive studies of molecular and genetic changes that are not ethically possible in humans. However, to align the different experimental approaches used in preclinical animal studies (invasive: cellular and molecular outcomes) and in human studies (non-invasive: e.g., TMS and motor-evoked potentials (MEPs), electroencephalography (EEG), optical imaging, positron emission tomography

(PET), magnetic resonance imaging (MRI), behaviour) is difficult. The purpose of this thesis is to investigate neural plasticity induced by low-intensity rTMS (LI-rTMS) and its mechanisms of action non-invasively in rats. To address this broad aim, this thesis uses healthy rats and a rat model of depression to examine in-vivo effects of LI-rTMS in normal and abnormal systems on brain function, chemistry and structure using MRI as well as on behaviour and gut microbiome. These effects are then related to possible cellular and molecular mechanisms.

This literature review comprises information taken directly from a review article (Seewoo et al., 2018a) and a book chapter (Seewoo et al., 2019b) which have been previously published (see Appendix A and B respectively). First, the principle underlying TMS and different stimulation paradigms are described, with specific focus on frequency of stimulation which is investigated within this thesis. The non-invasive methods for monitoring the effects of TMS are then described with reference to human and clinical studies. Next, current understandings of biological mechanisms for rTMS are discussed as observed in animal and cellular studies. This thesis investigates only LI-rTMS but literature for both LI-rTMS and rTMS are reviewed, and I argue that high and low-intensity rTMS may share some common modes of action. Since the majority of this thesis describes the effect of rTMS on functional connectivity of the brain, rTMS frequencies and their specific effects in human functional connectivity studies are described in greater detail. The potential therapeutic applications of combined rTMS/MRI human studies are then discussed, along with the current clinical applications of rTMS, with the focus being depression. The importance of altered gut microbiome as a pathology of depression is also reviewed briefly. Finally, the need for

use of non-invasive MRI in animal rTMS studies is highlighted. Comparison of rTMS effects in human and animal studies provides insight into the usefulness of animal models in understanding and improving rTMS based treatments for humans. The potential challenges associated with using MRI and rTMS in animals are also reviewed. The chapter concludes by outlining the scope and aims of this thesis.

1.2. The principle underlying TMS

Faraday's law of electromagnetic induction states that moving magnetic fields can induce a transient electrical current in a nearby conductor (Faraday, 1840). TMS applies this principle to induce electrical currents in adult human brains (Walsh, 1998). A wound coil is placed on the scalp of the subject over the region of interest (Figure 1.1). The magnetic field, induced by the current flowing through the TMS coil, passes into the brain and induces currents within the brain, stimulating neuronal activity and affecting brain function (Walsh, 1998). The magnetic fields pass freely into the brain, unimpeded by skin, muscle or skull because magnetic fields are not blocked by non-magnetic objects (unlike electricity, which cannot flow through non-conducting materials).

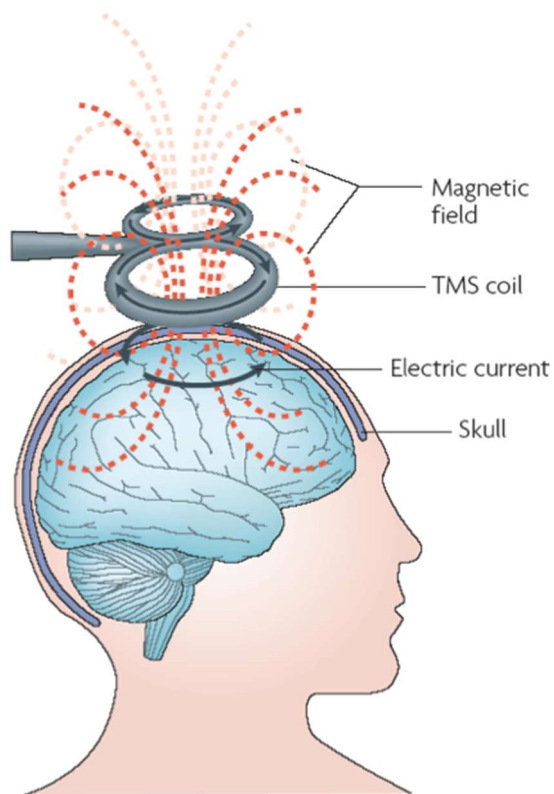


Figure 1.1. Neuronal activation by TMS using a "figure-of-eight" coil. The electrical current in the coil (black arrows in the coil) generates a magnetic field (red), which induces a current in the brain (black arrows in brain). This causes stimulation of neurons, with the optimum site of activation being under the midpoint of the figure-of-eight. The electrical current in the coil and the current induced in the brain by the magnetic field flow in the same plane, tangential to the skull-brain surface. TMS stimulates activity in neurons, affecting the functioning of the cortex (Walsh, 1998). The effects of TMS on neural function are then measured indirectly, for example by recording muscle activity in the thumb (Walsh, 1998; Edwards et al., 2008). Reprinted by permission from Springer Nature Customer Service Centre GmbH: Springer. *Nature Reviews Neuroscience*. Is there a future for therapeutic use of transcranial magnetic stimulation? by Ridding and Rothwell (2007).

1.3. TMS Protocols

Early TMS devices emitted only a single, brief magnetic pulse and were generally used to deliver a strong stimulus that triggered action potential firing in a pathway and elicited a peripheral response (e.g., muscle contraction). Modern devices can generate long trains of closely spaced pulses, called repetitive TMS (rTMS), at different rates (frequencies) and in different patterns. rTMS can have effects on neuro-excitability and behaviour that exceed the duration of the stimulation.

The factors that determine the magnitude, duration, and direction (increase or decrease) of a change in excitability of the brain can be divided into three principal categories —strength of stimulation (intensity of magnetic pulse), geometry (coil shape and orientation), and timing (the pattern, frequency, and duration of pulse delivery).

Magnetic field strength is typically expressed in Tesla (T). A classic TMS device creates a moderately powerful magnetic field of 1 to 2.5 T (Rossini et al., 1994) that is associated with action potential firing in underlying cortical tissue (Pashut et al., 2011).

More recently, LI-rTMS protocols have been used which induce weak currents that do not induce action potentials, but nonetheless induce plasticity by other mechanisms, as discussed below. Geometry refers to the interaction of the spatial distribution and orientation of the induced electric field with the cortical neuroanatomy. For example, circular coils generate a diffuse magnetic field, while “figure-of-eight” coils are widely used to produce focal stimulation of a small brain area (Thielscher and Kammer, 2004) and still other coil configurations have been designed for stimulating deep brain regions (Deng et al., 2014). How the cortex responds to magnetic stimulation also depends on the fine and gross three-dimensional structure of the cortex. For example, computational modelling suggests that TMS stimulates axons more effectively than nerve cell bodies and that cortical infoldings will influence which brain region is most strongly activated. Models also suggest that TMS preferentially stimulates neural processes that run in parallel with the axis of the magnetic coil, meaning that all pathways within a particular radius of the coil may not be equally stimulated (Lefaucheur, 2008). The effect of experimental design and technical parameters, including the coil shape and orientation, and the duration of stimulation, are reviewed

elsewhere (Klomjai et al., 2015). Here I will focus on frequency of stimulation because this is the key factor that I have addressed in my experiments.

The frequency of stimulation depends on the inter-pulse interval (number of pulses per second) and the pattern of stimulation (presence and length of intervals between trains of pulses). The four most commonly used rTMS paradigms are 1 Hz, 10 Hz, continuous theta burst stimulation (cTBS), and intermittent theta burst stimulation (iTBS) (see Figure 1.2 below). Other complex stimulation patterns, such as the biomimetic high-frequency stimulation or BHFS (Hamada et al., 2008; Lefaucheur, 2009; Martiny et al., 2010; Rodger et al., 2012) based on endogenous neuronal firing patterns, are being investigated based on the rationale that TMS that mimics endogenous neuronal firing will drive cortical networks more powerfully than simple, regular firing frequencies.

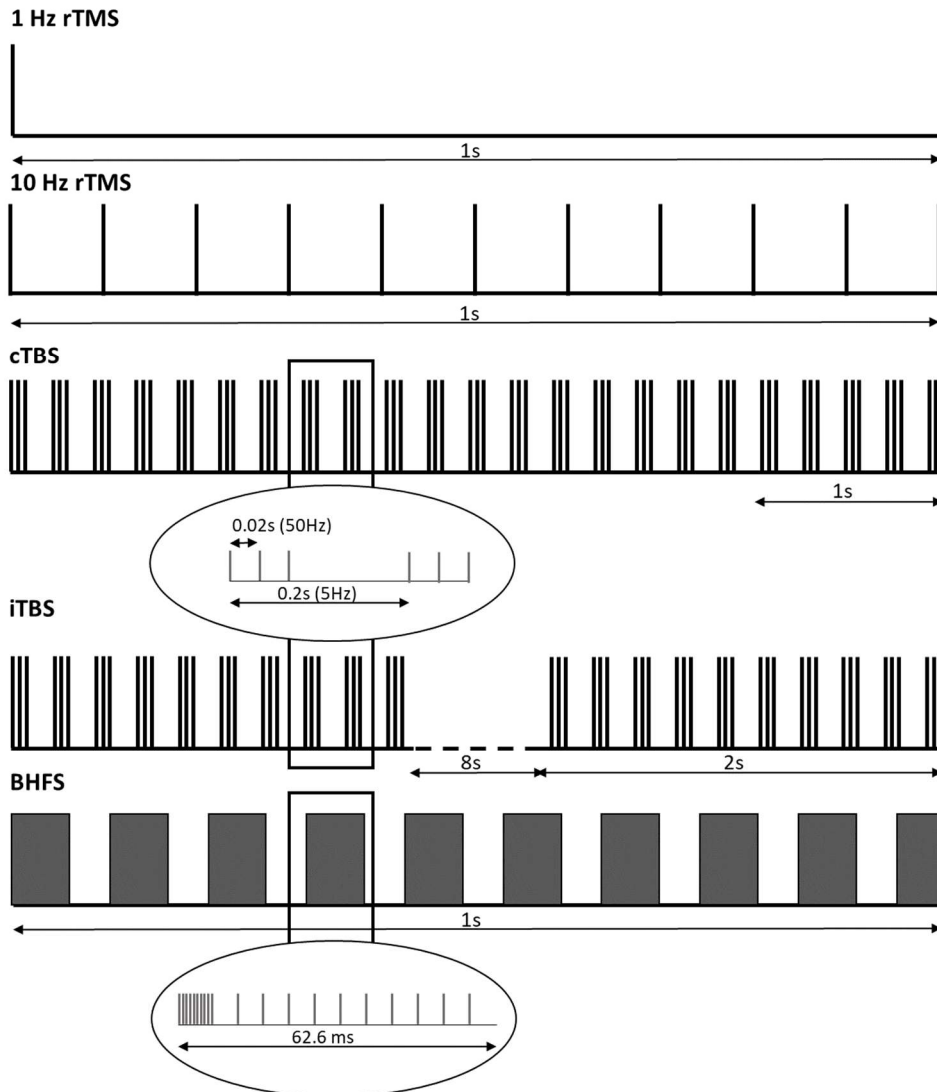


Figure 1.2. Repetitive Transcranial Magnetic Stimulation (rTMS) protocols. Simple frequencies (1 Hz and 10 Hz) consist of identical stimuli spaced by an identical inter-stimulus interval. Theta burst stimulation (TBS) involves bursts of high-frequency stimulation (3 pulses at 50 Hz) repeated with an interval of 0.2 s (5 Hz). In continuous TBS (cTBS), bursts are applied continuously for 40 s (i.e., 600 stimuli) without breaks. In an intermittent TBS (iTBS) protocol, bursts are delivered for 2 s, then repeated every 10 s (2 s of TBS followed by a break of 8 s) for a total duration of 190 s (i.e., 600 stimuli). Biomimetic High-Frequency Stimulation (BHFS) involves 62.6 ms trains of 20 pulses repeated at a frequency of 9.75 Hz.

Simple frequencies like 1 Hz (1 pulse per second) and 10 Hz (10 pulses per second) are used to deliver regular continuous stimulus trains with no inter-train interval. A large body of literature shows that low-frequency (1 Hz) rTMS decreases brain excitability while high-frequency (10 Hz) rTMS increases brain excitability in humans (for review, see Klomjai et al., 2015).

In contrast to the simple frequencies, TBS uses a composite stimulation pattern, consisting of repeating bursts of stimuli (Larson et al., 1986). Each burst consists of three pulses of stimulation at 50 Hz, and the bursts are repeated at 5 Hz (0.2 s) (for review, see Cárdenas-Morales et al., 2010). This pattern of stimulation is based on the endogenous brain oscillations observed in the hippocampus (Huang et al., 2005), with human hippocampal theta oscillations being at a lower frequency (around 3 Hz) than the hippocampal theta oscillations of rats (8 Hz) (Watrous et al., 2013; Jacobs, 2014). These repeating bursts are delivered continuously (cTBS) or intermittently (iTBS, bursts repeated at variable intervals) (Larson et al., 1986; Cárdenas-Morales et al., 2010). Continuous and intermittent TBS generally have opposing effects on brain excitability (Chung et al., 2016). For example, cTBS stimulation of the human motor cortex inhibits corticospinal outputs whereas application of iTBS in the same region is associated with a significant strengthening of spinal outputs from the motor cortex (Huang *et al.* 2005). There has been particular interest in the clinical application of complex rTMS protocols because they have been shown to generate lasting brain modulatory effects that are equivalent to simple stimulation protocols (e.g., 1 Hz) but can be elicited using a shorter period of less intense magnetic stimulation (Huang et al., 2005; Chung et al., 2016).

BHFS is a complex wave form (Martiny et al., 2010) that replicates the patterns of nerve activation in muscles during exercise (Rodger et al., 2012) and is based on the patent PCT/AU2007/000454 of Global Energy Medicine. It involves a total of 10 min stimulation period and comprises of 62.6 ms trains of 20 pulses, repeated at a frequency of 9.75 Hz (Grehl et al., 2015). The trains are repeated at 6.71 Hz for 1 min

(warm-up), 10.1 Hz for 8 min (treatment), and 6.26 Hz for the last minute (cooldown) (Rodger et al., 2012). Although it has not been applied therapeutically in humans, animal research has shown that it causes reorganisation of abnormal neural networks (Rodger et al., 2012; Makowiecki et al., 2014) and induce climbing fibre re-innervation to denervated hemi-cerebellum (Morellini et al., 2015).

1.4. Monitoring the effects of TMS

Delivery of a single, high-intensity TMS pulse can produce cortical currents that fire action potentials in neurons within a particular neuronal pathway, eliciting a measurable peripheral response. The most widespread application of this approach has been to stimulate the primary motor cortex with TMS to generate a muscle twitch. Electrical recording from the stimulated muscle allows detection of motor evoked potentials (MEPs) that provide an indication of the excitability of the motor cortex and of the integrity of associated corticospinal pathways (Rossini et al., 1994; Lee et al., 2006; Wassermann and Zimmermann, 2012). rTMS can be used to generate a lasting change in the excitability of the motor cortex that is apparent in MEP recordings (Lee et al., 2006; Klomjai et al., 2015). Although MEPs, which are currently the most common outcome measure used in humans, can also be measured in animals (Rotenberg et al., 2010; Sykes et al., 2016), this approach lacks sensitivity and can be applied only to motor cortical areas. However, the vast majority of TMS research and clinical treatments target non-motor regions such as the prefrontal or sensory cortex (e.g., Schneider et al., 2010; Liston et al., 2014; Jansen et al., 2015; Valchev et al., 2015), with effects that extend to deeper regions that cannot be probed by MEPs (e.g., Komssi et al., 2004). Analogous to measuring motor cortical excitability with MEPs,

changes in intracortical excitability in non-motor regions can be monitored by combining TMS with electroencephalograms (EEG) or optical imaging from other cortical regions (Ilmoniemi and Kičić, 2010) in humans and in animal models. However, EEG (e.g., Komssi et al., 2004; Benali et al., 2011) and optical imaging (e.g., Allen et al., 2007; Kozel et al., 2009) have restricted depth of recording and can detect rTMS-induced functional changes only in the most superficial regions of the brain.

The ability to measure whole-brain functional changes before and after rTMS is important because rTMS can induce widespread changes in both cortical and subcortical networks. Currently, PET and MRI are the only techniques capable of measuring the functional effects of rTMS in the whole brain. Combined rTMS/PET has been used in humans (e.g., Paus et al., 1997; Kimbrell et al., 1999; Speer et al., 2000; Conchou et al., 2009) and animal models (e.g., Gao et al., 2010; Salinas et al., 2013). However, a major disadvantage of PET with regards to safety is the use of radiotracers, exposing subjects to ionizing radiation. A single PET scan using a standard radiotracer dose leads to radiation exposure up to an order of magnitude greater than that received annually from background radiation. Therefore, longitudinal rTMS/PET studies requiring repeated measurements are not ethically feasible. MRI, on the other hand, does not require the use of ionizing radiation and therefore, is a safe imaging tool appropriate for repeated long-term experiments.

In the last two decades, several magnetic resonance (MR) techniques have been developed to provide unique and non-invasive measurement capabilities for studies of basic brain function and brain diseases in humans. MRI uses a powerful, varying magnetic field, much stronger and more diffuse than magnetic fields associated with

rTMS, to non-invasively image the brain (McRobbie et al., 2007). The same instrument is used to obtain different types of information, e.g., changes in brain functional connectivity, changes in the concentration of neurometabolites in different brain regions and changes in micro and macro structure of the brain. MRI can be used to compare brain function, chemistry, and structure of patients with a diseased state to the healthy population and track improvement in these measures following treatment.

1.4.1. Changes in functional connectivity: fMRI

fMRI detects changes in brain activity during an active task and resting-state fMRI (rs-fMRI) provides information about the connectivity between brain regions at rest, i.e., when no specific stimulus or task is presented. Rs-fMRI detects brain regions whose patterns of spontaneous blood oxygen level-dependent (BOLD) contrast fluctuations are temporally correlated when the subject is at rest. These brain regions with coherent spontaneous fluctuations in activity form an organized network called the resting-state network (Biswal et al., 1995). Bohning et al. (1998) were the first to demonstrate the feasibility of combining TMS and fMRI protocols, by performing TMS stimulation inside an MRI scanner. TMS applied to the primary motor cortex (M1) in humans resulted in a significant increase in activity in M1 as detected by the fMRI scan. Soon after, the same authors demonstrated that there was a significant increase in activity not only in M1 but also in areas distal to the stimulation site (e.g., the contralateral M1 and ipsilateral cerebellum), illustrating the potential of this technique for mapping connectivity patterns between brain areas (Bohning et al., 1999). The ability of rTMS to target both local and remote brain regions was confirmed by Bestmann et al. (2004), who used interleaved rTMS/fMRI to compare different intensities of rTMS (Figure 1.3). They showed that fMRI can detect effects of rTMS

delivered at an intensity that does not elicit a motor response (i.e., MEP). Therefore, fMRI provides a significant improvement in terms of sensitivity and resolution over MEPs.

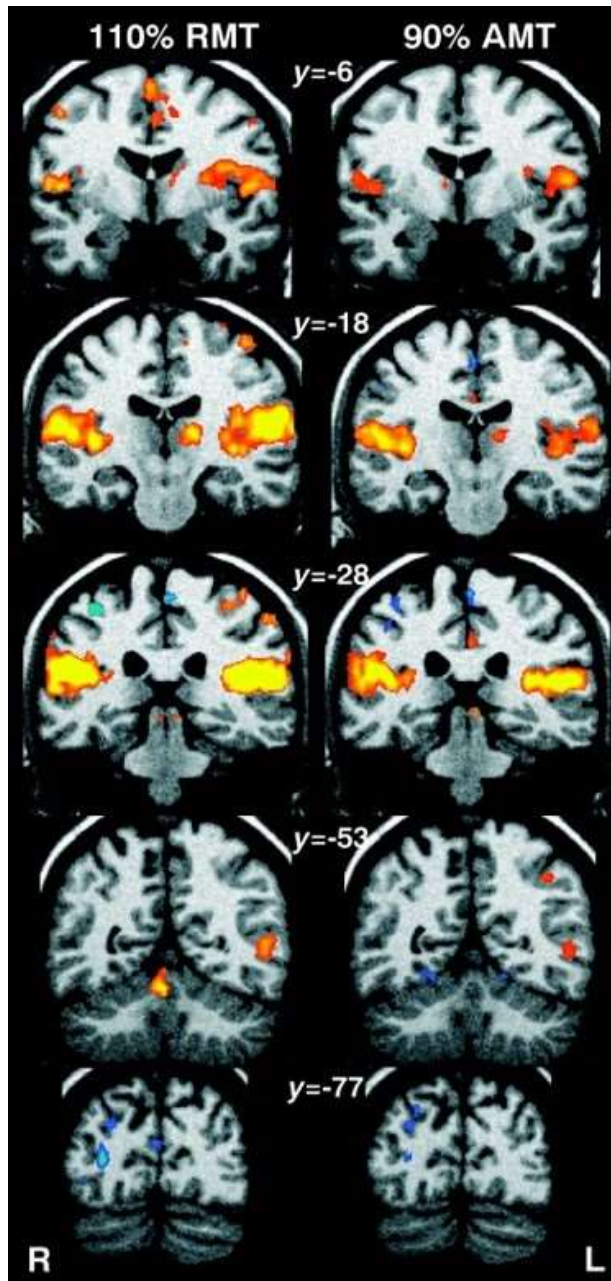


Figure 1.3. Human fMRI data showing whole-brain effects of (left) high-intensity rTMS at 110% resting motor threshold (RMT), and (right) low-intensity rTMS at 90% active motor threshold (AMT). Coronal standard MNI brain sections (Talairach coordinates indicated) with superimposed fMRI results are shown. Areas of significant ($n = 11$, corrected $p < 0.01$) activations during rTMS compared to rest have been coloured red-yellow, and decrease in fMRI signal in blue. Suprathreshold rTMS induced an increase in activity in the stimulated left sensorimotor cortex, medial supplementary and cingulate motor area, auditory cortex, lateral postcentral region, and left thalamus. Decrease in activity was observed in the right

sensorimotor cortex and occipital cortex. Subthreshold rTMS produced similar but smaller activations, with no significant changes in the stimulated brain region. Image from Bestmann et al. (2004). Permission to reuse Figure 7 from the article was granted by John Wiley and Sons and Copyright Clearance Center through their RightsLink® service on 10th of June 10 2020.

Since then, a range of combined rTMS/fMRI human studies has been conducted to record the rTMS-induced changes in hemodynamic activity both in healthy subjects and subjects with neurological disorders (Schneider et al., 2010; Fox et al., 2012a). In healthy subjects, for example, fMRI was used to detect plastic changes induced in the brain after 5 Hz rTMS was applied to the right dorsolateral prefrontal cortex (DLPFC) (Esslinger et al., 2014). No change in activation was detected at the stimulation site, but there was increased connectivity within the right DLPFC as well as from the stimulated DLPFC to the ipsilateral superior parietal lobule, which is functionally associated with the right DLPFC during working memory (Esslinger et al., 2014). This increased connectivity was associated with a decrease in reaction time during a working memory task (*n*-back task). These results suggested the presence of rTMS-induced plasticity in prefrontally connected networks downstream of the stimulation site (Esslinger et al., 2014). Similar results were found when Valchev et al. (2015) delivered a continuous train of theta burst stimulation (cTBS) to the left primary somatosensory cortex of healthy volunteers. Functional connectivity between the stimulated brain region and several functionally connected brain regions, including the dorsal premotor cortex, cerebellum, basal ganglia, and anterior cingulate cortex, decreased. Another study applying high-frequency (10 Hz) rTMS to the right DLPFC in healthy volunteers while passively viewing emotional faces found significant right amygdala activity attenuation when evaluating negatively valenced visual stimuli (Baeken et al., 2010b). Taken together, these studies show that rTMS can have

widespread effects, not limited to the stimulated brain area and demonstrate that brain stimulation studies and treatment plans need to take network-level effects into account. Although the hippocampus as a deep brain structure is unlikely to be directly modulated by rTMS, which affects only superficial regions immediately beneath the coil, an ipsilateral change in the hippocampus was detected following multiple-session high-frequency (20 Hz) stimulation to the left lateral parietal cortex of healthy adults (Wang et al., 2014). Increased functional connectivity was observed and this change was correlated with improved associative memory performance. The effect of rTMS on these brain regions (e.g., cerebellum, basal ganglia, cingulate cortex, amygdala, hippocampus) are interesting because they have therapeutic implications which will be summarized in Section 8, along with more detailed effects of rTMS on functional connectivity in the intact normal state versus diseased states.

The default mode network (DMN), a resting-state network with a synchronized activity pattern, shows highest activation when the subject is at rest and is deactivated in goal-oriented tasks (Raichle et al., 2001). The DMN has been associated with cognitive performance and is thought to play an important role in neuroplasticity through the consolidation and maintenance of brain functions (Marcotte et al., 2013). For example, a higher resting-state activity within the DMN is hypothesized to favour network efficiency (Kelly et al., 2008), while decreased connectivity between the frontal and posterior DMN brain regions is associated with functional deficits (Davis et al., 2009). Consistent with these hypotheses, patients with neurological and psychiatric disorders show DMN dysregulation compared with healthy individuals (for review, see Van den Heuvel and Hulshoff Pol, 2010). Disruptions in functional connectivity between brain

regions forming part of the DMN have been implicated, *inter alia*, in patients with conditions like Alzheimer's disease (Greicius et al., 2004), multiple sclerosis (Lowe et al., 2002; Sbardella et al., 2015), autism (Cherkassky et al., 2006; Kennedy et al., 2006), epilepsy (Waites et al., 2006), depression (Greicius et al., 2007), schizophrenia (Bluhm et al., 2007; Whitfield-Gabrieli et al., 2009), aphasia (Marcotte et al., 2013), and addiction (Sutherland et al., 2012; Lerman et al., 2014).

Given that the pathophysiology of many psychiatric and neurological disorders is believed to be related to altered neural connectivity and network dynamics, interleaved rTMS/fMRI protocols provide an opportunity to investigate altered patterns of neural activity in these disorders (for review, see Hampson and Hoffman, 2010). The activation patterns in healthy individuals and patients with neurological or psychiatric conditions can be compared after an rTMS session to determine how these patterns are disrupted in the disease state (Hampson and Hoffman, 2010). For example, Schneider et al. (2010) examined the effect of 5 Hz rTMS on the primary somatosensory cortex in patients with dystonia (a condition associated with impaired somatosensory ability) and healthy controls based on their ability to discriminate between two stimulation frequencies applied to the right index finger before and after the rTMS session. An fMRI scan was carried out together with the tactile discrimination task. Without rTMS application, patients showed relative overactivity in the basal ganglia compared to healthy controls (Figure 1.4A). rTMS led to improved performance in this task in healthy controls but not in the patients. There was increased activity detected in the stimulated primary somatosensory cortex and bilateral premotor cortex in both groups (Figure 1.4B and 1.4C) but fMRI detected an increase in activity

in the basal ganglia in healthy subjects only (Figure 1.4D), suggesting abnormal functional connectivity in the cortico-basal network in dystonia. The authors hypothesized that this could be related to altered sensory circuits and sensorimotor integration in patients with dystonia.

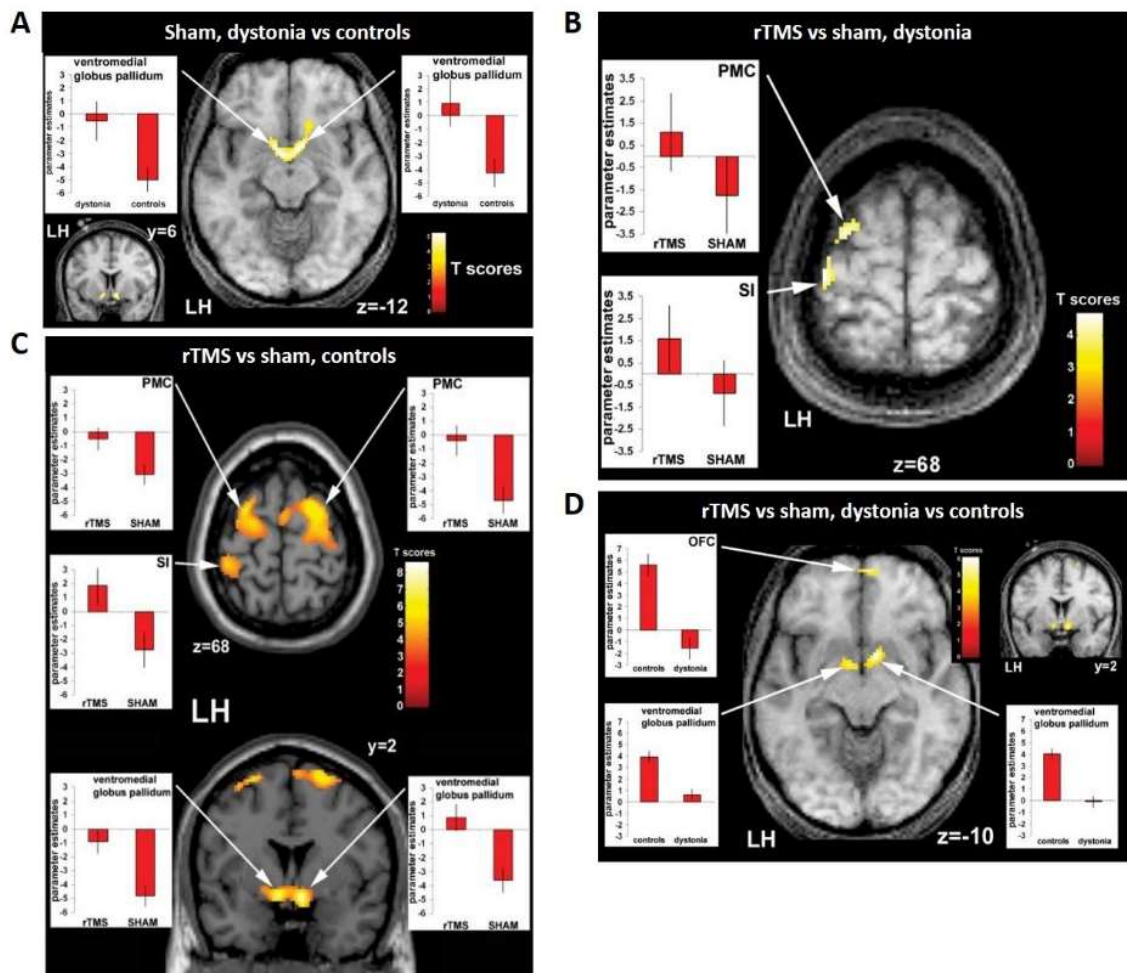


Figure 1.4. Evidence of functional connectivity abnormalities in patients with dystonia and changes following rTMS. (A) Connectivity maps of patients versus controls during the sham condition showing bilaterally greater activity in the ventromedial pallidum of patients compared to healthy controls. Effects of rTMS (real versus sham condition) on neuronal activity during sensory discrimination task in dystonia patients (B) and controls (C). Both patients with dystonia (B) and healthy controls (C) show relatively greater activity ipsilaterally in the left premotor cortex (PMC) and the left sensorimotor cortex (S1) following after real-rTMS compared to sham stimulation. In addition, there is activation of the ventromedial pallidum bilaterally in healthy controls, but not in patients with dystonia. (D) Interaction (group x condition) during rTMS in patients with dystonia compared to controls. Compared to controls, dystonia patients show reduced activity in the left orbitofrontal cortex (OFC) and the ventromedial pallidum bilaterally after real-rTMS compared to sham stimulation (D). Image from Schneider et al. (2010). Permission to reuse Figures 3 and 4 from the article was granted by John Wiley and Sons and Copyright Clearance Center through their RightsLink® service on 10th of June 2020.

Interestingly, rTMS has been shown to modulate functional connectivity in humans, but the direction (increase or decrease in activity) and extent of this modulation depend on the rTMS protocol used, as we review below (Fox et al., 2012a; more recent articles: Popa et al., 2013; Glielmi et al., 2014; Jansen et al., 2015; Li et al., 2016). Using fMRI, increases and decreases in functional activity have been found depending on the stimulated brain region and the frequency of rTMS, allowing insight into how rTMS affects complex brain circuits (Bohning et al., 1999; Kimbrell et al., 1999).

1.4.2. Changes in neurometabolic levels: MRS

Proton magnetic resonance spectroscopy (¹H-MRS) uses the same hardware as MRI to measure the levels of various metabolites in the brain. ¹H-MRS is extensively used in biomarker studies of neurological and psychiatric conditions because it enables non-invasive detection and quantification of neurometabolites directly in affected brain regions. The majority of studies exploring the effect of rTMS on neurochemical concentrations have been performed in patients with depression (Yüksel and Öngür, 2010; Zheng et al., 2010; Zheng et al., 2015; Croarkin et al., 2016; Dubin et al., 2016; Birur et al., 2017), but also in patients with schizophrenia (Klär et al., 2010; Birur et al., 2017; Dlabac-de Lange et al., 2017), epilepsy (Kristsen et al., 2013) and addiction (Qiao et al., 2016; Hone-Blanchet et al., 2017).

The effect of rTMS in neurometabolic concentrations depends on the neuropsychiatric condition and brain region and the interpretation of the meaning of the differences in neurometabolite levels depends on what is known about their biochemical functions. The commonly studied neurometabolites are creatine (Cr), phosphocreatine (PCr), combined Cr + PCr (tCr), glutamine (Gln), glutamate (Glu), combined Glu + Gln (Glx)

and γ -aminobutyric acid (GABA). Cr and PCr levels are a reflection of cellular adenosine triphosphate (ATP) metabolism (Pouwels and Frahm, 1998; Rae, 2014). They are easily detected and therefore, tCr is often used as the internal reference peak and other metabolites are reported as a ratio to tCr (Block et al., 2009; Walter et al., 2009; Xu et al., 2013a). Gln is the major precursor for neuronal Glu and GABA and has been used as an index of glutamatergic activity. Glu is the principal excitatory neurotransmitter in the central nervous system (CNS) (90% of synapses) while GABA is the principal inhibitory neurotransmitter, with GABAergic inter-neurons making up 15–20% of cortical neurons (Buzaki et al., 2007). Glx reflects the interaction of Glu and Gln and therefore, a change in Glx level indicates a change in glutamatergic neurotransmitter regulation (Kousi et al., 2013). Lower levels of Glx in the cortex as a result of altered Glu-Gln cycling is being increasingly recognised to be linked to the pathophysiology of several neuropsychiatric conditions including depression (Mirza et al., 2004; Hasler et al., 2007a; Moriguchi et al., 2019) and schizophrenia (Th  berge et al., 2003).

Accordingly, high-frequency rTMS to the prefrontal cortex has been found to increase cortical Gln and Glu levels in healthy volunteers (Michael et al., 2003), in patients with depression (Luborzewski et al., 2007; Yang et al., 2014b) and schizophrenia (Dlabac-de Lange et al., 2017). Studies on changes in GABA are less clear-cut probably due to poor signal resolution between these low-concentration metabolites in weaker magnetic fields (Puts and Edden, 2012). Nevertheless, several studies have consistently reported significant reductions in cortical GABA levels in depression (Hasler et al., 2007a; Price et al., 2009) and high-frequency rTMS has been shown to increase GABA concentration in the prefrontal cortex of patients with depression (Dubin et al., 2016).

1.4.3. Changes in structure: structural MRI and diffusion MRI

Structural MRI is increasingly being used for anatomical phenotyping in neuroscience research to elucidate relationships between structure and function. Anatomical MRI of the brain relies on proton density (amount of water) and T_1 and T_2 relaxation differences between tissue types such as grey matter compared to white matter (McRobbie et al., 2007). In T_1 -weighted images, only fat-containing tissue appear bright and since the CSF contains no fat, it appears black and grey matter is darker than white matter. In T_2 -weighted images, compartments filled with water like the cerebrospinal fluid appear bright while tissues with a high lipid content like the white matter appear dark. The local differences in fluid and fat content translate into different shades of grey that serve to outline the shapes and sizes of the brain's various subregions. Structural MRI data can be used to measure brain volumes, brain surface area or changes in brain foldings, the volume of regions of interest, diffuse changes in grey/white matter content or to assess localized lesions. These anatomical images are also used to map fMRI and DTI data which are usually acquired at much lower resolution. There is considerable evidence that many neuropsychiatric conditions are associated with abnormal volumes of brain subregions compared with healthy controls. For example, the volumes of several brain subregions are altered in depression (Kempton et al., 2011). Hippocampal atrophy is a well-researched pathophysiology of depression (Videbech and Ravnkilde, 2004; McKinnon et al., 2009; Brown et al., 2014). Repeated high-frequency rTMS to the left prefrontal cortex has been shown to rescue hippocampal volume (Hayasaka et al., 2017) and the volume of other brain regions such as the anterior cingulate, middle temporal gyrus, insula and angular gyrus (Lan et al., 2016; Taïb et al., 2018).

Diffusion MRI is used to detect changes in the white matter microstructure. Brownian motion of water molecules is restricted by the axonal membrane, such that water molecules diffuse along the axons, in the direction of least resistance. Fractional anisotropy (FA) is one of the most commonly studied diffusion measures. It is a scalar value between zero to one and measures the restriction of diffusion, a value of 0 being isotropic (no restriction) and 1 being restricted in all but one axis. Mean FA in the left middle frontal gyrus has been shown to be significantly reduced in treatment-resistant patients but rescued by high-frequency rTMS to the left DLPFC (Peng et al., 2012). Importantly, the increase in FA post-stimulation was correlated with the decrease in depressive symptoms (Peng et al., 2012). Similarly, another study found greater mean FA values in the left prefrontal white matter of patients with depression following active rTMS compared to sham rTMS (Kozel et al., 2011).

Given the high translatability of MRI, combined rTMS/MRI is a powerful tool amenable to visualising rTMS-induced changes at a high spatio-temporal resolution in both humans and animals. This integrated method can potentially help unravel the physiological processes underlying the rTMS-induced changes in the cortex and connected brain regions. Comparison between animal models and human studies will enable the identification of optimal combinations of rTMS parameters (e.g., frequency), and improve the efficacy of rTMS as a therapeutic tool. Additionally, the use of complementary experimental techniques through multimodal animal studies will allow one to study how rTMS-induced changes in neuronal activity translate into behavioural, cellular and molecular changes and therefore, have a better understanding of the underlying mechanisms of rTMS.

1.5. Biological mechanisms of TMS

Even though rTMS is being used extensively in a clinical context and clinical trials are abundant, not much is known about the brain and cellular mechanisms underlying its efficacy (Muller-Dahlhaus and Vlachos, 2013). Certainly, the intense neuronal activity generated by rTMS stimulation can alter nerve cell function by influencing gene expression (Pridmore and Belmaker, 1999). Importantly, these lasting changes in gene expression are not restricted to the site of magnetic stimulation but can be expressed in remote brain regions, possibly in response to the spread of electrical activity via brain networks (Fujiki and Steward, 1997; Ji et al., 1998). In addition to these distributed changes in gene expression, rTMS can alter the expression of secreted proteins, such as the growth factor BDNF (brain-derived neurotrophic factor), that could further distribute rTMS-induced change within the brain (Ljubisavljevic et al., 2015). Changes in gene expression induced by rTMS depend on the frequency and pattern of stimulation and are associated with improved recovery from brain injury in animals (Pridmore and Belmaker, 1999; Ljubisavljevic et al., 2015). Thus, there is evidence that using different rTMS paradigms has the potential to selectively stimulate gene expression in healthy and dysfunctional brain networks.

An area of particular interest to scientists unravelling the biological mechanisms of rTMS has been the similarities between processes activated by rTMS and those involved in forms of long-term synaptic plasticity, long-term potentiation (LTP) and long-term depression (LTD). LTP and LTD generate lasting change (strengthening and weakening respectively) in the strength of a particular synaptic connection depending on the pattern of activity at that synapse (Klompaj et al., 2015). LTP, in particular, has

been extensively investigated in the hippocampus as the cellular mechanism for learning and memory (Nicoll, 2017).

There are various parallels between processes that are well-documented in synaptic plasticity research and those reported in association with rTMS. For example, high-frequency synaptic activation generally induces LTP (synaptic strengthening) whereas low-frequency stimulation is more commonly associated with LTD (synaptic weakening). A similar trend for high-frequency stimulation to excite and low-frequency stimulation to inhibit neural networks has been reported in rTMS research, as discussed above.

There is also some overlap in the molecular players involved in LTP and in the response to rTMS. For example, LTP depends on the modulation of NMDA and AMPA receptors (Herring and Nicoll, 2016). A persistent increase in the number of hippocampal NMDA receptors has been documented in response to high-intensity, high-frequency rTMS (Kole et al., 1999; Gersner et al., 2011). Lasting modulation of AMPA receptor GluR1 subunits, increasing the calcium permeability of the receptor, has also been documented following high-frequency, high-intensity rTMS stimulation (Gersner et al., 2011). The upregulation of BDNF reported following rTMS (described above and see also Gersner et al., 2011; Rodger et al., 2012) also features in the molecular mechanism for LTP (Patterson et al., 1996; Lu, 2003; Bramham, 2008).

However, the synapse-specificity of LTP is one of its core features and in this area, synaptic plasticity research diverges somewhat from TMS research. At most synapses, LTP occurs only if two connected neurons are synchronously activated. An offset in activation of mere milliseconds can transition plasticity from LTP to LTD at a given

synapse. It is certainly conceivable that repeated, TMS-induced activity could induce LTP by synchronously activating particular synapses in the brain. It is less clear how that LTP might influence the spread of activity through a complex neural network, where strengthening of one synapse can simultaneously promote strengthening and weakening of others and when the stimulus is being applied in a very diffuse manner compared to the targeted stimulation of synaptic pairs of neurons in synaptic plasticity research. TMS studies have documented complex effects of both high and low frequency stimulation that cannot be simply characterised as either potentiating or depressing (Houdayer et al., 2008), likely reflecting distributed impacts on excitatory and inhibitory cortical pathways. Translating this complexity to produce optimised, predictable outcomes for patients remains a challenge in the field. Nevertheless, human rTMS/fMRI studies have consistently identified functional connectivity changes specific to different rTMS stimulation frequencies as described below.

1.6. rTMS frequencies and their specific effects in human functional connectivity studies

1.6.1. Simple stimulation protocols

There is considerable evidence from MEP and animal studies that that low-frequency (< 5 Hz) rTMS has long-term synaptic depression (LTD) like effects and thereby decreases brain excitability (Klomjai et al., 2015; Wilson and St George, 2016). The inhibitory effect of low-frequency rTMS has been confirmed in studies of the DMN. For example, van der Werf et al. (2010b) applied 1 Hz rTMS for two sessions over the left DLPFC of healthy volunteers. The rTMS sessions appeared to decrease resting-state network activity within the DMN, with the reductions happening in the temporal lobes, distant from the stimulated region. More specifically, they found that the

hippocampus had reduced activation bilaterally following the application of low-frequency rTMS. They hypothesized that this change in neuronal activity of the hippocampus could arise from a change in cortical excitability or the transcallosal spread of rTMS effects inducing bilateral inhibition. The inhibitory effect of low-frequency rTMS was also confirmed in a resting-state connectivity study between motor regions in healthy individuals (Glielmi et al., 2014). Interestingly, 1 Hz, an inhibitory frequency, is thought to decrease the activity of inhibitory neurones in the stimulated hemisphere, causing a reduction in the inhibitory interhemispheric drive, which in turn leads to an increase in excitability of the contralateral hemisphere. For example, O'Shea et al. (2007) found that even when 1 Hz stimulation over the left dorsal premotor cortex had no effect on behaviour, there was a compensatory increase in activity in the right dorsal premotor cortex and connected medial premotor areas. This contralateral effect of 1 Hz rTMS has been utilized to treat patients with stroke by applying low-frequency stimulation to the unaffected hemisphere to decrease transcallosal inhibition of the lesioned hemisphere and consequently improve motor function in such patients. An rTMS/fMRI study by Grefkes et al. (2010) recruited patients with mild to moderate unilateral hand weakness after a first-ever subcortical ischemic stroke in the middle cerebral artery. Each subject underwent a baseline fMRI scan, a post-sham stimulation scan, and a post 1 Hz stimulation scan. rTMS applied over contralesional M1 significantly improved the motor performance of the paretic hand, and the improvement in symptoms was correlated with the functional connectivity results. The fMRI data showed a decrease in negative transcallosal influences from the contralesional M1 and an increase in functional connectivity between the ipsilesional supplementary motor area (SMA) and M1.

In contrast to low-frequency stimulation, high-frequency (≥ 5 Hz) rTMS has long-term synaptic potentiation (LTP) like effects and increases brain excitability (Klomjai et al., 2015; Wilson and St George, 2016). In patients with stroke, high-frequency rTMS is sometimes applied directly to the affected hemisphere to increase excitability and promote plasticity of the lesioned hemisphere. For example, rs-fMRI demonstrated a bilateral increase in M1 connectivity in such patients after 10 days of 5 Hz rTMS applied ipsilesionally (Li et al., 2016). There was also increased connectivity between the stimulated ipsilesional M1 and the SMA, bilateral thalamus, contralesional postcentral gyrus, and superior temporal gyrus and decreased connectivity between the stimulated ipsilesional M1 and the ipsilesional postcentral gyrus, M1, middle frontal gyrus, and superior parietal gyrus. An improved interhemispheric functional connectivity was also found in a case study of post-stroke apathy by Mitaki et al. (2016) when 5 Hz rTMS was applied to the SMA of each hemisphere of the patient over the course of two weeks. The improvement in the interhemispheric functional disconnection was correlated with the patient's recovery from post-stroke apathy.

Even though the studies tend to have small sample sizes (Watrous et al., 2013), these results show that understanding the effects of rTMS on multiple brain regions is important and that the effects can be determined to some extent by specific rTMS protocols. There is a significant opportunity to develop other stimulation paradigms systematically, which might have different neuronal effects and to produce precise and reproducible effects in the brains of patients.

1.6.2. Complex stimulation patterns

The effect of TBS on the brain depends on the pattern of stimulation (Ljubisavljevic et al., 2015). For example, when cTBS is applied for 40 s (i.e., 600 stimuli) to M1 in humans, there is a decrease in brain excitability (Green et al., 1997). In contrast, when intermittent TBS (iTBS), with a 2 s train of TBS repeated every 10 s for 190 s (i.e. 600 stimuli), there is an increase in brain excitability (Green et al., 1997). Even though recent studies show evidence of substantial inter- and intra-individual variability in response to TBS (Zangen and Hyodo, 2002; Cho et al., 2012), the two main modalities, in general, have opposite effects on brain excitability.

Research on the DMN extends our understanding of the effects of TBS. iTBS applied over the left and right lateral cerebellum in patients with progressive supranuclear palsy for 10 sessions over the course of two weeks lead to an increased signal in the caudate nucleus bilaterally within the DMN (Brusa et al., 2014). iTBS also increased the efficiency of the impaired functional connectivity between the cerebellar hemisphere and the contralateral M1 observed in these patients compared with healthy individuals and patients with Parkinson's disease. The enhanced functional connectivity between the cerebellar hemisphere, the caudate nucleus, and the cortex was accompanied by an improvement of dysarthria in all patients. iTBS was also shown to have a dose-dependent effect on excitability and functional connectivity within the motor system (Nettekoven et al., 2014). When applied over the M1 of healthy volunteers, iTBS increased the resting-state functional connectivity between the stimulated M1 and premotor regions bilaterally. iTBS also increased connectivity between M1 and the ipsilateral dorsal premotor cortex when the number of stimuli was increased. The authors hypothesized that dense connections between M1 and the regions showing

increased functional connectivity might facilitate simultaneous stimulation of these interconnected brain areas by the iTBS protocol, thereby modulating the synchrony of the resting activity in those regions.

There have also been studies of the inhibitory action of cTBS on brain activity using fMRI. Following eight sessions of 30 Hz cTBS applied to the SMA over 2 consecutive days, patients with Tourette syndrome or chronic tic disorder showed a significant reduction in the activity of SMA and left and right M1 activation during a finger-tapping exercise, suggesting inhibition in the motor network. However, improvement in symptoms was not significantly different between test and control subjects, perhaps because of the small sample size. Similar to 1 Hz rTMS, cTBS has been shown to disinhibit contralateral targets; in healthy individuals, cTBS application to the right Heschl's gyrus did not induce changes in the stimulated brain region, but significantly increased activity in the contralateral Heschl's gyrus, postcentral gyrus, and left insula and in the bilateral lateral occipital cortex (Andoh and Zatorre, 2012). The mechanisms underlying this interhemispheric interaction are not well understood but could be related to short-term plasticity or compensatory mechanisms to preserve function by increasing the activity of homologous brain regions in the contralateral hemisphere (Andoh and Zatorre, 2012).

In summary, a range of frequencies and stimulation patterns have been tested in human subjects and have specific impacts on brain function and network connectivity. Information about the extent to which the functional connectivity within and between different networks can be modulated by different rTMS protocols may prove helpful in the development of treatment options for dysfunctional connectivity.

1.7. Potential applications of combined rTMS/fMRI studies in human diseases

1.7.1. Change in connectivity post rTMS linked to improvement in symptoms

Change in functional connectivity achieved using rTMS as a treatment method can be used to determine the neural mechanisms of improvement in symptoms in patients.

For example, a longitudinal study by Gonzalez-Garcia et al. (2011) used fMRI to

investigate the mechanisms by which 25 Hz rTMS (10 trains of 100 pulses) over M1 for three months improves the motor symptoms of patients with Parkinson's disease.

rTMS was found to cause an increase in activity in the caudate nucleus during a simple motor task (finger-tapping test). fMRI also showed a decline in activity in the SMA, which was accompanied by an increase in its functional connectivity to the prefrontal areas. These changes substantiated the beneficial effect of rTMS on the symptoms of Parkinson's disease observed in these patients.

Another way to analyze the link between rTMS therapy and improvement in symptoms is to use rs-fMRI to detect the change in functional connectivity after rTMS. Popa et al. (2013) found that the connectivity within both the cerebello-thalamo-cortical network and the DMN was compromised in patients with essential tremors. Application of 1 Hz rTMS for five consecutive days bilaterally over lobule VIII of the cerebellum appeared to have re-established the connectivity in the cerebello-thalamo-cortical network only, and this change in functional connectivity was accompanied by a significant improvement in symptoms. Another study that also used an rTMS/rs-fMRI protocol carried out a whole-brain connectivity analysis to unravel the effect of rTMS on functional connectivity and motor symptoms in patients with multiple system atrophy

(Chou et al., 2015). 5 Hz rTMS was applied over the left M1 of such patients for 10 sessions over the course of two weeks. Only the active rTMS group showed a significant improvement in motor symptoms, and these improvements were correlated to the modulation of functional links connecting to the default mode, cerebellar, and limbic networks by high-frequency rTMS. These findings suggest that rTMS can be used to target specific brain networks as a therapy for patients with multiple system atrophy.

1.7.2. Predicting susceptibility to rTMS therapy

More recently, baseline functional connectivity was shown to be a potential predictor of response to rTMS treatment, for example, in Mal de Debarquement Syndrome, a neurological condition representing a persistent false perception of rocking and swaying following exposure to unfamiliar motion patterns (Yuan et al., 2017). Pre- and post-rTMS rs-fMRI were carried out to assess functional connectivity changes as a result of daily rTMS treatment to the DLPFC (1200 pulses of 1 Hz rTMS over right DLPFC followed by 2000 pulses of 10 Hz rTMS to the left DLPFC) over five consecutive days. A significantly positive baseline functional connectivity between the right DLPFC and the right entorhinal cortex and between the left DLPFC and bilateral entorhinal cortex were identified in patients showing improvement in symptoms following treatment, but not in patients whose symptoms worsened or remained unchanged (Figure 1.5A). Improvement in symptom severity was correlated with a decrease in functional connectivity between the left entorhinal cortex and posterior DMN regions such as the contralateral entorhinal cortex, the right inferior parietal lobule, and the left precuneus (Figure 1.5B). Therefore, rs-fMRI potentially could be used to predict the susceptibility of patients to rTMS therapy and track symptom improvement.

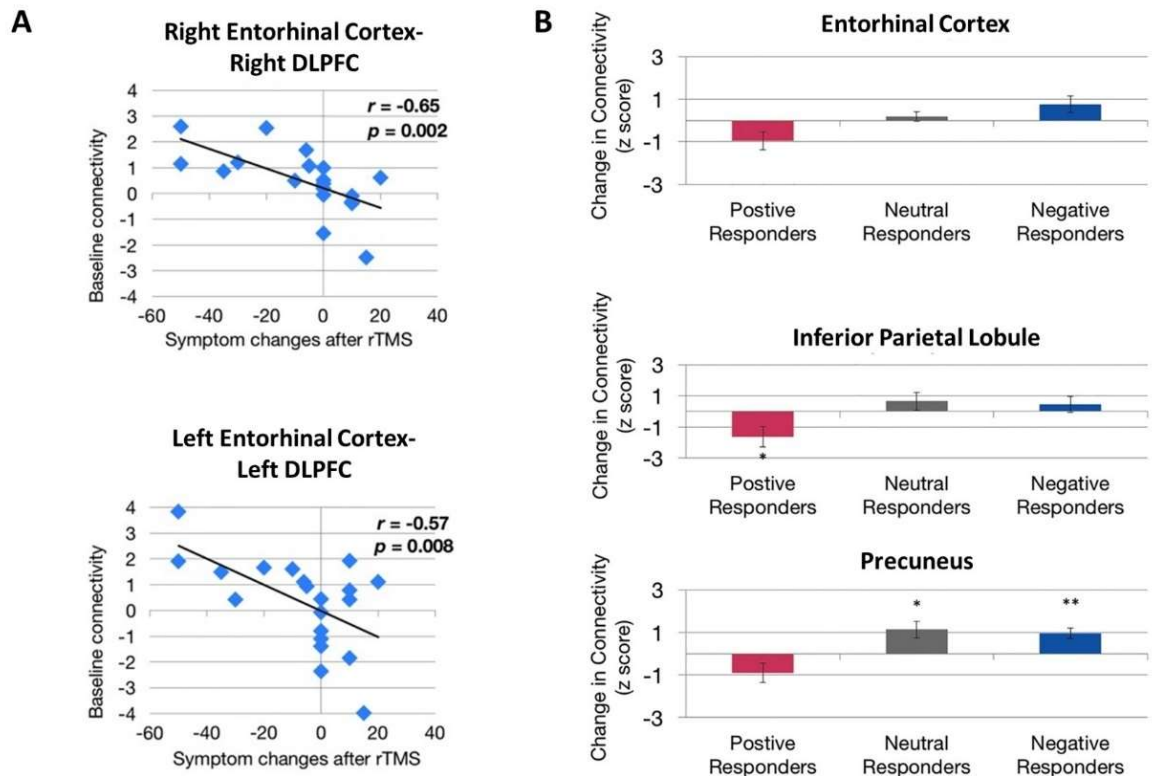


Figure 1.5. Evidence of correlation between behavioural improvements and functional connectivity before and after rTMS treatment. (A) Correlation between baseline entorhinal cortex–dorsolateral prefrontal cortex (DLPFC) functional connectivity and treatment response. Higher baseline functional connectivity exhibited by both right entorhinal cortex–right DLPFC connectivity (top) and left entorhinal cortex–left DLPFC connectivity (bottom) is associated with a greater magnitude of symptom reduction (change < 0) after rTMS. (B) Directional effect of functional connectivity changes between the left entorhinal cortex and the right entorhinal cortex (top), right inferior parietal lobule (middle), and the left precuneus. Functional connectivity between these regions decreased in patients showing improvement in symptoms (positive responders) compared with patients whose symptoms remained unchanged (neutral responders) or worsened (negative responders). * and ** indicate significant changes for $p < 0.05$ and $p < 0.01$, respectively. Image from Yuan et al. (2017), an open-access article distributed under the terms of the Creative Commons Attribution License, which permits unrestricted use, distribution, and reproduction in any medium, provided the original work is properly cited.

1.7.3. Other outcomes

Combining fMRI and rTMS has proven useful for investigating a range of other neural functions, providing evidence supporting the following: the functional relevance of the parietal cortex for visuospatial functions (Sack et al., 2002); a link between neural activity in the left inferior prefrontal cortex and episodic memory formation (Köhler et al., 2004); the involvement of premotor cortical areas in speech perception (for review,

see Iacoboni, 2008); the presence of functional asymmetry highlighting interhemispheric differences in the auditory network (Andoh et al., 2015); and enabled targeting of stimulation based on the individual's MRI anatomy, functional connectivity results or activated brain regions during specific tasks (e.g., Sack et al., 2002; Fitzgerald et al., 2009; Eldaief et al., 2011; Binney and Lambon Ralph, 2015; Nierat et al., 2015; Valchev et al., 2015).

1.8. Depression

Major depressive disorder is a debilitating neuropsychiatric disease with significant morbidity and mortality due to the risk of suicide. Antidepressants are typically a first-line treatment for depression. However, up to one-third of adults have treatment-resistant depression (TRD) that does not respond to pharmacotherapy. Repetitive transcranial magnetic stimulation (rTMS) has been used clinically for TRD for over a decade. George *et al.* (1995) were the first to use rTMS as a treatment for depression and its efficacy in medication-resistant patients has been validated by numerous clinical trials (Gaynes et al., 2014). In 2008, an rTMS device produced by Neuronetics Inc. (Malvern, PA, USA) was approved by the Food and Drug Administration in the United States for the treatment of patients with major depressive disorder who are resistant to at least one antidepressant drug (O'Reardon et al., 2007). Other rTMS devices (Magventure, Magstim) have since been approved. The diagnosis of depression in humans is primarily based on a persistent negative mood, clinical symptoms, and changes in behaviour. In the last two decades, there have been ongoing efforts to understand the etiological factors underlying depression in the hope that they can be exploited for therapeutic benefit. Several clinical fMRI studies suggest

that depression is related to aberrant intrinsic functional brain connectivities, which can influence the patients' response to treatment (Drysdale et al., 2017; Rolls et al., 2018; Shao et al., 2018). Another pathophysiology of depression that is increasingly gaining attention is altered gut microbiome as described below.

1.8.1. Depression and the brain functional connectivity

Although research on brain functional connectivity changes and their relationship to the major symptoms of depression is still in its infancy, to date, studies consistently report abnormal patterns of connectivity in patients with depression when compared to healthy individuals. Drysdale et al. (2017) found two groups of functional connectivity features that were linked to specific combinations of clinical symptoms in patients with depression. Anhedonia and psychomotor retardation were primarily linked to frontostriatal and orbitofrontal connectivity features, while anxiety and insomnia were primarily linked to a different group of primarily limbic connectivity features involving the amygdala, ventral hippocampus, ventral striatum, subgenual cingulate, and lateral prefrontal control areas. Testing the abnormalities in these connectivity features, based on their rs-fMRI data, revealed that not all patients with depression had the same functional connectivity patterns. They could be categorized, with high sensitivity and specificity, into four biotypes based on the distinct patterns of dysfunctional connectivity in the frontostriatal and limbic networks, which were most homogeneous within the subtypes and most dissimilar between subtypes. Moreover, patients with these neurophysiological subtypes of depression had different susceptibility to rTMS therapy: after five weeks of high-frequency rTMS delivered to the dorsomedial prefrontal cortex, biotype 1 patients showed a significant response to rTMS therapy (82.5% of that group), and biotype 2 patients were the least responsive

(25.0%). This study suggests that heterogeneous symptom profiles in depression could be caused by distinct patterns of dysfunctional connectivity and that categorizing patients into subtypes based on these patterns might enable the prediction of treatment response to rTMS.

Two years earlier, Downar et al. (2015) found that the resting-state functional connectivity features of the DLPFC to the subgenual cingulate cortex in patients with major depressive disorder could predict response either to 10 Hz or iTBS rTMS therapy. The role of subgenual cingulate connectivity in patients with depression has been indicated in several other studies (Greicius et al., 2007; Fox et al., 2012b; Liston et al., 2014; Hopman et al., 2017). More recent studies have since confirmed that it is possible to predict the response to iTBS or 10 Hz rTMS using resting-state functional connectivity between ventral striatum and bilateral frontal pole, as well as between the left DLPFC and the left anterior cingulate cortex (Dunlop et al., 2017). Therefore, rs-fMRI potentially could be used to select optimal rTMS parameters for the treatment of patients with depression.

1.8.2. Depression and the gut microbiome

The mammalian gut contains trillions of microbes collectively referred to as the gut microbiota, mostly located in the large intestine of the gastrointestinal tract (Gilbert et al., 2018). The gut microbiome is known to be involved in several processes. For example, these microorganisms play a key role in the metabolism of dietary nutrients and drugs, the absorption and distribution of dietary fat, the development of a complete immunological repertoire and protection against pathogens (Collins et al., 2012). In health, the intestinal barrier is selectively permeable, facilitating nutrient

absorption while preventing the entry of pathogens and toxins and the gut microbiome maintain epithelial integrity by regulating mucin production and tight junction protein expression (Ulluwishewa et al., 2011; Natividad and Verdu, 2013; Kelly et al., 2015). However, throughout a person's lifetime, the gut microbiota is shaped by various environmental factors including diet, exposure to pathogens, use of antibiotics and inflammation (Ley et al., 2008; Natividad and Verdu, 2013). These factors can lead to the growth of pathogenic bacteria and hence altered microbial composition or dysbiosis (Ley et al., 2008; Natividad and Verdu, 2013). Dysbiosis is associated with impaired intestinal permeability, resulting in increased exposure of the body to substances in the gut, leading to an immune response (Collins and Bercik, 2009; Ulluwishewa et al., 2011; Perez-Burgos et al., 2012). This condition is known as 'leaky gut'.

Mounting evidence supports the influence of the gut microbiome on the local enteric nervous system and its effects on brain chemistry and relevant behaviour and 'leaky gut' has been linked to several psychiatric disorders including depression (Collins and Bercik, 2009; Borre et al., 2014; Cruz-Pereira et al., 2020). For example, studies have shown that patients with major depressive disorder have elevated levels of peripheral blood antibodies to lipopolysaccharides derived from Gram-negative gut bacteria compared to healthy subjects (Maes et al., 2008). Additionally, the use of antibiotics in newborns less than one year of age has been associated with childhood behavioural difficulties and symptoms of depression (Slykerman et al., 2017).

The vagus nerve is an important bidirectional signalling pathway between the local enteric nervous system and the central nervous system and several lines of evidence

suggest that it is involved in both mood regulation and gut inflammation (Collins et al., 2012; Perez-Burgos et al., 2012; Cruz-Pereira et al., 2020). The vagus nerve can be stimulated by enterobacterial products such as endotoxins or inflammatory cytokines such as interleukin-1 β and tumour necrosis factor α (Borovikova et al., 2000), which are known to be elevated in depression (Yang et al., 2007; Himmerich et al., 2019). Vagus nerve stimulation, an FDA-approved treatment for patients with TRD (Cristancho et al., 2011), is believed to alter the levels of serotonin, GABA, and glutamate within the brain (Ressler and Mayberg, 2007). These neurometabolites are also known to be altered by TMS in depression (Ben-Shachar et al., 1997; Luborzewski et al., 2007; Dubin et al., 2016), but there is no evidence showing an effect of either vagus nerve stimulation or rTMS on the gut microbiome (Breit et al., 2018; Haney et al., 2018). In this thesis, changes in microbiome diversity will be integrated into the study of rTMS in depression and associated brain functional connectivity changes.

1.9. Need for animal rTMS/MRI studies

The induction of plasticity as described in previous sections has been the driving force behind clinical studies of rTMS as a potential treatment of neurological and psychiatric conditions. However, even in neurologically normal subjects, the variability in response to rTMS is high and therefore several studies show mixed or conflicting results (Maeda et al., 2000). For example, the overall size of the treatment effect of rTMS is small in patients with schizophrenia (see review Dlabáč-de Lange et al., 2010). The effect size is smaller (and in some studies non-significant) when low-frequency rTMS is used compared to high-frequency rTMS, although negative effects (greater effect in sham stimulation group than rTMS group) have also been reported when using high-

frequency rTMS. Additionally, even though rTMS has been approved for the treatment of TRD, several human studies have shown unimpressive results when comparing active rTMS to sham treatment (Garcia-Toro et al., 2001; Ontario, 2016) or when testing the efficacy of rTMS as an add-on treatment with antidepressants (Hansen et al., 2004; Kedzior et al., 2015).

In part, this reflects the relatively recent emergence of TMS as a therapeutic option and the fact that its safety and tolerability meant that it was very rapidly adopted as a clinical tool, without the underpinning biological research that precedes the clinical use of many medical treatments. However, these conflicting results also reflect genuine challenges associated with the technique. In particular, the potential diversity of rTMS protocols (in terms of stimulus intensity, duration, pattern, site of application and others) means that direct comparisons between studies are often impossible. In addition, the outcomes of rTMS treatment, like many treatments for complex neurological and psychiatric disorders, depend very much on the characteristics of the individual being treated. There is increasing evidence that the effects of TMS stimulation vary depending on biological sex and genetic profile, as well as with time-varying factors such as age, diet and exercise status, even in healthy individuals (for review, see Ridding and Ziemann, 2010). Responses in patient populations are further complicated by interactions between rTMS therapeutic outcomes and other treatments (e.g. pharmacological) that patients may be undergoing at the same time (Breden Crouse, 2012).

To unravel these sources of variability, to maximise the safety of rTMS therapies and to optimise their effectiveness, requires a better scientific understanding of the

mechanisms by which TMS affects the brain (Muller-Dahlhaus and Vlachos, 2013; Seewoo et al., 2018a). The extent to which variability is introduced into the experiments can be reduced in animal studies by controlling for gender, age, diet, drugs, genetic background, and time at which experiments are carried out. Therefore, animal models of rTMS can possibly mitigate the confounding effects of variability in rTMS effects and help identify the relative contributions and possible impacts of these factors.

Interleaving rTMS and MRI has opened doors to many possibilities in the clinical setting. However, there have been no reports of animal studies using those same techniques. MRI in rodent research is becoming increasingly popular because of its high translatability. Moreover, rodent rs-fMRI studies have confirmed that rodents possess a DMN similar to humans despite the distinct evolutionary paths of rodent and primate brains (Figure 1.6: Lu et al., 2012). Because rodents are widely used as preclinical models of neuropsychiatric disease (e.g., Tan et al., 2013; Yang et al., 2014a; Yang et al., 2015; Zhang et al., 2015; Kistsen et al., 2016), a thorough understanding of how rTMS affects the rodent brain function is of particular importance for both interpreting rodent MRI data and translating findings from humans to animals and back again.

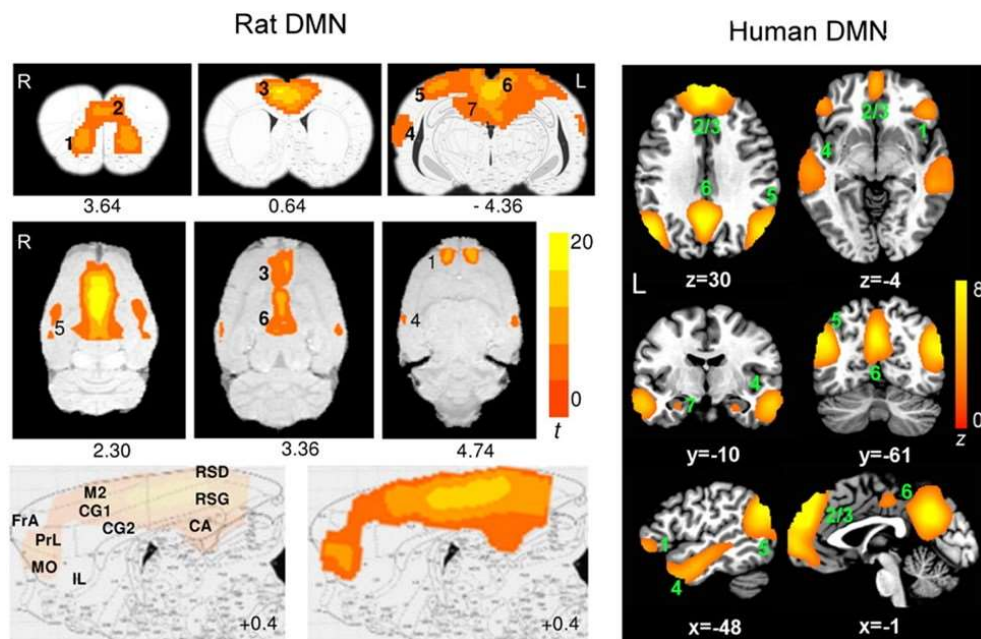


Figure 1.6. Evidence of translatability of fMRI studies: similar brain regions forming part of the default mode network (DMN) in the rat (Paxino's atlas coordinates indicated) and human (Talairach coordinates indicated) brains. Connectivity maps are shown in the coronal (A), axial (B) and sagittal (C) planes. Significant clusters for rat DMN (left) include: 1, orbital cortex; 2, prelimbic cortex (PrL); 3, cingulate cortex (CG1, CG2); 4, auditory/temporal association cortex (Au1, AuD, AuV, TeA); 5, posterior parietal cortex; 6, retrosplenial cortex (corresponding to the posterior cingulate cortex in humans); 7, hippocampus (CA1). The sagittal plane (medial–lateral: +0.4 mm) also shows: FrA, frontal association cortex; MO, medial orbital cortex; RSG/RSD, granular/dysgranular retrosplenial cortex. Color bar indicates t scores ($n = 16$, $t > 5.6$, corrected $p < 0.05$). Significant clusters for human DMN (right) include: 1, orbital frontal cortex; 2/3, medial prefrontal cortex/anterior cingulate cortex; 4, lateral temporal cortex; 5, inferior parietal lobe; 6, posterior cingulate cortex; 7, hippocampus/parahippocampal cortex. Color bar indicates z scores ($n = 39$, $z > 2.1$, corrected $p < 0.05$). Image adapted from Lu et al. (2012), an open-access article under the creative commons license and can be republished without the need to apply for permission provided the material is cited correctly and is republished under the same license.

1.9.1. Potential for linking functional connectivity changes post rTMS to genetic/molecular changes

Animal models provide a unique opportunity to combine techniques: changes in functional connectivity between spatially separated brain regions caused by long-term modulation of network dynamics by rTMS, can be studied in parallel with changes in behavioural measures, and followed by invasive procedures to detect cellular and molecular changes, all within the same animal. As shown in human rTMS/fMRI studies, the functional connectivity effects of rTMS are distributed across the whole brain. But,

even when in-depth studies of the molecular mechanisms are carried out (e.g., quantification of gene expression in multiple brain regions using low-density PCR arrays by Ljubisavljevic et al., 2015), how these molecular changes from animal studies underpin functional connectivity changes described in humans remains unclear. Future studies should aim to identify brain regions affected by the stimulation in animals using fMRI and then rTMS mechanisms further elucidated in the same individuals, for example by measuring changes in gene expression in the corresponding brain regions postmortem. Such correlational approaches will provide a compelling view of how rTMS affects the brain at systems levels.

1.9.2. Potential for linking functional connectivity changes post rTMS to structural changes

A more detailed understanding of how rTMS treatment leads to long-term modulation of network dynamics will be essential for the interpretation of neuropsychological and cognitive effects of rTMS in a clinical context. Combined rTMS/fMRI studies in animals can be used in longitudinal studies to investigate the long-term effects of rTMS. For example, fMRI can be used to measure cumulative effects of repeated rTMS delivery, following which fluorescent dye tracers can be injected into the brain to anatomically label neuronal pathways of interest identified by fMRI. Conducting neuronal tract tracing after an fMRI study could elucidate whether long-term treatment with rTMS can eventually elicit changes in fibre tracts in the brain. More global anatomical information can also be obtained through multimodal MRI as described above. Analyzing functional connectivity and anatomical connectivity within the same animals will provide information about how observed functional changes correlate with the structural changes detected via diffusion or anatomical MRI or even at a cellular level

using neuronal tracing. Although there is a general trend towards functional and structural connectivity being strongly associated, there are some mismatches within the DMN whereby regions showing high correlation have low fibre connectivity (Hsu et al., 2016). Therefore, future studies to investigate whether the effect of rTMS on functional connectivity is related to fibre connectivity are warranted.

1.9.3. Combined rTMS/fMRI studies using depression models

An important recent development in animal research has been the use of rs-fMRI for the characterisation of models of neuropsychiatric disorders. Studies have revealed abnormal functional connectivity patterns in animal models due to pharmacological modulations or genetic manipulations which mimic connection abnormalities observed in corresponding human disorders (Jonckers et al., 2015; Gozzi and Schwarz, 2016; Gorges et al., 2017). These animal models represent a powerful tool to understand the neurobiological basis of the reported ability of rTMS to assist in remediating functional dysconnectivity observed in human disorders.

Depression is a heterogeneous and complex disorder and therefore different animal models have different advantages for studying specific aspects of the disease.

Maternal separation, social defeat, unpredictable chronic mild stress and chronic restraint stress animal models are behavioural models of depression based on different principles of how adverse events during one's life contribute to depressive symptoms in humans. Maternal separation is a type of early life stress model whereby the pups are separated from their mothers during the postnatal period. In the social defeat model, social conflict is the primary stressor whereby a male rodent introduced into the home cage of an older, aggressive and dominant male rodent is attacked and

defeated by the resident male. In unpredictable chronic mild stress, the rodent is subjected to a series of different unpredictable stressors daily such as food/water deprivation, cage tilt, overnight illumination, immobilisation and mild electric shocks over a period of several weeks. In the chronic restraint stress (CRS) model, the rat is restrained for several hours daily for weeks. The continuous and predictable nature of this stress is designed to mimic the everyday stress that people experience such as a stressful job or financial stresses. Other models include the olfactory bulbectomy which involves the surgical extraction of the olfactory bulb and genetic models which are based on the manipulation of the serotonin system.

First, fMRI can be used to identify the abnormal functional connectivity in an animal model specific to a neurological disorder. For example, the Wistar-Kyoto rat, a genetic model for depression that has shown resistance to acute antidepressant treatment (Lahmame et al., 1997; López-Rubalcava and Lucki, 2000), also shows functional connectivity anomalies between the hippocampus, cortical, and sub-cortical regions (Williams et al., 2014), as has been observed in humans with major depressive disorder. Future studies can investigate the effects of rTMS on such animal models.

Functional connectivity changes post-rTMS treatment can then be linked to improvement in symptoms (through behavioural tests) as well as to any induced molecular and cellular changes (through postmortem analysis).

Several behavioural tests can be done to evaluate the effectiveness of the model in inducing depression-like behaviours in the rodents and/or the effect of treatment by measuring different types of symptoms. For example, the forced swim test measures learned helplessness (Bogdanova et al., 2013). While an animal placed in water would

normally attempt to escape, rodents with depression-like behaviours tend to stop exhibiting the escape response more quickly and float instead. The sucrose preference test measures anhedonia, a typical symptom of depression (Liu et al., 2018). While rodents prefer drinking water with dissolved sucrose over regular water, animals with depression-like behaviours exhibit a loss of interest in the sucrose water which was previously pleasurable. Open-field and elevated plus maze tests are both commonly used to assess anxiety (Walf and Frye, 2007). They are both based on the principle that non-anxious rodents are more likely to explore open spaces while anxious rodents prefer to hide in corners or enclosed areas.

Therefore, extending the use of combined rTMS/fMRI techniques in various types of neurological and psychiatric conditions using appropriate animal models is a promising avenue for understanding the fundamental properties of the functional re-organization in these conditions in a unique way. While the use of combined rTMS/MRI techniques in rodent research has great potential because of its high translatability, there are challenges as we review below.

1.10. Challenges associated with rTMS/fMRI studies in animals

1.10.1. Choice of animal model and development of rTMS coils

A wide range of animal models have been used with the aim of understanding the underlying mechanisms and optimising the therapeutic applications of rTMS: rats (Tan et al., 2013; Yang et al., 2015; Zhang et al., 2015), mice (Kistsen et al., 2016), guinea pigs (Mulders et al., 2016), rabbits (Guo et al., 2008), felines (Allen et al., 2007; Valero-Cabr e et al., 2007), and in a very limited way, non-human primates (Valero-Cabr e et al., 2012; Salinas et al., 2013; Mueller et al., 2014). These animal models have

contributed considerably to our current understanding of the non-invasive neuromodulatory effects of rTMS (reviewed in Tang et al., 2015). However, the variation in brain structure and the smaller sized brains of non-human animals present a fundamental challenge in the application of rTMS and interpretation of its effects.

Non-human primates are clearly the closest to humans in terms of brain structure and size and have the advantage that they can be taught behavioural tasks similar to those used in human rTMS studies. However, the high cost of using non-human primates limit opportunities for invasive studies in large numbers of animals. Rodents, on the other hand, although they are the most commonly used laboratory animals, have important differences in brain structure compared to humans. Their smooth cortex possesses a very different geometry from the highly folded human cortex and this is an important consideration because the characteristics of the electric field induced by rTMS are predicted to be influenced by the orientation of the tissue relative to the coil (Opitz et al., 2011). In addition to differences in brain structure, the small size of the rodent brain presents a serious challenge. In humans, rTMS is most commonly delivered using a coil shaped like a "figure-of-eight" (Figure 1.7A). This configuration provides a stimulation hotspot at the intersection of the loops that can be positioned over the target brain region to provide focal stimulation. Adjacent brain areas also receive stimulation but at much lower intensity. In most animal models, even the smallest commercially available rTMS coil results in a different ratio between head size and coil size from that in humans, reducing stimulation focality and efficiency (Rodger and Sherrard, 2015).

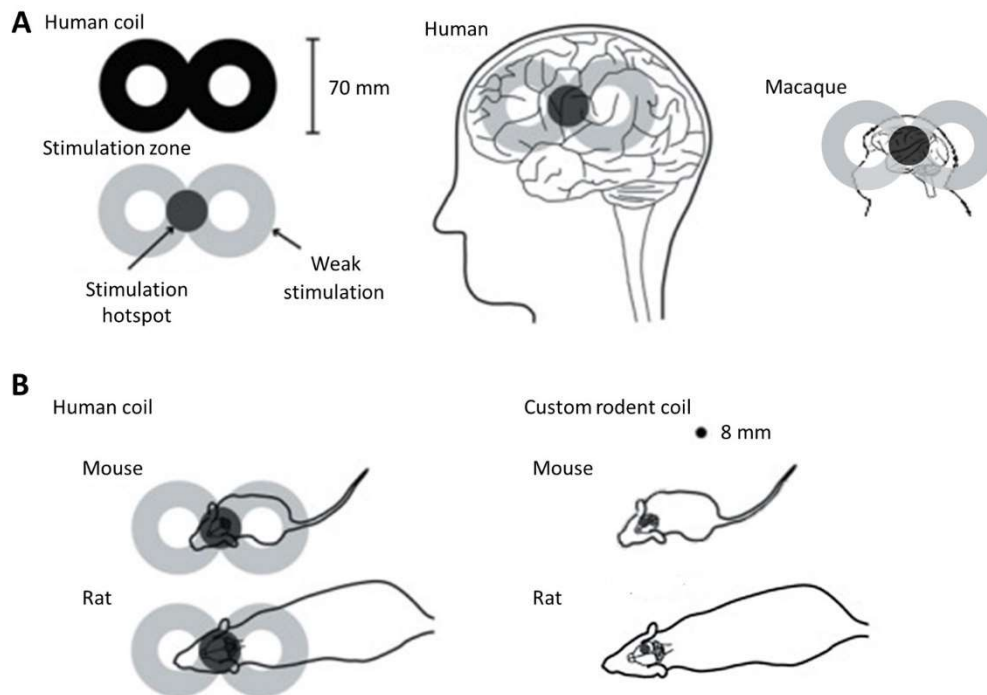


Figure 1.7. rTMS coil size with respect to brain sizes of humans, macaque and rodents. For all panels, coils are shown in black and the approximate location of the induced current is in grey. (A) Typical human “figure of eight” coil with stimulation hotspot at the intersection of the loops in dark grey showing the “focal” stimulation in humans and macaques. When applied to the head, the hotspot is positioned over the target brain region, but the rest of the brain also receives stimulation, albeit at a lower intensity. However, when this human coil is applied in rodents (B), the hotspot is no longer focal relative to the target, but rather stimulates the entire head and an appreciable portion of the body (left). This reduces the efficiency of magnetic induction and changes the properties of the induced current. To address this problem, custom-made round coils (right) have been used to deliver focal stimulation in rodents (Rodger et al., 2012; Makowiecki et al., 2014; Tang et al., 2016b). Although these deliver low-intensity magnetic fields, the induced current is fully contained within the brain, increasing the efficiency of induction. The coils are small enough to stimulate one hemisphere in both mice and rats. Image adapted from Rodger and Sherrard (2015), an open-access article distributed under the terms of the Creative Commons Attribution-Noncommercial-Share Alike 3.0 Unported, which permits unrestricted use, distribution, and reproduction in any medium, provided the original work is properly cited.

Currently, magnetic field strengths that are equivalent to those used in human rTMS cannot be delivered to the brains of laboratory rodents with a focality greater than hemispheric (Sjöström et al., 2008). Several animal rTMS studies use human 70 – 80 mm figure-of-eight coils (Yang et al., 2015; Zhang et al., 2015) or large (diameter 50 – 150 cm) round coils (Ji et al., 1998; Tan et al., 2013; Kistsen et al., 2016) while others use smaller 25 – 40 mm figure-of-eight coils (Muller et al., 2014; Sykes et al., 2016) and

miniaturised (diameter < 1 cm) circular coils (Mulders et al., 2016) delivering low-intensity rTMS. Using a standard, human-sized “figure-of-eight” coil in mice stimulates the entire brain and often an appreciable portion of the body (Figure 1.7B). The discrepancy in size, therefore, precludes easy interpretation and translation of animal results into clinical applications. Many rodent studies are therefore compromised by the use of large, human-scale coils to deliver rTMS (e.g., Yang et al., 2014a; Yang et al., 2015; Zhang et al., 2015). Miniaturised rTMS coils more closely mimic focal human rTMS in rodents. For example, custom-made 8mm diameter round coils have been used to stimulate one hemisphere in both mice and rats (Rodger et al., 2012; Makowiecki et al., 2014), with the induced current fully contained within the brain, increasing the efficiency of induction. However, there is a heat dissipation problem when using small round coils (Cohen and Cuffin, 1991; Wassermann and Zimmermann, 2012), limiting the intensity of the magnetic field to levels roughly 10-100 times lower than those commonly applied in humans (low-intensity; LI-rTMS) (Rodger and Sherrard, 2015).

Despite the existing inability to deliver the same magnetic field parameters in humans and in animals with small brains (Rodger and Sherrard, 2015), beneficial effects are seen in animal models of neurological disease using human rTMS coils (e.g., Tan et al., 2013; Yang et al., 2015; Zhang et al., 2015; Kistsen et al., 2016) and small LI-rTMS coils (Makowiecki et al., 2014; Clarke et al., 2017), suggesting that both approaches have therapeutic potential. Because fMRI can detect both high and low-intensity rTMS effects in the brain, this technique will be useful in establishing a direct comparison of

different intensity magnetic field effects in human and animal brains. This information is imperative if we are to define the best clinical protocols for rTMS.

1.10.2. Use of anesthetics in animal fMRI studies

Although fMRI can be performed on awake, normally behaving animals that have been extensively trained and habituated (Brydges et al., 2013; Kenkel et al., 2016), one advantage of rs-fMRI is that being a task-free technique, functional connectivity can be investigated in anaesthetised animals without relying on or being confounded by behaviour. In human studies, the physiological condition of the subject is assumed to be relatively constant throughout an fMRI scan session (Pan et al., 2015). On the other hand, in animal fMRI, the use of anesthesia is generally required to immobilize the animal and reduce stress (Vincent et al., 2007; Pan et al., 2015). Isoflurane is the anesthetic of choice for repeated long-term experiments because of its ease of use and control, and rapid reversibility (Masamoto and Kanno, 2012a). However, anesthetics, including isoflurane, might confound the imaging results as they may cause alterations in neural activity, vascular reactivity, and neurovascular coupling. Isoflurane decreases excitatory and increases inhibitory transmission, causing an overall suppression of neural activity, most likely by modulating the intracellular concentration of calcium (Gomez and Guatimosim, 2003; Ouyang and Hemmings, 2005). As such, the ability of high-frequency rTMS to depolarise neurons is impaired in the presence of isoflurane (Gersner et al., 2011). Additionally, isoflurane, being a GABAergic anesthetic, induces vasodilation through the activation of ATP-sensitive potassium channels of smooth muscle cells in cerebral arteries (Ohata et al., 1999b; Pan et al., 2015). Vasodilation leads to an increase in cerebral blood flow, which can be interpreted as an increase in activity. Moreover, the use of an isoflurane-only anesthetic regime has been reported

to decrease inter-thalamic connectivity, thalamo–cortical connections, and DMN–thalamic network connections (Bukhari et al., 2017a). These potential confounding effects of isoflurane should be taken into account when interpreting findings.

An alternative to general anesthesia is sedation, for example using medetomidine or its active enantiomer, dexmedetomidine. These drugs lack the dose-dependent vasodilation and neural suppression observed with isoflurane use. However, being α 2-adrenergic agonists, they activate α 2-adrenergic receptors and cause a decrease in cerebral blood flow, potentially because of increased vascular resistance via cerebral vasoconstriction (Prielipp et al., 2002). Moreover, there is a potential issue with prolonged studies because the dose of medetomidine needs to be increased after 2 hours to maintain sedation (Pawela et al., 2009). Furthermore, the use of a medetomidine-only anesthetic regime produced decreased inter-cortical connectivity (Bukhari et al., 2017a).

Interestingly, using a combination of low-dose isoflurane and medetomidine appears to mitigate some of these factors. This anesthetic combination not only allows stable sedation for over four hours (Lu et al., 2012) but also maintains strong inter-cortical and cortical-subcortical connectivity (Grandjean et al., 2014; Bukhari et al., 2017a). The BOLD signal was determined to be maximally stable approximately 90 min after the initiation of medetomidine infusion, suggesting that fMRI data should be collected at this time (Lu et al., 2012). Moreover, data were reproducible from repeated fMRI experiments on the same animal one week apart (Lu et al., 2012). The high reproducibility and minimal impact on network connectivity of the

medetomidine/isoflurane combination anesthesia make it a preferred anesthetic regime for prolonged and longitudinal rs-fMRI studies in rodents.

1.10.3. Rs-fMRI studies in rodents — challenges in data analysis

As with human data, rodent rs-fMRI data need to undergo extensive pre-processing prior to analysis. Rodent studies have used a variety of software packages such as Statistical Parametric Mapping (SPM) (e.g., Jonckers et al., 2011), Analysis of Functional NeuroImages (AFNI) (e.g., Hsu et al., 2016), BrainVoyager (e.g., Hutchison et al., 2010), and Functional MRI of the Brain (FMRIB) Software Library (FSL) (e.g., Tambalo et al., 2015), which were designed for human fMRI data. Therefore, modifications to the data format and pre-processing steps are often necessary to undertake analysis of rodent brain data. For example, the field of view can be altered by up-scaling the voxel sizes by a factor of 10 to be closer to the size of a human brain (Tambalo et al., 2015). Likewise, because of the smaller size of the rodent brain, higher spatial smoothing may be required in animal fMRI data to increase the signal-to-noise ratio without reducing valid activation. Temporal band-pass filtering can also be used to reduce hardware noise, low-frequency signal drifts, and some artifacts caused by cardiac rhythm and respiration, as well as thermal noise (for review, see Pan et al., 2015). Recently, Zerbi et al. (2015) described the use of single-session independent component analysis (ICA) in the FSL for significantly improved artifact reduction in rs-fMRI rodent data. This method removes signals from common sources, for example, breathing, which can be isolated into separate components and removed as noise from the data. Additionally, because of the difference in the shape of human and animal brains, skull-stripping—a fully-automated step in human fMRI data pre-processing required to prevent extra-brain matter from interfering with the results—is still largely performed through

manual segmentation in animal studies (Sierakowiak et al., 2015; Zerbi et al., 2015). Before analysis, normalization to map functional networks onto a common space is necessary to allow for comparison across subjects or groups. However, because not all rodent strains have an available standard template or atlas for co-registration, some studies acquire and use high-resolution structural images or group-averaged images as a common space (Sierakowiak et al., 2015; Zerbi et al., 2015).

Two of the popular methods for rs-fMRI data are seed-based connectivity analysis (e.g., Hutchison et al., 2010; Sierakowiak et al., 2015; Huang et al., 2016) and ICA (e.g., Hutchison et al., 2010; Jonckers et al., 2011; Lu et al., 2012; Zerbi et al., 2015; Hsu et al., 2016). Seed-based correlation, used in the earliest functional connectivity studies, is a hypothesis-driven approach, which is particularly attractive for area-based hypotheses-driven rs-fMRI studies in rodents. The temporal correlation of all voxels within the brain is analyzed relative to user-defined seed voxel or small region of interest (Joel et al., 2011). However, seed-points can differ in their location between studies, which affects the connectivity patterns considerably and renders comparisons between studies difficult. In addition, this method is not suitable for exploratory analyses. In contrast, the use of data-driven ICA enables the identification of networks of functional connectivity within the entire brain without *a priori* knowledge and thus is a less biased approach (Cole et al., 2010). Moreover, this approach might improve reproducibility because there is no (arbitrary) seed selection (Rosazza et al., 2012). However, the results might depend on the number of components used. Despite the rodent DMN producing similar spatial patterns and being robust irrespective of the number of components (Lu et al., 2012), the number of components chosen can

impact on the ease of analysis. For example, Jonckers et al. (2011) and Hsu et al. (2016) chose 15-components in ICA over ICAs repeated with a higher number of components to avoid splitting of the DMN or splitting of some brain regions into different components. Therefore, despite ICA becoming increasingly popular for the analysis of rodent rs-fMRI data, challenges remain as there is no set protocol for selecting the number of components.

1.11. Summary

Considered together, the human studies discussed in this review demonstrate the broad relevance and significance of the results from combined rTMS/MRI protocols. Results from human studies to date *inter alia* have permitted the characterization of corrupted networks in diseased states, as well as intriguing glimpses into how alterations in functional connectivity patterns after rTMS are correlated with improvements in symptoms. There is also exciting evidence that functional connectivity can be used to predict responses to rTMS treatment with high reliability. Although methodological challenges remain in the use of brain imaging techniques in rodents, we anticipate that the use of fMRI to study rTMS in animal models will not only permit more detailed characterizations of how different rTMS protocols affect network dynamics and connectivity but will also elucidate how these changes reflect the manifestation of symptoms in preclinical models. Linking these functional changes to the molecular and cellular changes currently known in rodents will provide new insights into the fundamental mechanisms of brain plasticity and how to use it therapeutically.

1.12. Thesis scope and aims

As demonstrated in this literature review, little is known about the mechanisms underlying the mode of action of rTMS. Effective development of new therapies based on rTMS will require a cyclical from bench-to-bedside-to-bench approach. Rodents are widely used as preclinical models of various neuropsychiatric diseases and, therefore, a thorough understanding of how LI-rTMS affects the rodent brain activity, chemistry, and structure through basic research is of particular importance, followed by the study of disease-specific animal models with the aim to translate findings to the clinic. The broad aim of this thesis is to use complementary experimental techniques (e.g., resting-state fMRI, MRS, anatomical MRI, DTI) to allow us to have a better understanding of the underlying mechanisms of LI-rTMS and of how to interpret rodent MRI data.

Chapters 2 and 3 describe two studies conducted for the technical development of rodent MRI protocols for data collection and analysis. In chapter 2, we aimed to refine the anaesthetic protocol employed in rodent fMRI studies. The use of a combination of isoflurane, an anaesthetic agent and medetomidine, a sedative agent, during the acquisition of rodent fMRI data is generally recommended but no study has investigated the pharmacokinetics of medetomidine during isoflurane anaesthesia in Sprague Dawley rats. In this study, we describe the therapeutic serum concentration of medetomidine when administered with isoflurane and recommend standardisation of the combination anaesthesia protocol. In chapter 3, we aimed to refine the data analysis workflow employed in rodent fMRI studies. The two most widely used methods for analysing brain functional connectivity are seed-based correlation analysis

(SCA) and independent component analysis (ICA) but there is no consensus on the optimal combination of analytical steps and how to execute them. This study investigates these two methods and provides detailed instructions and bash scripts for the analysis of rs-fMRI data.

Chapters 4 and 5 describe two studies conducted for investigating the effects of LI-rTMS on healthy rats. Although there is considerable evidence for the clinical relevance of rTMS and disturbed functional connectivity in many neurological and psychiatric disorders, the therapeutic effect of rTMS is not yet well understood. Understanding the neural effects of rTMS in healthy controls is an essential prerequisite in examining the mechanism of any therapeutic effects in disease models. In chapter 4, we examined the immediate effect of one session of LI-rTMS on brain functional connectivity using rs-fMRI and in chapter 5, we examined the long-term effects of repeated LI-rTMS delivery on both brain functional connectivity using rs-fMRI as well as neurometabolites using MRS. Both studies also aimed to compare different frequencies of LI-rTMS to investigate possible mechanisms of LI-rTMS. These two studies in healthy animals provided evidence of translational validity suggesting that LI-rTMS in rodents is a useful model to include in a translational pipeline to inform and guide clinical application of rTMS.

Chapters 6 and 7 describe the application of these findings on a disease model. The overall aim of these two chapters was to be able to expand the knowledge of the underlying pathology of a specific preclinical model of depression and the mechanisms of rTMS in this model. In Chapter 6, multimodal MRI was used to identify brain changes in animals following CRS and these measures were correlated with

behavioural changes to validate this model of depression. In Chapter 7, we investigated how these changes were altered following LI-rTMS and determined whether they could be linked to improvement in symptoms through behavioural tests. This will help elucidate mechanisms of action of LI-rTMS as well as potentially the targeted underlying pathology in depression.

Chapter 8 describes the longitudinal effect of LI-rTMS treatment on the brain white matter microstructure of healthy and CRS rats using advanced diffusion imaging techniques. In the first part of the chapter, diffusion kurtosis imaging data acquired in experiments described in Chapter 5 was used to investigate the effects of 10 Hz and 1 Hz LI-rTMS on diffusion metrics which are inferred to relate to brain microstructure. The second part of this chapter uses two types of diffusion data acquired in experiments described in Chapters 6 and 7 to determine the effects of CRS and LI-rTMS on the brain microstructure. Additionally, changes in myelination within the corpus callosum following CRS and LI-rTMS was determined using immunohistochemistry. This study is the first to demonstrate LI-rTMS-induced changes brain white matter connectivity and integrity non-invasively in healthy and CRS rats.

Chapter 9 describes the effect of CRS on the gut microbiome of rats and whether LI-rTMS treatment restores balance in healthy vs pathogenic bacteria in the gut. Several lines of evidence suggest that the products from an altered gut microbiome can activate the vagus nerve and that such activation plays a critical role in mediating effects on the brain and behaviour in depression. To the best of our knowledge, no study has looked into whether the CRS depression model replicates the altered gut

microbiome seen in humans with depression and how rTMS treatment affects the gut microbiome.

Overall, this thesis focuses on studying the mechanisms of LI-rTMS in healthy animals as well as in an animal model of depression using similar techniques as in human studies (multimodal MRI, behavioural tests, and gut microbiome analysis). An improved basic understanding of mechanism will help tailor personalised treatment protocols to suit individuals and therefore, increase the therapeutic efficacy of this treatment.

Chapter 2

Methods Development: The pharmacokinetics of medetomidine administered subcutaneously during isoflurane anaesthesia in Sprague-Dawley rats

Published as: Kint, L.T., Seewoo, B.J., Hyndman, T.H., Clarke, M.W., Edwards, S.H., Rodger, J., Feindel, K.W. & Musk, G.C., 2020. The pharmacokinetics of medetomidine administered subcutaneously during isoflurane anaesthesia in Sprague-Dawley rats. *Animals*. 10, 1050. doi: 10.3390/ani10061050 (Appendix C)

Rodents, including rats, are used as animal models for research investigating neurological diseases in humans. In magnetic resonance imaging (MRI) studies, the use of anaesthesia is generally required to immobilise the animal and reduce stress. Blood-oxygenation-level-dependent (BOLD) functional MRI (fMRI) studies rely on the coupling between local blood flow and local neuronal activity but the use of anaesthesia alters neurovascular coupling, which may confound the imaging results. BOLD signals are considered accurate when they produce an image reflective of brain activity in the awake state. To minimize the variation between studies, anaesthetic protocols should be similar. A common anaesthetic regime is the combination of two drugs – medetomidine and isoflurane. Anaesthetic protocols involving the combined use of the sedative agent, medetomidine, and the anaesthetic agent, isoflurane, are increasingly being used in fMRI studies of the rodent brain as using a combination of low-dose isoflurane and medetomidine appears to maintain strong inter-cortical and cortical-subcortical brain functional connectivity like in the awake state and allows stable sedation for over four hours. Despite the popularity of this combination, a standardised protocol for the combined use of medetomidine and isoflurane has not been established, resulting in many variations in the reported doses of these drugs and

how they are administered. To provide some evidence to facilitate the standardisation of anaesthetic protocols, this study was performed to elucidate the details of what the body does to these drugs when they are administered in a certain way. Using mass spectrometry, serum concentrations of medetomidine were measured in Sprague-Dawley rats during medetomidine and isoflurane anaesthesia. Three groups of rats were studied to determine the desired dose of medetomidine when isoflurane is used at a low dose (approximately 0.5%). The data suggests that a steady-state serum concentration of medetomidine, when administered with 0.5% (vapouriser setting) isoflurane, can be achieved with an initial subcutaneous dose of 0.12 mg/kg of medetomidine followed by a 0.08 mg/kg/h subcutaneous infusion of medetomidine. Consideration of these results for future studies will facilitate the standardisation of medetomidine and isoflurane anaesthetic protocols during fMRI data acquisition.

2.1. Introduction

Anaesthetic protocols using a combination of medetomidine and isoflurane, are increasingly being used in functional magnetic resonance imaging (fMRI) studies of the rodent brain (Sommers et al., 2002; Weber et al., 2006; Pawela et al., 2009; Jonckers et al., 2011; Lu et al., 2012; Fukuda et al., 2013; Sierakowiak et al., 2015; Zerbi et al., 2015; Hsu et al., 2016; Seewoo et al., 2019c). The use of medetomidine for these studies was first reported in 2002 (Sommers et al., 2002), whilst the use of low dose isoflurane (< 0.5% vapouriser setting) in conjunction with medetomidine as an anaesthetic regime was first reported in 2012 (Weber et al., 2006; Lu et al., 2012; Fukuda et al., 2013).

Medetomidine is an α_2 -adrenoceptor agonist that causes sedation, hypertension, bradycardia, respiratory depression, hyperglycaemia, diuresis, muscle relaxation and analgesia (Yaksh, 1985; De Sarro et al., 1987; Doze et al., 1989; Savola, 1989; Stenberg, 1989; Gellai, 1990; Schmeling et al., 1991; Correa-sales et al., 1992; Mirski et al., 1994; Bol et al., 1997; Pypendop and Verstegen, 1998; Miyazaki et al., 1999; Sinclair, 2003; Kanda and Hikasa, 2008; Zuurbier et al., 2008; Talukder and Hikasa, 2009). The potency and receptor selectivity of medetomidine has led to its widespread use in veterinary anaesthesia, mostly in dogs and cats (Virtanen et al., 1988). Medetomidine causes sedation through the activation of central α_2 -adrenoceptors in the locus coeruleus, which prevents excitatory neurotransmitter release in the central nervous system and thereby depresses cortical arousal (De Sarro et al., 1987; Doze et al., 1989; Correa-sales et al., 1992). Vascular side effects of medetomidine occur due to the activation of peripheral α_2 -adrenoceptors, which causes a transient and marked increase in

systemic vascular resistance (Savola, 1989; Schmeling et al., 1991). This vasoconstriction is followed by a decrease in vascular tone due to suppression of central nervous system-mediated sympathetic stimulation on blood vessels.

Isoflurane is a GABAergic fluorinated ether that causes anaesthesia, respiratory depression, bronchodilation, vasodilation, hypotension and muscle relaxation (Eger, 1984; Dohoo, 1990). Isoflurane is commonly used for clinical and veterinary anaesthesia due to its rapid onset of action, short recovery time, safety and titratability (Paddleford, 1988; Dohoo, 1990; Ludders, 1992). The minimum alveolar concentration of isoflurane in adult Sprague-Dawley rats is $1.46 \pm 0.06\%$ (Mazze et al., 1985).

The benefit of combining medetomidine with isoflurane specifically for fMRI studies has been described. When $> 0.1\%$ isoflurane is administered with medetomidine, the epileptic activity caused by medetomidine is suppressed (Mirski et al., 1994; Miyazaki et al., 1999; Fukuda et al., 2013). Furthermore, the drug combination allows for maintenance of a steady state of anaesthesia for > 4 h, with consistent fMRI data (Lu et al., 2012). In contrast, when medetomidine is administered alone via a constant rate infusion (subcutaneous (SC) or intravenous (IV)), it is not possible to maintain a steady state of sedation for > 3 h. It has been reported that medetomidine administered alone can only be used in fMRI experiments > 3 h if the initial infusion dose is increased three-fold after 90 min, or if medetomidine is specifically administered using an initial IV injection of at least 0.05 mg/kg medetomidine followed by a subsequent continuous SC or IV infusion of at least 0.1 mg/kg/h medetomidine, whereby the initial

dose cannot be omitted, and the dose cannot be decreased (Pawela et al., 2009; Paasonen et al., 2018).

Despite the increasing popularity of this combination of medetomidine and isoflurane, a standardised anaesthetic protocol for their combined use for rodent brain fMRI studies has not been established (Fukuda et al., 2013; Brynildsen et al., 2017). Various protocols are described with variable doses of both medetomidine and isoflurane, different routes of administration of medetomidine, and variation in the time of fMRI data collection relative to the time of medetomidine administration (Lu et al., 2012; Fukuda et al., 2013; Grandjean et al., 2014; Zerbi et al., 2015; Hsu et al., 2016; Pirttimaki et al., 2016; Brynildsen et al., 2017). For example, in seven rodent fMRI studies employing medetomidine and isoflurane anaesthesia, the dose of isoflurane for maintenance of anaesthesia varied from 0.25–1.4% (Lu et al., 2012; Fukuda et al., 2013). Furthermore, reported loading doses for medetomidine range from 0.03 to 0.15 mg/kg and the subsequent infusion doses range from 0.03 to 0.1 mg/kg/h (Grandjean et al., 2014; Pirttimaki et al., 2016). In addition, the initial injection was administered via the IV, intramuscular, intraperitoneal or SC routes and the infusion via the IV, intramuscular or SC routes. The time of fMRI data collection after the initial administration of medetomidine ranged from 15 min to 90 min (Lu et al., 2012; Grandjean et al., 2014; Hsu et al., 2016). This variation in the use of medetomidine and isoflurane in rodent brain fMRI studies may be attributed to a lack of comprehensive data on the pharmacokinetics and pharmacodynamics of medetomidine in rodents. Importantly, the serum concentration of medetomidine when administered with low dose isoflurane for rodent brain fMRI studies is unknown. Thus, the rationale for the

administration of medetomidine alongside isoflurane for rodent brain fMRI studies is largely derived empirically (Sommers et al., 2002; Weber et al., 2006; Pawela et al., 2009; Jonckers et al., 2011; Lu et al., 2012; Fukuda et al., 2013; Sierakowiak et al., 2015; Zerbi et al., 2015; Hsu et al., 2016). However, there is now evidence that both resting-state and evoked blood-oxygen-level-dependent (BOLD) fMRI signals are altered by the type of anaesthetic drug(s) used and their dose (Masamoto et al., 2007; Masamoto et al., 2009; Masamoto and Kanno, 2012b; Jonckers et al., 2014; Bukhari et al., 2017b; Hamilton et al., 2017; Sirmipilatzte et al., 2019; van Alst et al., 2019). Thus, the many aforementioned inconsistencies in the use of medetomidine and isoflurane may be hindering the interpretation, generalisation, meta-analysis and reproducibility of rodent brain fMRI studies.

Medetomidine substantially reduces the dose of isoflurane required to achieve stable anaesthesia, therefore minimising anaesthetic-induced distortions of BOLD fMRI signals. When dogs are administered a dose of 0.03 mg/kg IV medetomidine, there is a reduction of the minimum alveolar concentration of isoflurane by 47.2% (Ewing et al., 1993). Furthermore, when rodents are anaesthetised with a combined medetomidine and isoflurane dose of 0.06 mg/kg/h IV and 0.5–0.6%, respectively, they exhibit levels of anaesthesia comparable to rodents treated either medetomidine 0.1 mg/kg/h IV or isoflurane 1.3% (Brynildsen et al., 2017). Reducing the dose requirement of each drug is beneficial, as high doses of each drug in isolation are associated with significant drug-specific distortions of BOLD fMRI signals (Brynildsen et al., 2017). This artefact occurs because BOLD fMRI studies rely on the coupling between local blood flow and local neuronal activity (known as neurovascular coupling) to infer and therefore

measure neural activity (Hillman, 2014; Gao et al., 2017b; Sirmipilatzte et al., 2019). BOLD signals in anaesthetised rodents are considered an accurate measure of neural activity when they produce an image reflective of brain activity in the awake rodent. Conversely, BOLD signals are considered inaccurate when they produce an image reflective of fMRI-induced-stress or anaesthetic-induced changes in the BOLD effect (Brynildsen et al., 2017; Chuang et al., 2019). Recent evidence suggests that BOLD fMRI signals obtained during medetomidine and isoflurane anaesthesia can be used to accurately measure rodent brain activity (Brynildsen et al., 2017). This attribute can be partially explained by the synergistic effects of the drugs on preserving neurovascular coupling (Lu et al., 2012; Pirrtimaki et al., 2016). When administered alone, medetomidine alters the BOLD effect by causing cerebral vasoconstriction, bradycardia, decreased cerebral blood flow and altered astrocyte activity (Prielipp et al., 2002; Fukuda et al., 2013; Pirrtimaki et al., 2016). In contrast, when isoflurane is administered alone, it alters the BOLD effect by inducing vasodilation in cerebral vasculature (Iida et al., 1998; Pawela et al., 2009). Accordingly, when medetomidine and isoflurane are administered together, medetomidine appears to attenuate isoflurane-induced cerebral vasodilation, leading to better preservation of neurovascular coupling (Ohata et al., 1999a).

To better utilise medetomidine and isoflurane anaesthesia in rodent fMRI studies, their use should be standardised. To this end, the pharmacokinetic profile of medetomidine during combined medetomidine and isoflurane anaesthesia needs to be elucidated, and the serum concentration of medetomidine in this context needs to be identified. The aim of this study was to describe the pharmacokinetics of

medetomidine during isoflurane anaesthesia and determine the serum concentration of medetomidine when administered with 0.5% (vapouriser setting) isoflurane so that an evidence-based dosing regimen of medetomidine could be determined for rat brain fMRI studies.

2.2. Materials and Methods

The study was approved by the University of Western Australia's Animal Ethics Committee (RA/3/100/1599) and conducted in accordance with the Australian Code for the care and use of animals for scientific purposes, 8th edition (National Health and Medical Research Council, 2013). The rats were housed in an AAALAC (Association for the Assessment and Accreditation of Laboratory Animal Care) facility.

2.2.1. Animals

Twenty-four male, eight-week-old, Sprague-Dawley rats (*Rattus norvegicus*) were imported from the Animal Resources Centre (Canning Vale, WA, Australia) as specific pathogen-free rats. Rats were transported in groups to the animal care facility and held for at least three days prior to the study. The rats were housed in a temperature-controlled environment on a 12 h light-dark cycle with food and water *ad libitum* at M-block in QEII Medical Centre (Nedlands, WA, Australia). The cages were individually ventilated with minimum dimensions of 38.8 cm wide, 40.6 cm long and 21 cm high on coarse aspen bedding. The rats were housed in pairs, fed a commercial rat diet (Specialty Feeds Meat Free Rat and Mouse Diet, Glen Forrest, Australia) that was autoclaved prior to introduction into the animal facility and were provided with acidified drinking water (pH 2.5–3). Food was not withheld prior to anaesthesia. On the

day of the procedure, the rats were transferred to the Centre for Microscopy Characterisation and Analysis (University of Western Australia, Nedlands, Australia).

2.2.2. Experimental procedure

The rats were randomly allocated to three experimental groups: Group T for determination of the target serum concentration of medetomidine when administered with low dose isoflurane for rodent brain fMRI studies ($n = 8$); Groups IV and SC for determination of the SC bioavailability of medetomidine during isoflurane anaesthesia ($n = 8$ each).

On the days of the procedures, the rats were anaesthetised with isoflurane (Isothesia™, Henry Schein Animal Health, 2000, Australia) in an induction chamber (4% isoflurane in 100% medical oxygen, 2 L/min). Once adequately anaesthetised (recumbent, no response to toe pinch) the rats were transferred onto the experimental benchtop and positioned for delivery of isoflurane throughout the experiment (0.5–2% isoflurane vapouriser setting in 100% medical oxygen, 1.5 L/min, Darvall Zero Dead Space face mask circuit, Advanced Anaesthesia Specialists) under a heat lamp. Physiological monitoring included body temperature, respiratory rate, heart rate, electrocardiography (PC-SAM Small Animal Monitor, SA Instruments Inc., 1030 System), exhaled isoflurane and CO₂ (data not shown) (ISATM Sidestream Gas Analyzer, Masimo Sweden AB and PHASEIN and Lightning Multi-Parameter Monitor Vetronic Services Ltd., Newton Abbot, UK) and blood glucose concentration (Accu-Chek Guide, Roche, Mannheim, Germany). These variables were recorded every 5 min. A single rat was studied at any one time, during the hours of 8 a.m. and 6 p.m.

Medetomidine (1 mg/mL, Ilium Medetomidine Injection, Troy Laboratories Pty. Limited, Glendenning, Australia) was administered according to the treatment group. In Group T, rats were administered an initial dose of medetomidine of 0.05 mg/kg SC over 1 s via a 29 G insulin syringe (BD Ultra-Fine Insulin Syringe, Becton Dickinson Pty Ltd., Macquarie University Research Park North Ryde, Australia), immediately followed by a continuous medetomidine infusion of 0.15 mg/kg/h SC, administered via a 25 G butterfly catheter connected to a single syringe infusion pump (Legato 100 Syringe Pump, KD Scientific Inc., Holliston, MA, USA). This protocol was developed empirically and used in our laboratory (Seewoo et al., 2019c). In the IV and SC groups, rats were manually administered a single dose of either IV (through a catheter placed in a lateral tail vein) or SC (under the skin over a flank) medetomidine at 0.05 mg/kg. The concentration of isoflurane was immediately reduced to 0.5% after administration of the initial dose of medetomidine and then subsequently altered to maintain an adequate depth of anaesthesia as assessed by response to toe pinch, heart rate and respiratory rate.

For serial blood sampling, a catheter was placed in the lateral tail vein (22 G, 1 IN, BD Angiocath IV Catheter, BD Australia, Seven Hills, NSW, Australia), secured with surgical tape and flushed with heparinised saline (5 IU/mL). In Group T, blood samples were collected 60 and 90 min after the initial dose of medetomidine. The conditions during anaesthesia were consistent with those observed in previous studies performed in this laboratory and were considered suitable for identification of the target concentration of medetomidine. In the IV group, blood was collected before medetomidine administration and 2, 5, 10, 20, 30, 60, 120 and 180 min afterwards. In the SC group,

blood was collected before medetomidine administration and 10, 20, 30, 40, 50, 60, 120, 180 and 240 min afterwards. Following collection of the final sample, but before recovery from anaesthesia, the rats were euthanised via an intraperitoneal or IV injection of pentobarbitone (160 mg/kg, Lethabarb, Jurox, Rutherford, Australia).

2.2.3. Blood sampling

Approximately 0.5 mL of blood was collected at each timepoint by inserting a 23 G butterfly catheter (SV*23BLK, Terumo Australia Pty Ltd., Macquarie Park, NSW, Australia) into the injection port of the tail vein catheter. The initial saline-diluted drops of blood were discarded before sample collection. A glucometer was used to immediately measure the blood glucose concentration (Accu-Chek Guide, Roche, BellaVista, Australia). After each sample, the catheter was flushed with 0.5 mL of heparinised saline (5 IU/mL) to prevent clot formation in the catheter and replace blood volume. In the event that sufficient blood could not be collected from the catheter, blood was drawn percutaneously from the lateral saphenous veins, medial saphenous veins or femoral arteries through a butterfly catheter.

All blood samples were collected in 3 mL Eppendorf tubes and allowed to clot at room temperature for 10 min before refrigeration. Refrigerated samples were centrifuged within 4 h of collection using an Eppendorf MiniSpin plus centrifugation at 2000× *g* for 10 min. Approximately 0.2 mL of serum supernatant from each sample was collected and transferred into new 3 mL Eppendorf tubes. These serum samples were then frozen at -80 °C.

2.2.4. Serum analysis

The analyses were performed at Metabolomics Australia (University of Western Australia, Nedlands, Australia). Medetomidine concentrations of the serum samples were analysed using a liquid chromatography-tandem mass spectroscopy (LC-MS/MS) technique. The internal standard during analysis was medetomidine- $^{13}\text{C}_3$ hydrochloride (Sapphire Bioscience, Redfern, Australia).

To process the serum for analysis, 20 μL of serum were added to 50 μL of working internal standard (50 ng/mL labelled medetomidine- $^{13}\text{C}_3$ in 50:50 methanol:water plus 0.1% formic acid) and vortexed for 10 s. The mixture was then vortexed with 1 mL ethyl acetate for 120 s, after which they were centrifuged at 3000 rpm for 5 min. Then, 900 μL solvent were evaporated to dryness for 30 min at 40 °C before being reconstituted in 70 μL of 50:50 methanol:water.

Processed serum extracts of 2 μL were run on an Agilent 6460 LC-MS/MS in 2D mode using isotope dilution to adjust for instrument response. Solvent A was LC-MS/MS grade water (Thermo Optima) with 0.1% formic acid (Merck). Solvent B was LC-MS/MS grade methanol (B & J) and 0.1% formic acid (Merck). Column one was an Agilent 2.1 \times 50 mm 2.6 μm C18 Poroschell and column two was a Phenomenex Kinetex 3 \times 150 mm 2.6 μm Biphenyl phase. The flow rate was set at 0.5 mL/min and a gradient was run from 50% B to 80% B in 10 min. The column was washed with 98% B and then returned to 50% B by 7 min. Compounds were heart cut from column one to column two between 0.4–0.9 min. Medetomidine and medetomidine- $^{13}\text{C}_3$ were monitored with transitions 201 > 95 and 204.1 > 98, respectively, with a collision energy of 15. Assay calibration was achieved by spiking drug-free matrix-matched rat plasma to create a

calibration curve, with the r^2 typically > 0.9999 . Assay precision was assessed during the project by extracting 4 samples in triplicate and the intra-assay CV ranged from 2.1–5.7%. The limit of quantitation for the assay was 0.1 ng/mL.

2.2.5. Pharmacokinetic and pharmacodynamic calculations

The maximum serum concentration (C_{max}) of medetomidine following SC administration was the highest measured concentration for each animal. The time at C_{max} (t_{max}) was also determined. The elimination rate constant (λ_z) was calculated as the negative slope of the semilogarithmic plot of each animal created from the terminal three time points ($t = 120, 180$ and 240 min). The elimination half-life ($t_{1/2\beta}$) was calculated as $\ln(2)/\lambda_z$. The area under the serum concentration-time curve ($AUC_{0 \rightarrow \infty}$) was estimated by the trapezoidal rule extrapolated to infinite time. Standard formulae were used to calculate the total body clearance ($Cl = \text{dose}/AUC$) (Toutain and Bousquet-Melou, 2004b) and volume of distribution at pseudo-equilibrium ($Vd_{area} = Cl/\lambda_z$) (Toutain and Bousquet-Melou, 2004c).

The target serum concentration of medetomidine (C_{target}) was obtained from the rats in Group T and was taken as the mean serum concentration of MED at $t = 60$ and 90 min. The loading dose (LD) was estimated from the product of Vd_{area} and C_{target} . The maintenance dose rate (MD) was calculated from the product of Cl and C_{target} .

2.2.6. Trial of results

To trial the calculated drug administration regime for SC administration of medetomidine an additional two rats were administered medetomidine with isoflurane to ensure the conditions for anaesthesia were stable and uneventful. The dose of medetomidine in these two trials was an initial SC dose of 0.12 mg/kg

medetomidine delivered over 5 s followed by SC infusion of 0.08 mg/kg/h with 0.5% (vapouriser setting) isoflurane.

2.2.7. Statistical analyses

Data were tested for normality using a D'Agostino and Pearson test and compared using Student's *t*-test or Mann–Whitney test (GraphPad Prism). The *p*-value used to define statistical significance was 0.05. Data are expressed as mean \pm standard deviation or as otherwise stated.

2.3. Results

2.3.1. Group T

The rats weighed 333.2 ± 19.3 g ($n = 6$). Data from two rats were excluded from the study due to inaccurate weight records at the time of anaesthesia and therefore incorrect doses of medetomidine being administered. Otherwise, anaesthesia was uneventful and a stable heart rate (307.9 ± 30.7 bpm), respiratory rate (52.9 ± 8.3 breaths/min) and normothermic temperature (38.1 ± 0.7 °C) were maintained. The blood glucose concentration at 60 min was 20.9 ± 3.0 mmol/L and at 90 min was 23.2 ± 2.6 mmol/L (Figure 2.1). The vapouriser setting for inhaled isoflurane was maintained at 0.5% after induction of anaesthesia, whereby from 5 to 90 min after the initial dose of medetomidine the exhaled isoflurane concentration was $0.49 \pm 0.05\%$ (Table 2.1).

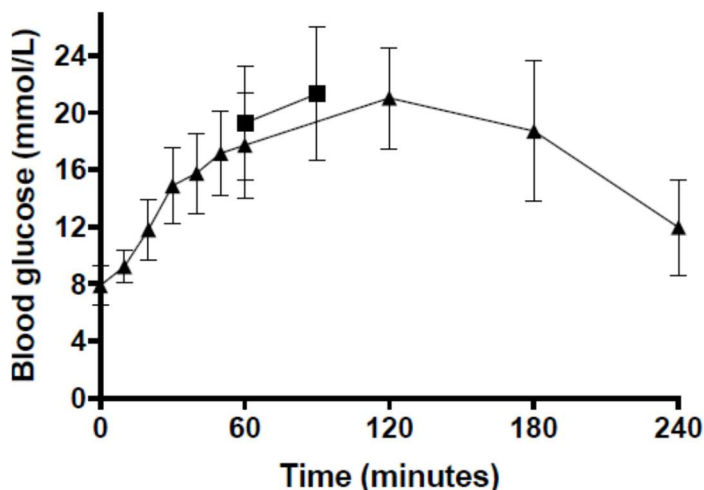


Figure 2.1. Time course of mean (\pm standard deviation) blood glucose concentration during anaesthesia of Sprague-Dawley rats in Group T (0.05 mg/kg medetomidine subcutaneous (SC) followed by a continuous infusion of 0.15 mg/kg/h SC with 0.5% isoflurane; squares) and Group SC (0.05 mg/kg medetomidine SC; triangles).

Table 2.1. Mean (\pm standard deviation) concentration of expired isoflurane during administration of isoflurane after an initial dose of medetomidine of 0.05 mg/kg SC followed by a continuous medetomidine infusion of 0.15 mg/kg/h SC (Group T) or a medetomidine dose of 0.05 mg/kg SC (Group SC). The delivery of isoflurane was adjusted as necessary to maintain an adequate depth of anaesthesia, as assessed by response to toe pinch, heart rate, respiratory rate and expired carbon dioxide concentration. Only results for the first 90 min are shown.

Expired Isoflurane (%)								
	5 min	10 min	15 min	25 min	35 min	45 min	60 min	90 min
Group T ($n = 6$)	0.6 (\pm 0.2)	0.6 (\pm 0.4)	0.5 (\pm 0.3)	0.5 (\pm 0.04)	0.5 (\pm 0.1)	0.5 (\pm 0.1)	0.4 (\pm 0.1)	0.5 (\pm 0.1)
Group SC ($n = 7$)	1.2 (\pm 0.5)	1.0 (\pm 0.5)	1.0 (\pm 0.3)	1.0 (\pm 0.1)	1.0 (\pm 0.1)	1.0 (\pm 0.1)	1.0 (\pm 0.2)	1.2 (\pm 0.3)

The serum medetomidine concentration at 60 min after the initial medetomidine dose was 13.9 ± 3.9 ng/mL (range 9.9–20.8 ng/mL) which was similar to that at 90 min ($p = 0.329$): 15.0 ± 2.0 ng/mL (range 12.0–18.1 mg/mL). Therefore, for the purposes of identifying the serum concentration of medetomidine when administered with low dose isoflurane for rat brain fMRI studies, these data were grouped, and the target serum concentration of medetomidine was determined to be 14.4 ± 3.0 ng/mL.

2.3.2. Group IV

The rats weighed 333.6 ± 17.2 g ($n = 8$). In seven of the Group IV rats, respiratory arrest was observed immediately after manual administration of the IV injection of medetomidine, and gentle external chest compressions were performed. After 2 min, spontaneous ventilation resumed. Anaesthesia was otherwise uneventful. The blood glucose concentration peaked at 60 min at 16.6 ± 2.4 mmol/L and at 180 min at 11.2 ± 2.3 mmol/L.

Fifteen minutes after the administration of IV medetomidine, half of the rats required the vapouriser setting for isoflurane to be increased from 0.5% isoflurane. By 35 min, all the rats required the vapouriser setting for isoflurane to be increased from 0.5% isoflurane and maintained at approximately 1–2%.

The serum medetomidine concentration peaked at 2 min at 754.6 ± 672.5 ng/mL (range 122.1–2139.4 ng/mL). Given the variability of these data, the IV group was excluded from pharmacokinetic calculations.

2.3.3. Group SC

The rats weighed 317.9 ± 19.9 g ($n = 7$). Data from one rat (the first) was excluded from the study as it was administered an initial SC dose of medetomidine of 0.1 mg/kg and became apnoeic for approximately 2 min, requiring external chest compressions. The seven subsequent rats were administered a lower dose of 0.05 mg/kg SC medetomidine and anaesthesia was uneventful. The blood glucose concentration peaked at 120 min at 20.4 ± 3.4 mmol/L (Figure 2.1).

The inhaled isoflurane concentration required to maintain an adequate depth of anaesthesia throughout the procedure in Group SC was more variable than in the

other groups (Table 2.1). The serum medetomidine concentration peaked at 60 min at 3.4 ± 0.9 ng/mL (Figure 2.2).

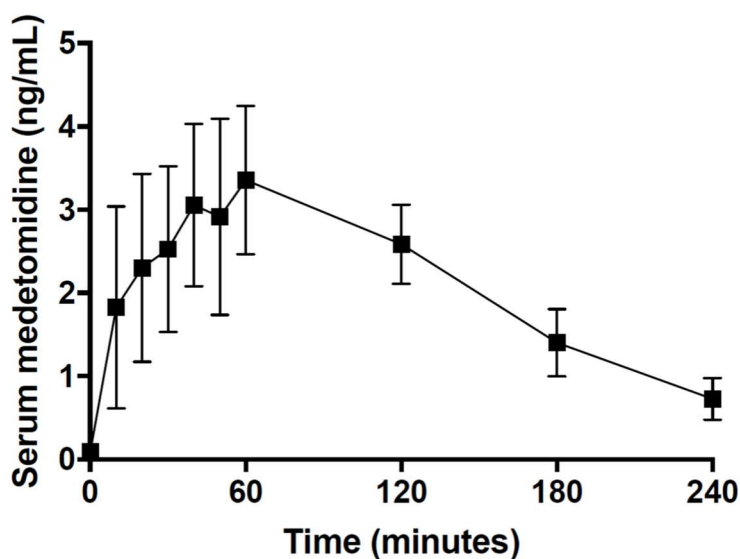


Figure 2.2. Time course of mean (\pm standard deviation) serum medetomidine concentration after subcutaneous administration of 0.05 mg/kg medetomidine in six Sprague-Dawley rats.

2.3.4. Pharmacokinetic calculations

The pharmacokinetic and pharmacodynamic parameters were calculated from the mean serum medetomidine concentration data (Table 2.2). To achieve a target medetomidine concentration of 14.4 ± 3.0 ng/mL an initial SC dose of 0.12 mg/kg medetomidine followed by SC infusion of 0.08 mg/kg/h medetomidine should be administered during isoflurane anaesthesia.

Table 2.2. Individual and mean (\pm standard deviation) pharmacokinetic (PK) and pharmacodynamic parameters after administration of 0.05 mg/kg SC medetomidine in seven Sprague-Dawley rats. C_{max} = maximum serum concentration; t_{max} = time of C_{max} ; λ_z = elimination rate constant; $t_{1/2\beta}$ = elimination half-life; $AUC_{0 \rightarrow \infty}$ = area under the serum concentration time curve from time = 0 to ∞ ; Cl = total body clearance; Vd_{area} = volume of distribution at pseudo-equilibrium; LD = loading dose; MD = maintenance dose.

Rat ID	C_{max} (ng/mL)	t_{max} (min)	λ_z (/min)	$t_{1/2\beta}$ (min)	$AUC_{0 \rightarrow \infty}$ (ng.min/mL)	Cl (mL/kg/min)	Vd_{area} (L/kg)	LD (mg/kg)	MD (mg/kg/h)
R	4.9	60	0.0095	73.0	664.7	75.2	7.9	0.1142	0.0651
S	3.3	60	0.0118	58.7	570.8	87.6	7.4	0.1070	0.0758

T	4.4	50	0.0112	61.9	610.1	82.0	7.3	0.1055	0.0709
U	3.7	40	0.0130	53.3	485.3	103.0	7.9	0.1143	0.0891
V	2.9	120	0.0107	64.8	511.8	97.7	9.1	0.1316	0.0845
W	2.8	60	0.0112	61.9	485.6	103.0	9.2	0.1325	0.0891
X	3.3	120	0.0084	82.5	704.4	71.0	8.5	0.1218	0.0614
Mean (SD)	3.6 (0.7)	72.9 (30.6)	0.0108 (0.0014)	65.2 (9.0)	576.1 (81.1)	88.5 (12.1)	8.2 (0.7)	0.1181 (0.0101)	0.0765 (0.0105)

2.3.5. Trial of results

Two additional rats were administered medetomidine with isoflurane at the doses calculated in this study. The vapouriser setting for isoflurane could be maintained at or below 0.5% and anaesthesia was uneventful. Given the calculated initial dose was higher than that used in groups SC and IV, the initial dose was administered over five seconds to mitigate the risk of apnoea (as observed in the IV group and the first rat in the SC group that was administered 1.0 mg/kg SC). Apnoea did not occur when the initial dose was delivered over five seconds.

2.4. Discussion

The present study shows that steady-state serum concentrations of medetomidine will be achieved in male Sprague-Dawley rats if an initial SC dose of medetomidine of 0.12 mg/kg is administered in combination with continuous 0.5% (vapouriser setting) isoflurane, followed by SC infusion of medetomidine at 0.08 mg/kg/h. This regime appears to provide suitable conditions for anaesthesia when the initial dose is delivered over five seconds. This result is within the range of doses reported in the literature (Pirttimaki et al., 2016; Brynildsen et al., 2017).

The Group T result was used as the target serum concentration of medetomidine when administered with 0.5% (vapouriser setting) isoflurane. The anaesthetic protocol in this group was based on consultation with researchers using combined medetomidine and

isoflurane anaesthesia in ongoing resting-state rodent fMRI studies. Given the apparent empirical success of the protocol in achieving strong and reproducible fMRI signals (Seewoo et al., 2019c), rats under this protocol were hypothesised to achieve a steady-state concentration of medetomidine. Data from rats in Group SC were used to determine the SC bioavailability of medetomidine during combined medetomidine and isoflurane anaesthesia. Collectively, the data from the two groups were used to inform the SC administration of medetomidine in rodents with low dose isoflurane.

The intention was to use data from both the IV and SC groups to perform pharmacokinetic calculations. However, the data from Group IV were excluded from the analysis due to considerable variation in this data set. We attribute the variation to the use of a single cannula for both IV drug administration and subsequent serial blood sampling. Issues arising from the use of a single cannula have been investigated and described by Gaud et al. (2017). They report that the use of a single cannula is not suitable for pharmacokinetic studies. Some compounds will experience non-specific binding to the cannula that may contaminate the first few blood samples taken from the cannula and lead to overestimation of serum concentrations (Gaud et al., 2017). Manually flushing the cannula with heparinised saline can help dislodge bound medetomidine, therefore reducing serum concentration overestimation. However, the flushing can also cause increased variation in measured serum medetomidine concentration due to the random error associated with repeated hand-operated techniques. This oversight likely led to inaccurate serum concentrations in the Group IV and hence the exclusion of these data.

The Group T data suggest that a steady-state serum medetomidine concentration of 14.4 ± 3.0 ng/mL is suitable for rats undergoing brain fMRI with 0.5% (vapouriser setting) isoflurane. This combination of drugs creates conditions suitable for prolonged anaesthesia (hours) without major anaesthetic-specific distortion of BOLD fMRI signals (Seewoo et al., 2019c). Future studies could consider using various doses of medetomidine and isoflurane to better define the therapeutic range for these drugs in the context of optimising the quality of fMRI images.

In the present study, the elimination half-life of medetomidine in rats was calculated to be $65.2 (\pm 9.0)$ min. Similar values were calculated by Bol et al. (56.2 and 57.4 min) in a study of dexmedetomidine that was administered to Harlan-Sprague-Dawley male rats by two different IV infusion protocols (Bol et al., 1997). In our study, and the work by Bol et al. (1997), drug concentrations were analysed for 210–240 min, and in neither study did blood medetomidine nor dexmedetomidine concentrations become undetectable. In contrast, a slower elimination half-life (1.6 h) was reported by Salonen (1989) after tritium (^3H)-labelled medetomidine was administered SC to male and female Sprague-Dawley rats. Furthermore, Salonen (1989) detected plasma radioactivity at five and eight hours after administration of ^3H - medetomidine. The persistence of medetomidine at these time points (five and eight hours) may suggest that in our four-hour study, and in the study by Bol et al. (1997), the elimination rate constant was overestimated and therefore the elimination half-life was underestimated. This parameter could be explored in future studies by quantifying blood medetomidine (or dexmedetomidine) levels for several hours after administration.

The first rat in Group SC was administered a rapid initial dose (< one second, delivered manually) of 0.1 mg/kg SC medetomidine and became apnoeic for approximately two minutes. This response was not previously observed when the initial SC medetomidine dose was mechanically delivered in one second. Thus, the decision was made to alter the initial SC dose in Group SC from 0.1 mg/kg to 0.05 mg/kg for the remaining seven rats in that group. Although rats in Group IV also became apnoeic after administration of medetomidine, the dose in this group was not altered. The rationale to not alter the dose in Group IV was that transient apnoea could be managed with manual external chest compressions with the rat in sternal recumbency. To mitigate the risk of apnoea, the initial dose could be delivered over a longer time period; so during the trial of the calculated initial and infusion dose, the initial dose was administered over five seconds by the infusion pump. The conditions during anaesthesia were stable and uneventful.

Measurement of blood glucose concentrations was performed opportunistically and was not the primary aim of the project. Nevertheless, hyperglycaemia developed in all the rats in this study and although this side effect of medetomidine is described in rats its impact on experimental outcomes is not clear (Callahan et al., 2014). The mechanism of hyperglycaemia is a combination of anti-ADH (antidiuretic hormone) effects and alterations in insulin sensitivity, resulting in an osmotic diuresis (Lemke, 2007). This side effect of administration of medetomidine should be considered when designing anaesthetic regimens for research.

There are a number of limitations to this study which must be considered when interpreting the results. Only male, eight-week-old, Sprague-Dawley rats were used in this small study. This cohort limits the direct applicability of the results to female rats,

other rat strains and mice. The age of the rats in this study is also a limitation of the model as adult animals may have a different pharmacokinetic profile for medetomidine. Future studies could expand the applicability of these results by investigating the pharmacokinetics of medetomidine in female rats, pregnant rats, obese rats, and different ages and strains of rats and mice. In addition, the pharmacokinetic calculations could only be performed with serum concentrations of medetomidine that were obtained following SC administration. The data from Group IV was unfortunately excluded. Nevertheless, the data from Group SC were utilized in isolation, which meant that during the sampling period, the serum concentrations of medetomidine were assumed to be in pseudo-equilibrium. Thus, calculating the volume of distribution using the area method (Vd_{area}) was appropriate (Toutain and Bousquet-Melou, 2004a). The loading dose should be calculated using the volume of distribution calculated at steady state (Vd_{ss}). Given Vd_{area} is usually only larger than Vd_{ss} by a small amount, our calculated loading dose is likely to still be a reliable estimate. Furthermore, single doses of medetomidine and isoflurane were evaluated in this study as the aim was to determine a target concentration of medetomidine based upon empirical evidence of using these doses. Future work should consider the evaluation of alternative doses and their impact on fMRI outputs. Finally, the target dose as determined by Group T was based on the premise that quality fMRI images were acquired (in previous work in the lab) with the empirical protocol. Correlation of our conclusions with the quality of fMRI images has not been performed.

For studies where multiple imaging sessions are scheduled and the animals recover from anaesthesia, the administration of atipamezole is prudent. This drug antagonises

medetomidine and is routinely administered in the laboratory in which this study was performed when rats recover from anaesthesia.

The benefit of combined medetomidine and isoflurane anaesthetic protocols in rodent brain fMRI studies may be compromised by inconsistencies in these anaesthetic protocols between studies. Anaesthetics alter BOLD fMRI signals and these inconsistencies hinder the interpretation, generalisation, meta-analysis and reproducibility of rodent brain fMRI studies. Future brain fMRI studies should consider an evidence-based approach to the use of medetomidine and isoflurane anaesthetic protocols to standardise the regime between studies.

2.5. Conclusion

The data suggest that a serum medetomidine concentration of 14.4 ± 3.0 ng/mL is suitable for rats undergoing brain fMRI with 0.5% (vapouriser setting) isoflurane.

Chapter 3

Methods Development: An analytical workflow for seed-based correlation and independent component analysis in interventional resting-state fMRI studies

Published as: Seewoo, B.J., Joos, A.C. & Feindel, K.W., 2020. An analytical workflow for seed-based correlation and independent component analysis in interventional resting-state state fMRI studies. 165: 26–37. *Neuroscience Research*. doi: 10.1016/j.neures.2020.05.006 (Appendix D)

Resting-state functional MRI (rs-fMRI) measures brain activity while a subject is at rest.

This technique relies on the fact that when an area of the brain is in use, blood flow to that region also increases and therefore, there is a change in blood oxygenation. The goal of rs-fMRI data analysis is to detect correlations in activity between brain regions by using this blood-oxygen-level-dependent (BOLD) contrast. However, the BOLD signature of brain activity is relatively weak and thus, other sources of noise in the acquired data must be carefully controlled. This means that a series of processing steps must be performed on the acquired images before the actual statistical search for correlations in brain activity can begin. Independent component analysis (ICA) and seed-based correlation analysis (SCA) are the two most widely used methods for analysing rs-fMRI data. However, there seems to be no established workflow of optimal combination of analytical steps and how to execute them. This strongly limits the comparability of rs-fMRI results and makes establishing a suitable data analysis pipeline for researchers new to the field difficult.

In this chapter, rodent rs-fMRI data from longitudinal brain stimulation studies described in Chapters 5 and 6 were used to investigate these two methods using FSL,

both qualitatively and quantitatively. Specifically, I examined: (1) RSN identification and group comparisons in ICA, (2) ICA-based denoising compared to nuisance signal regression in SCA, and (3) seed selection in SCA. The findings from this chapter confirm that these three factors have a drastic impact on the results of the rs-fMRI data analysis. In ICA, using a baseline-only template resulted in detection of greater functional connectivity within RSNs and more sensitive detection of group differences than when an average pre/post-stimulation template was used. In SCA, the use of an ICA-based denoising method in the preprocessing of rs-fMRI data instead of nuisance regression, and the use of seeds from individual functional connectivity maps in running group comparisons, increased the sensitivity of detecting group differences by preventing the reduction of signals of interest.

These findings can be directly applied to both animal and human rs-fMRI studies to improve the reliability of results and comparability across studies. To encourage and facilitate uptake of our analysis pipelines, detailed instructions and bash scripts are provided in the supplementary material (Appendix D) for the practical execution of the analysis steps described in this chapter.

3.1. Introduction

Functional magnetic resonance imaging (fMRI) is a powerful tool for brain research and has great potential in diagnosing and tracking the treatment of neurological disorders. fMRI primarily uses the blood-oxygen-level-dependent, or BOLD, contrast as an indirect measurement of brain activity. Functional connectivity, which refers to the strongly correlated time signal of spatially remote brain regions, can be observed both during the execution of a task or at rest, that is, in the absence of a specific task or stimulus. A functional brain network observed at rest is called a resting-state network (RSN) and the associated imaging technique is resting-state fMRI (rs-fMRI). Patients with neurological and psychiatric disorders such as Alzheimer's disease, Parkinson's disease and depression have been found to exhibit abnormal connectivity within their RSNs compared to healthy individuals (Seeley et al., 2009; Lee et al., 2013a; Gorges et al., 2017).

Using rs-fMRI has several important advantages. Firstly, multiple RSNs can be studied simultaneously and RSNs can be detected in subjects who are not able to or are not trained to perform a specific task (Lee et al., 2016). The absence of a task also makes rs-fMRI studies less laborious in terms of the imaging procedure (Lee et al., 2016).

Additionally, RSNs are quite consistent among mammalian species, which allows for an easier translation of results from animal studies to clinical applications (Pawela et al., 2008; Becerra et al., 2011; Gorges et al., 2017). Furthermore, RSNs are also largely similar between awake and anaesthetised states, which is especially important in paediatric and animal studies for prevention of motion artefacts (Liang et al., 2012; Paasonen et al., 2018; Seewoo et al., 2018a). However, despite the usefulness of rs-

fMRI in a clinical and preclinical setting, analysis steps to obtain significant and reliable results from the noisy raw data are extensive and complex and there are numerous different analysis pipelines in the literature.

Several statistical approaches exist for obtaining the functional connectivity maps and identifying the RSNs in rs-fMRI data (Cole et al., 2010; Lv et al., 2018). The two most widely used approaches are region of interest (ROI) or seed-based correlation analysis (SCA) (Biswal et al., 1995; Cordes et al., 2000) and independent component analysis (ICA) (Calhoun et al., 2001; Beckmann et al., 2005; Calhoun and de Lacy, 2017). In SCA, the rs-fMRI timeseries of a predefined brain region is correlated with the timeseries of all other voxels in the brain to obtain a map of the functional connectivity for each subject/imaging session. This predefined brain region is called the seed or the ROI and is usually selected based on a hypothesis or task-dependent activation map. For example, in primates, placing a seed in the posterior cingulate cortex is often used to find the default mode network (DMN), a large-scale brain network, separate from other RSNs (Greicius et al., 2003; Korgaonkar et al., 2014; Sierakowiak et al., 2015). Based on the individual functional connectivity maps, a higher-order statistical analysis can then be performed to identify group differences. In contrast to SCA, no prior knowledge is needed for ICA. ICA decomposes 4D rs-fMRI data of the whole brain into a number of spatially maximally independent 3D maps, called components, consisting of potentially distant brain regions with highly synchronized activity (similar time courses). ICA can identify several RSNs at the same time. Single-session ICA looks for patterns in each subject/imaging session separately, whereas group ICA tries to identify common patterns across multiple subjects and/or timepoints. In the functional

MRI of the Brain (FMRIB) software library (FSL), the dual-regression tool can be subsequently used for higher-order statistical analyses to determine differences between groups.

However, whether SCA or ICA or hybrid methods should be preferred remains unclear (Cole et al., 2010; Kelly et al., 2010; Joel et al., 2011; Rosazza et al., 2012; Smith et al., 2014; Neha and Gandhi, 2016; Wu et al., 2018). This strongly limits the comparability of rs-fMRI results and makes establishing a suitable data analysis pipeline for researchers new to the field difficult. Additionally, prior to identifying RSNs and calculating group differences, several steps of pre-processing must be employed such as head motion correction, brain extraction and co-registration to a brain atlas (Van den Heuvel and Hulshoff Pol, 2010; Gorges et al., 2017). A considerable variety of pre-processing methods exist and the ways in which these steps are executed in the literature are also variable (e.g., Lu et al., 2010; Ciric et al., 2017). For example, there are several denoising methods that can be used to clean the BOLD fMRI signal and these methods have been extensively compared and reviewed in the literature (Pruim et al., 2015; Caballero-Gaudes and Reynolds, 2017; Parkes et al., 2018).

In this article, we investigate several main aspects of ICA and SCA with the aim to provide a combination of analytical steps which produce the most reliable results using FSL. We specifically address the choice of template for ICA and the de-noising and ROI selection methods for SCA, using longitudinal rat brain rs-fMRI data for demonstration. We hypothesise that the use of the recommended all-data template in ICA will not be applicable to longitudinal studies due to the introduction of bias towards post-treatment data. We further hypothesise that despite the long-standing practice of

using ICA and SCA separately, use of a hybrid method will improve the results of SCA, both in terms of network identification and detection of group differences. We also provide bash scripts and detailed instructions on how to perform each step of the data analysis using FSL (Jenkinson et al., 2012), enabling researchers new to the field to perform analyses more efficiently.

3.2. Materials and Methods

All experimental procedures were approved by the UWA Animal Ethics Committee (RA/3/100/1430 and RA/3/100/1640) and conducted in accordance with the *National Health and Medical Research Council Australian code* for the care and use of animals for scientific purposes. All investigators were trained in animal handling by the UWA Programme in Animal Welfare, Ethics, and Science (PAWES) and had valid Permission to Use Animals (PUA) licenses.

3.2.1. Resting-state fMRI data

3.2.1.1. Animals

Rodent rs-fMRI data from our previous longitudinal brain stimulation study (Seewoo et al., 2019c) were used to evaluate the two most commonly used methods for analysing rs-fMRI data: ICA and SCA. To maximise the use of collected data, rs-fMRI data and T2-weighted images collected using the same acquisition and anaesthesia protocols in adult (6–8 weeks old, 150–250 g) male Sprague Dawley rats from more recent experiments were also included in the analyses for the baseline group (n = 11 from Seewoo et al. (2020b) and n = 33 unpublished). Adult male Sprague Dawley rats (150–250 g; 6–8 weeks old) were sourced from the Animal Resources Centre (Canning Vale, WA, Australia) and were maintained in a temperature-controlled animal care facility

on a 12-hour light-dark cycle with *ad libitum* food and water. All rats acclimatized to their new environment for one week following their arrival.

We have used baseline rs-fMRI data acquired from a total of 62 animals (n = 11 from Seewoo et al. (2020b), n = 18 from Seewoo et al. (2019c), n = 33 unpublished) and post-stimulation data from nine animals (Seewoo et al., 2019c). In brief, following baseline rs-fMRI data acquisition, nine animals received daily brain stimulation for 15 consecutive days. Low-intensity repetitive transcranial magnetic stimulation (LI-rTMS) was delivered at 10 Hz (10 pulses per second) to the right brain hemisphere of the nine awake and behaving rats daily for a period of 10 minutes (6,000 pulses) using a custom-built round coil (Grehl et al., 2015; Seewoo et al., 2018b). For these animals, imaging was conducted pre-stimulation on Day 0 (baseline), Day 7 and Day 14. After Day 14, daily stimulation was ceased, but the animals were again imaged on Day 21 and Day 34.

During imaging, anaesthesia was induced with 4% isoflurane followed by subcutaneous bolus administration of medetomidine (0.05-0.1 mg kg⁻¹). During initial scanning, isoflurane (2%) in medical air was delivered via a nose cone with continuous subcutaneous infusion of medetomidine (0.15 mg kg⁻¹ h⁻¹). Following 15 min of infusion, isoflurane was gradually reduced to 0.25-0.75%. These anaesthetic doses were empirically determined to ensure the respiratory rate was between 50-80 breaths/minute. A combination of low-dose isoflurane and medetomidine is the recommended anaesthetic protocol for longitudinal rodent rs-fMRI experiments that has been shown to yield similar RSN connectivity as the awake condition (Paasonen et

al., 2018; Seewoo et al., 2018a). Body temperature and respiratory rate were monitored using a PC-SAM Small Animal Monitor (SA Instruments Inc., 1030 System).

3.2.1.2 MRI data acquisition

All MR images were acquired with a Bruker BioSpec 9.4 T scanner (AVANCE III HD, ParaVision 6.0.1) using a volume transmit and rat-brain quadrature receive radiofrequency coil combination. High-resolution T2-weighted coronal images were acquired using a multi-slice 2D RARE (rapid acquisition with relaxation enhancement) sequence with fat suppression from 21 x 1-mm-thick interlaced slices with slice gap of 0.05 mm and: field-of-view (FOV) 28.0 mm x 28.0 mm; matrix size 280 x 280; in-plane pixel size 0.1 mm x 0.1 mm; repetition time (TR) 2500 ms; echo time (TE) 33 ms; RARE factor 8; echo spacing 11 ms; number of averages (NA) 2; number of dummy scans (DS) 2; flip angle (α) 90°; receiver bandwidth 34722.2 Hz; and scan time 2 min 55 s. Before rs-fMRI data acquisition, B0 shimming was completed for a region of interest covering the brain using the Bruker Mapshim routine. Rs-fMRI scans were acquired using a single-shot gradient-echo EPI (echo planar imaging) sequence. Scan parameters were: FOV 28.2 mm x 21.0 mm, matrix size 94 x 70, in-plane pixel size 0.3 mm x 0.3 mm, TE 11 ms, and TR 1500 ms, 21 slices with a thickness of 1 mm and a gap of 0.05 mm. The receiver bandwidth was 326087.0 Hz. Each rs-fMRI dataset comprised 300 repetitions, resulting in a scanning time of 7.5 min. The images acquired and analysed during the study are available from the corresponding author on reasonable request.

3.2.2. Common image pre-processing steps for ICA and SCA

The data analysis pipeline is illustrated in Figure 3.1 and detailed scripts for executing each step can be found in the Supplementary Material (Appendix D). Most of the pre-processing and analysis steps were performed using the Functional MRI of the Brain (FMRIB) Software Library (FSL) v5.0.10 (Jenkinson et al., 2012). The Bruker data was exported from ParaVision 6.0.1 into DICOM (Digital Imaging and Communications in Medicine; <http://dicom.nema.org/>) format (Bidgood Jr et al., 1997) and then converted into NifTI (Neuroimaging Informatics Technology Initiative, <https://nifti.nih.gov/>) using the dcm2nii (64-bit Linux version 5 May 2016) converter (Rorden et al., 2007). Pre-processing of fMRI data included: (i) reorienting the brain into left-anterior-superior (LAS) axes (radiological view), (ii) skull-stripping using the qimask utility from QUantitative Imaging Tools or QUIT (Wood, 2018), and (iii) upscaling the voxel sizes by a factor of 10 (Tambalo et al., 2015). See Supplementary Script S1 in Appendix D for details.

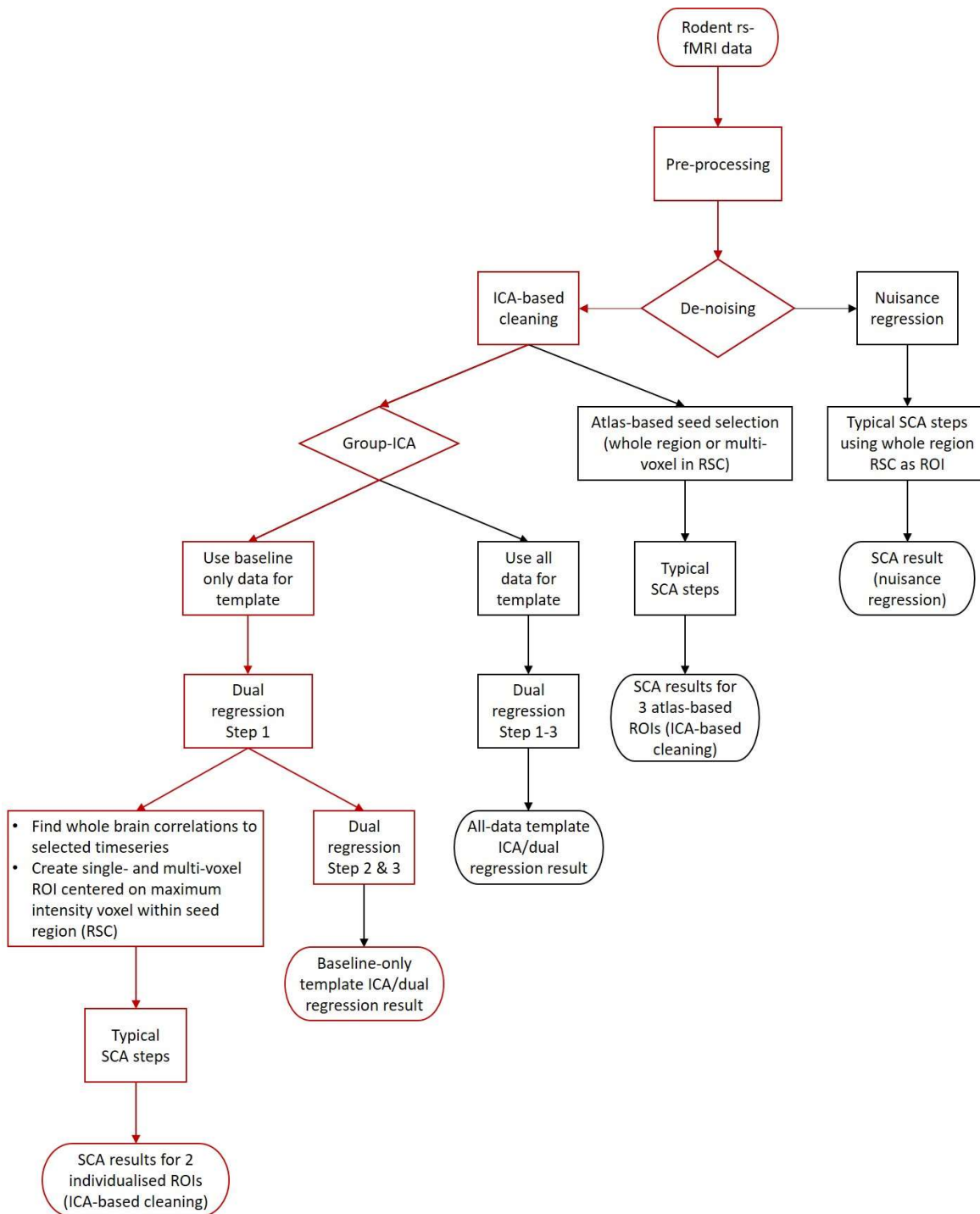


Figure 3.1. Data analysis pipeline. Functional connectivity maps and group differences were obtained from rat rs-fMRI data to investigate three aspects of data analysis: use of baseline-only vs all-data template in independent component analysis (ICA), use of ICA-based cleaning or nuisance regression in denoising data for seed-based correlation analysis (SCA) and seed selection for SCA. Whole region, multi-voxel and/or single-voxel regions of interest (ROIs) were selected within the retrosplenial cortex (RSC). Both atlas-based and individualised ROIs were investigated. The recommended pathways for ICA and SCA are depicted in red.

3.2.3. Independent component analysis

3.2.3.1. Image pre-processing

Single-session ICA was carried out for each brain-extracted image in FSL/MELODIC (Multivariate Exploratory Linear Decomposition into Independent Components; Beckmann et al., 2005) with the Gaussian kernel filter set to a full-width half maximum (FWHM) of 6.25 mm (twice final voxel size: Mikl et al., 2008) and a temporal high pass filter cut-off of 100 s. Motion correction (Jenkinson et al., 2002) was also applied to spatially realign the functional images to the middle volume of a serial acquisition (see Supplementary Script S2 in Appendix D for details). FSL/FIX (FMRIB's ICA-based Xnoiseifier v1.06) was manually trained by hand-labelling ICA's decomposition of 60 datasets into signal or noise based on each component's time-course, frequency, and spatial map as described by Salimi-Khorshidi et al. (2014) (see Supplementary Figures 3.1 and 3.2 for examples of noise and signal components respectively). Then, the motion parameters and the noise components of all filtered datasets from MELODIC were automatically classified and regressed by FSL/FIX at a threshold of 20 (Griffanti et al., 2014; Salimi-Khorshidi et al., 2014). The de-noised fMRI images for each session were then co-registered to their respective T2-weighted images using six-parameter rigid body registration using FLIRT (FSL Linear Image Registration Tool; Jenkinson and Smith, 2001; Jenkinson et al., 2002) and normalised to a Sprague Dawley brain atlas (Papp et al., 2014; Kjonigsen et al., 2015; Sergejeva et al., 2015) with nine degrees of freedom registration. The atlas was first down-sampled by a factor of eight to better match the voxel size of the 4D functional data.

3.2.3.2. Image analysis

Multi-subject temporal concatenation group-ICA as implemented in FSL/MELODIC was carried out on baseline rs-fMRI data to identify template rodent networks. The ICA algorithm was restricted to 15 components based on other rs-fMRI studies in rodents (Jonckers et al., 2011; Zerbi et al., 2015; Seewoo et al., 2018b). Using more components can lead to further splitting of some of the networks, but was not found to provide any benefits by studies investigating the effect of the number of components (Jonckers et al., 2011; Lu et al., 2012). Three of the 15 group-ICA identified components from the baseline-only rs-fMRI data were considered for further analysis: component 1 (C1), the interoceptive network; component 2 (C2), the default mode network; and component 3 (C3), the salience network. These components were chosen because they comprise of the most commonly studied RSNs in the literature and conform with the rules of RSN identification proposed by Grandjean et al. (2019) such as strong homotopic bilateral organisation of the network. The reliability of network identification was tested and confirmed by bootstrapping the number of animals.

The general linear model tool was used to set up comparisons (t-contrasts) between the relevant RSNs at the five different timepoints for dual regression analysis ($n = 9$ animals \times 5 timepoints). Please note that while all available baseline data ($n = 62$) was used to create the baseline-only template, only data from the rTMS study was used in the comparisons for determining group differences ($n = 9$ at baseline; see Table 3.1). Analysis for between-group differences was then conducted on the relevant RSNs using the FSL dual regression approach (Rytty et al., 2013; Nickerson et al., 2017) that allows for voxel-wise comparisons of rs-fMRI data. First, the group-average set of

spatial maps were regressed (as spatial regressors in multiple regression) into the subject's 4D space-time dataset for each subject at each timepoint. A set of subject/timepoint-specific timeseries was therefore obtained, one per group-level spatial map. Next, timeseries were regressed as temporal regressors (multiple regression) into a single 4D dataset, resulting in a set of subject/timepoint-specific spatial maps, which were subject-level representations of these components at each timepoint (Beckmann et al., 2009). We then tested for group differences using FSL's randomise nonparametric permutation-testing tool, with 5000 permutations, using a threshold-free cluster enhanced (TFCE) technique and family-wise error (FWE) correction to control for multiple (spatial) comparisons. The resulting statistical maps were thresholded to $p < 0.00625$ to account for the eight different longitudinal comparisons using the conservative Bonferroni correction. These eight comparisons between the five different time points were chosen based on the design of the longitudinal study. A threshold of 30 adjacent voxels was used for the cluster size. Cluster size thresholds reported in the literature mostly vary between 10 and 50 (e.g., Zhang et al., 2014; Mueller et al., 2017).

The group-ICA algorithm was re-run on all longitudinal rs-fMRI data ($n = 9$ animals \times 5 timepoints) to identify the RSNs (see Table 3.1). The components from this all-data template were visually compared to the previous baseline-only template. The quality of RSN identification was assessed based on similarity to rodent RSNs reported in the literature (Lu et al., 2012; Zerbi et al., 2015; Bajic et al., 2016; Grandjean et al., 2019). The group differences found based on the all-data template were then quantitatively compared to the results of the baseline-only template. For this comparison, only the

interoceptive network (C1) was used, since the default mode network (C2) in the all-data template overlapped with another network, and for the salience network (C3), no significant changes were found in the previous publication (Seewoo et al., 2019c).

Since the visual comparison of identified RSNs is somewhat subjective, the quantitative comparison of group differences is a more meaningful approach for assessing the quality of different analysis pipelines.

In addition to baseline-only and all-data templates, the group-ICA algorithm was also used to create balanced templates of four different combinations of timepoints: Day 0/Day 7, Day 0/Day 14, Day 14/Day 21 and Day 14/Day 34 (see Table 3.1). This allowed testing of group differences based on balanced templates as well, as is often done in studies with pre-post treatment or healthy-pathological design (e.g., Filippini et al., 2009; Filippini et al., 2012; Zamboni et al., 2013).

Table 3.1. ICA templates and group comparisons.

Template type	Data used for making template	Data used in dual regression
Baseline-only template	n = 11 from Seewoo et al. (2020b), n = 18 from Seewoo et al. (2019c) and n = 33 unpublished	Day 0 (n = 9), Day 7 (n = 9), Day 14 (n = 9), Day 21 (n = 9) and Day 34 (n = 9)
All-data template	Day 0 (n = 9), Day 7 (n = 9), Day 14 (n = 9), Day 21 (n = 9) and Day 34 (n = 9)	Day 0 (n = 9), Day 7 (n = 9), Day 14 (n = 9), Day 21 (n = 9) and Day 34 (n = 9)
Balanced template	Day 0 (n = 9) and Day 7 (n = 9)	Day 0 (n = 9) and Day 7 (n = 9)
Balanced template	Day 0 (n = 9) and Day 14 (n = 9)	Day 0 (n = 9) and Day 14 (n = 9)
Balanced template	Day 14 (n = 9) and Day 21 (n = 9)	Day 14 (n = 9) and Day 21 (n = 9)
Balanced template	Day 14 (n = 9) and Day 34 (n = 9)	Day 14 (n = 9) and Day 24 (n = 9)

3.2.4. Seed-based correlation analysis

3.2.4.1. Denoising

Data processing for SCA was carried out using FSL/FEAT (FMRI Expert Analysis Tool) Version 6.00, largely according to the steps described in Haneef et al. (2014). The data were denoised using two methods: nuisance regression (see Supplementary Script S3 in Appendix D for details) and ICA-based cleaning as described above (Supplementary Script S4 in Appendix D). Please note that there are other denoising methods implemented in different fMRI data analysis software such as the popular CompCor method in CONN (Whitfield-Gabrieli and Nieto-Castanon, 2012) and C-PAC (Craddock et al.) packages which is an extension of the nuisance regression model using principal

components derived from white matter and CSF (Behzadi et al., 2007). These methods will not be investigated in this study because they are not implemented within FSL and an aim of this study is to provide a streamlined data analysis pipeline for rodent fMRI data within FSL. For nuisance regression, the following pre-statistics processing was applied in the first-level FEAT analysis: motion correction using MCFLIRT (Jenkinson et al., 2002), grand-mean intensity normalisation of the entire 4D dataset by a single multiplicative factor, and high-pass temporal filtering (Gaussian-weighted least-squares straight line fitting, with $\sigma = 5000.0s$). Registration to high resolution structural and standard space images was carried out using FLIRT (Jenkinson and Smith, 2001; Jenkinson et al., 2002). To remove potential contributions of physiological noise, timeseries extracted from individual white matter and cerebral spinal fluid masks were regressed out, along with head motion parameters using FILM (FMRIB's Improved Linear Model) with local autocorrelation correction (Woolrich et al., 2001). Spatial smoothing using a Gaussian kernel of FWHM 6.25 mm and high-pass temporal filtering (Gaussian-weighted least-squares straight line fitting, with $\sigma = 50.0 s$) were also applied in this step.

3.2.4.2. ROI selection

The retrosplenial cortex (RSC) was chosen as the brain region for seeding to obtain the rat DMN because the RSC robustly elicits DMN maps and is not lateralized (Lu et al., 2012; Huang et al., 2016). The RSC region is one of the major hubs of the DMN in rodents, which corresponds to the posterior cingulate cortex in primates (Sugar et al., 2011). To determine the effects of ROI size and placement on the calculated resting-state connectivity, five ROIs were selected within this region within the ICA- cleaned data: three from the atlas (Figure 3.2) and two from individual ICA functional

connectivity as described by Sohn and colleagues (Sohn et al., 2015). Individualised ROIs were based on the voxel (within the RSC) with maximum correlation to each individual animal's C1 timeseries as identified by ICA (see Supplementary Script S5 in Appendix D for details). The following ROIs were used: whole RSC (RSC_W); anterior many-voxels 5 mm spherical ROI (RSC_{AMV}) centred at $x = 29$, $y = 71$, and $z = 49$; posterior many-voxels 5 mm spherical ROI (RSC_{PMV}) centred at $x = 29$, $y = 62$, and $z = 51$; individualised many-voxels 5 mm spherical ROI (individualised RSC_{MV}); and individualised single-voxel ROI (individualised RSC_{SV}).

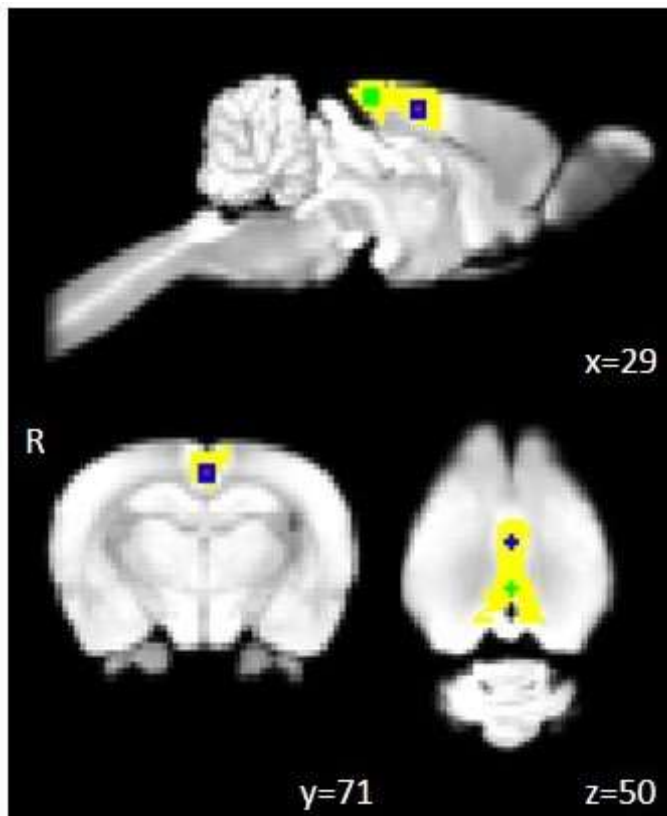


Figure 3.2. Atlas-based regions of interest positioning within the retrosplenial cortex.

The figure shows the position of the ROIs used in seed-based correlation analyses overlaid on the rat brain atlas (down-sampled by a factor of eight): whole region, yellow; anterior many-voxels 5 mm spherical ROI, blue; and posterior many-voxels 5 mm spherical ROI, green. The numbers on the bottom right corner of the slices refer to the slice position on the atlas. The slices correspond to traditional radiographic orientation; the right hemisphere of the brain corresponds to the left side of the coronal and axial slices.

3.2.4.3. Image analysis for identifying RSNs and detecting group differences

After ROI selection, the data were demeaned and the average time courses of the ROIs were used in a first-level FEAT analysis to generate whole-brain correlation maps.

Higher-level analysis was carried out using OLS (ordinary least squares) simple mixed effects (Beckmann et al., 2003; Woolrich et al., 2004; Woolrich, 2008). Z (Gaussianised T/F) statistic images were automatically thresholded non-parametrically using clusters determined by $z > 2$ and a (corrected) cluster significance threshold of $p = 0.05$ (Worsley, 2001b).

To study the effect of de-noising methods and ROI selection on RSN identification, average whole-brain correlation maps were calculated using only the baseline data of the 62 rats. The results were compared visually. To study the sensitivity of de-noising methods and different ROI selections for detecting group differences, higher-level analysis was also carried out using the longitudinal data only ($n = 9$ per timepoint). Like for ICA, the conservative Bonferroni correction was used to correct for multiple comparisons (eight contrasts, $p < 0.00625$) and accordingly, all statistical maps were thresholded to $z > 2.5$. The results were compared visually and quantitatively. For the quantitative comparisons, a cluster threshold of 30 adjacent voxels was applied. As an indicator of the sensitivity for detecting group differences, the number of significant clusters, total number of significant voxels and maximum z-score in each of the comparisons were used.

3.3. Results

3.3.1. Choice of template for independent component analysis

3.3.1.1. Identification of RSNs

Homologous networks were identified when group-ICA was performed on baseline-only rs-fMRI data and on all rs-fMRI data (i.e., pre and post stimulation). When comparing the templates qualitatively (Figure 3.3), baseline-only networks exhibited more widespread overall connectivity in terms of the spatial distribution of the RSNs and stronger functional connectivity (higher z-scores) between brain regions within those networks, especially within the default mode network, as compared to the all-data networks.

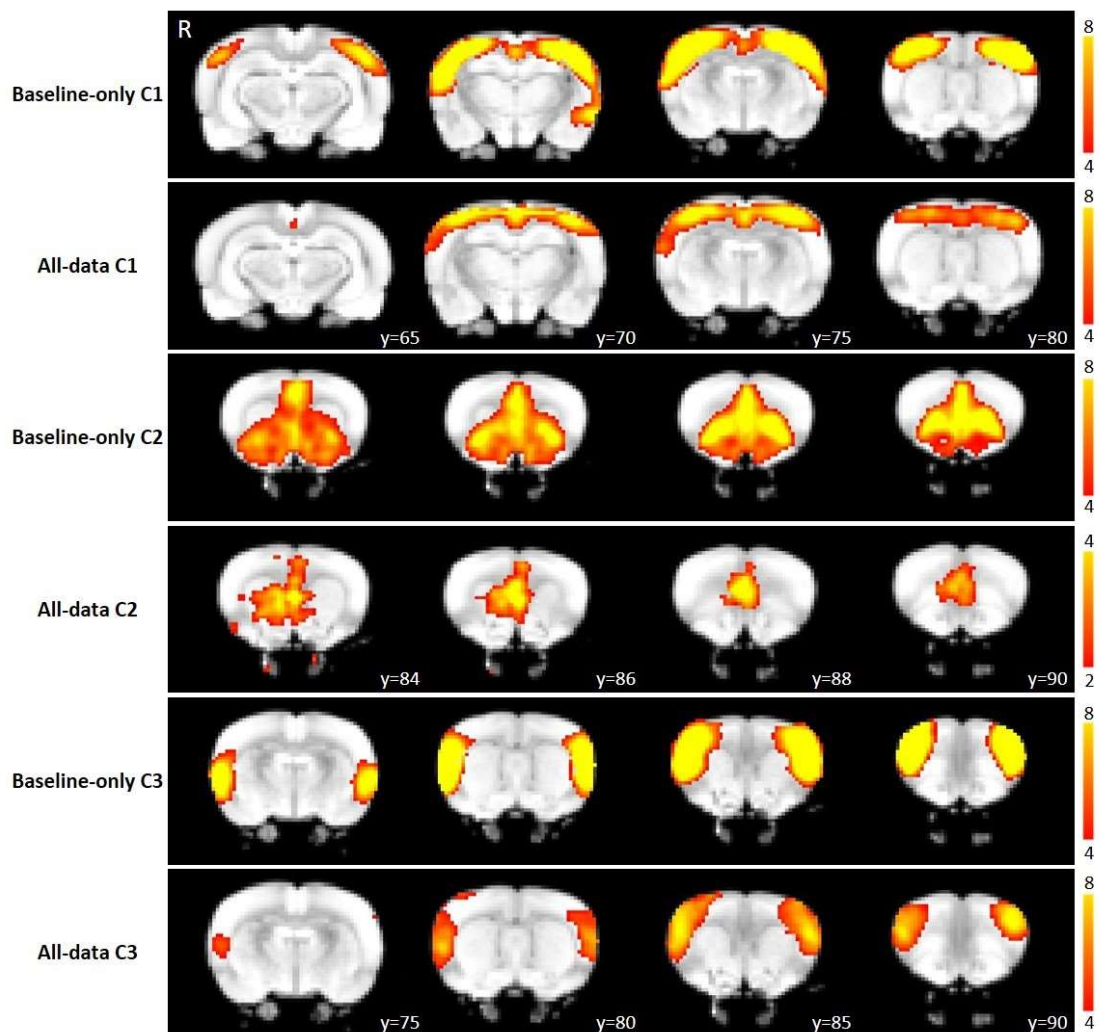


Figure 3.3. Resting-state networks resulting from group-ICA. The figure illustrates coronal slices of RSNs identified in rs-fMRI scans of 6-8 weeks old male Sprague Dawley rats. The components were classified as follows: C1, interoceptive network; C2, default mode network; and C3, salience network. The spatial colour-coded z-maps of these components are overlaid on the rat brain atlas (down-sampled by a factor of eight) and the number on the bottom right corner of each slice refers to the slice position on the atlas. The same slices are shown for RSNs of baseline rs-fMRI scans (n = 62) and all pre and post treatment data (n = 45). The RSN maps are represented as z-scores (lower threshold at $z > 4$, except for all-data C2 where $z > 2$), with a higher z-score (yellow) representing a greater correlation between the time course of that voxel and the mean time course of the component. The slices correspond to traditional radiographic orientation; the right hemisphere of the brain corresponds to the left side of the image.

3.3.1.2. Sensitivity of dual regression to group differences

Dual regression analysis was carried out using C1 of the baseline-only template and the homologous component found in the all-data template and in each of the four balanced templates. No significant group differences were found in the all-data or balanced templates using the strict Bonferroni correction and a threshold for the cluster size of 30 voxels. With the baseline-only template, significant clusters were found for Day 14 > Day 21 (1 cluster of 109 voxels) and for Day 14 > Day 34 (1 cluster of 71 voxels). Therefore, the use of baseline-only template RSNs resulted in increased sensitivity of the dual regression tool in detecting between-group differences.

3.3.2. Considerations for using seed-based correlation analysis

3.3.2.1. Effect of de-noising method and ROI selection for RSN identification

The effect of two de-noising methods, nuisance regression and ICA-based cleaning, was investigated for SCA of the whole retrosplenial cortex (RSC_w) seed from baseline data of 62 rats. While only the interoceptive network (C1-equivalent) was identified in the nuisance regressed data (Figure 3.4B), both the interoceptive network (C1-equivalent) and default mode network (C2-equivalent) were identified in ICA-cleaned data (Figure 3.4C). Overall, the connectivity obtained after ICA-based cleaning was higher and more widespread than after nuisance regression.

The connectivity maps resulting from the different ROI selections using the ICA-cleaned data are shown in Figure 3.4D-G. In general, both the interoceptive and default mode networks were successfully identified using all seeds. However, the RSC_{PMV} seeded map exhibited relatively little functional connectivity overall, especially further away from the ROI between slices at $y = 70$ and $y = 88$ where the corresponding ICA networks show most connectivity. Of all results, the RSC_W seeded map exhibited the highest and most widespread connectivity. The two maps obtained using the individualized ROIs showed almost identical functional connectivity patterns and together with the RSC_{AMV} seeded map, they were most similar to the ICA C1 and C2 networks.

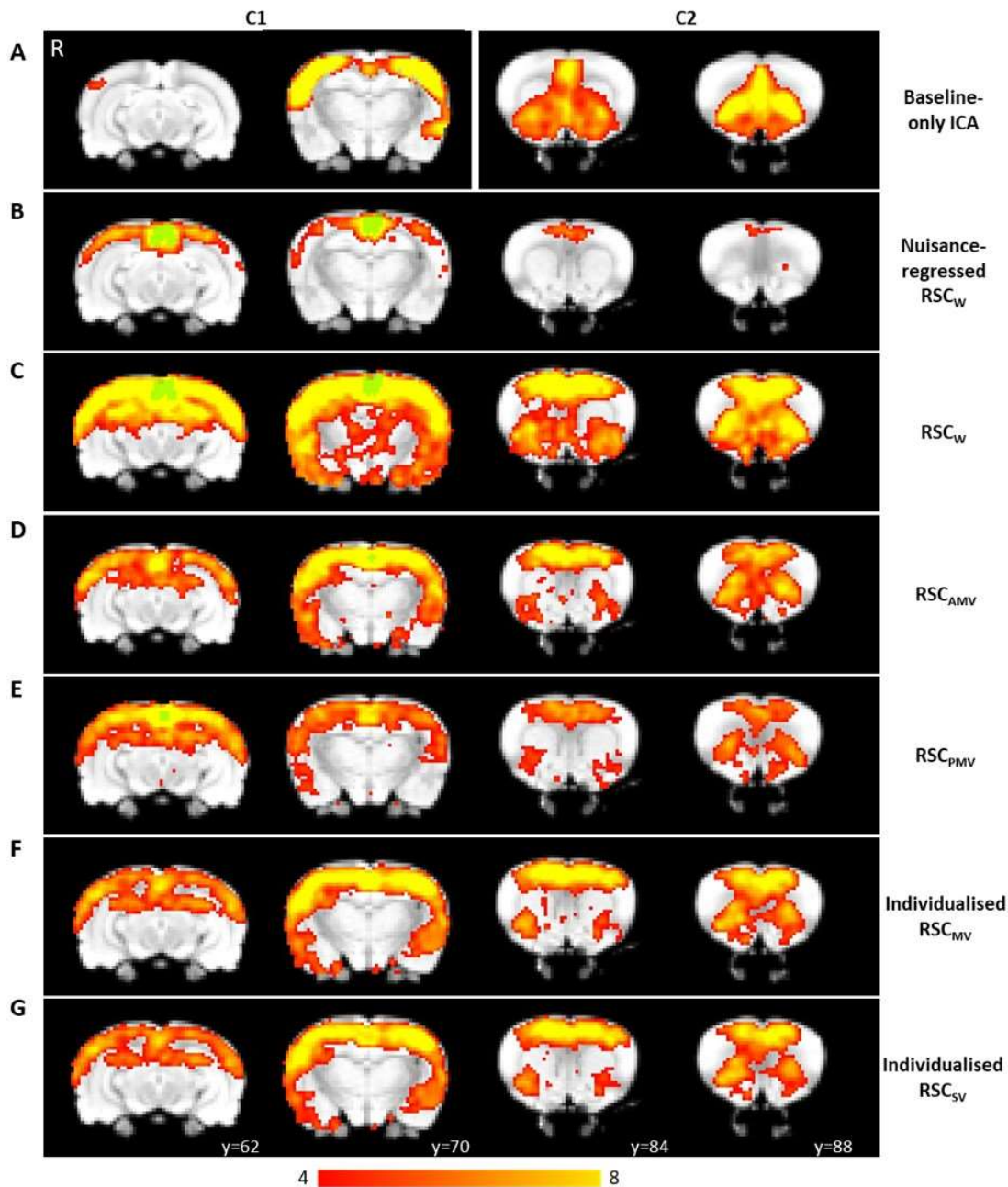


Figure 3.4. Interoceptive network (C1) and default mode network (C2) identified from group-ICA and SCA using baseline rs-fMRI data. The figure illustrates coronal slices of the interoceptive network (C1)/default mode network (C2) identified from: (A) group-ICA; (B) whole-brain correlations of the whole RSC region (RSCW) to the nuisance-regressed rs-fMRI data; and whole-brain correlations of the (C) whole RSC region (RSCW), (D) anterior many-voxels ROI (RSCAMV), (E) posterior many-voxels ROI (RSCPMV), (F) individualised many-voxels ROI (individualised RSCMV), and (G) individualised single-voxel ROI (individualised RSCSV) to the ICA-cleaned rs-fMRI data. The spatial colour-coded z-maps of these components are overlaid on the rat brain atlas (down-sampled by a factor of eight) and the numbers at the bottom refer to the slice position on the atlas. The RSN maps are represented as z-scores ($n = 62$, lower threshold at $z > 4$). R denotes the right brain hemisphere.

3.3.2.2. Sensitivity of methods for detecting group differences

The quantitative results of the group comparisons using different de-noising methods and ROI selections are presented in Table 3.2. SCA of the whole region ROI (RSC_W) based on nuisance regressed de-noising detected few significant differences between the groups. Among the ICA-cleaned atlas-based SCA methods, the anterior multi-region ROI (RSC_{AMV}) achieved better sensitivity to group differences than the whole region ROI (RSC_W) and the posterior multi-region ROI (RSC_{PMV}). The two individualised SCA approaches performed similarly and were the only methods that found significant differences for all eight tests.

To get an idea of the spatial distribution of significant voxels, example slices for the two comparisons with the highest number of significant voxels are shown in Figure 3.5. The results based on the nuisance regressed data are left out since they do not contain any significant voxels in the slices shown here. The maps for the two individualised SCA approaches are very similar and the significant voxels in the atlas-based results are largely located in the same regions as the voxels in the individualised SCA maps.

Table 3.2. Functional connectivity changes within the interoceptive/default mode networks using different ROIs within the retrosplenial cortex for seed-based correlation analysis of ICA-cleaned rs-fMRI data. rs-fMRI data were obtained at: baseline, Day 0; after seven stimulation session, Day 7; after 14 stimulation sessions, Day 14; seven days after daily stimulation was stopped, Day 21; and 20 days after stimulation was stopped, Day 34. Eight contrasts were tested: e.g., ‘Day 7 > Day 0’ tests for whether functional connectivity on Day 7 was greater than functional connectivity on Day 0. Values reported are number of clusters consisting of more than 30 adjacent voxels, total number of significant voxels ($z > 2.5$ or $p < 0.00625$) and the maximum z score.

Contrasts	Statistics	Atlas-based ROIs				Individualised ROIs	
		Nuisance-regressed RSC _W	RSC _W	RSC _{AMV}	RSC _{PMV}	RSC _{MV}	RSC _{SV}
Day 0 > Day 7	No of clusters	-	3	7	3	8	6
	No of voxels	-	114	1137	258	823	595
	Max z-value	-	3.27	4.6	4.43	4.31	4.31
Day 7 > Day 0	No of clusters	-	-	-	-	1	2
	No of voxels	-	-	-	-	96	187
	Max z-value	-	-	-	-	3.7	3.81
Day 0 > Day 14	No of clusters	4	-	5	-	7	6
	No of voxels	224	-	925	-	2659	2403
	Max z-value	4.06	-	4.69	-	5.9	5.27
Day 14 > Day 0	No of clusters	1	-	1	-	5	7
	No of voxels	59	-	66	-	914	1091
	Max z-value	4.13	-	3.83	-	4.62	4.89
Day 14 > Day 21	No of clusters	1	2	1	-	6	7
	No of voxels	53	403	47	-	1566	1632
	Max z-value	3.74	4.11	3.39	-	5.06	4.72
Day 21 > Day 14	No of clusters	-	-	3	1	4	8
	No of voxels	-	-	197	82	601	568
	Max z-value	-	-	4.58	3.66	4.49	4.43
Day 14 > Day 34	No of clusters	-	8	4	6	9	13
	No of voxels	-	1300	497	357	2700	2754
	Max z-value	-	4.62	4.25	3.81	5.29	5.45
Day 34 > Day 14	No of clusters	-	-	-	-	1	3
	No of voxels	-	-	-	-	121	179
	Max z-value	-	-	-	-	3.75	4.13

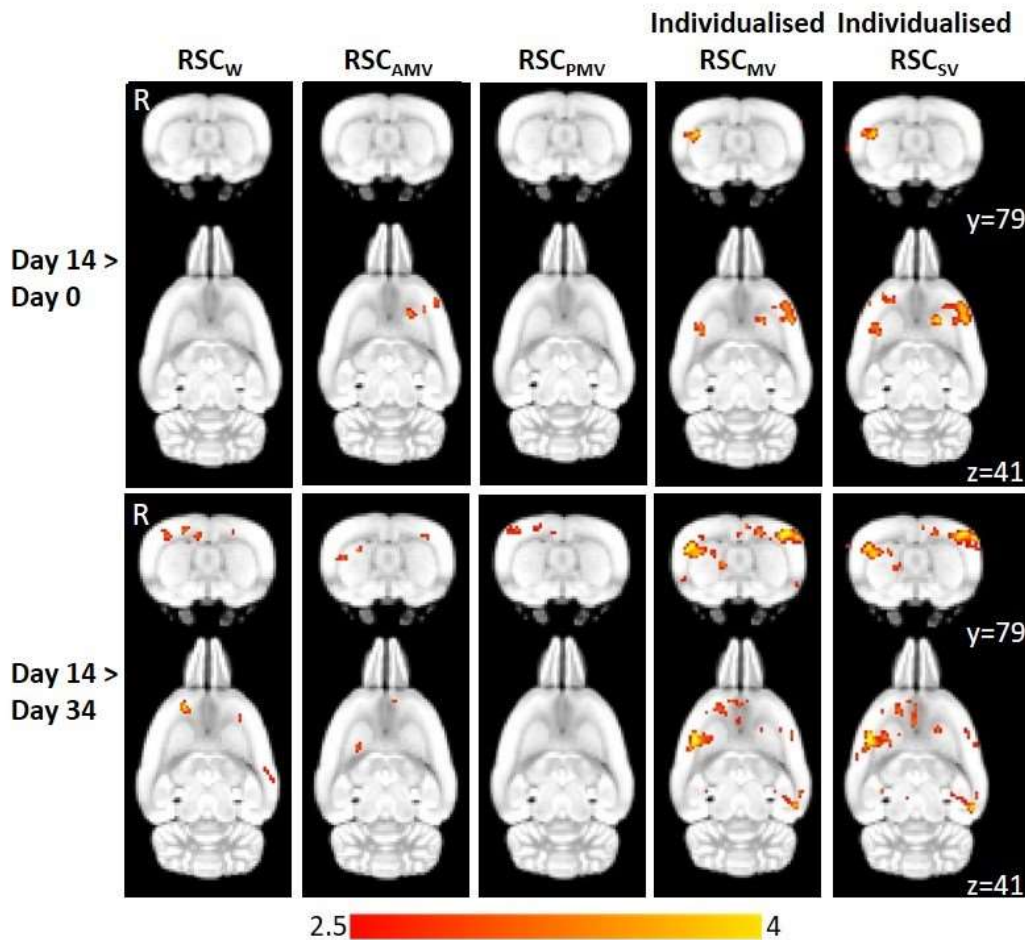


Figure 3.5. Comparison of SCA results when using atlas-based seeds vs individualised seeds on ICA-cleaned data. The figure illustrates coronal and corresponding axial slices of the results of two comparisons (Day 14 greater than Day 0 and Day 14 greater than Day 34). The spatial colour-coded z-value maps of these components are overlaid on the rat brain atlas (down-sampled by a factor of eight) and the numbers on the right refer to the slice position on the atlas. The z-maps are represented as z-values corrected for multiple comparisons using Bonferroni correction ($n = 9$ per timepoint, thresholded at $z > 2.5$ or $p < 0.00625$). The slices correspond to traditional radiographic orientation; the right hemisphere of the brain corresponds to the left side of the image.

3.4. Discussion

We investigated the two most widely used methods for analysing rs-fMRI data (ICA and SCA) to provide an optimum combination of analytical steps which produce the most reliable results. We demonstrate that the results of ICA are affected by the choice of network templates. An average pre-post treatment template obtained using all data in ICA rendered the identification of the DMN difficult and the dual regression tool less sensitive to stimulation-induced changes within the RSNs compared to

baseline-only templates. When denoising rs-fMRI data for SCA, ICA-based cleaning was superior to the traditionally used nuisance regression method both in terms of the quality of the RSNs generated and in the detection of group differences. These data indicate that nuisance regression may reduce signals of interest in addition to noise signals. Additionally, the use of individualised ROIs instead of atlas-based ROIs considerably increased the sensitivity of SCA to the identification of RSNs and detection of group differences. Hence, we suggest the use of a healthy or pre-treatment template in ICA and the use of ICA-based denoising and individualised ROIs in SCA. We did not directly compare ICA and SCA since these two approaches are conceptually different and use distinct statistical methods for the higher-level analysis.

3.4.1. Choice of RSN template for dual regression analysis

Several recent studies have suggested the use of a set of healthy template networks for dual regression (Rytty et al., 2013; Griffanti et al., 2016; Nickerson et al., 2017), while others recommend to have an equal number of subjects for pre and post treatment or healthy controls and patients for a “balanced” template when using an all-data template method (e.g., Filippini et al., 2009; Filippini et al., 2012; Zamboni et al., 2013). We visually compared the quality of three of the most commonly studied RSNs (interoceptive network, DMN and salience network) and when only baseline data was used, we found that the strength of functional connectivity between brain regions within those networks was considerably stronger, especially within the DMN, as compared to the all-data networks. Using a baseline-only template also resulted in better sensitivity for group differences compared to the all-data template. This might be due to the all-data template being strongly biased towards post-stimulation networks.

The use of a balanced number of healthy controls and patients in the template creates an average healthy-pathological template. However, an unbiased average all-data template cannot be obtained in longitudinal studies like the present one due to repeated measurements, or in cases where there are several pathological RSN subtypes (e.g. in depression as identified by Drysdale et al., 2017). To use an unbiased template in dual regression in these cases, a different average template can be used for each comparison. Nevertheless, previous studies have shown that dual regression is better able to detect differences from a “healthy” brain rather than from an average template (e.g., Griffanti et al., 2016). Our results obtained using balanced templates of four different combinations of timepoints confirm this finding. Therefore, we recommend the use of a pre-treatment or healthy template, both for longitudinal studies and for studies with pre-post treatment/healthy-pathological design.

Template networks could also be sourced from group-ICA of an independent set of subjects, such as an out-of-sample functional atlas (Schultz et al., 2014; Szewczyk-Krolikowski et al., 2014). However, we do not recommend the use of a functional atlas for rodent studies as the atlas may be devoid of information related to study-specific variations contained in group-ICA components of the original data. Such study-specific variations could be the type and dose of anaesthetic used, both of which alter the relative localisation and strength of connectivity within specific networks and even the presence of some RSNs (Williams et al., 2010; Masamoto and Kanno, 2012a; Grandjean et al., 2014; Paasonen et al., 2018). In the present study, the use of a study-specific template is not expected to introduce significant anaesthetic-related variation because all fMRI data used here were acquired under the same anaesthetic protocol.

3.4.2. Considerations for using seed-based correlation analysis

The results of this study strongly suggest that functional connectivity maps obtained after ICA-based cleaning exhibit higher and more widespread overall connectivity than maps obtained after nuisance regression. Furthermore, the nuisance regression in SCA seems to lead to lower sensitivity in the detection of group differences, probably due to a reduction of signals of interest (Bright and Murphy, 2015). Signals of interest may become obfuscated when using nuisance regression due to partial volume effects when drawing the ROIs for CSF and white matter. Therefore, spatial ICA-based cleaning should be considered the preferred method for denoising.

Another reason for choosing ICA-based cleaning over nuisance regression is that whether global signal regression should be performed as part of the nuisance regression is unclear (Murphy et al., 2009; Caballero-Gaudes and Reynolds, 2017; Murphy and Fox, 2017). These conflicting recommendations prevent a meaningful choice of a specific method and result in poor comparability across studies. While spatial ICA-based cleaning does not remove global noise, temporal ICA has recently been shown to be superior to global signal regression as global noise is removed without removing the mean signal (Glasser et al., 2018). The main disadvantage of ICA-based cleaning is that the noise components need to be manually identified, although classification software can subsequently be trained to perform this automatically (using FIX in FSL, for example).

The present study confirms previous findings demonstrating that ROI selection can have a drastic effect on the outcome of SCA in terms of RSN identification and sensitivity for detecting group differences (for review, see Cole et al., 2010; Marrelec

and Fransson, 2011; Sohn et al., 2015; Irajil et al., 2016). Song and colleagues also showed that ROI size can considerably affect reproducibility (Song et al., 2016). When investigating brain regions that are only partially activated according to ICA, the importance of adequate ROI selection is rather obvious since placing a seed outside an RSN will likely result in very little functional connectivity. The RSC, on the other hand, is fully activated as part of the interoceptive network and the DMN and the choice of ROI can therefore be expected to be less critical. Indeed, in the present study, all investigated SCA approaches were able to at least identify the DMN using a seed placed in the RSC. This could have been facilitated by the low individual variability of laboratory rats in terms of functional networks before treatment.

For non-baseline time points, however, the individual variability regarding the functional connectivity maps is likely to be higher. This makes the choice of ROI more crucial when performing group comparisons. The individualised/hybrid approach performed according to the study by Sohn and colleagues (Sohn et al., 2015) is based on the voxel that best represents the time series of one particular RSN for each individual animal. This explains why this method is able to detect group differences very well. Using an atlas-based seed, this optimal voxel can be too diluted if choosing a very large seed such as RSC_w or it might not be part of the seed volume for some animals at non-baseline time points, such as in the case of small seeds like RSC_{PMV/AMV}. The ability of a method to sensitively pick up group differences is most important for animal and human studies. Due to its superior performance in this regard, we recommend the individualised approach when using SCA. Note that functional connectivity patterns can be influenced by the cytoarchitecture of specific brain

regions (Goense et al., 2012; Huber et al., 2017; Mishra et al., 2019; Zhang et al., 2019) and studies interested in investigating functional connectivity changes in inter-layer cortico-cortical microcircuits may need to restrict their single-voxel individualised ROIs to potential functional sublayers of the brain region.

3.4.3. Study limitations

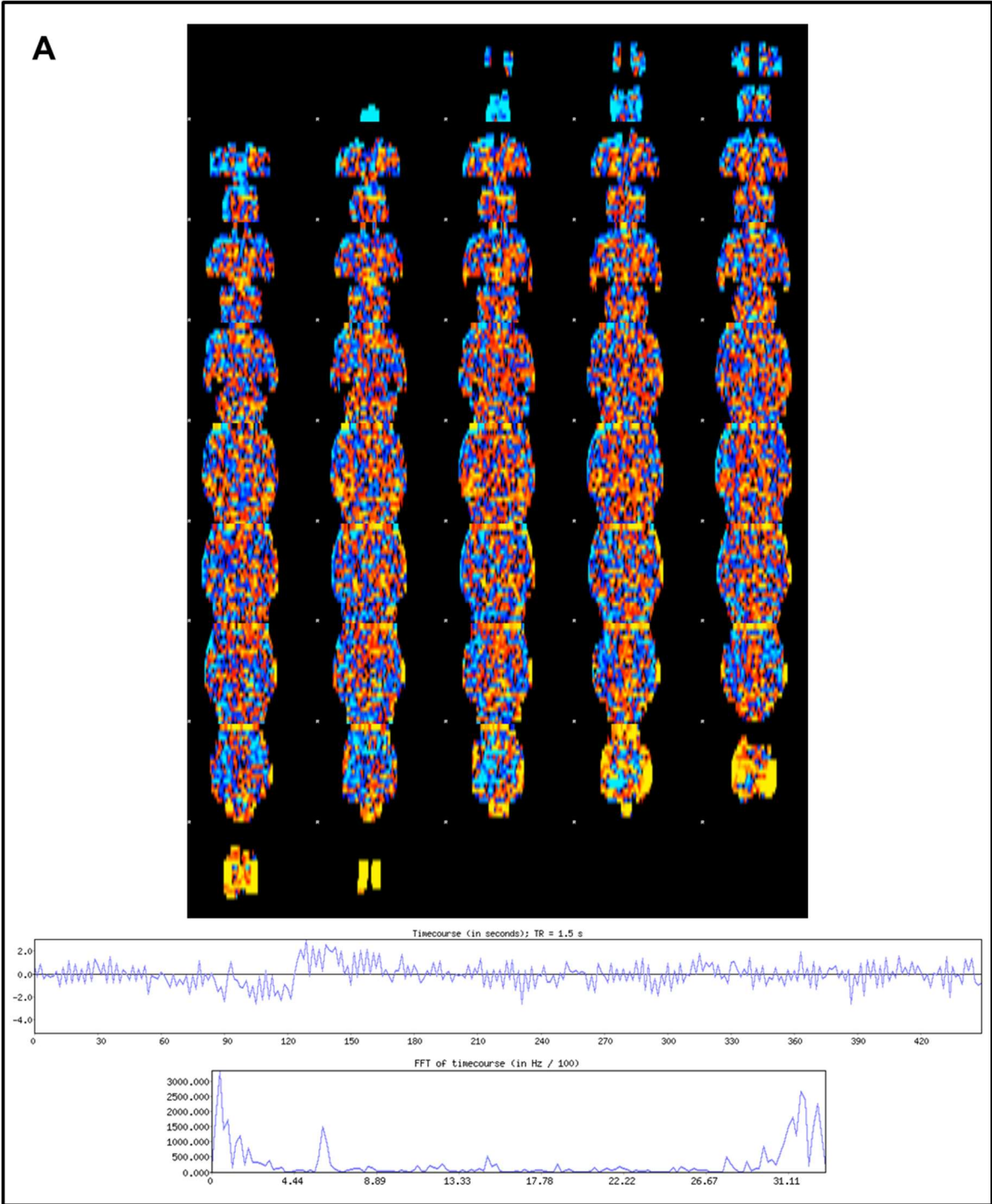
This study has a few limitations in terms of generalisability. First, the use of anaesthesia during data acquisition can alter the BOLD signal detection and hence functional connectivity (Pawela et al., 2009; Williams et al., 2010). A combined isoflurane and medetomidine anaesthetic protocol was chosen because previous studies have demonstrated minimal impact on functional connectivity patterns of rodents compared to the awake state (Paasonen et al., 2018; Grandjean et al., 2019). Animal studies using different anaesthetic protocols could obtain results that vary from what has been shown here. Second, we only use the RSC region to study and demonstrate the effect of ROI selection on SCA results. Seeds placed in other regions might exhibit different behaviour. Third, since this study was performed using animals, the results might not be entirely translatable to humans. However, given that fMRI data analyses are carried out in vastly the same way in FSL, irrespective of these three aspects, we do not expect the limitations to have a significant impact on the generalisability of our conclusions.

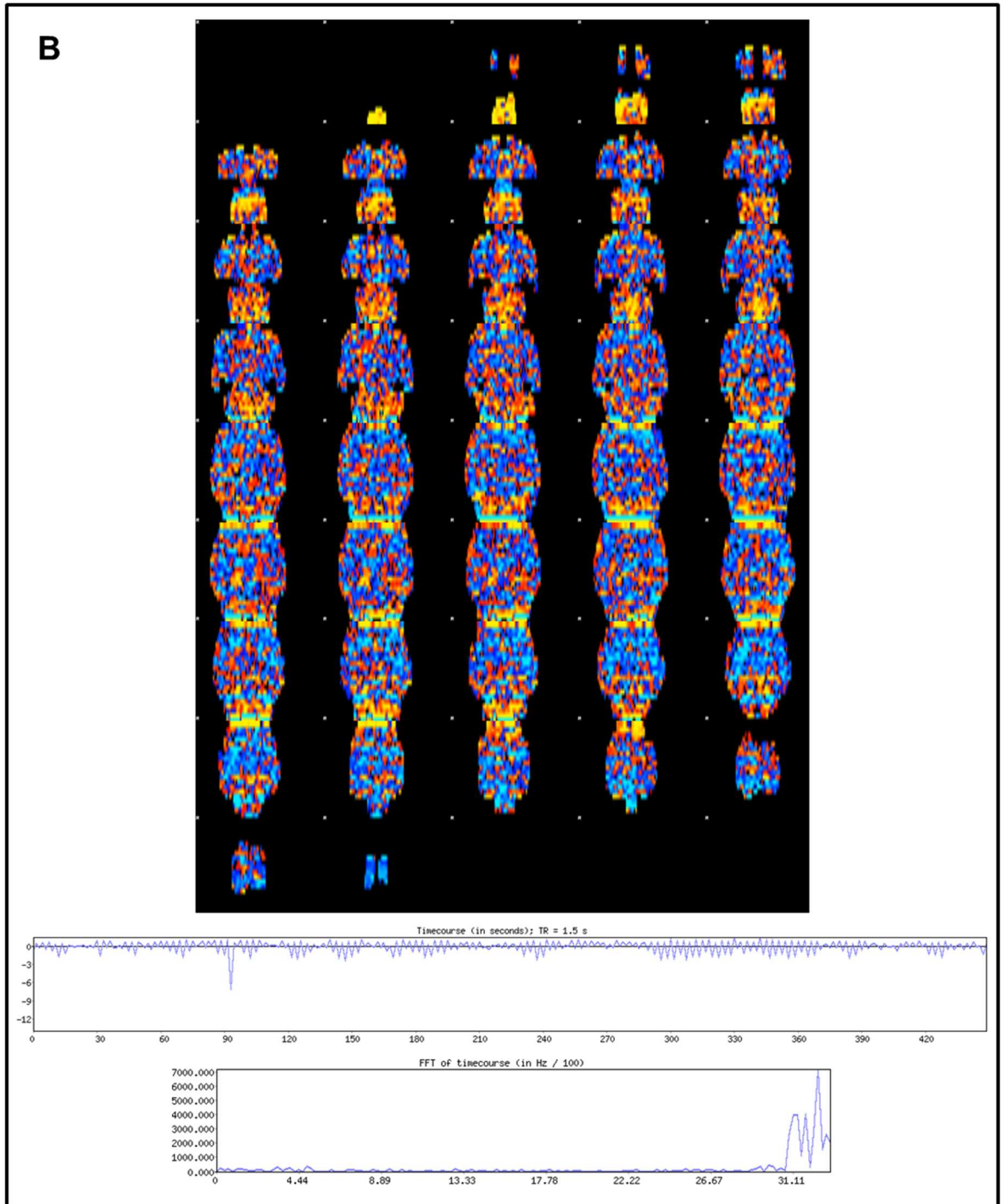
3.5. Conclusion

While rs-fMRI is a powerful tool for brain research and has great potential in diagnosing and tracking the treatment of neurological disorders, all rs-fMRI studies suffer from a common drawback: the extensive and complex data analysis procedures

necessary to obtain significant and reliable results from the noisy raw data are often completed inconsistently across studies. The ICA method as applied to rs-fMRI has been improving over the past 20 years and is well-suited for exploratory studies, being data-driven and not requiring *a priori* knowledge regarding timecourse or region of interest. On the other hand, SCA is traditionally the most used rs-fMRI analysis method, usually adopted when there is a strong hypothesis or *a priori* assumptions. Despite the long-standing practice of using these two methods separately, we have shown that both the use of ICA-based denoising and individualisation of ROIs using ICA-identified functional connectivity maps in SCA significantly improved the results of our rs-fMRI analyses, both in terms of network identification and detection of group differences. We strongly recommend the use of the streamlined workflow provided here to improve the reliability of results, comparability of RSNs and detection of group differences in rodent rs-fMRI data analysed with ICA or SCA. We also encourage further investigation of the suitability of this workflow for human rs-fMRI data.

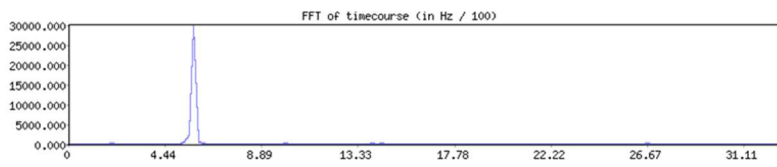
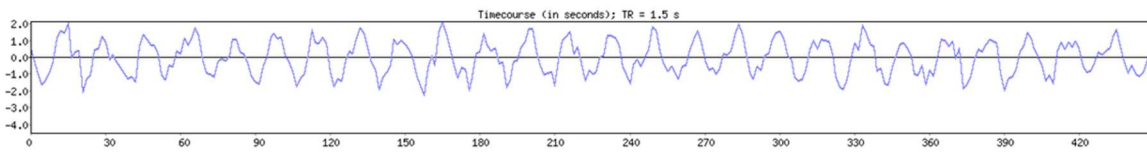
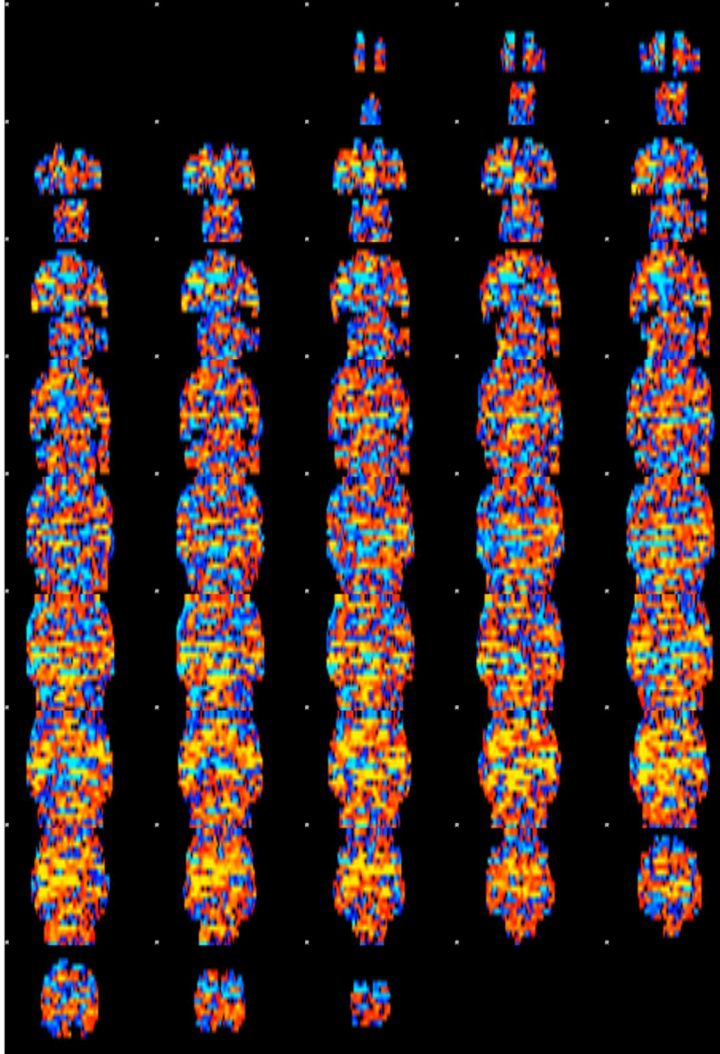
3.6. Supplementary Figures

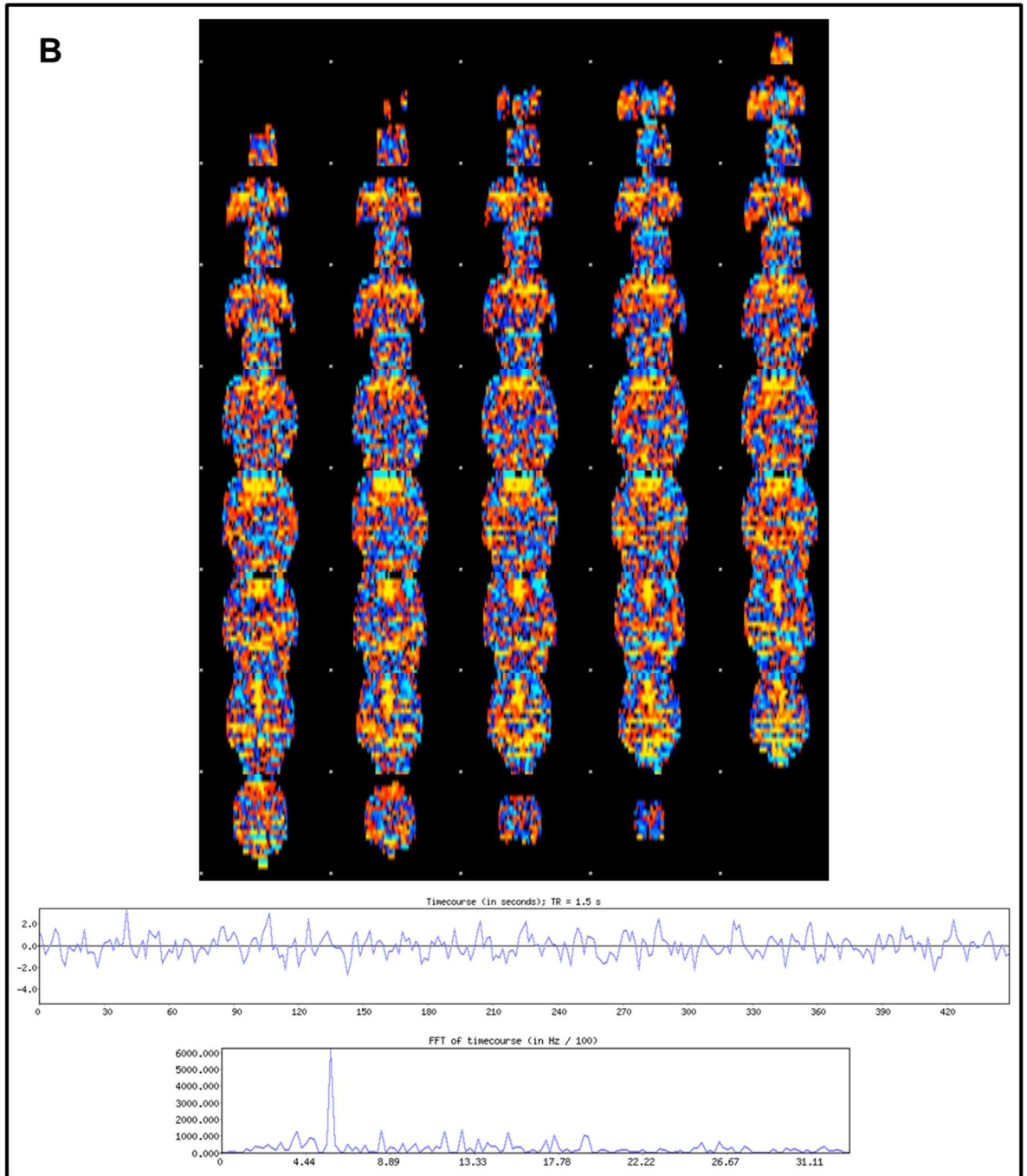




Supplementary Figure 3.1. Characteristic spatial map, time series and power spectra for motion-related (A) and high frequency (B) noise components from single-session ICA. Noise components have several small clusters in their spatial maps, multiple spikes in their time series and high-frequency peaks in their power spectra.

A





Supplementary Figure 3.2. Characteristic spatial map, time series and power spectra for signal components from single-session ICA. Signal components usually have large clusters in their spatial maps, smooth time series (no spikes) and a single low-frequency peak in their power spectra at around 0 –0.06 Hz (A). Components with occasional spikes in their time series and small higher frequency peaks in their power spectra are still classified as signal if large clusters are present in their spatial maps and the major peak in the power spectra is at low-frequency (0 –0.06 Hz) (B).

Chapter 4

Immediate effects of low-intensity repetitive transcranial magnetic stimulation on brain activity in healthy rats

Published as: Seewoo, B.J., Feindel, K.W., Etherington, S.J. & Rodger, J., 2018. Resting-state fMRI study of brain activation using low-intensity repetitive transcranial magnetic stimulation in rats. *Scientific Reports*. 8, 6706. doi: 10.1038/s41598-018-24951-6 (Appendix E)

Repetitive transcranial magnetic stimulation (rTMS) is a non-invasive neuromodulation technique that has shown therapeutic potential in a range of neurological and psychiatric conditions. Interleaving resting-state functional MRI (rs-fMRI) and rTMS has allowed for direct visualisation of the effects of rTMS on resting-state neuronal networks, e.g., the default mode network. However, there have been no reports of animal studies using those same techniques. Because rodents are widely used as preclinical models of various neuropsychiatric conditions, a thorough understanding of how rTMS affects the rodent resting-state networks is of particular importance before disease-specific animal models can be used with the aim to translate findings to the clinic (depression model used in Chapters 6-9). To our knowledge, this is the first rodent study to use rs-fMRI to examine the immediate effects of low-intensity rTMS (LI-rTMS) in healthy rats.

Using anaesthetised Sprague-Dawley rats, rs-fMRI data was acquired before and after control or LI-rTMS at 1 Hz, 10 Hz, continuous theta burst stimulation (cTBS) or biomimetic high-frequency stimulation (BHFS). Independent component analysis revealed LI-rTMS-induced changes in the resting-state networks (RSN): (i) in the somatosensory cortex, the synchrony of resting activity decreased ipsilaterally

following 10 Hz and bilaterally following 1 Hz stimulation and BHFS, and increased ipsilaterally following cTBS; (ii) the motor cortex showed bilateral changes following 1 Hz and 10 Hz stimulation, a contralateral decrease in synchrony following BHFS, and an ipsilateral increase following cTBS; and (iii) hippocampal synchrony decreased ipsilaterally following 10 Hz, and bilaterally following 1 Hz stimulation and BHFS. Similar to human rTMS, LI- rTMS altered the resting-state activity of neurons directly at the site of stimulation (e.g., cortex) as well as in remote but inter-connected brain regions (e.g., hippocampus). The present findings also demonstrate that LI-rTMS modulates functional links within the rat RSN with frequency-specific outcomes, and the observed changes are similar to those described in humans following rTMS. Therefore, these findings have relevance for establishing a direct comparison between how magnetic fields affect human and animal brains through the use of brain imaging and ultimately, define the best clinical protocols for rTMS.

4.1. Introduction

Repetitive transcranial magnetic stimulation (rTMS) has been shown to have therapeutic potential for a range of psychiatric conditions, including unipolar (Xia et al., 2008; Gaynes et al., 2014) and bipolar depression (Xia et al., 2008), schizophrenia (Dlabač-de Lange et al., 2010), obsessive-compulsive disorder (Jaafari et al., 2012) and post-traumatic stress disorder (Clark et al., 2015) as well as neurological conditions such as Parkinson's disease (Arias-Carrion, 2008), dystonia (Machado et al., 2011), tinnitus (Soleimani et al., 2015), epilepsy (Pereira et al., 2016) and stroke (Corti et al., 2012). rTMS has also shown promising results in the treatment of pain syndromes such as migraine (Lipton and Pearlman, 2010) and chronic pain (Galhardoni et al., 2015).

Even though rTMS is being used in a clinical setting and clinical trials are abundant, little is known about the mechanisms underlying its efficacy (Wassermann and Lisanby, 2001). This knowledge gap is in part because human studies use mostly non-invasive methods such as functional magnetic resonance imaging (fMRI), TMS and behaviour to investigate the effects of rTMS while animal studies mostly use invasive methods.

Resting-state fMRI (rs-fMRI) is used to detect functionally linked brain regions whose patterns of spontaneous blood-oxygenation-level-dependent contrast fluctuations are temporally correlated when the subject is at rest, that is, when no specific stimulus or task is presented (Biswal et al., 1995). Brain regions with coherent spontaneous fluctuations in activity form an organised network called the resting-state network (RSN) (Biswal et al., 1995). The default mode network (DMN) is one of the RSNs with a synchronised activity pattern. The DMN has been associated with cognitive performance and is thought to play an important role in neuroplasticity through the

consolidation and maintenance of brain function (Marcotte et al., 2013). rTMS is able to modulate the resting-state activity of the brain and DMN plasticity is sensitive to rTMS in humans but the direction (increase or decrease in activity) and extent of this modulation depends on the rTMS protocol used (Fox et al., 2012a; Popa et al., 2013; Glielmi et al., 2014; Jansen et al., 2015; Li et al., 2016).

Interleaving rs-fMRI and rTMS has opened doors to many possibilities in the clinical setting as rs-fMRI allows for direct visualisation of rTMS-induced effects in the brain. However, there have been no reports of animal studies using those same techniques (Seewoo et al., 2018a). Because rodents are widely used as preclinical models of various neuropsychiatric diseases, a thorough understanding of how rTMS affects the rodent DMN is of particular importance for both interpreting rodent rs-fMRI data and translating findings between animal models and humans. The present study aimed to investigate whether low intensity (LI) rTMS, which allows focal application of low intensity pulsed magnetic fields to one hemisphere of the brain in rodents, alters the strength or the spatial distribution, or both, of the RSN activity in rats. We used LI-rTMS because of its relatively high focality compared to rTMS delivered at high intensity using human rTMS equipment (Tang et al., 2016b), and LI-rTMS has previously been shown to induce cellular and molecular changes in rodent brains (Rodger et al., 2012; Makowiecki et al., 2014; Tang et al., 2016a). We show that LI-rTMS alters the resting-state activity of neurons directly at the site of stimulation as well as in brain regions that have direct connections with the site of stimulation. Moreover, the magnitude and pattern of the change in resting-state neuronal activity depend on the frequency and pattern of LI-rTMS. Therefore, these findings have

relevance for establishing a direct comparison between human and animal models in terms of how magnetic fields affect resting neuronal activity and ultimately, may prove helpful in the development of evidence-based rTMS treatment protocols to modify functional connectivity abnormalities.

4.2. Methods

4.2.1. Ethics statement

Experimental procedures were approved by the UWA Animal Ethics Committee (RA/3/100/1430) and Murdoch Animal Ethics Committee (IRMA2848/16) and conducted in accordance with National Health and Medical Research Council Australian code for the care and use of animals for scientific purposes.

4.2.3. Animals

Six adult male Sprague Dawley rats between 6 and 8 weeks old (150-250 g) were sourced from the Animal Resources Centre (Canning Vale, WA, Australia). They were maintained in a temperature-controlled animal care facility on a 12-hour light-dark cycle with food and water *ad libitum* with one-week habituation before the start of experiments.

4.2.4. Experimental Protocol

During each session, the animal was first anaesthetised using isoflurane gas and was kept under isoflurane anaesthesia throughout the experiment. Each rat received LI-rTMS for 10 minutes to the right hemisphere with one of four stimulation protocols (1 Hz, 10 Hz, combined theta burst stimulation (cTBS) and biomimetic high-frequency stimulation (BHFS), randomised order) in the morning once a week for four weeks (Figure 4.1). The timing of the experiments was dependent on the availability of

imaging equipment but at least one week was allowed between sessions to allow for any effect of LI-rTMS to subside (Li et al., 2013). Rs-fMRI scans were performed immediately before and after the stimulation session. In addition, sham/0 Hz stimulation was delivered on a randomly determined day, prior to completion of the randomly selected stimulation protocol for that day. Sham stimulation and post-sham rs-fMRI scan were carried out only once for each animal. Animals were kept for up to 12 weeks and were euthanised after the last rTMS/fMRI session using carbon dioxide asphyxiation.

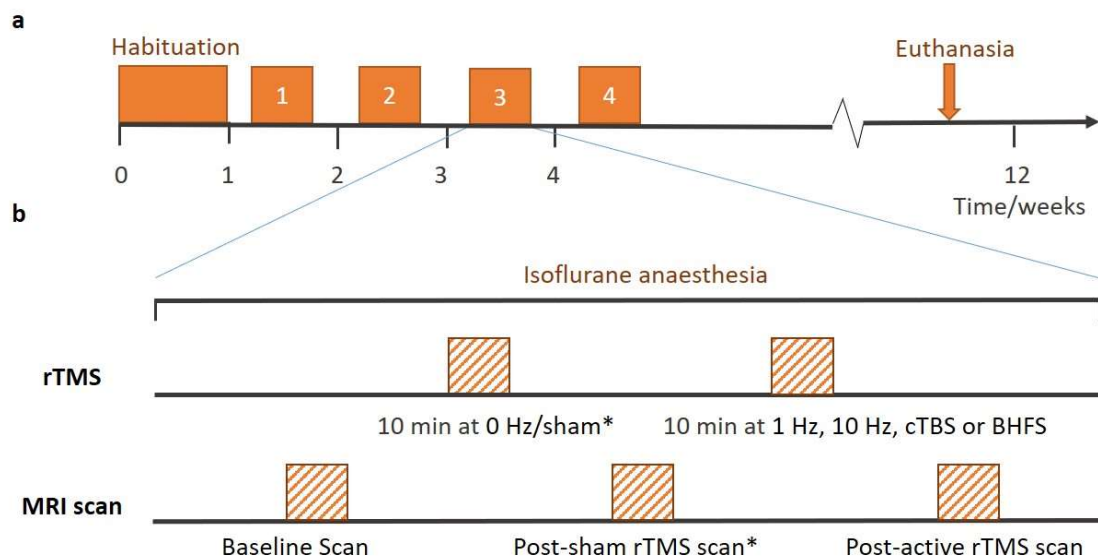


Figure 4.1. Experimental protocol. A. Timeline for a single rat from the time of its arrival. The experiment consisted of a habituation period followed by 4 sessions of fMRI-LI-rTMS-fMRI. Sessions 1 to 4 were the same, except for the frequency of LI-rTMS used and whether 0 Hz/sham stimulation preceded actual stimulation. B. Protocol for a single LI-rTMS/rs-fMRI session. During each session, baseline rs-fMRI data were acquired after which stimulation using a specific protocol (1 Hz, 10 Hz, BHFS or cTBS) was delivered. A post-procedure rs-fMRI scan was then carried out. *Sham stimulation and post-sham LI-rTMS scan were carried out only once for each animal. The session during which sham stimulation was delivered and the frequency at which active LI-rTMS was delivered during the same session was randomly determined.

4.2.4. Animal preparation for MRI

Once fully anaesthetised in an induction chamber (4% isoflurane in 100% medical oxygen, 2 L/min), the animal was transferred to a heated imaging cradle and anaesthesia was maintained with a nose cone (1-2.5% isoflurane in 100% medical oxygen, 1 L/min). Body temperature, respiratory rate, heart rate, and arterial blood oxygen saturation were monitored using a PC-SAM Small Animal Monitor (SA instruments Inc., 1030 System).

4.2.5. rTMS procedure

LI-rTMS was delivered using a custom-built round coil (8 mm inside diameter, 16.2 mm outside diameter, 10 mm thickness, 0.25 mm copper wire, 6.1 Ω resistance, 462 turns) placed on the right side of the rat brain next to the right ear (Grehl et al., 2015). The coil and pulse generator (Model EXLAB606, Serial Number 00003) were designed and built by Global Energy Medicine (Perth, WA, Australia). The device is described in detail in Grehl et al. (2015). Each stimulation protocol (1 Hz, 10 Hz, cTBS or BHFS) had a specific pre-programmed card such that when inserted into the generator, the phase transitions were triggered automatically (see Supplementary Table 4.1). Limitations of the equipment meant that intermittent theta burst stimulation (iTBS), commonly used in humans (Cárdenas-Morales et al., 2010), could not be delivered (the maximum pulse interval was 1s).

4.2.6. Magnetic field measurements

The magnetic field generated by the coil was measured using a gaussmeter connected to an oscilloscope. The transverse Hall probe was fixed to a stereotaxic frame and manipulated around the coil. Measurements were taken in the perpendicular (xy) and

parallel (z) axes relative to the main axis of the coil. Due to the axial symmetry of the circular coil, measurements in the x axis also represent the y axis and are therefore referred to as xy. The Hall probe head was positioned near the centre of the coil, at the edge and half-way between the centre and the edge of the coil (xy, z = 0 mm). At each of these three positions on the coil, the probe was repositioned at 1 mm increments away from the coil surface to a maximum distance of 10 mm (zmax = +10 mm) to determine the intensities at which different parts of the brain received the stimulation. The monophasic pulse generated an intensity of approximately 13 mT at the surface of the cortex, which is below motor threshold (Grehl et al., 2015).

4.2.7. MRI data acquisition

All MR images were acquired with a Bruker Biospec 94/30 small animal MRI system operating at 9.4 T (400 MHz, H-1), with an Avance III HD console, BGA-12SHP imaging gradients, an 86 mm (inner diameter) volume transmit coil and a rat brain surface quadrature receive coil. ParaVision 6.0.1 software was used to control the scanner and set the experimental tasks. Following a tri-plane scan to determine the position of the rat brain, high-resolution T2-weighted coronal images were acquired using a multi-slice 2D RARE (Rapid Acquisition with Relaxation Enhancement) sequence with fat suppression from 21 x 1-mm-thick interlaced slices with slice gap of 0.05 mm and: field-of-view (FOV) = 28.0 mm x 28.0 mm; matrix size (MTX) = 280 x 280; 0.1 mm x 0.1 mm in-plane pixel size; repetition time (TR) = 2500 ms; echo time (TE) = 33 ms; RARE factor = 8; echo spacing = 11 ms; number of averages (NA) = 2; number of dummy scans (DS) = 2; flip angle (α) = 90⁰; receiver bandwidth (BW) = 34722.2 Hz; and scan time = 2 min 55 s. Prior to acquiring the fMRI data, B0 shimming was completed for a region of interest covering the brain using the Bruker Mapshim routine. T2* weighted

fMRI images were acquired using a single-shot echo planar imaging (EPI) sequence with: FOV = 28.2 mm x 21.0 mm; MD = 94 x 70; 0.3 mm x 0.3 mm in-plane pixel size; TR = 1500 ms; TE = 11 ms; NA = 1; DS = 8; 300 repetitions; BW = 326087.0 Hz; 58/70 partial Fourier acquisition in the phase encode dimension; and scan time = 7 min 30 s. All radio frequency pulse shapes were calculated automatically using the Shinnar-Le Roux algorithm (Shinnar et al., 1989a, b; Shinnar et al., 1989c; Shinnar and Leigh, 1989; Pauly et al., 1991). The images acquired and analysed during the study are available from the corresponding author on reasonable request.

4.2.8. Image processing

Most of the pre-processing and analyses were performed using FSL v5.0 (Functional MRI of the Brain (FMRIB) Software Library) (Jenkinson et al., 2012). The Bruker data was exported from ParaVision 6.0.1 into DICOM (Digital Imaging and Communications in Medicine) format (Bidgood Jr et al., 1997) (<http://dicom.nema.org/>) and then converted into NifTI (Neuroimaging Informatics Technology Initiative, <https://nifti.nimh.nih.gov/>) using the dcm2nii converter (64-bit Linux version 5 May 2016) (Rorden et al., 2007). Pre-processing of fMRI data included: (i) upscaling the voxel sizes by a factor of 10 (Tambalo et al., 2015); (ii) motion correction using FSL/MCFLIRT (Linear Image Registration Tool with Motion Correction) (Jenkinson et al., 2002) to spatially realign the functional images to the middle volume of a serial acquisition; and (iii) reorienting the brain into left-anterior-superior (LAS) axes (radiological view). Intracranial binary brain masks were created manually using ITK-SNAP 3.4.0 (Yushkevich et al., 2006) (www.itksnap.org) for each functional and anatomical data sets and were used to extract the brain using the flsmaths tool. Post-stimulation images were co-registered to the baseline fMRI image using 6 parameter

rigid body registration with the default correlation ratio cost metric in the FSL/FLIRT (Linear Image Registration Tool) (Jenkinson and Smith, 2001; Jenkinson et al., 2002). Single-session independent component analysis (ICA) was carried out for each brain-extracted image in FSL/MELODIC (Multivariate Exploratory Linear Decomposition into Independent Components) (Beckmann et al., 2005) with the Gaussian kernel filter set to a full-width half maximum (FWHM) of 5 mm and a temporal high pass filter cut-off of 100 s. Based on the characteristics (spatial, temporal and frequency domains) of the components from ICA, they were then manually labelled as 'signal' or 'noise' and the data was 'cleaned' by removing the noise components using the `fsl_regfilt` command on the filtered data from MELODIC. The pre- and post-stimulation de-noised fMRI images for each session were then co-registered to their respective T2-weighted images using 6 parameter rigid body registration (Lu et al., 2010). To facilitate automated processing, the images were normalized to a Sprague Dawley brain atlas (Papp et al., 2014; Kjonigsen et al., 2015; Sergejeva et al., 2015) using FLIRT with 9 degrees of freedom 'traditional' registration. The atlas was first down-sampled by a factor of 8 to better match the voxel size of the 4D functional data. All subsequent analyses were conducted in the atlas standard space.

4.2.9. Image analysis

Multi-subject temporal concatenation group-ICA was performed to determine group differences by comparing pre- and post-stimulation fMRI images. The ICA algorithm was restricted to 15 components on the basis of other rs-fMRI studies in rodents (Jonckers et al., 2011; Zerbi et al., 2015) and was performed with the MELODIC toolbox. Group-ICA on the pre-stimulation datasets was also carried out with 30

components to determine whether 15 components were sufficient to identify the DMN. Given the limited sample size and the novelty of the parameters of interest, we report the results based on a cluster-forming threshold of $z > 2$, corresponding to an uncorrected p-value < 0.0455 for a two-tailed hypothesis. The group-ICA components for the pre-stimulation group ($z > 2$) were visually inspected, and the DMN identified (Figure 4.2) based on the spatial patterns in reference to known anatomical and functional locations using a rat brain atlas (Paxinos and Watson, 1998). After identifying the DMN (Figure 4.3), pre- and post-rTMS homologous ICA components were visually compared to determine the effect of LI-rTMS on the DMN.

As data were acquired for each animal at four different timepoints, the reproducibility of the group-ICA results over time and between subjects was also investigated. The pre-stimulation datasets were thresholded to a z-score higher than 2, binarised and then summed to give cumulative reproducibility maps for each subject (Figure 4.4). The regions where the voxels have a z-score of 2 or higher for one, two, three or four sessions are shown in different colours.

4.3. Results and Discussion

Rs-fMRI studies in rodents have previously shown that rodents possess a DMN similar to humans despite the distinct evolutionary paths between rodent and primate brains (Lu et al., 2012). In this study, we compared spontaneous activity in the brain at rest before and after the animals received active or sham LI-rTMS over the right hemisphere. The RSN in the rat brain was inferred based on synchronous fluctuations of the haemodynamic signals identified by ICA of pre-stimulation rs-fMRI data. ICA of post-stimulation rs-fMRI data showed that 10 Hz stimulation, BHFS and cTBS caused

mostly ipsilateral changes in synchrony of resting activity while 1 Hz stimulation resulted in bilateral changes in synchrony, with the contralateral changes being more prominent than ipsilateral changes. When compared with results from rTMS/fMRI studies in humans, our findings suggest that repetitive transcranial magnetic stimulation, whether in the form of conventional high-intensity rTMS in humans, or the lower intensity version LI-rTMS used here in rats, has similar effects on human and rat resting brain activity. Therefore, LI-rTMS/fMRI studies in animal models may be useful in refining clinical protocols for humans.

4.3.1. Identification of resting-state brain networks

The pre-stimulation group data were analysed using the group-ICA algorithm, and the resting-state networks were identified (Figure 4.2). The components obtained from MELODIC were overlaid on the rat brain template to which they were originally co-registered and the distribution of the synchronised voxels was investigated using the digital brain atlas labels. Based on visual inspection of the spatial map for each of the 15 components and the consistency of the spatial distribution with known neuroanatomical regions from the brain atlas, six non-artefactual circuits could be identified, which formed part of the putative DMN (Figure 4.3). The remaining nine components were classified as noise (see examples in Supplementary Figure 4.1).

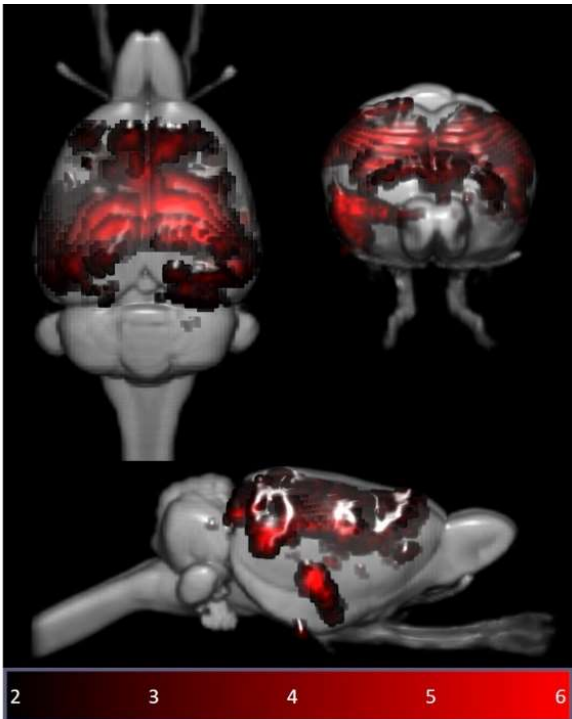


Figure 4.2. Independent component maps of pre-stimulation rs-fMRI group overlaid on 3D-rendered standard Sprague Dawley brain atlas. The figure shows the superior view (top left), anterior view (top right) and lateral view (bottom) of the chosen six non-artefactual independent components from the group-ICA. The spatial colour-coded z-maps of these components are overlaid on the brain atlas (down-sampled by a factor of 8). A higher z-score (bright red) represents a higher correlation between the time course of that voxel and the mean time course of the components. Colour bar indicates z-scores ($n = 24$, thresholded at $z > 2$, uncorrected p -value < 0.0455 for a two-tailed hypothesis).

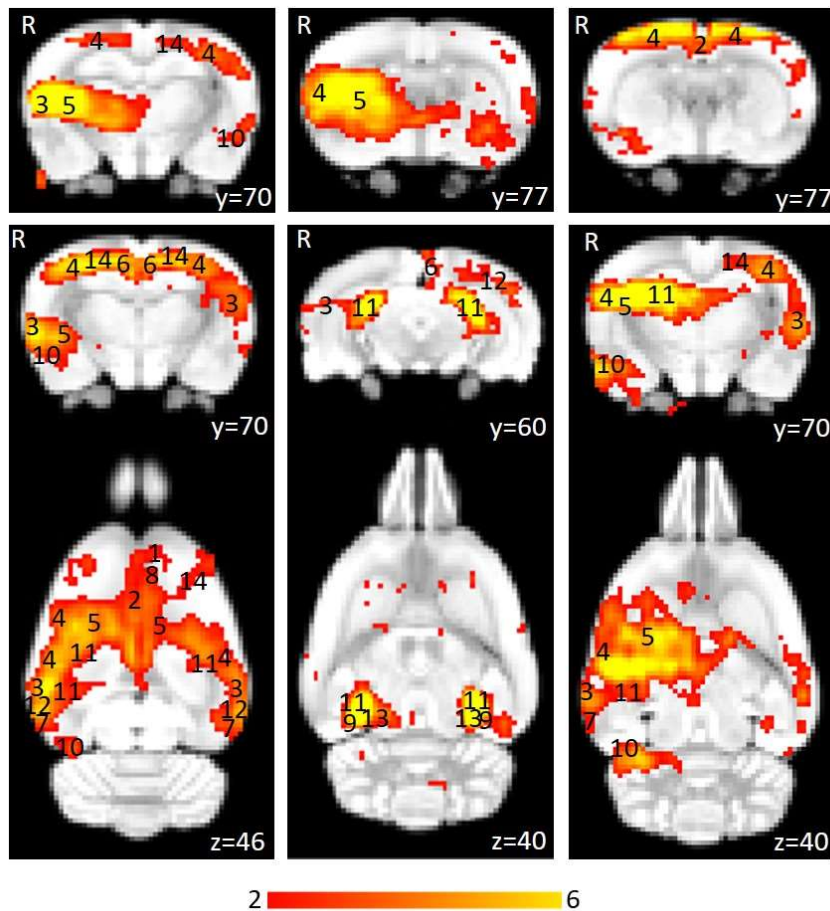


Figure 4.3. Thresholded independent component spatial maps showing the resting-state network in the pre-stimulation rs-fMRI group-ICA dataset. The figure shows six independent components from the group-ICA, three coronal slices and three coronal slices with their corresponding axial slices. The spatial colour-coded z-maps of these components are overlaid on the brain atlas (down-sampled by a factor of 8). A higher z-score (yellow) represents a higher correlation between the time course of that voxel and the mean time course of this component. Significant clusters within the components include various brain regions: 1, orbital cortex; 2, cingulate cortex; 3, auditory cortex; 4, somatosensory cortex; 5, striatum/caudate putamen; 6, retrosplenial cortex; 7, temporal association cortex; 8, prelimbic cortex; 9, parasubiculum; 10, entorhinal cortex; 11, hippocampus; 12, visual cortex; 13, inferior colliculus; 14, motor cortex. R denotes right hemisphere. x, y, z refer to the coordinates in standard Sprague Dawley template space. Colour bar indicates z-scores ($n = 24$, thresholded at $z > 2$, uncorrected p -value < 0.0455 for a two-tailed hypothesis).

The DMN in rats has previously been described as consisting of the orbital cortex (Lu et al., 2012; Sierakowiak et al., 2015; Zerbi et al., 2015; Hsu et al., 2016; Huang et al., 2016), cingulate cortex (Jonckers et al., 2011; Lu et al., 2012; Sierakowiak et al., 2015; Zerbi et al., 2015; Hsu et al., 2016; Huang et al., 2016), auditory cortex (Lu et al., 2012; Hsu et al., 2016; Huang et al., 2016), somatosensory cortex (Huang et al., 2016),

striatum/caudate putamen (Huang et al., 2016), retrosplenial cortex (Lu et al., 2012; Sierakowiak et al., 2015; Zerbi et al., 2015; Huang et al., 2016), temporal association cortex (Lu et al., 2012; Zerbi et al., 2015; Hsu et al., 2016), prelimbic cortex (Sierakowiak et al., 2015; Zerbi et al., 2015; Hsu et al., 2016), parasubiculum (Zerbi et al., 2015), entorhinal cortex (Zerbi et al., 2015), hippocampus (Lu et al., 2012; Hsu et al., 2016; Huang et al., 2016) and visual cortex (Lu et al., 2012; Hsu et al., 2016). Figure 4.3 provides the ICA components with clusters corresponding to these regions. The motor cortex and inferior colliculus, which form part of the RSN (Jonckers et al., 2011) have also been identified.

In the pre-stimulation group, the ICA components forming the RSN showed bilateral symmetry in resting activity (Figure 4.2). However, four of the chosen non-artefactual ICA components (Figure 4.3) had spatially asymmetrical correlations between homologous brain regions. In some components, the homologous brain region was completely absent (no correlation at that particular time point) while in some components, the spatial extent of the clusters was larger in one hemisphere. The 'dominant' hemisphere with increased ipsilateral cluster size was the same between sessions and across all animals (Figure 4.4). Coherent neuronal oscillations or spontaneous rhythmic activity are believed to show which brain regions are coupled for joint processing for a specific function, and the resulting hemodynamic responses are interpreted as functional connectivity between these areas (Nikouline et al., 2001). MacDonald et al. (1996) measured the oscillations of the auditory and somatosensory cortex in anaesthetised rats and found that the oscillations in the somatosensory cortex were stronger in one hemisphere. Other similar behavioural and

electrophysiological studies have shown that homologous brain regions can function both unilaterally and bilaterally (Banich and Belger, 1990; Nikouline et al., 2001). This functional ability is a possible explanation for the apparently stronger synchrony in resting-state activity unilaterally in some brain regions within those ICA components. For example, the first ICA component in Figure 4.3 shows that there is strong synchrony in the resting activity of the right auditory cortex (3) and right striatum (5), but there are no clusters for homologous brain regions in the left hemisphere. Such asymmetries in functional networks have previously been reported in resting-state network studies using ICA (Fransson et al., 2009; Hutchison et al., 2010; Zerbi et al., 2015). The unilateral components could represent stronger local connectivity, which could be both independent of, and synchronised with, the inter-hemispheric connectivity within the RSN.

Interestingly, some brain regions, including the auditory cortex (3) and striatum (5), show unilateral synchrony in some components and bilateral synchrony in others. A previous study using ICA to identify resting-state networks in rats also reported that functionally connected regions can split into separate components (Hutchison et al., 2010). Similar observations were made when the group-ICA algorithm was limited to 30 components instead of 15. The observed z-score ICA spatial maps of 30-component analysis were very similar to the 15-component analysis but the increased number of components caused components belonging to the same functional networks to split into different components previously identified in Hutchison et al. (2010). The resting activity of these brain regions split into different components based on higher local synchrony in activity (Jonckers et al., 2011; Zerbi et al., 2015). Overall, these results

confirm that the group-ICA algorithm can cause homologous brain regions within the DMN to appear in separate components and the extent of this is dependent on the strength of bilateral synchrony and the total number of components (Jonckers et al., 2011; Zerbi et al., 2015).

4.3.2. Reproducibility over time and between subjects

Each animal was scanned at four timepoints, enabling the investigation of the reproducibility of the group-ICA results over time and between subjects using pre-stimulation rs-fMRI data (Figure 4.4A). The reproducibility maps illustrate that the middle part of the clusters show overlap for all or at least three timepoints while the border of the clusters represents data from only one or two time points. Most of the scatter and single-voxel correlations come from single sessions (shown in grey). This indicates that the central resting-state activity is reproducible, even when the rs-fMRI data acquisition is separated by a week or more.

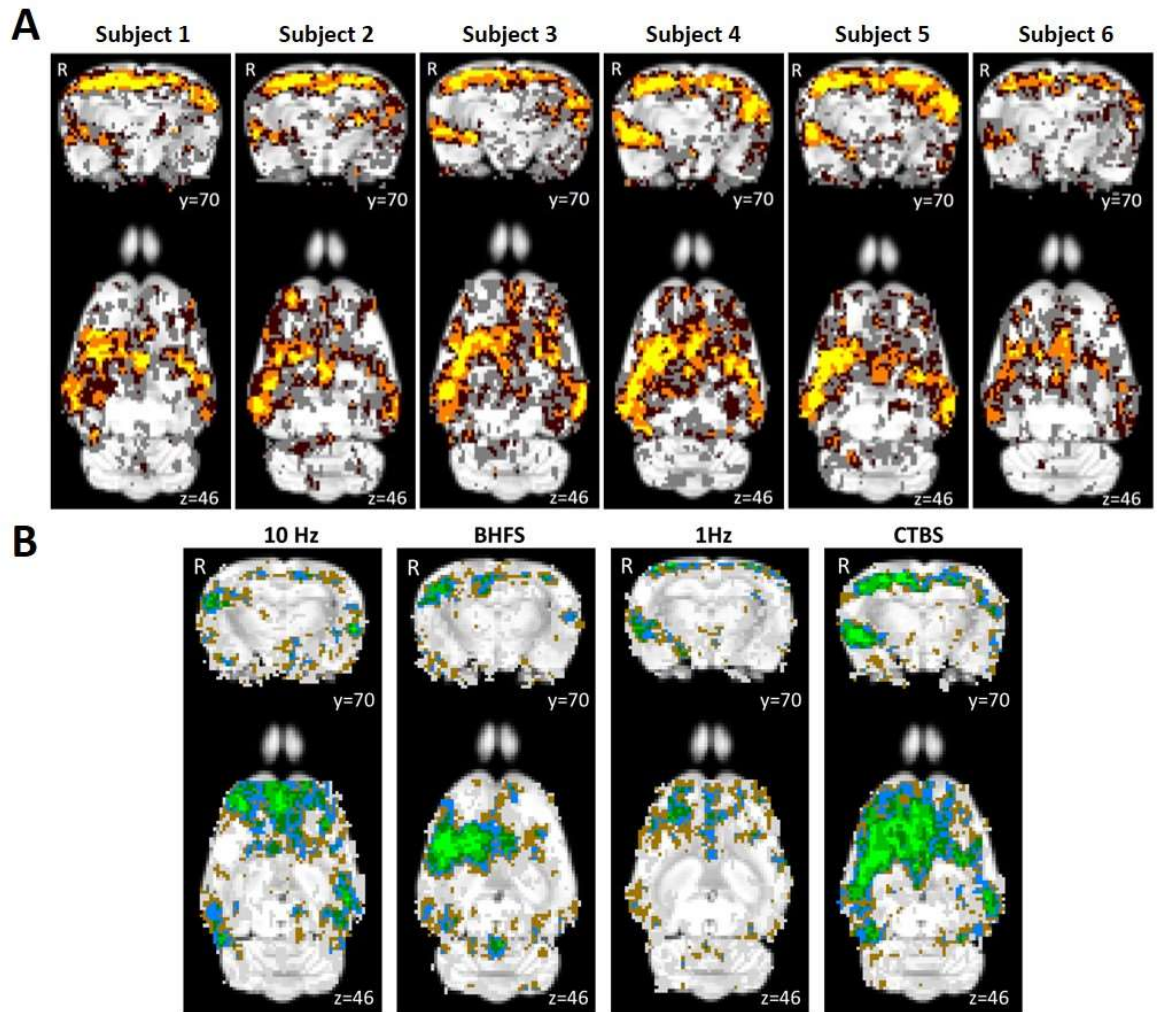


Figure 4.4. Reproducibility between sessions and between subjects of a representative group-ICA component. A. Pre-stimulation session cumulative score maps of six subjects over the four different time points overlaid on the Sprague Dawley rat brain atlas (down-sampled by a factor of 8). x, y and z refer to the coordinates in standard Sprague Dawley template space. Colour code: voxels with z-value greater than 2 (uncorrected p-value < 0.0455 for a two-tailed hypothesis) for: 1 session, grey; 2 sessions, dark brown; 3 sessions, orange; 4 sessions, yellow. B. Animal cumulative score maps of six subjects following stimulation at 10 Hz, BHFS, 1 Hz and cTBS overlaid on the Sprague Dawley rat brain atlas (down-sampled by a factor of 8). x, y and z refer to the coordinates in standard Sprague Dawley template space. Colour code: voxels with z-value greater than 2 (uncorrected p-value < 0.0455 for a two-tailed hypothesis) for: 1 animal, grey; 2 animals, brown; 3 animals, blue; 4 animals, dark green; 5 animals, green; 6 animals, bright green.

Comparing the session cumulative maps between subjects, shows that the same pattern is seen in each of the six animals. Similar to the intersession reproducibility, the central part of the representative component for the animal cumulative maps (Figure 4.4B) overlaps for more animals, while the voxels towards the border tend to

represent data from single animals. This shows that the post-stimulation rs-fMRI data are reproducible between subjects as well.

Although our study did not address how long LI-rTMS effects persist after stimulation, the high reproducibility of baseline scans in the same animals a week apart suggest that any effect of stimulation has subsided. This is in line with studies in humans suggesting that rTMS effects are transient, lasting less than an hour. Future studies can take advantage of the longitudinal opportunities of rs-fMRI to study the duration of LI-rTMS effects at short timescales of hours to days.

4.3.3. Effects of LI-rTMS on resting-state brain activity

LI-rTMS was delivered to the right brain hemisphere (Figure 4.5) with one of four stimulation protocols (1 Hz, 10 Hz, cTBS and BHFS) and group-ICA components for each post-stimulation dataset were compared to the non-artefactual components identified in the pre-stimulation group to investigate the effect of LI-rTMS. Changes in synchrony of resting activity are reported only for those changes involving whole brain regions, as identified in the atlas. There were no changes in any of the DMN components after sham stimulation. However, there were clear changes in the synchronised activity following active LI-rTMS (Figure 4.6). Both excitatory frequencies (10 Hz and BHFS) displayed more noticeable ipsilateral changes in the strength of correlation within the DMN. The inhibitory frequency, 1 Hz, showed bilateral changes in most components, although there were more contralateral than ipsilateral changes in the synchronised activity of brain regions. cTBS caused mostly ipsilateral increases in synchrony, and the effects were not as widespread as the other LI-rTMS protocols (See Supplementary Table 4.2).

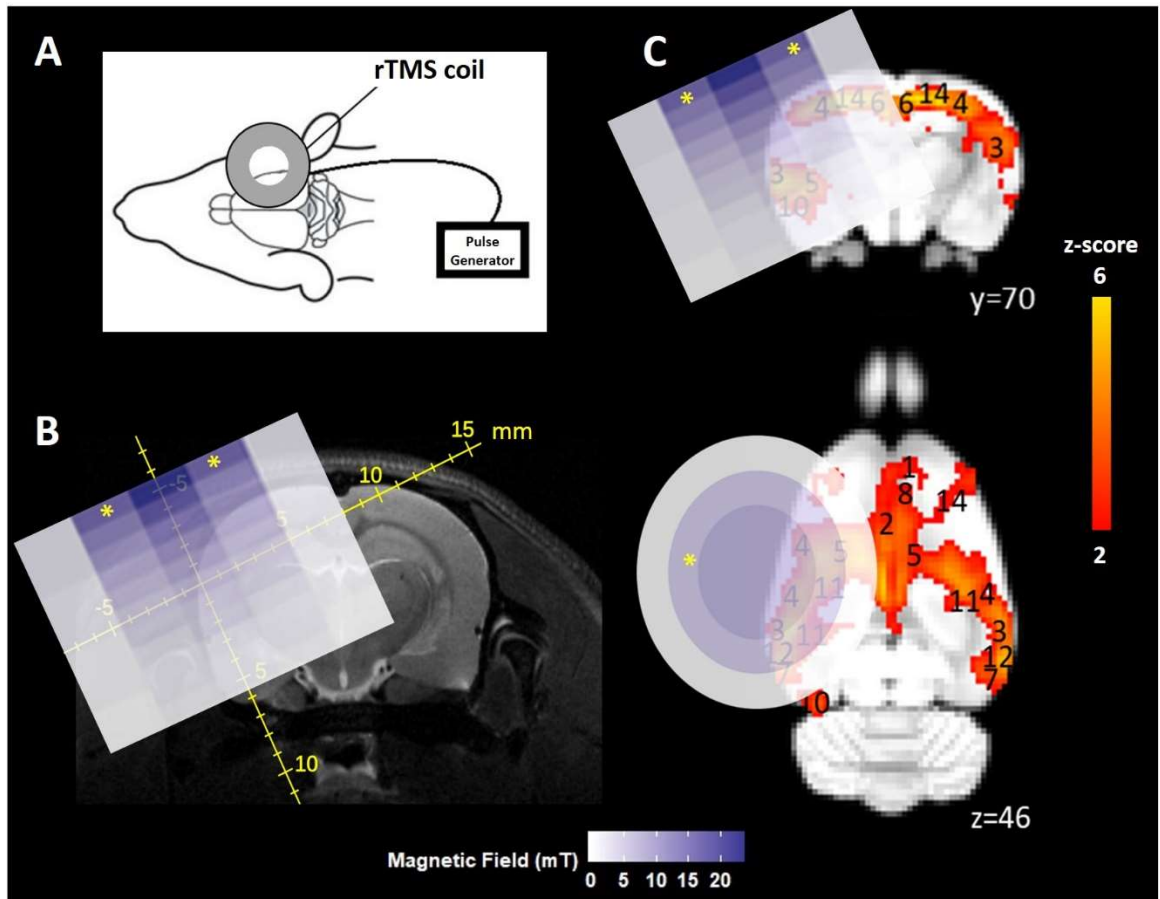


Figure 4.5. Coil position and magnetic field. A. Coil position relative to rat head and brain. B. 2D representation of the magnetic field induced by the LI-rTMS coil superimposed on a representative raw T2-weighted brain image with scale in mm. Measurements were taken on a hall device at 1 mm increments. C. 2D representation of the magnetic field induced by the LI-rTMS coil superimposed on colour-coded coronal and axial slices for a representative pre-stimulation group-ICA component overlaid on the Sprague Dawley brain template (down-sampled by a factor of 8). White-blue colour bar indicates magnetic field intensities. Yellow-red colour bar indicates z-scores ($n = 24$, thresholded at $z > 2$, uncorrected p -value < 0.0455 for a two-tailed hypothesis). x , y , z refer to the coordinates in standard Sprague Dawley template space. "*" indicates where electric field is induced.

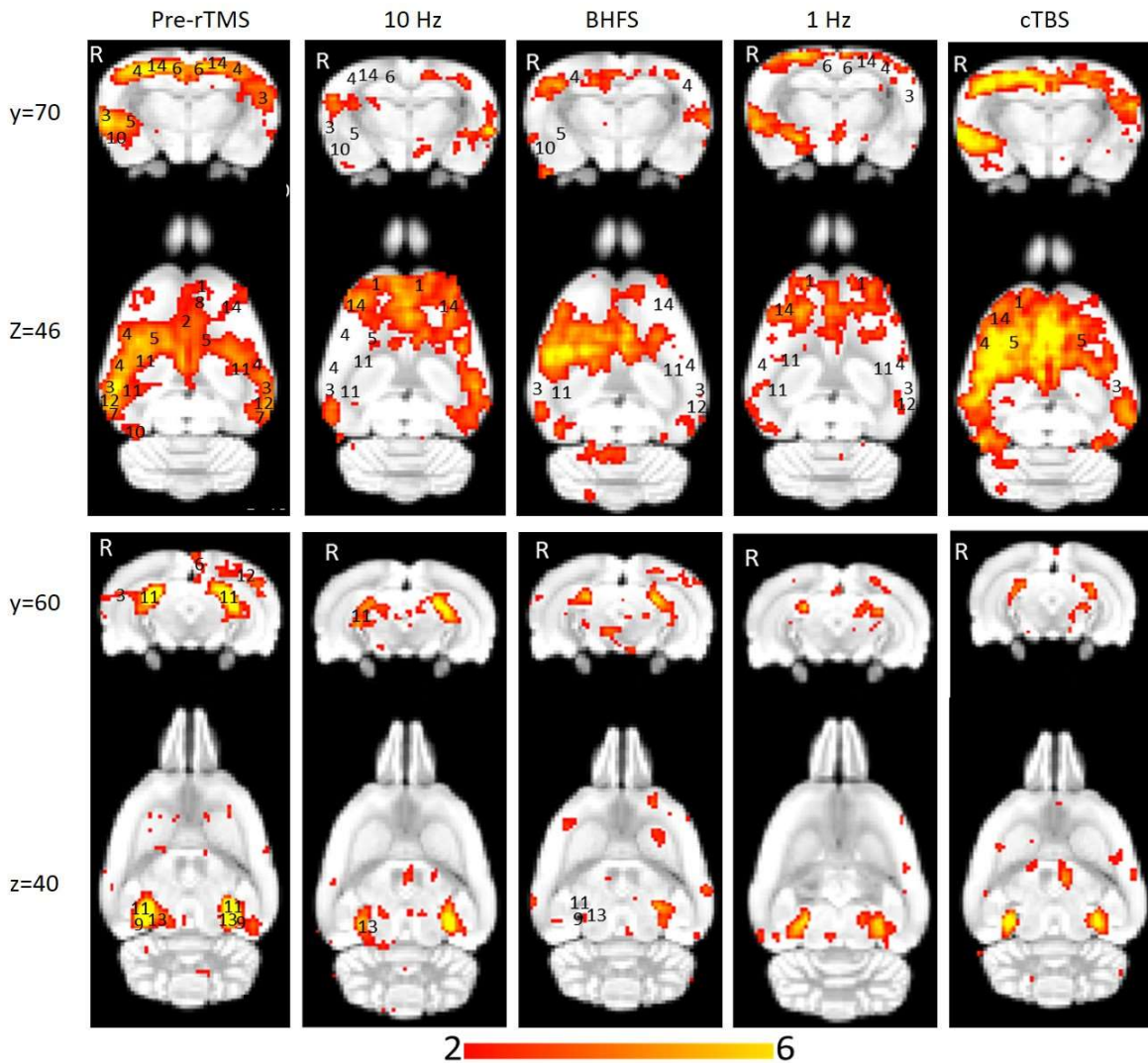


Figure 4.6. Homologous group-ICA components showing synchronised resting-state neuronal activity of isoflurane-anaesthetized rats before and after LI-rTMS at four frequencies: 10 Hz, BHFS, 1 Hz and cTBS. The post-stimulation colour-coded z-maps were derived from group-ICA on six animals and were overlaid on the Sprague Dawley brain template (down-sampled by a factor of 8). Coronal and axial slices for two representative ICA components are shown before (left) and after (right) stimulation at each of the four LI-rTMS protocols. A higher z-score (yellow) represents a higher correlation between the time course of that voxel and the mean time course of this component. Significant clusters within the components include various brain regions: 1, orbital cortex; 2, cingulate cortex; 3, auditory cortex; 4, somatosensory cortex; 5, striatum/caudate putamen; 6, retrosplenial cortex; 7, temporal association cortex; 8, prelimbic cortex; 9, parasubiculum; 10, entorhinal cortex; 11, hippocampus; 12, visual cortex; 13, inferior colliculus; 14, motor cortex. R denotes right hemisphere. x, y, z refer to the coordinates in standard Sprague Dawley template space. Colour bar indicates z-scores (thresholded at $z > 2$, uncorrected p -value < 0.0455 for a two-tailed hypothesis).

A change in the synchrony of resting-state activity in a specific brain region can be related to either an increase or a decrease in activity of that area compared to other

brain regions within the same network. A decrease in synchrony, for example, does not necessarily mean a decrease in activity. In human rTMS, high-frequency stimulation (≥ 5 Hz) mostly causes an increase in cortical excitability while 1 Hz and cTBS are predominantly inhibitory frequencies, causing a decrease in cortical excitability (Klomjai et al., 2015; Wilson and St George, 2016). However, excitability changes following LI-rTMS are not characterised to a sufficient degree to allow unequivocal interpretation of our rs-fMRI results. Nonetheless, early indications are that LI-rTMS may induce similar excitability changes to human (high intensity) rTMS, despite different magnetic field intensities (Tang et al., 2016a). Therefore, we discuss the changes in synchrony we observed in rats in the context of excitability changes reported in human rTMS literature but do so with caution. Herein, the discussion focuses on the effect of LI-rTMS on the somatosensory cortex, motor cortex and hippocampus.

4.3.3.1. Somatosensory and Motor cortex

In the present study, an ipsilateral decrease in the synchrony of the resting activity of the somatosensory cortex was observed following 10 Hz LI-rTMS. Our finding is compatible with those of an fMRI study by Schneider et al. (2010) showing an increase in activity of the targeted brain region when 5 Hz rTMS (considered to be excitatory and have roughly equivalent effects to 10 Hz; Wilson and St George, 2016) was applied over the left primary somatosensory cortex.

In contrast, when comparing the spatial maps post-cTBS with the pre-stimulation group, there is a clear increase in the synchronised activity in the ipsilateral versus the contralateral somatosensory cortex (Figure 4.6). This is in agreement with a study by

Rai et al. (2012) evaluating the effect of cTBS over the left somatosensory cortex by measuring the change in tactile acuity of the contralateral hand. They noted a decrease in neural activity within the stimulated cortex after cTBS application, which may indicate that cTBS can reduce sensory processing in the ipsilateral cortex. The increase in synchrony of resting-state activity in the present results and the localised decrease in activity in the ipsilateral somatosensory cortex following cTBS in Rai's study appear to reflect similar trends, suggesting that cTBS effects on the somatosensory cortex may be restricted to the stimulated hemisphere and not spread bilaterally.

The effects of 1 Hz LI-rTMS are more variable across studies and may differ more between rodent LI-rTMS and human rTMS. While reports in humans suggest a purely uni-hemispheric effect of rTMS, the present results show bilateral and even contralateral outcomes following LI-rTMS. Enomoto et al. (2001) examined the changes in excitability of the sensory cortex following rTMS by measuring changes in the somatosensory evoked potentials and found that 1 Hz rTMS over the left primary motor cortex suppressed the activity of only the ipsilateral sensory cortex. Similarly, Vidoni et al. (2010) studied the impact of 1 Hz rTMS over the left primary somatosensory cortex by observing cutaneous somatosensation and found that while the right hand was significantly impaired, the ipsilateral left hand was unaffected. In contrast, we found that the synchrony of the resting activity of the somatosensory cortex was decreased bilaterally following 1 Hz stimulation. Although we cannot rule out a lack of focality in the present study relative to human studies, some components nonetheless showed an exclusively contralateral decrease in synchrony, while those

with bilateral decrease showed a stronger ipsilateral decrease in the synchrony of resting activity within the same component, suggesting that changes induced by 1 Hz rTMS are likely to be complex.

There is also evidence that 1 Hz rTMS in other brain regions has effects on the contralateral hemisphere, which is congruent with some of the results herein on synchrony of resting activity. 1 Hz, being an inhibitory frequency, is thought to decrease the activity of inhibitory neurones in the stimulated hemisphere, causing a reduction in the inhibitory interhemispheric drive, which in turn leads to an increase in excitability of the contralateral hemisphere. This effect of 1 Hz rTMS has been exploited in treating stroke patients by applying low-frequency stimulation to the unaffected hemisphere to decrease transcallosal inhibition of the lesioned hemisphere and consequently improve motor function in stroke patients (Mansur et al., 2005; Takeuchi et al., 2005; Fregni et al., 2006). That the motor cortex in both hemispheres experiences a change in neuronal excitability following 1 Hz rTMS on one hemisphere may explain the bilateral changes in synchrony observed in the present study.

Interestingly, applying high-frequency rTMS to the lesioned hemisphere can have a similar effect by improving ipsilesional hemispheric excitability and hence improving motor rehabilitation. In a stroke study, 5 Hz (high-frequency) rTMS was applied ipsilesionally, and a bilateral increase in motor connectivity was found (Li et al., 2016).

In accordance with this study, we also found a bilateral increase in the synchrony of resting activity in the motor cortex following 10 Hz stimulation.

Previous human studies have found that there are bilateral changes in the motor cortex activity following cTBS stimulation (Huang et al., 2005; Huang and Mouraux,

2015). However, in the present study, only an ipsilateral increase in the synchronised activity of the motor cortex was observed following cTBS LI-rTMS to the right hemisphere of the rat brain. Although one can argue that there were also contralateral changes in synchrony of resting-state activity following cTBS (Figure 4.6), these changes have not been reported because they did not encompass entire brain regions, as identified in the atlas, and similar spurious changes were found in the sham data. The intrinsic differences between the methods used to detect changes in correlation and activity or the limitations in imaging measurements like EPI distortions could be the cause of this inconsistency.

4.3.3.2. Hippocampus

While the proximal changes in the DMN may reflect direct stimulation of those brain regions, the very low intensity of the magnetic field applied in LI-rTMS (Figure 4.5) means that any change in the activity of the hippocampus would likely be indirect and due to the modulation of functionally connected regions. We detected an ipsilateral decrease in the synchronised activity of the hippocampus following 10 Hz stimulation. This result is supported by Wang et al. (2014) who applied high-frequency (20 Hz) stimulation to the left lateral parietal cortex of healthy adults to non-invasively enhance the targeted cortical-hippocampal networks and study their role in associative memory. An ipsilateral change in the hippocampus was detected following multiple-session stimulation and the increased functional connectivity was correlated with improved associative memory performance. Hence, the present results display a correlation profile that is coherent with what is known about the effect of high-frequency rTMS on the hippocampus in the literature.

After 1 Hz stimulation, we found a bilateral decrease in the synchrony of hippocampal activity relative to other brain regions. Van der Werf et al. (2010a) also determined that the hippocampus had reduced activation bilaterally following the application of low-frequency rTMS over the left dorsolateral prefrontal cortex. They hypothesised that this change was not due to direct stimulation because the changes in neural activity were observed distally relative to the site of stimulation. Consistent with this finding, the change in the synchronised activity of the hippocampus observed in the resting-state network in the present study could, therefore, be due to the change in cortical excitability or the transcallosal spread of LI-rTMS effects inducing bilateral inhibition as discussed above for motor and somatosensory cortices.

BHFS is a relatively new pattern of stimulation and its use in humans has yet to be reported. As such, there is little information about the effects of BHFS in the literature. Studies using BHFS LI-rTMS in mice have shown increased structural plasticity of visual pathway topography in the midbrain, thalamus and cortex (Rodger et al., 2012; Makowiecki et al., 2014) and altered density of GFAP astrocytes in a mouse model of brain injury (Clarke et al., 2017), possibly via intracellular calcium increases and changes in gene expression (Grehl et al., 2015). However, how these cellular and molecular changes might relate to resting-state network changes remains unclear. In the present study, like 1 Hz stimulation, BHFS had a bilateral effect on the synchronised activity in the somatosensory cortex and the hippocampus. Motor cortex resting activity following BHFS LI-rTMS showed a contralateral decrease in the synchrony compared to other brain regions, a different effect than observed with the

other three LI-rTMS protocols. Further studies in animals and humans are warranted in an effort to investigate the effects of BHFS on the resting-state networks.

4.3.4. Use of anaesthetics in rs-fMRI and rTMS studies in rodents

Combined rTMS/rs-fMRI studies allow direct comparison between human and animal investigations, but these comparisons are complicated by the use of anaesthesia in animals. In human studies, the physiological condition of the subject can be assumed to be relatively constant throughout an rs-fMRI scan session (Pan et al., 2015). In contrast, in animal rs-fMRI, the use of anaesthesia is required to immobilise the animal and reduce stress (Vincent et al., 2007; Pan et al., 2015).

However, the effects of anaesthetics may confound both imaging and rTMS experiments, as these neuroactive substances may cause alterations in neural activity, vascular reactivity and neurovascular coupling. Nonetheless, the DMN has been shown to persist irrespective of the depth and type of anaesthetics used (Lu et al., 2007; Vincent et al., 2007; Kannurpatti et al., 2008; Zhao et al., 2008), and many rTMS studies using other (non-fMRI) methodologies have employed the use of anaesthetics (e.g., ketamine, pentobarbital, midazolam, isoflurane, propofol, and urethane) and have demonstrated the induction of neuronal plasticity in these anaesthetised animals (Gersner et al., 2011; Tang et al., 2015; Sykes et al., 2016), albeit with some impact of anaesthesia on rTMS outcomes (Gersner et al., 2011; Sykes et al., 2016). Urethane in particular is commonly used in rTMS rodent electrophysiology studies because of its minimal effects on cortical excitability, ability to preserve spinal reflexes and capacity to maintain a stable resting motor threshold over an extended period (Vahabzadeh-Hagh et al., 2012; Sykes et al., 2016). However, urethane has mutagenic, carcinogenic,

and hepatotoxic properties, which limit its use to acute and terminal experimental investigations. Longitudinal experiments in animals, such as those described here, therefore require alternative anaesthetic options.

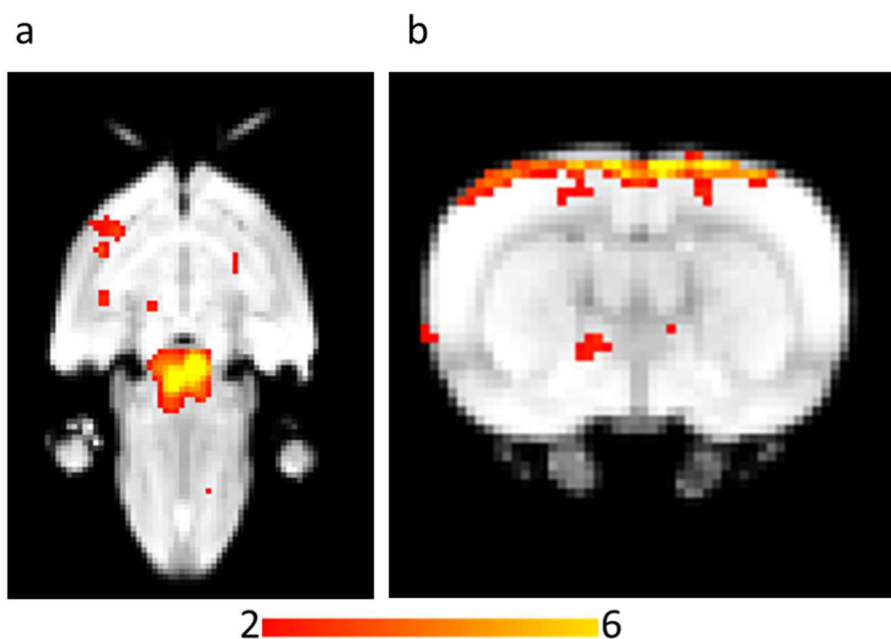
In the present study, we have used isoflurane, even though studies indicate that it has some concerns in the context of both rTMS and fMRI imaging. Isoflurane may affect the intracellular concentration of calcium (Gomez and Guatimosim, 2003), potentially modulating presynaptic transmission and/or postsynaptic excitability. Isoflurane also decreases excitatory and increases inhibitory transmission, causing an overall suppression of neural activity (Gomez and Guatimosim, 2003; Ouyang and Hemmings, 2005). As such, in the presence of isoflurane, the ability of high-frequency rTMS to depolarise is impaired (Gersner et al., 2011). Additionally, isoflurane, being a GABAergic anaesthetic, induces vasodilation (Ohata et al., 1999b), particularly in deep anaesthesia, through the activation of ATP-sensitive potassium channels of smooth muscle cells in cerebral arteries (Pan et al., 2015). Vasodilation leads to an increase in cerebral blood flow, which may be interpreted as an increase in activity. Despite these confounding factors, isoflurane is the anaesthetic of choice for repeated long-term experiments because of its ease of use and control, and rapid reversibility (Masamoto and Kanno, 2012a). Isoflurane levels can be kept within a specified range (1-2.5% in the present study) within and between experiment sessions. The concentration of isoflurane can also be adjusted (within the specified range: 1-2.5%) based on the physiological monitoring recordings to keep the physiological parameters from fluctuating outside the set range. The lack of change in synchronised resting activity observed after sham stimulation in our study provides confidence that the

experimental conditions were stable over time and within and between individuals. Moreover, the reproducibility maps (Figure 4.4A and 4.4B) show that the correlation at the centre of a cluster was always greater than a z-score of 2 irrespective of the timepoint and animal, suggesting that our results have biological significance.

4.4. Conclusion

To date, all reported studies on the effects of rTMS on the structure and function of the DMN have been conducted in humans. To the best of our knowledge, the present study is the first to show evidence of alterations in the resting-state networks caused by LI-rTMS in a pre-clinical model and most of the observed changes are consistent with those described in the human rTMS literature. Nonetheless, the precise mechanisms generating these changes in resting neuronal activity remain to be elucidated. Furthermore, it is interesting that rTMS and LI-rTMS may have a similar impact on the DMN of humans and animals, despite significant differences in intensity and focality of stimulation. To better understand the mechanisms underlying the reported clinical benefits of rTMS in different neurological and psychiatric conditions, relevant animal models could be used to link the LI-rTMS-induced changes in resting brain activity to changes in symptoms (through behavioural tests). Subsequent invasive techniques such as molecular studies can then be used to explore those effects in greater detail and provide information about how observed functional changes reflect those detected at a molecular and cellular level. This study provides a framework to use brain imaging to explore how LI-rTMS affects the rodent resting brain activity, promoting evidence-based translation to human treatments.

4.5 Supplementary Figures and Tables



Supplementary Figure 4.1. Two independent components — one axial slice (a) and one coronal slice (b) — from group-ICA classified as ‘noise’ components. A shows highly synchronised resting activity in the brainstem while B shows highly synchronised activity only at the dorsal part of the coronal slice. Colour bar indicates z-scores (thresholded at $z > 2$, uncorrected p-value < 0.0455 for a two-tailed hypothesis).

Supplementary Table 4.1. Total number of pulses delivered during 10 min LI-rTMS at the different frequencies used. Adapted from Grehl et al. (2015)

Frequency	Description	Total number of pulses delivered
0 Hz (sham)	Coil not activated	0
1 Hz	1 pulse per second	600
10 Hz	10 pulses per second	6,000
cTBS	3 pulses at 50 Hz, repeated at 5 Hz (Cárdenas-Morales et al., 2010)	9,000
BHFS	62.6 ms trains of 20 pulses, repeated at 9.75 Hz (Grehl et al., 2015)	120,000

Supplementary Table 4.2. Summary of changes in the default mode network in brain regions post-rTMS using 10 Hz and BHFS excitatory frequencies and 1 Hz and cTBS inhibitory frequencies on the right (R) side (ipsilateral changes) and on the left (L) side (contralateral changes) of the brain. The numbers in brackets correspond to the numbers used to denote the different brain regions in Figure 5. ‘↑’ refers to an increase in correlated activity, ‘↓’ refers to a decrease in correlated activity and ‘-’ means no change.

Region	Function	Excitatory frequencies				Inhibitory frequencies			
		10 Hz		BHFS		1 Hz		cTBS	
		R	L	R	L	R	L	R	L
Orbital cortex (1)	Decision making and emotional processing	↑	↑	-	-	↑	↑	↑	-
Auditory cortex (3)	Hearing functions	↓	-	↓	↓	-	↓	-	↓
Somatosensory cortex* (4)	Receives all sensory input	↓	-	↓	↓	↓	↓	↑	-
Striatum (5)	Facilitates voluntary movement	↓	-	↓	-	↓	-	↑	↑
Retrosplenial cortex (6)	Episodic memory and spatial navigation	↓	-	-	-	↓	↓	-	-
Entorhinal cortex (10)	Learning and memory	↓	-	↓	-	-	-	-	-
Hippocampus* (11)	Regulates emotions, spatial learning and memory	↓	-	↓	↓	↓	↓	-	-
Visual cortex (12)	Receives and processes visual input	-	-	-	↓	-	↓	-	-
Inferior colliculus (13)	Part of the auditory system	↓	-	↓	-	-	-	-	-
Motor cortex* (14)	Motor function and motor planning	↓↑	↑	-	↓	↑	↓	↑	-

**These brain regions are the primary targets of stimulation.*

Chapter 5

Long-term effects of repeated low-intensity repetitive transcranial magnetic stimulation on brain activity and chemistry in healthy rats

Published as: Seewoo, B.J., Feindel, K.W., Etherington, S.J. & Rodger, J., 2019. Frequency-specific effects of low-intensity rTMS can persist for up to 2 weeks post-stimulation: A longitudinal rs-fMRI/MRS study in rats. *Brain Stimulation*. 12, 1526–1536. doi: 10.1016/j.brs.2019.06.028 (Appendix F)

Despite the increasing use of rTMS to modulate dysfunctional brain networks in humans, the mechanisms underlying its therapeutic effects, particularly in cortical circuits, still require elucidation. There is anecdotal evidence that the therapeutic benefits of rTMS tend to wear off after cessation of treatment, suggesting that there is an urgent need to characterise the persistence of rTMS effects. An ideal approach for the longitudinal study of brain function is to use non-invasive magnetic resonance-based techniques. In Chapter 4, we showed that a single session of LI-rTMS in healthy rats has frequency-specific effects on functional links within resting-state brain networks that are similar to those described in humans following rTMS. This evidence of translational validity suggests that LI-rTMS in rodents is a useful model to include in a translational pipeline to inform and guide clinical application of rTMS, particularly given the cost and logistical challenges of longitudinal studies in humans.

In the present chapter, we used resting-state functional MRI (rs-fMRI) to examine the long-term changes in rodent functional neuronal networks and proton (^1H) magnetic resonance spectroscopy (MRS) to non-invasively assay neurometabolic changes in the sensorimotor cortex of healthy rats following repeated LI-rTMS. LI-rTMS was delivered to the right brain hemisphere of awake and behaving rats ($n = 18$) accustomed to the

procedure. Stimulation was delivered using the same custom-built round coil as in Chapter 4 at a frequency of 10 Hz or 1 Hz for a period of 10 min daily for 2 weeks.

We found that daily 10 Hz stimulation increased resting-state network connectivity and GABA, glutamine and glutamate levels while 1 Hz stimulation had subtler but opposite effects: 1 Hz stimulation decreased connectivity and glutamine levels.

Following stimulation cessation, the induced changes decreased to baseline levels within three weeks in the 10 Hz group but were sustained in the 1 Hz group. Therefore, this study confirms the frequency-specific effects of LI-rTMS and further suggests that effects of 1 Hz stimulation, although milder, may persist longer after cessation of treatment compared to those of 10 Hz stimulation. The transient connectivity changes following 10 Hz stimulation suggest that treatment protocols involving this frequency may require ongoing maintenance sessions to maintain therapeutic effects.

5.1. Introduction

Repetitive transcranial magnetic stimulation (rTMS) is a non-invasive neuromodulation technique widely applied in therapeutic and investigative studies of neuropsychiatric conditions including depression (Xia et al., 2008; Gaynes et al., 2014), schizophrenia (Dlabač-de Lange et al., 2010), and Parkinson's disease (Arias-Carrion, 2008). Despite the increasing use of rTMS to modulate dysfunctional brain networks in humans, the mechanisms underlying its therapeutic effects, particularly in cortical circuits, still require elucidation. Furthermore, patients report that therapeutic benefits of rTMS wear off after treatment finishes (e.g., Abraham and O'Brien, 2002; Janicak et al., 2010), suggesting an urgent need to characterise the persistence of rTMS effects.

Therapeutic rTMS application utilises different stimulation frequencies to elicit different cortical changes: low-frequency (< 5 Hz) stimulation has inhibitory and high-frequency (> 5 Hz) has excitatory effects on the cortex, albeit with some individual variability (Ridding and Ziemann, 2010; Wilson and St George, 2016). Preclinical models have identified gene and protein expression changes associated with these frequency-specific changes in excitatory and inhibitory circuit activity (Funke and Benali, 2011; Vlachos et al., 2012; Makowiecki et al., 2014; Mulders et al., 2016). In addition, changes in neurotransmitters Glutamate (Glu), γ -aminobutyric acid (GABA), and glutamine (Gln), the major precursor for neuronal glutamate and GABA (Yüksel and Öngür, 2010), are central to excitability changes observed following stimulation (Zangen and Hyodo, 2002; Vlachos et al., 2012; Tang et al., 2015). High-frequency stimulation increases excitatory neuronal activity (Tang et al., 2016a; Banerjee et al., 2017) and induces a long-lasting increase in glutamatergic synaptic strength consistent

with long-term potentiation (LTP) of excitatory circuits (Vlachos et al., 2012), while simultaneously reducing the strength of GABAergic synapses (Makowiecki et al., 2014; Lenz et al., 2016). Conversely, 1 Hz stimulation increases inhibitory circuit activity by increasing GABA levels (Feng et al., 2019) and modulates expression of calcium-binding proteins in inhibitory interneurons (Funke and Benali, 2011; Mulders et al., 2016).

Although animal models have revealed some key mechanisms of rTMS, in most preclinical studies, changes in the brain are investigated post-mortem, providing only a snapshot of rTMS-induced changes. Additionally, most animal and human studies focus on events occurring minutes to hours after single or multiple stimulations.

Consequently, the development of rTMS effects over time, and the stability of its after-effects, have not been explored.

Non-invasive magnetic resonance (MR) based techniques are ideal for longitudinal studies of brain function and neuroplasticity (Pelled, 2011). Resting-state functional magnetic resonance imaging (rs-fMRI) is the technique of choice for examining long-term changes in functional networks (Jonckers et al., 2015; Gozzi and Schwarz, 2016; Gorges et al., 2017; Seewoo et al., 2018a; Seewoo et al., 2018b), while proton (^1H) magnetic resonance spectroscopy (MRS) is one of only few methods that can non-invasively assay neurometabolic changes. Rs-fMRI identifies brain regions showing synchronised resting activity which form organised networks called resting-state networks (RSNs) (Biswal et al., 1995). RSN dysregulations, and accompanying neurometabolic changes, have been identified in patients with neuropsychiatric disorders (Van den Heuvel and Hulshoff Pol, 2010), e.g., schizophrenia and depression (Birur et al., 2017). Both RSN functional connectivity (FC) and neurometabolite levels in

humans are sensitive to rTMS and clinical improvements are associated with changes in RSNs (for review, see Seewoo et al., 2018a). However, there have been no reports of longitudinal studies to characterise the timecourse of changes in RSNs or neurometabolites during and after rTMS treatment.

A single session of low-intensity rTMS (LI-rTMS) in rats has frequency-specific effects on RSNs similar to those described in humans following rTMS (Seewoo et al., 2018b). This evidence of translational validity suggests that LI-rTMS in rodents can be a useful model in a translational pipeline to inform and guide clinical application of rTMS, particularly given the cost and logistical challenges of longitudinal human studies. For example, recent active fMRI/rTMS studies in animal models of traumatic brain injury have shown that repeated delivery of high-frequency rTMS increased primary somatosensory activity in response to forelimb stimulation, indicating restored cortical function (Lu et al., 2015; Shin et al., 2018). The present study used rs-fMRI and MRS in rats to investigate the emergence of LI-rTMS-induced changes in FC and neurometabolite levels respectively and their maintenance for up to three weeks. Two weeks of daily stimulation resulted in significant changes in FC and neurometabolites that outlasted the duration of stimulation. A better understanding of rTMS effects on RSNs and neurometabolites may prove helpful in the development of long-lasting treatment options to modify dysfunctional connectivity detected in several neuropsychiatric disorders.

5.2. Materials and Methods

5.2.1. Animals

Experimental procedures were approved by the UWA Animal Ethics Committee (RA/3/100/1430) in accordance with the *Australian code for the care and use of animals for scientific purposes*. 18 adult male Sprague-Dawley rats (6-8 weeks old, 150-250g) from the Animal Resources Centre (Canning Vale, Western Australia) were maintained in a temperature-controlled animal care facility on a 12-hour light-dark cycle with food and water *ad libitum*. Animals were euthanised after the last imaging session using CO₂ asphyxiation.

5.2.2. Experimental Protocol

Following acquisition of baseline rs-fMRI data, all animals received daily 10 min LI-rTMS at 10 Hz or 1 Hz for 15 days ($n = 9/\text{group}$, Figure 5.1). LI-rTMS was delivered using a custom-built round coil (described in detail in Grehl et al., 2015; Seewoo et al., 2018b) held by the experimenter between the right eye and ear (~13 mT at cortical surface). Animals were habituated to handling and to the coil for one week, as described previously (Rodger et al., 2012; Makowiecki et al., 2014). Imaging was conducted under isoflurane-medetomidine combination anaesthesia weekly during stimulation. Another two imaging sessions were performed seven and 20 days after stimulation was ceased for the 10 Hz group, and seven and 14 days after stimulation was ceased for the 1 Hz group. The only difference between the imaging timeline of the two groups was the timing of the last imaging session (20 days after stimulation cessation for the 10 Hz group and 14 days after stimulation cessation in the 1 Hz group) due to MRI hardware failure that delayed scanning of the 10 Hz group. After the

scanning procedure, medetomidine was antagonised by an injection of atipamezole.

See supplementary methods for further details, drug dosing, etc.

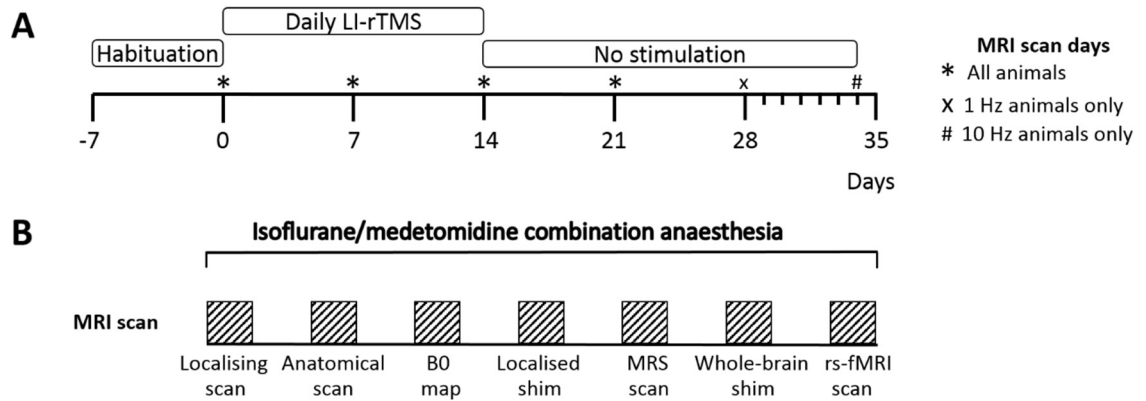


Figure 5.1. Timeline of an experiment for one rat. A. The experiment consisted of an initial one-week period of habituation upon arrival of the animal, after which the rats had five sessions of MRI scans, each separated by at least one week. Day 0 was the first imaging session for acquiring baseline resting-state activity and neurometabolite levels. For the first two weeks, animals were stimulated daily for 10 min at 10 Hz (6,000 pulses) or 1 Hz (600 pulses). Stimulation was ceased after 15 days of stimulation (after Day 14), but the animals were still imaged on Day 21 (all animals), Day 28 (1 Hz animals) and Day 34 (10 Hz animals). These five imaging timepoints will be referred to as: baseline, after seven (SD7) and 14 days (SD14) of daily stimulation and either 20 days (10 Hz group) or 14 days (1 Hz group) after stimulation cessation (PSD20 or PSD14 respectively). B. Protocol for a single scan session. During each session, the animal was under a combination of isoflurane and medetomidine anaesthesia throughout the experiment. Each session consisted of the acquisition of a localising scan, an anatomical scan, a B0 map, a localised shim, an MRS scan, whole brain shim, and an rs-fMRI scan.

5.2.3. Data acquisition

All MR images were acquired with a 9.4 T Bruker Biospec 94/30 small animal MRI using the imaging protocol as described in the supplementary methods and in (Seewoo et al., 2018b). Briefly, the acquisition protocol included the following sequences: 1) multi-slice 2D RARE (rapid acquisition with relaxation enhancement) sequence for three T2-weighted scans (TR = 2500 ms, TE = 33 ms, matrix = 280 x 280, 21 coronal and axial slices, 20 sagittal slices, thickness = 1 mm); 2) single-shot gradient echo EPI (TR = 1500 ms, TE = 11 ms, matrix = 94 x 70, 21 coronal slices, thickness = 1 mm, pixel size = 0.3 x 0.3 mm², flip angle = 90°, 300 volumes) for resting-state; and 3) point-resolved

spectroscopy (PRESS) sequence with one 90° and two 180° pulses, and water suppression for ¹H-MRS (TE = 16 ms, TR = 2500 ms) with 64 averages (Supplementary Table 5.1) with a 3.5 × 2 × 6 mm³ voxel placed over the right sensorimotor cortex (Figure 5.2).

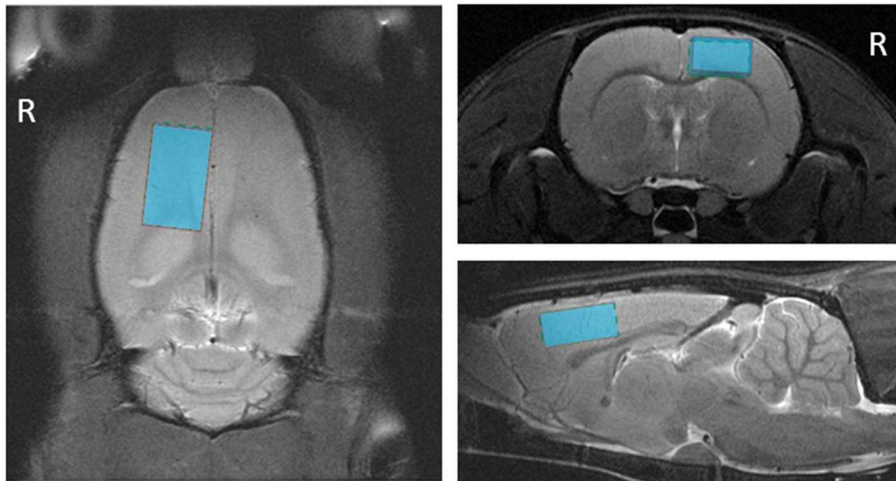


Figure 5.2. Volume of interest (VOI) positioning. The figure shows the position of the MRS voxel (size of 3.5 mm × 2 mm × 6 mm) on the right sensorimotor cortex (ipsilateral to LI-rTMS delivery) on T2-weighted images for proton nuclear magnetic resonance spectroscopy.

5.2.4. Image processing and analysis

Image processing was performed as described in Seewoo *et al.* (Seewoo et al., 2018b), with the following changes: 1) qimask utility from QUIT (QUantitative Imaging Tools) used for skull-stripping (Wood, 2018); 2) Gaussian kernel filter was set to a full-width half maximum of 6.25mm for single-session independent component analysis (ICA); and 3) FIX (FMRIB's ICA-based Xnoiseifier v1.06; threshold 20) was trained to automatically remove noise components (See Supplementary Methods for more details) (Griffanti et al., 2014; Salimi-Khorshidi et al., 2014).

Because of the exploratory nature of this study, an ICA-based approach was used to identify whole-brain FC changes. Multi-subject temporal concatenation group-ICA was carried out on baseline rs-fMRI data using MELODIC to identify template RSNs (Figure

5.3). The ICA algorithm was restricted to 15 components based on other rs-fMRI studies in rodents (Jonckers et al., 2011; Zerbi et al., 2015; Seewoo et al., 2018b). Dual regression analysis was then conducted on relevant RSNs for between-timepoint comparisons (Rytty et al., 2013; Nickerson et al., 2017), controlling for family-wise error (FWE) and using a threshold-free cluster enhanced (TFCE) technique to control for multiple comparisons ($p < 0.05$). Regions showing significant differences (Figure 5.4-5.5) were then labelled using a rat brain atlas (Paxinos and Watson, 1998).

5.2.5. MRS data analysis and presentation

MRS data was analysed in LCModel (“Linear Combination of Model spectra” version 6.3-1L) (Provencher, 2001) using a set of simulated basis set provided by the software vendor. Individual metabolite concentrations were computed using the unsuppressed reference water signal for each individual scan. The Cramér-Rao lower bounds (CRLBs) were calculated by LCModel and reported as the percentage of the estimated concentrations to determine reliability of the metabolite estimates (see Supplementary Table 5.2 for quantification details). The metabolites of interest were GABA and Glu, the major neurotransmitters in the brain, Gln, a neurotransmitter precursor, and combined glutamate-glutamine (Glx). All results presented for the metabolite concentrations are expressed as Tau ratios (metabolite concentration/Tau concentration) because (i) Tau peak could be identified with high reliability by LCModel (CRLB < 10%), and (ii) to the best of our knowledge, there is no literature showing high (HI) or low intensity rTMS-related changes in Tau. To improve sensitivity for detecting changes in glutamate-glutamine cycle function, we also report results for Glu/Gln ratios for detecting LI-rTMS-induced changes in neurotransmission. Analyses and plots of metabolites ratios were carried out using RStudio version 3.5.2

(<http://www.rstudio.com/>). Three data points from each group were excluded from the analyses due to identification as outliers by boxplots, bad shimming and/or bad voxel positioning leading to high CRLB values. Repeated-measures ANOVA ('lme4' and 'lmerTest' packages) was utilised to test for between-timepoint differences. When significant main effects of timepoints were found, *post hoc* pairwise differences were calculated ('glht' in 'multcomp' package) to determine significant changes in metabolite ratios between two timepoints (Figure 5.6). Tukey all-pair comparisons were carried out and Bonferroni-Holm adjusted p values reported.

5.3. Results

5.3.1. Template RSNs identified by group-ICA

Template rodent RSNs were identified from baseline data to avoid including LI-rTMS-related RSN alterations in the template components and thus increase the sensitivity of dual regression in detecting between-group differences (Rytty et al., 2013). Based on visual inspection of the 15 components identified by group-ICA, four components (Figure 5.3) were identified as classical rodent RSNs (e.g., Becerra et al., 2011; Zerbi et al., 2015; Bajic et al., 2016; Hsu et al., 2016). The remaining eleven components were classified as noise (see examples in Supplementary Figure 5.1). Component 1 is dominated by a cortical ribbon, and interoceptive (Becerra et al., 2011) and default mode network (DMN) (Lu et al., 2012) structures (Table 5.1) are grouped to form a network. Component 2 (cortico-striatal-thalamic network) includes similar structures as C1 (see Table 5.1 for differences). A similar network was identified by (Bajic et al., 2016) in infant rats, without the high correlation in the cortex seen in C2 but with a greater correlation to the hippocampus. Component 3 (basal ganglial network) mostly involves subcortical regions (Table 5.1), similar to the network reported in infant rats

by Bajic *et al.* (Bajic *et al.*, 2016). Component 4 presents characteristics of the salience network, showing specific overlap with the insular and somatosensory cortices (Bajic *et al.*, 2016).

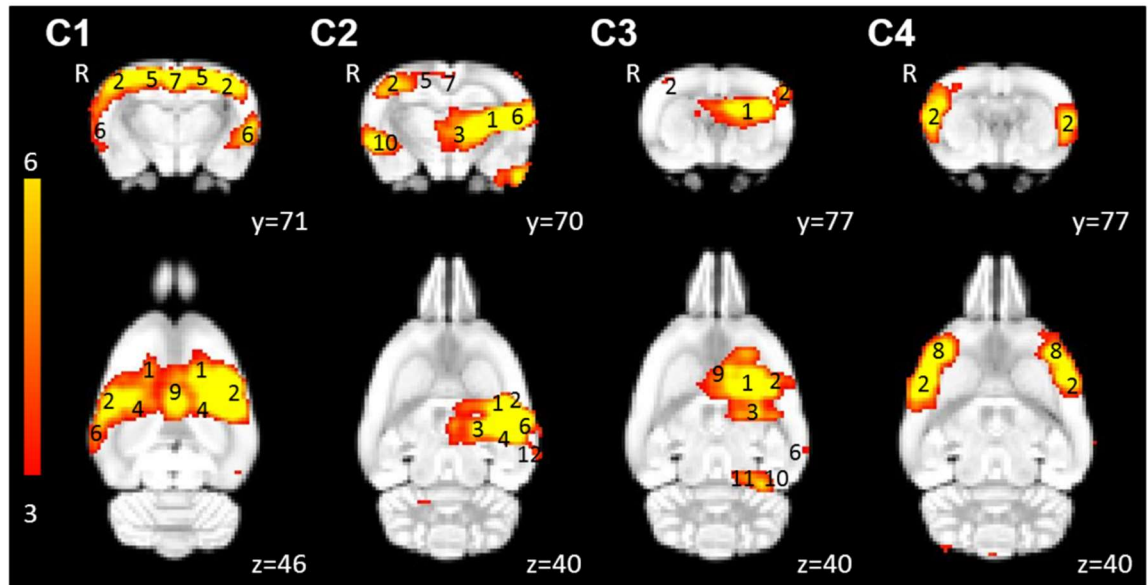


Figure 5.3. Template resting-state networks from baseline rs-fMRI scans. The figure illustrates coronal and corresponding axial slices of four RSNs (C1–C4) that were identified in the baseline rs-fMRI scans of 6–7-week-old male Sprague Dawley rats under isoflurane-medetomidine combination anaesthesia. The four components were classified as follows: C1, interoceptive/DMN network; C2, cortico-striatal-thalamic network; C3, basal ganglial network; and C4, salience network. The spatial colour-coded z-maps of these components are overlaid on the rat brain atlas (down-sampled by a factor of eight) and the numbers on the bottom right corner of each slice refer to the position on the atlas. The RSN maps are represented as z-scores ($n = 22$, thresholded at $z > 3$), with a higher z-score (yellow) representing a greater correlation between the time course of that voxel and the mean time course of the component. R denotes right hemisphere. Significant clusters within the components include various brain regions: 1, striatum/caudate putamen; 2, somatosensory cortex; 3, thalamus; 4, hippocampus; 5, motor cortex; 6, auditory cortex; 7, retrosplenial cortex; 8, insular cortex; 9, cingulate cortex; 10, entorhinal cortex; 11, inferior colliculus; 12, association cortex.

Table 5.1. Summary of brain regions within the four components identified by group-ICA.

Components	Networks	Brain regions
C1	Interoceptive/default mode network	Cortical regions, e.g., the somatosensory cortex, motor cortex, auditory cortex, retrosplenial cortex, and cingulate cortex as well as the striatum and hippocampus.
C2	Cortico-striatal-thalamic network	Similar to C1, excluding the cingulate cortex but including the entorhinal cortex. Predominantly within the cortex, striatum, and thalamus.
C3	Basal ganglial network	Subcortical, mostly the striatum.
C4	Salience network	Insular and somatosensory cortex.

5.3.2. Functional connectivity changes

Rs-fMRI data was acquired at five timepoints: baseline, after seven stimulation sessions (SD7), after 14 stimulation sessions (SD14), seven days after stimulation cessation (PSD7), and either 20 days (10 Hz group) or 14 days (1 Hz group) after stimulation cessation (PSD20 or PSD14 respectively). Overall, dual regression revealed that 10 Hz LI-rTMS induced significant potentiation of FC in C1, C2, and C3 (Figure 5.4) while 1 Hz LI-rTMS significantly attenuated FC in C2, C3, and C4 (Figure 5.5).

Daily 10 Hz stimulation significantly increased FC of several brain regions to C1 by SD7 (Figure 5.4A) and this increase was even greater on SD14. Following stimulation cessation, C1 FC decreased back to baseline levels over 20 days, with the drop being more significant and widespread on PSD20 than on PSD7. There were no significant differences between PSD7 and PSD20 or between baseline and both PSD7 and PSD20, showing that FC returned to baseline within one week after stimulation was stopped. C2 FC was unchanged on SD7 but significantly increased by SD14 (Figure 5.4B). FC returned to and remained stable at baseline by PSD7. Similarly, C3 FC to the left somatosensory cortex, striatum and dorsal hippocampus peaked at SD14 (Figure 5.4C) and decreased back to baseline by PSD7. Surprisingly, C3 FC on SD14 was also found to be significantly reduced in the right striatum, insular cortex, bilateral ventral hippocampus, thalamus, and auditory cortex, returning to baseline by PSD7 as well (see more detailed changes in Supplementary Table 5.3).

In the 1 Hz group, C2 FC to the left somatosensory significantly dropped after 14 stimulation sessions (Figure 5.5A). C2 FC to the right thalamus and left striatum was elevated on PSD14 compared to SD14 despite there being no significant changes in

these regions compared to baseline at both timepoints. Additionally, there was a significant decrease C3 FC on SD14 (Figure 5.5B) that was sustained on PSD7 but had returned to baseline by PSD14. In contrast, the decreased C4 FC to the right somatosensory cortex noted on SD14 stayed below baseline on PSD7 and had further decreased by PSD14 to also encompass the left somatosensory cortex (Figure 5.5C).

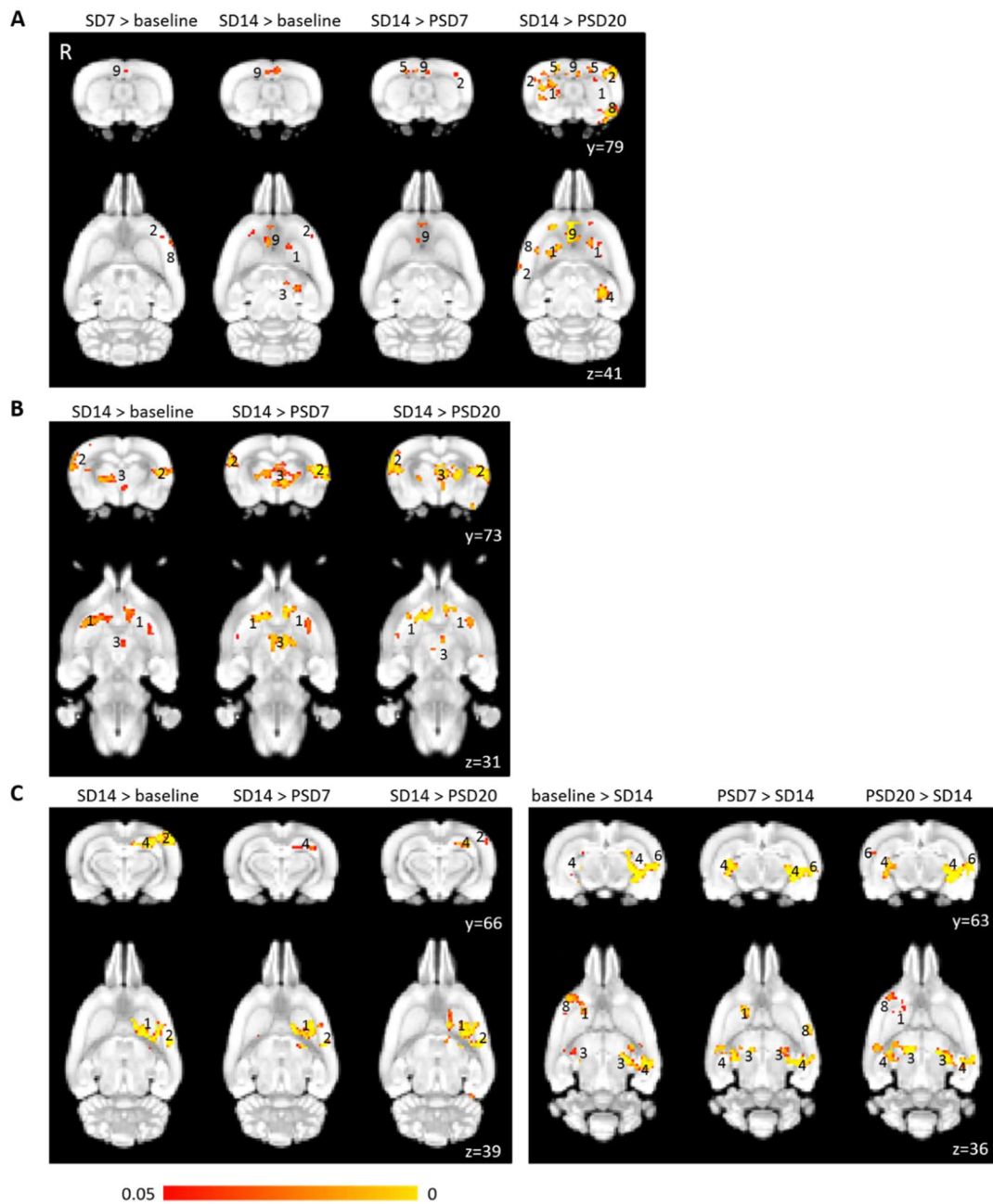


Figure 5.4. Functional connectivity changes within the (A) interoceptive/default mode network, (B) cortico-striatal-thalamic network and (C) basal ganglia network induced by 10 Hz LI-rTMS. The figure illustrates changes between five timepoints: baseline,

after seven (SD7) and 14 days (SD14) of daily stimulation and after seven (PSD7) and 20 days (PSD20) post-stimulation cessation. The spatial colour-coded p-value maps of these components are overlaid on the rat brain atlas (down-sampled by a factor of eight) and the numbers on the right refer to the slice position on the atlas. The dual regression maps are represented as p-values corrected for multiple comparisons at voxel level ($n = 9$, thresholded at $p < 0.05$). R denotes right hemisphere. Significant differences were found in: 1, striatum/caudate putamen; 2, somatosensory cortex; 3, thalamus; 4, hippocampus; 5, motor cortex; 6, auditory cortex; 8, insular cortex; 9, cingulate cortex.

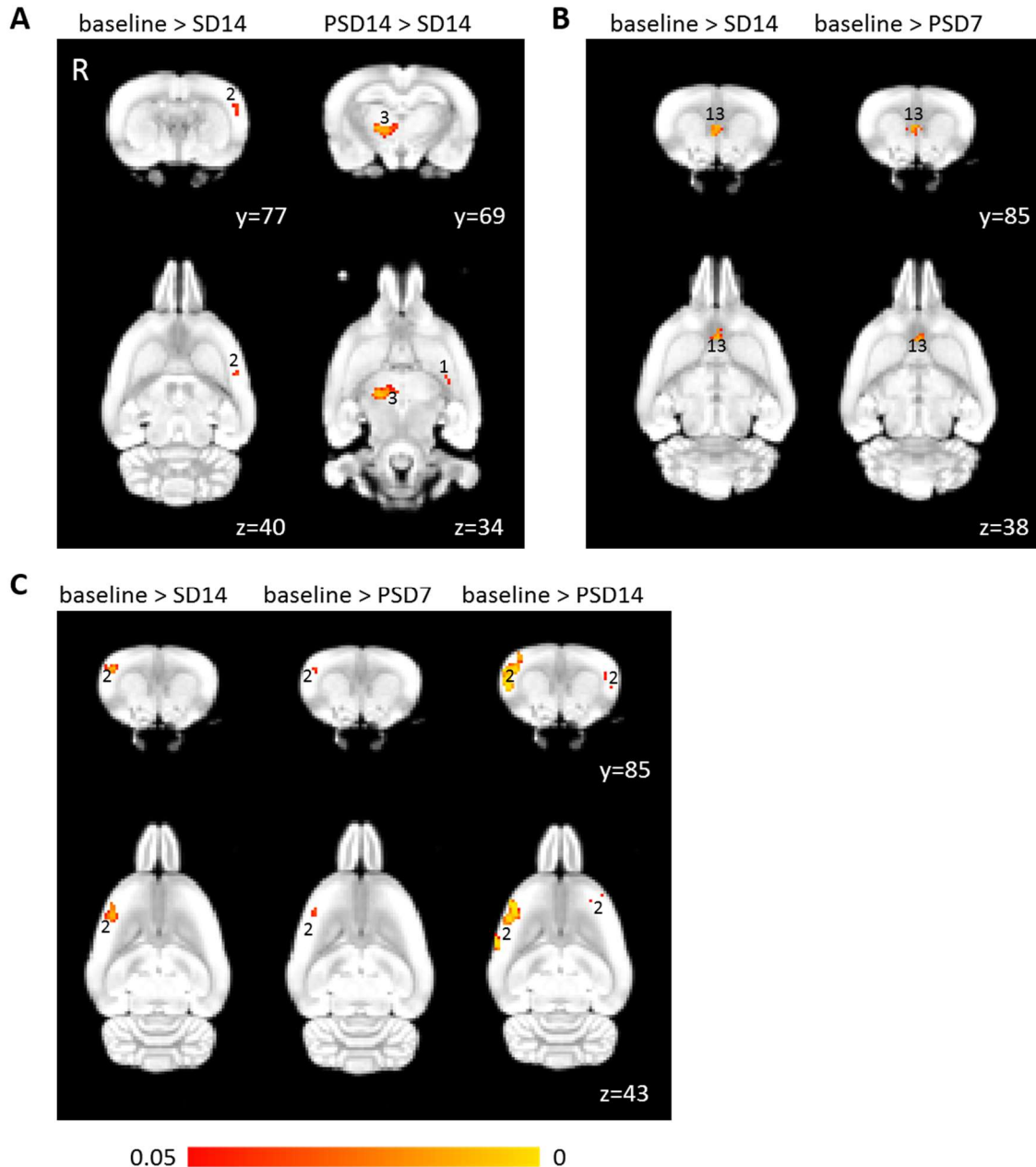


Figure 5.5. Functional connectivity changes within the (A) cortico-striatal-thalamic network, (B) basal ganglial network and (C) the salience network induced by 1 Hz LI-rTMS. The figure illustrates changes between five timepoints: baseline, after seven (SD7) and 14 days (SD14) of daily stimulation and after seven (PSD7) and 14 days (PSD14) post-stimulation cessation. The spatial colour-coded p-value maps of these components are overlaid on the rat brain atlas (down-sampled by a factor of eight) and the numbers on the right refer to the slice position on the atlas. The dual regression maps are represented as p-

values corrected for multiple comparisons at voxel level ($n = 9$, thresholded at $p < 0.05$). R denotes right hemisphere. Significant differences were found in: 1, striatum/caudate putamen; 2, somatosensory cortex; 3, thalamus; 13, prelimbic cortex.

5.3.3. Changes in metabolite ratios

To gain further insight into the association between FC and neurometabolic changes, we measured Gln, Glu, Glx and GABA levels in the sensorimotor cortex using $^1\text{H-MRS}$. Please note that herein we have chosen to report the MRS data as metabolite ratios relative to Tau, for the following reasons. Typically, *in-vivo* $^1\text{H-MRS}$ studies report metabolite concentrations in a relative manner using an internal concentration reference: water or any specific metabolite (Mikkelsen et al., 2017; Mikkelsen et al., 2019). The use of water as reference signal requires several uncertain corrections, for example due to partial volume and relaxation effects (Provencher, 2019). Moreover, the water concentration in brain tissue has to be determined because water signal arises from a combination of brain tissue and cerebrospinal fluid while detectable metabolites are exclusively found in brain tissue (Ernst et al., 1993; Gasparovic et al., 2006). Metabolite concentration ratios, as reported in this study, are less sensitive to these effects. The choice of the metabolite reference is arbitrary unless the metabolite concentration is expected to vary between groups and timepoints (Mikkelsen et al., 2019). To our knowledge, there is no literature showing rTMS-related changes in Tau, and accordingly we have chosen Tau as a concentration reference in our study (see Supplementary Table 5.5 for water-referenced metabolite concentrations in institutional units).

Spectra obtained were reproducible longitudinally (see example in Supplementary Figure 5.2). Unpaired Welch Two Sample t-test showed no significant differences in the baseline metabolite/Tau ratios between 10 Hz and 1 Hz groups.

Following 10 Hz stimulation, repeated-measures ANOVA revealed a main effect of timepoint for all five metabolite ratios investigated (Table 5.2). *Post hoc* comparisons showed a significant increase in Gln on SD7 compared to baseline (Figure 5.6), while Glu, Glx and GABA levels only increased non-significantly (see Supplementary Table 5.4 for mean metabolite concentrations). The levels of all four metabolites returned to baseline after an additional seven days of stimulation (i.e., no significant difference between baseline and SD14). After cessation of stimulation, Gln and Glx levels on PSD7 and PSD20 were significantly lower than on SD7. In contrast, Glu and GABA levels were only significantly lower than SD7 on PSD20. On the other hand, Glu/Gln levels decreased non-significantly from baseline with daily stimulation and increased significantly between SD7 and PSD7, and between SD14 and PSD7. There was a significant drop in Glu/Gln level on PSD20 compared to PSD7, i.e., Glu/Gln level decreased back to baseline by PSD20.

For the 1 Hz group, repeated-measures ANOVA did not detect significant timepoint-related changes in any metabolite ($p < 0.1$ for Gln, Glu and Glx; and $p > 0.1$ for GABA and Glu/Gln). Gln ($P = 0.0873$), Glu ($p = 0.0444$) and Glx ($p = 0.0229$) levels decreased to lower than baseline on PSD7, after cessation of stimulation (Figure 5.6).

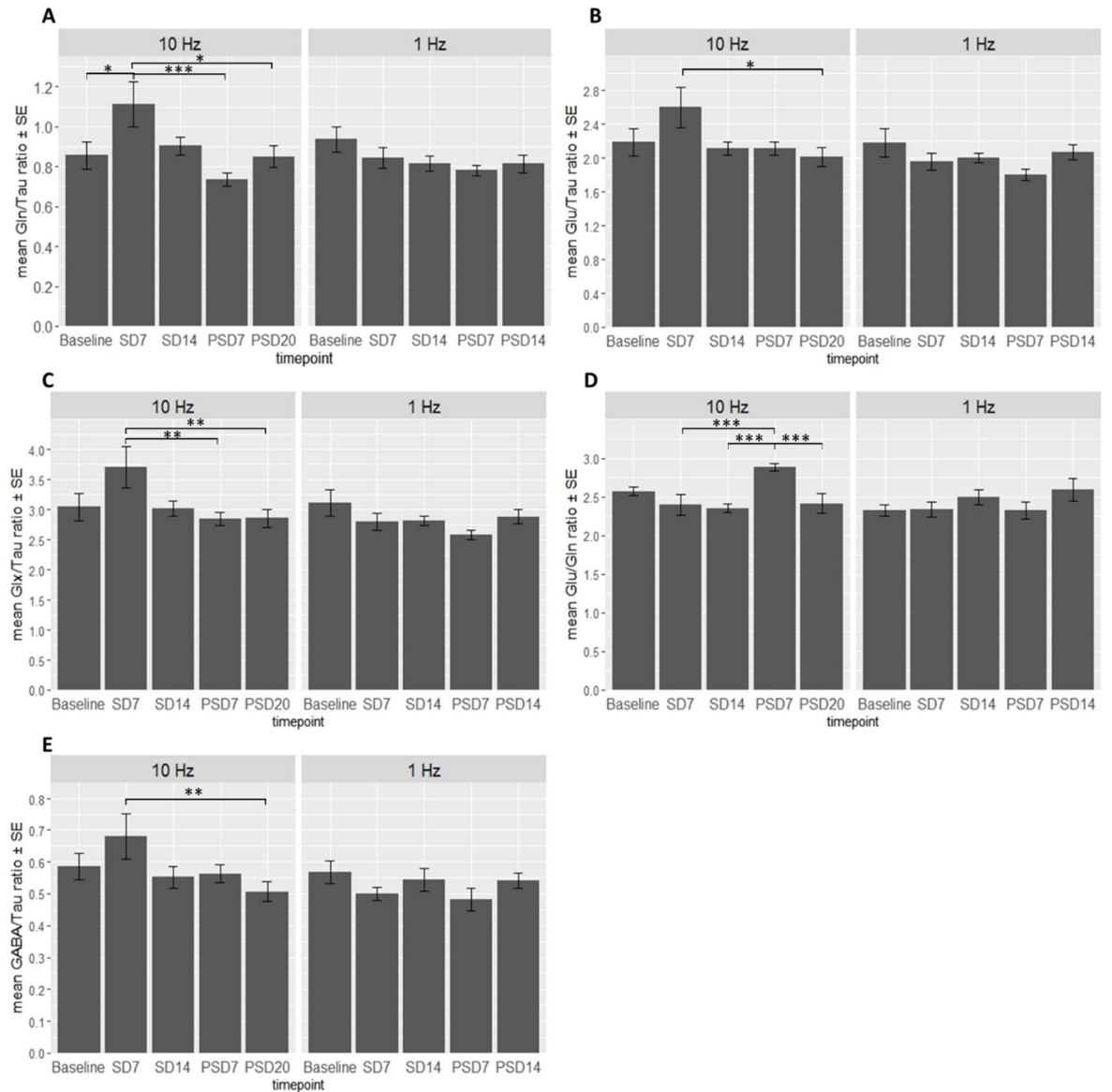


Figure 5.6. Longitudinal changes in metabolite ratios at the different timepoints in rat sensorimotor cortex following 10 Hz and 1 Hz LI-rTMS. All graphs show mean \pm standard error and post hoc pairwise differences results ($*p < 0.05$, $**p < 0.01$, $***p < 0.001$). The five metabolite ratios studied were as follows: A, glutamine (Gln)/Tau ratio; B, glutamate (Glu)/Tau ratio; C, glutamine + glutamate (Glx)/Tau ratio; D, glutamate/glutamine (Glu/Gln) ratio; and E, γ -aminobutyric acid (GABA)/Tau ratio.

Table 5.2. Summary of results from repeated-measures ANOVA of neurometabolite levels to test for main effect of timepoint.

Group	Metabolite	<i>F</i>	<i>P</i>
10 Hz	Gln/Tau	5.72	0.0016 **
	Glu/Tau	3.06	0.032 *
	Glx/Tau	3.87	0.012 *
	GABA/Tau	3.03	0.033 *
	Glu/Gln	6.02	0.0012 **
1 Hz	Gln/Tau	2.35	0.078 †
	Glu/Tau	2.30	0.082 †
	Glx/Tau	2.56	0.059 †
	GABA/Tau	1.33	0.28
	Glu/Gln	1.48	0.23

Significance codes: ** $p < 0.01$, * $p < 0.05$, † $p < 0.1$

5.4. Discussion

rTMS therapy is normally delivered to patients as a course of treatment over several weeks to induce lasting plastic changes. However, the stability of these changes remains unknown. This study examined both the emergence and maintenance of changes in FC and neurometabolite levels, assessed with rs-fMRI and MRS respectively, following repeated LI-rTMS in rats. Our study confirms the frequency-specific effects of LI-rTMS and further suggests that effects of 1 Hz stimulation, although milder, may persist for longer after cessation of treatment than the effects of 10 Hz stimulation. We discuss the longitudinal FC changes observed here in rats in the context of FC changes reported in human rTMS literature (healthy and patient populations). Although to directly extrapolate findings from healthy naïve rats to patients may be tenuous at this early stage of investigation, our findings support the existing use of

weekly maintenance treatments in 10 Hz treatment of depression (see review, Perera et al., 2016).

5.4.1. Functional connectivity changes in 10 Hz group

In line with previous studies showing increased excitability and induction of LTP following high-frequency rTMS, we found that daily 10 Hz LI-rTMS potentiated FC in the C1, C2 and C3 networks. Our results of increased FC in C1 and C2 are in agreement with findings from previous human studies reporting that rTMS increased FC of the DMN in patients with multiple system atrophy (Chou et al., 2015) and also of the cortico-striatal-thalamic network in patients with stroke (Chang et al., 2012) and in maladaptive emotion regulation (Salomons et al., 2014; Dunlop et al., 2016; Peters et al., 2016). Additionally, our finding of increased C3 FC to the left hippocampus, somatosensory cortex and striatum is comparable to the increased FC detected between the stimulated parietal cortex and the hippocampus following 20Hz rTMS in healthy adults (Wang et al., 2014) and the increased activity of the stimulated somatosensory cortex and the basal ganglia following 5 Hz rTMS in patients with focal dystonia (Schneider et al., 2010), although the increased FC observed here is in the contralateral hemisphere.

Interestingly, within C3 we also found decreased FC in several regions, which is in contrast with previous reports of increased activity in the temporal cortex and hippocampus after two sessions of 20Hz rTMS in humans (Xue et al., 2017). However, the decrease in C3 FC to some brain regions is potentially due to a change in their resting activity making them more synchronous to other components and therefore less synchronous to C3. There is considerable overlap in the brain regions showing a

decrease in FC to C3 and an increase in FC to other networks, e.g., increase in C1 FC to the left thalamus ($z = 40-41$), increase in C2 FC to the right thalamus ($z = 33-34$), and increase in C2 FC to the right striatum ($y = 84-86$).

In contrast to the significant changes observed after one day (Seewoo et al., 2018b) and after 15 days of stimulation, FC within all networks after stimulation cessation was not significantly different from baseline. However, changes in FC compared to SD14 were more widespread and significant on PSD20 than on PSD7, showing that the change in FC observed on SD14 compared to baseline decreased gradually, back to baseline, after daily stimulation was stopped. Our finding is relevant in refining an optimal strategy for maintenance treatments, particularly for depression in which 10 Hz stimulation is an approved treatment regime (although iTBS has recently also been approved (Blumberger et al., 2018; Lewis, 2018)). Most studies of rTMS treatment for depression focus on immediate and long-term effects, with only a few behavioural studies investigating the efficacy of “top-up” or maintenance rTMS delivery to prevent relapse (e.g., Abraham and O'Brien, 2002; Li et al., 2004; O'Reardon et al., 2005; Wang et al., 2017a). However, because these are performed in patients, there is considerable variation within such studies and establishing a reliable protocol is difficult. Our studies suggest that weekly maintenance stimulation delivery may be appropriate, but future studies should investigate if an optimal time can be identified for delivering “top-up” rTMS to maintain FC changes in humans.

5.4.2. Functional connectivity changes in 1 Hz group

Overall, 1 Hz stimulation had less widespread effects on FC than 10 Hz stimulation, which was also observed in our previous study looking at the immediate effects of one

10 min LI-rTMS session (Seewoo et al., 2018b). Additionally, in the present study, daily 1 Hz stimulation mostly attenuated FC. The differential effect-size and effect-direction between low- and high-frequency rTMS has been observed in previous studies (see review Thut and Pascual-Leone, 2010); induction of rTMS-related changes is known to be less likely with low- than high-frequency rTMS, and when changes are induced, the effect-direction is negative following low-frequency rTMS and more frequently positive following high-frequency rTMS.

There was a significant decrease in C2 FC to the left and C4 FC to the right somatosensory cortex on SD14. Similarly, a bilateral decrease in activity in somatosensory cortex following 1 Hz rTMS in healthy volunteers was observed by Min *et al.* (Min et al., 2016). However, in contrast to our findings, they observed more prominent and longer-lasting changes in the contralateral compared to the ipsilateral somatosensory cortex. Nevertheless, this difference might be related to the state dependency of rTMS effects (e.g., reported in Bilek et al., 2013) as Min and colleagues (Min et al., 2016) used a finger-tapping task instead of resting-state. Other rTMS studies have reported exclusively ipsilateral effects of 1Hz stimulation on the somatosensory cortex (Enomoto et al., 2001; Vidoni et al., 2010), but have used different stimulation and detection methodologies, making comparisons difficult.

Additionally, we observed a significant decrease in FC of the prelimbic cortex (homologous to human medial prefrontal cortex) to the basal ganglial network (C3), consistent with human literature showing attenuated FC between these two regions in healthy individuals following 1 Hz stimulation (Popa et al., 2017). Similarly, in patients with depression, 1 Hz rTMS has been shown to decrease activity in the prefrontal

cortex and the basal ganglia while 10 Hz rTMS, most often used to alter aberrant connectivity in depression (see review Anderson et al., 2016), increased activity within these regions (Kimbrell et al., 1999; Speer et al., 2000). Surprisingly, both frequencies are reported to have similarly beneficial outcomes in patients, with about half of the participants in each group responding to treatment (Eche et al., 2012). One study even reported that patients who benefit from one frequency might worsen from the other (Speer et al., 2000). This might be explained by the observation that patients can exhibit either hypoconnectivity between the ventromedial prefrontal cortex and ventral striatum, or hyperconnectivity between the dorsal prefrontal cortex and dorsal caudate (Furman et al., 2011). Therefore, pre-treatment FC within this network might play an important role in patients' antidepressant response to 1 Hz and 10 Hz rTMS (Drysdale et al., 2017).

Upon cessation of stimulation, C2 FC increased back to baseline, whereas the decrease in FC was sustained on PSD7 within C3 and even on PSD14 within C4. The continuous decrease in C4 FC following stimulation cessation is surprisingly strong and may be related to either a decrease in excitatory circuits or an increase in inhibitory mechanisms. Previous animal studies have consistently shown increases in inhibitory circuit function a few hours after 1 Hz stimulation, but there are few studies that measure changes occurring days or weeks after stimulation. One study in rats demonstrated increasing expression of cortical markers of inhibitory neurotransmission over seven days after a single 70 min 1 Hz stimulation (Trippe et al., 2009). Taken together, our findings of decreased C2, C3 and C4 FC suggest that 1 Hz stimulation may have a sustained effect on the RSN by increasing inhibitory

neurotransmission. LI-rTMS at 1 Hz may therefore be a useful tool for inducing long-term changes in brain function and warrants further investigation.

5.4.3. Changes in neurometabolite concentrations induced by 10 Hz and 1 Hz stimulation

Similar to our FC results, 10 Hz stimulation resulted in significant changes in neurometabolite concentrations, whereas 1 Hz effects were subtler but more sustained. Previous rodent studies also suggested that repeated 1 Hz stimulation has limited effects on cortical markers of neuroplasticity (Gersner et al., 2011) and induces only non-significant decreases in gene expression in the cortex (Ljubisavljevic et al., 2015). We are cognisant that the difference in effect size and persistence of 10 Hz and 1 Hz LI-rTMS might be related to differences in the total number of pulses applied (6,000 vs 600 pulses respectively) (Aydin-Abidin et al., 2006). For example, a systematic study found that 600 pulses of 10 Hz stimulation had an excitatory effect but 1,200 pulses had no effect (Aydin-Abidin et al., 2006).

To gain insight into the effect of LI-rTMS on excitatory and inhibitory networks within the sensorimotor cortex, we measured Gln and Glu, which have been positively correlated with various rTMS-measures of cortical excitability (Zangen and Hyodo, 2002; Vlachos et al., 2012; Tang et al., 2015). We also measured Glx (representing the sum of Gln+Glu) and Glu/Gln ratio to support the Gln and Glu data, as well as GABA, the main inhibitory neurotransmitter in the brain. *Post hoc* analyses revealed a significant but transient increase in Gln and non-significant increase in Glu, Glx and GABA following seven days (SD7) of 10 Hz stimulation. However, after an additional seven days of stimulation (SD14), levels of all four compounds returned to baseline. The noteworthy drop in metabolite levels observed on SD14 appears contradictory to

the maintained increase in FC shown by our rs-fMRI data at this time point. A possible explanation is that the increased excitability induced by 10 Hz LI-rTMS triggers homeostatic and/or metaplastic mechanisms to maintain a balance of excitation/inhibition in the brain (Abraham, 2008; Li et al., 2019) (previously shown in neuronal cultures (De Gois et al., 2005) and in rats (Trippe et al., 2009; Volz et al., 2013)), but without disrupting the increases in FC. Also, the MRS data reflect changes in the sensorimotor cortex only while FC changes were found in other brain regions as well. Nonetheless, the engagement of homeostatic control by 10 Hz LI-rTMS is consistent with the transient increase in Glu/Gln ratio on PSD7 and short duration of FC changes, which were no longer detected a week after stimulation cessation. The implication is that 10 Hz may initially induce stronger effects in neural circuits than 1 Hz, but as a result, recruits compensatory mechanisms which limit the duration of LI-rTMS effects. By contrast, 1 Hz, which has more subtle effects on FC and neurometabolites, elicits more persistent effects with a sustained decrease in cortical Gln, Glu and Glx seven days after cessation of stimulation (PSD7) and changes in FC compared to baseline in the C4 network persisting up to the last timepoint studied (PSD14).

Interestingly, the persistent decrease in GABA levels after cessation of 10 Hz stimulation, despite a lack of change in FC, is also consistent with a long-term facilitatory effect of 10 Hz stimulation acting via depression of GABAergic neurotransmission (see review Lenz and Vlachos, 2016). Given that inhibitory interneurons control the activity and excitability of cortical principal neurons (Tremblay et al., 2016), previous studies have suggested that depression of inhibitory

neurotransmission, as seen here, could facilitate associative plasticity (e.g., for improving learning and memory) in cortical networks (Lenz and Vlachos, 2016). This makes rTMS an attractive therapeutic intervention for several neuropsychiatric conditions associated with changes in inhibitory synaptic plasticity and excitation/inhibition-balance leading to behavioural and cognitive dysfunction (Steinberg et al., 2015), for example in schizophrenia (Yizhar et al., 2011; Rowland et al., 2013) and autism (Rubenstein and Merzenich, 2003).

The results of previous human MRS/rTMS studies are generally consistent with our findings, although use of healthy animals, the different number of stimulation sessions, as well as differences in intensity and frequency, preclude a direct comparison. Long-term (days to weeks) high-frequency rTMS to the prefrontal cortex increased cortical Gln and Glu levels in healthy volunteers (Michael et al., 2003), in patients with depression (Luborzewski et al., 2007; Yang et al., 2014b) and in patients with schizophrenia (Dlabac-de Lange et al., 2017). Interestingly, experiments in humans focussing on immediate effects rTMS detect a reduction in inhibitory synaptic interactions following high-frequency rTMS using motor evoked potentials (MEP) and paired-pulse protocols (reviewed in Fitzgerald et al., 2006). More recently, combined TMS paired-pulse and MRS studies show that the amount of intracortical inhibition does not correlate with the global levels of GABA in the primary motor cortex but may instead be linked to cortical glutamate levels (Tremblay et al., 2013). Taken together, studies in humans and in rodents concur that rTMS induces complex changes in inhibitory and excitatory circuits that evolve over time and may involve frequency-specific effects on different cell types (reviewed in Funke and Benali, 2010). Our

findings suggest that LI-rTMS in rodents induces changes that clearly reflect those occurring in humans following rTMS, and therefore provide a unique opportunity to combine non-invasive and invasive methods in the investigation of rTMS effects on neural circuitry.

Nevertheless, this is the first exploratory study of longitudinal effects of repeated LI-rTMS on rodent neurometabolites, and researchers interested in, for example, more subtle effects should consider dedicating more time to collect spectra with higher SNR. This may reduce the observed variability of some low concentration metabolites such as GABA and Gln. Additionally, researchers interested in effects of rTMS on GABA could consider using MEGA-PRESS (Mescher et al., 1998) or PRESS with TE (echo time) optimized for that metabolite (Dobberthien et al., 2018).

5.5. Conclusion

Information about the duration of the after-effects of rTMS therapy is vital for the development and improvement of rTMS use as a treatment in a clinical setting. Here, we present the first longitudinal rs-fMRI/MRS investigation of the duration of FC and neurometabolic changes induced by repeated LI-rTMS delivery. Our work confirms the frequency-specific effects of LI-rTMS and further suggests that effects of 1 Hz stimulation, although milder, may persist longer after cessation of treatment compared to those of 10 Hz stimulation. This study provides a framework to use non-invasive brain imaging to explore the duration of rTMS effects on resting brain activity in animal models of neurological and neuropsychiatric disorders such as depression for development and translation of optimised protocols to human patients. Further studies in animals and humans are warranted in effort to investigate potential

prolongation of FC effects through maintenance or “top-up” rTMS sessions weeks or months after the first set of treatment.

5.6. Supplementary Methods

5.6.1. Animal preparation for MRI

Rats were pre-anaesthetised in an induction chamber (4% isoflurane in medical air, 2L/min). Once fully anaesthetised, rats were transferred to a heated imaging cradle and anaesthesia was maintained with a nose cone (2% isoflurane in medical air, 1 L/min). Body temperature, respiratory rate, heart rate, and blood oxygen saturation were monitored using a PC-SAM Small Animal Monitor (SA Instruments Inc., 1030 System). A 25G butterfly catheter was implanted subcutaneously in the left flank to deliver a 0.05-0.1 mg/kg bolus injection and continuous infusion of medetomidine at 0.15 mg/kg/h using an infusion pump. After 15 min of infusion, or once breathing rate dropped below 50 breaths/min, isoflurane was gradually reduced from 2% to 0.25-0.75%. These anaesthetic doses were empirically determined to ensure the respiratory rate of the animals was between 40-60 breaths/min and pulse was between 250-380 beats/min. MRS and rs-fMRI scans were started only after the isoflurane concentration had been reduced for at least 15 min and physiology was stable during that time. After the scanning procedure, medetomidine was antagonized by an injection of atipamezole (0.1 mg/kg).

5.6.2. Data acquisition

All MR images were acquired with a Bruker Biospec 94/30 small animal MRI system operating at 9.4 T (400 MHz, H-1), with an Avance III HD console, BGA-12SHP imaging gradients, an 86 mm (inner diameter) volume quadrature transmit coil and a rat brain surface quadrature receive coil. Following a tri-plane scan to determine the position of

the rat brain, high-resolution T2-weighted coronal, axial and sagittal images were acquired using a multi-slice 2D RARE (rapid acquisition with relaxation enhancement) sequence with fat suppression from 21 x 1-mm-thick interlaced slices (20 slices for sagittal) with slice gap of 0.05 mm and: field-of-view = 28.0 mm x 28.0 mm; matrix size = 280 x 280; 0.1 mm x 0.1 mm in-plane pixel size; repetition time (TR) = 2500 ms; echo time (TE) = 33 ms; RARE factor = 8; echo spacing = 11 ms; number of averages (NA) = 2; number of dummy scans (DS) = 2; flip angle (α) = 90°; receiver bandwidth (BW) = 34722.2 Hz; and scan time = 2 min 55 s.

Prior to acquiring the MRS data, B0 shimming was completed for a region of interest covering the brain using the Bruker Mapshim routine. The T2-weighted images were used to place a 3.5 mm x 2 mm x 6 mm voxel of interest by hand over the right sensorimotor cortex (Figure 5.2). After localised shimming and water suppression adjustment using VAPOR (250 Hz bandwidth), a standard point-resolved spectroscopy (PRESS) sequence was used, with one 90° and two 180° pulses to create a spin echo, to acquire localised ¹H-MRS data. The following MR parameters were used: TR = 2500 ms, TE = 16 ms, NA = 64, DS = 2, spectral bandwidth = 4401.41Hz, scan time = 2 min 40 s, number of acquired points = 2048 yielding a spectral resolution of 1.07 Hz/pts after zero filling. Outer volume suppression was carefully applied using a slice thickness = 6 mm, gap to voxel = 1 mm and spoiler duration = 3 ms. A water unsuppressed scan was also acquired automatically to serve as a concentration reference. During the establishment of the MRS protocol, data was acquired with 64 averages, 128 averages and 256 averages to verify that the increased SNR obtained did not significantly

improve analysis with LCModel and hence, the concentrations of metabolites obtained (See Supplementary Table A.1).

Then the resting-state datasets were acquired using single-shot gradient echo EPI (Echo Planar Imaging) with TR 1500 ms and TE 11 ms. 21 coronal slices of 1 mm thickness and a gap of 0.05 mm were acquired with a FOV of 28.2 mm x 21.0 mm and a matrix size of 94 x 70 resulting in an in-plane pixel size of 0.3 mm x 0.3 mm. The receiver bandwidth was 326087.0 Hz. Each rs-fMRI dataset comprised 300 repetitions, resulting in a scanning time of 7.5 min.

5.6.3. Image processing

Most of the pre-processing and analyses were performed using FSL v5.0.10 (Functional MRI of the Brain (FMRIB) Software Library) (Jenkinson et al., 2012). The Bruker data was exported from ParaVision 6.0.1 into DICOM (Digital Imaging and Communications in Medicine) format (Bidgood Jr et al., 1997) (<http://dicom.nema.org/>) and then converted into NifTI (Neuroimaging Informatics Technology Initiative, <https://nifti.nih.gov/>) using the dcm2nii converter (64-bit Linux version 5 May 2016) (Rorden et al., 2007). Pre-processing of fMRI data included: (i) reorienting the brain into left-anterior-superior (LAS) axes (radiological view); (ii) skull-stripping using the qimask utility from QUIT (QUantitative Imaging Tools) (Wood, 2018); and (iii) upscaling the voxel sizes by a factor of 10 (Tambalo et al., 2015).

Single-session independent component analysis (ICA) was carried out for each brain-extracted image in FSL/MELODIC (Multivariate Exploratory Linear Decomposition into Independent Components) (Beckmann et al., 2005) with the Gaussian kernel filter set to a full-width half maximum (FWHM) of 6.25 mm, motion correction (Jenkinson et al.,

2002) to spatially realign the functional images to the middle volume of a serial acquisition and a temporal high pass filter cut-off of 100 s. After training, the motion parameters and the noise components of all filtered datasets from MELODIC were automatically classified and regressed by FSL/FIX (FMRIB's ICA-based Xnoiseifier v1.06) at a threshold of 20 (Griffanti et al., 2014; Salimi-Khorshidi et al., 2014). The de-noised fMRI images for each session were then co-registered to their respective T2-weighted images using six-parameter rigid body registration using FSL/FLIRT (Linear Image Registration Tool) (Jenkinson and Smith, 2001; Jenkinson et al., 2002) and normalised to a Sprague-Dawley brain atlas (Papp et al., 2014; Kjonigsen et al., 2015; Sergejeva et al., 2015) with nine degrees of freedom 'traditional' registration. The atlas was first down-sampled by a factor of eight to better match the voxel size of the 4D functional data. All subsequent analyses were conducted in the atlas standard space.

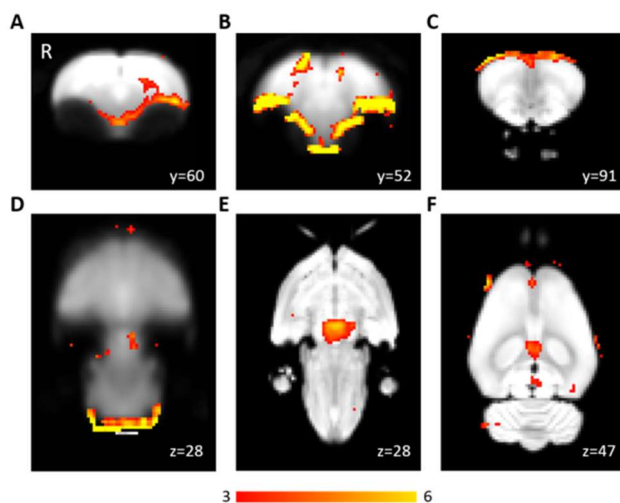
5.6.4. Image analysis

Multi-subject temporal concatenation group-ICA, as implemented in FSL/MELODIC, was carried out on baseline rs-fMRI data to identify template RSNs (Figure 5.3). The ICA algorithm was restricted to 15 components on the basis of other rs-fMRI studies in rodents (Jonckers et al., 2011; Zerbi et al., 2015; Seewoo et al., 2018b).

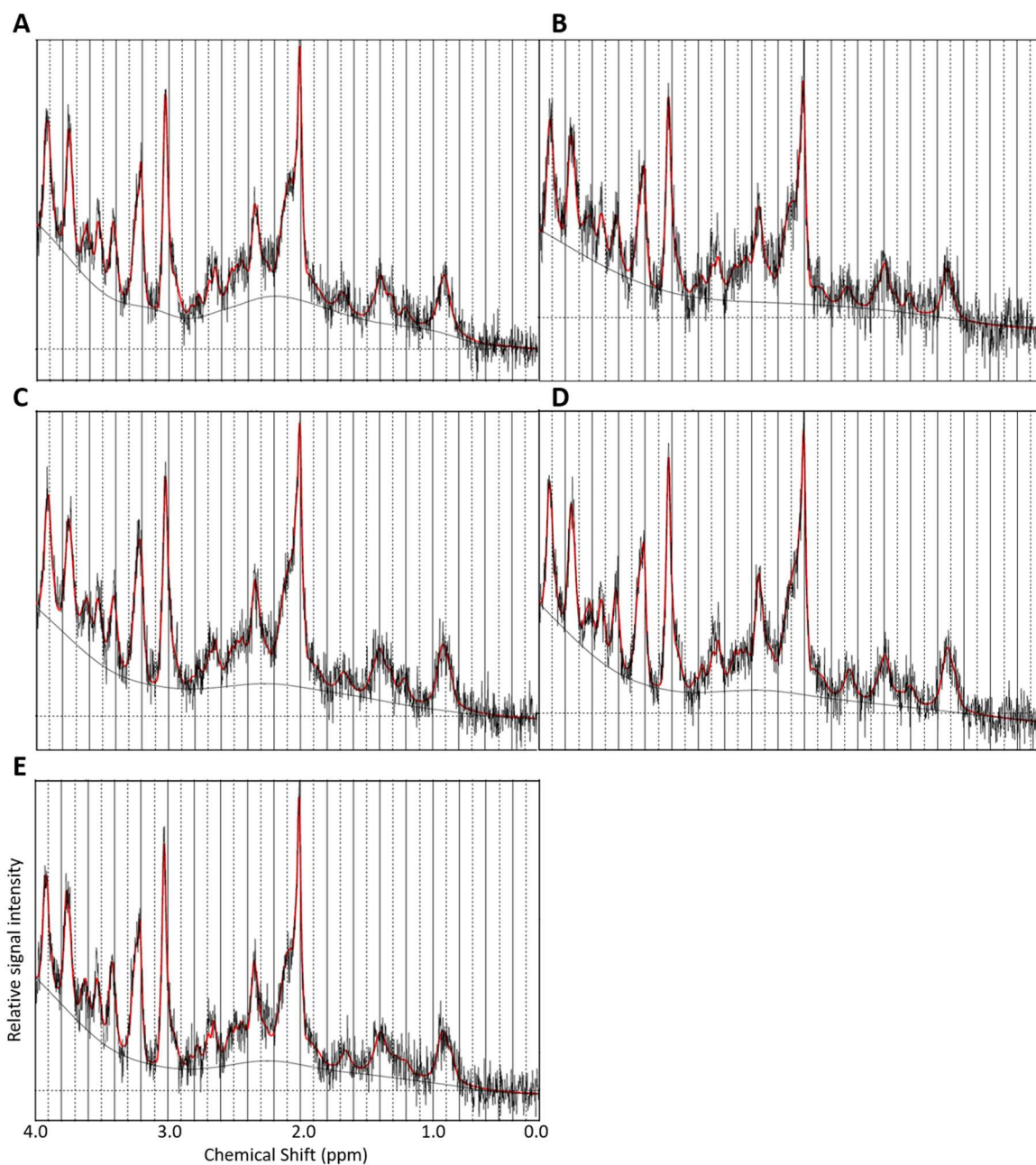
Dual regression analysis, which allows for voxel-wise comparisons of rs-fMRI data, was then conducted on the relevant RSNs using between-timepoint comparisons (t-contrasts) set up via the general linear model tool (Rytty et al., 2013; Nickerson et al., 2017). First, for each subject at each timepoint, the group-average set of spatial maps are regressed (as spatial regressors in a multiple regression) into the subject's 4D space-time dataset. This results in a set of subject/timepoint-specific timeseries, one

per group-level spatial map. Next, those timeseries are regressed (as temporal regressors, again in a multiple regression) into the same 4D dataset, resulting in a set of subject/timepoint-specific spatial maps, which are subject-level representations of these components at each timepoint (Beckmann et al., 2009). We then tested for group differences using FSL's randomise nonparametric permutation-testing tool, with 5000 permutations, controlling for family-wise error (FWE) and using a threshold-free cluster enhanced (TFCE) technique to control for multiple comparisons. The resulting statistical maps were thresholded to $p < 0.05$. Anatomical locations on the statistical maps showing significant differences (Figure 5.4-5.5) were then labelled using a rat brain atlas (Paxinos and Watson, 1998).

5.7. Supplementary Figures and Tables



Supplementary Figure 5.1. Example components — three coronal slices (A-C) and three axial slice (D-F) — from group-ICA classified as ‘noise’. The figure illustrates spatial colour-coded z-maps of noise components overlaid on the mean functional image (A, B and D) or on the rat brain atlas (C, E and F). A, B and D show highly synchronised activity at the edge of the brain. C shows synchronised activity outside the brain while E shows highly synchronised activity in the brainstem. F shows mostly single-voxel correlations of low z-scores. Colour bar indicates z-scores (thresholded at $z > 3$), with a higher z-score (yellow) representing a greater correlation between the time course of that voxel and the mean time course of the component. The numbers on the bottom right corner of each coronal and axial slices refer to the slice position on the atlas. The slices correspond to traditional radiographic orientation; the right hemisphere of the brain corresponds to the left side of the image.



Supplementary Figure 5.2. Representative spectra obtained from LCModel for proton spectroscopy data at baseline (A), after seven (B) and 14 (C) days of stimulation and seven (D) and 20 (E) days after daily stimulation was ceased. The figure shows spectra from a representative animal from the 10 Hz group depicting longitudinally reproducible peaks of various metabolites quantified using the LCModel.

Supplementary Table 5.1. Mean (\pm SE) signal-to-noise ratio (SNR), linewidth (full width at half-maximum, FWHM), Cramér-Rao lower bound (CRLB) values and neurometabolite concentrations (with reference to the unsuppressed water peak, in institutional units) for data acquired using 64, 128 and 254 averages. FWHM is calculated for the N-acetylaspartate+N-acetyl-aspartyl-glutamate (NAA) resonance at 2.01 ppm and SNR is the intensity of this resonance relative to the residual intensity. CRLB is the percent standard deviation of each metabolite, a measure of the reliability of the reported metabolite level.

Averages	64	128	256
SNR	16 \pm 2	21.5 \pm 0.5	28.5 \pm 1.5
FWHM (Hz)	10.6 \pm 2.2	9.6 \pm 1.2	10.6 \pm 2.2
CRLB (%)			
Gln	8 \pm 0	6 \pm 1	4.5 \pm 0.5
Glu	3 \pm 0	3 \pm 0	2 \pm 0
Glx	3 \pm 0	3 \pm 0	2 \pm 0
GABA	12.5 \pm 1.5	9.5 \pm 2.5	7.5 \pm 0.5
Tau	3.5 \pm 0.5	3 \pm 0	2.5 \pm 0.5
Concentration (I.U.)			
Gln	3.3 \pm 0.0	3.7 \pm 0.2	3.9 \pm 0.4
Glu	8.6 \pm 0.2	8.3 \pm 0.1	8.4 \pm 0.4
Glx	12.0 \pm 0.2	11.9 \pm 0.3	12.2 \pm 0.0
GABA	2.0 \pm 0.2	2.2 \pm 0.4	2.1 \pm 0.2
Tau	5.0 \pm 0.3	5.0 \pm 0.0	5.1 \pm 0.1

Supplementary Table 5.2. Mean (\pm SD) signal-to-noise ratio (SNR), linewidth (full width at half-maximum, FWHM), and Cramér-Rao lower bound (CRLB) for neurometabolite quantification at different timepoints for the 10 Hz and 1 Hz groups. FWHM is calculated for the N-acetylaspartate+N-acetyl-aspartyl-glutamate (NAA) resonance at 2.01 ppm and SNR is the intensity of this resonance relative to the residual intensity. CRLB is the percent standard deviation of each metabolite, a measure of the reliability of the reported metabolite level. The five imaging timepoints were: at baseline, after seven (SD7) and 14 days (SD14) of daily stimulation, seven days after stimulation cessation (PSD7) and either 20 days (10 Hz group) or 14 days (1 Hz group) after stimulation cessation (PSD20 or PSD14 respectively).

	Group	Baseline	SD7	SD14	PSD7	PSD20/PSD14
SNR	10 Hz	10.4 \pm 0.6	6.4 \pm 0.5	8.1 \pm 0.8	11.3 \pm 0.9	8.2 \pm 0.5
	1 Hz	10.1 \pm 0.6	12.0 \pm 0.8	11.0 \pm 0.9	9.1 \pm 0.5	9.2 \pm 0.4
FWHM (Hz)	10 Hz	13.3 \pm 0.9	16.4 \pm 1.1	17.9 \pm 1.4	12.9 \pm 1.3	15.4 \pm 0.8
	1 Hz	17.0 \pm 1.5	13.3 \pm 1.0	14.6 \pm 0.6	15.3 \pm 1.0	14.4 \pm 0.7
CRLB (%)						
Gln	10 Hz	11 \pm 1	14 \pm 3	12 \pm 2	11 \pm 1	12 \pm 1
	1 Hz	10 \pm 2	9 \pm 1	10 \pm 1	11 \pm 1	12 \pm 2
Glu	10 Hz	4 \pm 1	5 \pm 1	5 \pm 1	4 \pm 1	5 \pm 1
	1 Hz	4 \pm 1	4 \pm 1	4 \pm 1	4 \pm 1	4 \pm 0
GABA	10 Hz	14 \pm 3	18 \pm 3	17 \pm 4	14 \pm 4	17 \pm 3
	1 Hz	15 \pm 4	13 \pm 3	13 \pm 5	17 \pm 5	15 \pm 2

Supplementary Table 5.3. Summary of brain regions with significant ($p < 0.05$) changes in functional connectivity within the interoceptive/default mode network (C1), cortico-striatal-thalamic network (C2) and the basal ganglia network (C3)

following 10 Hz LI-rTMS. Five different timepoints were compared: (1) baseline, (2) after seven stimulation sessions (SD7), (3) after 14 stimulation sessions (SD14), (4) seven days after daily stimulation was stopped (PSD7), and (5) 20 days after stimulation was stopped (PSD20). Significant differences were found in various brain regions: 1, striatum/caudate putamen (CPu); 2, somatosensory cortex (SC); 3, thalamus (Th); 4, hippocampus (Hipp); 5, motor cortex (MC); 6, auditory cortex (Au); 7, retrosplenial cortex (RC); 8, insular cortex (In); 9, cingulate cortex (Cg); 10, entorhinal cortex (Ent); 11, inferior colliculus (IC); 12, association cortex (AC). R refers to the right side (ipsilateral changes), L refers to the left side (contralateral changes), ✓ refers to bilateral changes and × refers to no changes.

Component	Contrast	Brain regions											
		1 CPu	2 SC	3 Th	4 Hipp	5 MC	6 Au	7 RC	8 In	9 Cg	10 Ent	11 IC	12 AC
C1	SD7 > Baseline	×	L	×	×	L	×	×	✓	✓	×	×	L
	SD14 > Baseline	L	×	L	L	✓	×	✓	✓	✓	×	×	L
	SD14 > PSD7	✓	✓	×	L	✓	×	✓	R	✓	×	×	✓
	SD14 > PSD20	✓	✓	✓	✓	✓	✓	✓	✓	✓	✓	×	✓
C2	SD14 > Baseline	✓	✓	✓	×	×	✓	×	✓	×	×	×	×
	SD14 > PSD7	✓	✓	✓	×	×	✓	×	L	×	×	×	×
	SD14 > PSD20	✓	✓	✓	×	×	✓	×	✓	×	×	×	×
C3	SD14 > Baseline	L	L	✓	L	×	L	×	L	×	×	×	L
	SD14 > PSD7	L	L	✓	L	×	L	×	L	×	×	×	×
	SD14 > PSD20	L	L	L	L	×	L	×	L	×	L	×	×
	Baseline > SD14	✓	L	✓	✓	L	×	×	✓	×	×	×	L
	PSD7 > SD14	✓	L	✓	✓	×	×	×	✓	×	×	×	L
	PSD20 > SD14	✓	L	✓	✓	×	R	×	✓	×	×	×	L

Supplementary Table 5.4. Mean (\pm SE) neurometabolites at different timepoints for the 10 Hz and 1 Hz groups. The five imaging timepoints were: at baseline, after seven (SD7) and 14 days (SD14) of daily stimulation, seven days after stimulation cessation (PSD7) and either 20 days (10 Hz group) or 14 days (1 Hz group) after stimulation cessation (PSD20 or PSD14 respectively).

Group	Metabolite	Baseline	SD7	SD14	PSD7	PSD20/PSD14
10 Hz	Gln/Tau	0.86 \pm 0.07	1.11 \pm 0.11	0.90 \pm 0.04	0.73 \pm 0.03	0.85 \pm 0.05
	Glu/Tau	2.19 \pm 0.16	2.60 \pm 0.23	2.11 \pm 0.08	2.11 \pm 0.08	2.07 \pm 0.09
	Glx/Tau	3.05 \pm 0.23	3.71 \pm 0.34	3.02 \pm 0.12	2.84 \pm 0.11	2.86 \pm 0.15
	GABA/Tau	0.59 \pm 0.04	0.68 \pm 0.07	0.55 \pm 0.03	0.56 \pm 0.03	0.51 \pm 0.03
	Glu/Gln	2.57 \pm 0.06	2.40 \pm 0.13	2.35 \pm 0.05	2.89 \pm 0.05	2.41 \pm 0.13
1 Hz	Gln/Tau	0.94 \pm 0.06	0.86 \pm 0.05	0.81 \pm 0.04	0.78 \pm 0.02	0.81 \pm 0.05
	Glu/Tau	2.18 \pm 0.16	1.96 \pm 0.10	2.00 \pm 0.05	1.80 \pm 0.07	2.07 \pm 0.09
	Glx/Tau	3.12 \pm 0.22	2.80 \pm 0.14	2.82 \pm 0.08	2.58 \pm 0.08	2.89 \pm 0.12
	Glu/Gln	2.33 \pm 0.07	2.34 \pm 0.10	2.50 \pm 0.10	2.32 \pm 0.11	2.59 \pm 0.14

Supplementary Table 5.5. Raw concentration values of neurometabolites with reference to unsuppressed water signal (I.U.) at different timepoints for the 10 Hz and 1 Hz groups. The five imaging timepoints were: at baseline, after seven (SD7) and 14 days (SD14) of daily stimulation, seven days after stimulation cessation (PSD7) and either 20 days (10 Hz group) or 14 days (1 Hz group) after stimulation cessation (PSD20 or PSD14 respectively). Note that these concentrations have not been corrected for T1 or T2 relaxation, field inhomogeneities, or tissue composition and should not be directly compared with concentrations from other studies. Raw data for other metabolites is available from the corresponding author upon request.

		10 Hz					1 Hz				
Animal	Timepoint	Gln	Glu	Glx	GABA	Tau	Gln	Glu	Glx	GABA	Tau
A1	Baseline	2.818	7.292	10.11	1.614	3.503	4.013	8.775	12.788	2.69	4.298

	SD7	2.669	6.667	9.336	1.542	3.953	4.505	8.556	13.061	2.341	3.94
	SD14	3.158	8.036	11.194	2.006	4.735	3.445	8.633	12.078	2.481	4.023
	PSD7	3.062	6.372	9.435	1.607	3.968	2.975	6.012	8.987	1.253	3.736
	PSD20/PSD14	2.939	7.145	10.084	1.667	4.737	3.105	7.827	10.932	2.034	3.836
A2	Baseline	2.577	6.081	8.659	1.423	3.348	3.934	8.159	12.093	2.619	4.771
	SD7	3.61	7.346	10.956	1.902	2.909	3.919	8.418	12.337	2.104	4.762
	SD14	3.093	7.313	10.406	1.929	3.663	3.226	8.167	11.393	2.003	4.437
	PSD7	2.889	8.722	11.611	2.432	4.303	3.86	7.331	11.191	2.024	4.793
	PSD20/PSD14	3.038	7.605	10.643	1.8	4.656	3.672	7.468	11.14	2.167	4.278
A3	Baseline	2.824	7.014	9.838	1.746	2.086	2.998	6.929	9.927	1.491	2.904
	SD7	3.673	6.742	10.416	1.8	2.498	3.48	8.593	12.073	2.426	3.207
	SD14	3.783	8.75	12.533	2.477	2.379	3.323	8.149	11.472	2.667	4.132
	PSD7	3.241	8.97	12.211	2.338	3.543	3.183	7.997	11.18	1.97	4.074
	PSD20/PSD14	2.798	6.808	9.606	1.797	2.987	2.384	7.651	10.036	1.788	3.817
A4	Baseline	3.195	7.315	10.51	1.828	3.476	2.697	6.464	9.162	1.587	2.115
	SD7	3.013	7.555	10.567	2.23	2.108	3.415	9.178	12.592	2.084	3.725
	SD14	3.002	6.74	9.742	1.922	3.051	3.603	7.918	11.521	2.397	3.821
	PSD7	3.18	8.701	11.881	2.755	3.866	2.863	6.05	8.913	1.245	2.981
	PSD20/PSD14	3.493	7.628	11.121	2.052	3.655	2.885	8.081	10.966	2.238	3.272
A5	Baseline	2.794	7.451	10.245	1.965	3.748	3.502	7.665	11.168	1.696	4.033
	SD7	2.936	6.379	9.316	2.299	3.376	3.079	8.251	11.331	2.393	4.629
	SD14	2.647	6.65	9.297	1.647	2.798	3.211	8.224	11.435	2.206	3.63
	PSD7	2.84	7.852	10.691	1.935	3.742	3.294	7.703	10.996	1.717	3.395
	PSD20/PSD14	3.105	5.7	8.805	1.469	3.221	3.149	8.309	11.458	1.865	4.156
A6	Baseline	2.92	7.878	10.798	2.284	3.203	3.497	8.689	12.186	2.316	4.225
	SD7	2.016	6.496	8.512	1.376	3.145	3.608	7.57	11.179	2.056	4.21
	SD14	3.486	7.304	10.79	1.531	1.268	3.369	9.513	12.883	2.801	4.496
	PSD7	2.681	8.43	11.111	1.895	4.02	3.013	7.155	10.168	2.096	3.593
	PSD20/PSD14	3.298	8.453	11.752	1.838	3.848	3.121	7.33	10.451	2.168	4.19
A7	Baseline	2.497	7.038	9.535	2.297	3.566	2.878	6.194	9.072	1.972	3.828
	SD7	3.016	7.292	10.308	1.88	1.966	2.855	6.624	9.48	1.669	4.144
	SD14	2.65	6.176	8.826	1.26	2.772	2.575	7.832	10.407	2.103	4.46
	PSD7	2.706	8.021	10.726	2.203	4.126	2.874	7.771	10.645	2.06	4.481
	PSD20/PSD14	2.365	7.683	10.048	2.074	3.631	2.365	7.683	10.048	2.074	3.631
A8	Baseline	2.761	7.512	10.273	2.335	4.114	3.083	8.474	11.558	2.052	4.198
	SD7	2.46	6.161	8.622	1.393	2.14	3.181	7.805	10.986	1.906	3.926

	SD14	2.962	6.305	9.266	2.011	2.973	2.983	6.889	9.872	1.813	3.511
	PSD7	3.101	8.734	11.835	2.559	4.851	3.519	8.217	11.735	2.086	4.274
	PSD20/PSD14	3.701	7.919	11.62	2.175	3.912	3.701	7.919	11.62	2.175	3.912
A9	Baseline	2.918	7.382	10.299	2.012	3.526	3.116	7.485	10.601	1.869	2.637
	SD7	2.841	6.828	9.669	1.682	2.893	3.129	7.622	10.752	1.842	3.653
	SD14	3.272	7.699	10.971	2.006	3.544	3.639	7.425	11.065	1.319	3.91
	PSD7	2.99	8.61	11.6	2.068	4.031	3.216	7.784	11	2.497	4.15
	PSD20/PSD14	3.558	8.512	12.07	2.023	3.387	3.558	8.512	12.07	2.023	3.387

Chapter 6

Depression model: Validation of chronic restraint stress model of depression in rats using multimodal MRI

Published as: Seewoo, B.J., Hennessy, L.A., Feindel, K.W., Etherington, S.J., Croarkin, P.E. & Rodger, J., 2020. Validation of chronic restraint stress model in young adult rats for the study of depression using longitudinal multimodal MR imaging. *eneuro*. 7. doi: 10.1523/eneuro.0113-20.2020 (Appendix G)

Chapters 4 and 5 have shown that LI-rTMS has frequency-specific effects on the brain activity and chemistry of healthy rats. Given that rTMS is an FDA-approved treatment for depression, as a next step, we wanted to investigate the effects of LI-rTMS on an animal model of depression. Depression is a debilitating neuropsychiatric disorder with significant morbidity and mortality due to the risk of suicide. Antidepressants are typically a first line treatment for depression. However, up to one third of adults have treatment-resistant depression (TRD) that does not respond to pharmacotherapy. rTMS has been used clinically for TRD for over a decade. However, the mechanisms underlying the therapeutic effects of rTMS remain poorly understood. Additionally, depression is a complex condition and it is now widely accepted that besides changes in behaviour, depression in humans also involves disruptions in intrinsic functional connectivity of the brain, measured by resting-state functional MRI (rs-fMRI), neurometabolite levels, measured by proton magnetic resonance spectroscopy (MRS), and hippocampal volumes, measured by anatomical MRI. Animal models are an indispensable tool for studying aetiology, progress and treatment of depression. However, despite considerable prior efforts, there is ongoing controversy regarding the validity of extant rodent models of depression.

Chronic restraint stress (CRS) depression model in rats has been shown to elicit behavioural, gene expression, protein, functional connectivity and hippocampal volume changes similar to those in human depression. However, no study to date has examined the association between behavioural changes and brain changes within the same animals. Prior to testing the effects of LI-rTMS on this model, it was important to address this knowledge gap. This chapter specifically addresses the correlation between the outcomes of behavioural tests and multiple 9.4 T MRI modalities in the CRS model using data collected longitudinally in the same animals.

CRS involved placing young adult male Sprague Dawley rats in individual transparent tubes for 2.5 h daily over 13 days. Elevated plus-maze and forced swim tests confirmed the presence of anxiety-like and depression-like behaviours respectively post-restraint. Resting-state functional MRI data revealed hypoconnectivity within the salience and interoceptive networks and hyperconnectivity of several brain regions to the cingulate cortex. Proton magnetic resonance spectroscopy revealed decreased sensorimotor cortical glutamate, glutamine and combined glutamate-glutamine levels. Volumetric analysis of T2-weighted images revealed decreased hippocampal volume. Importantly, these changes parallel those found in human depression, suggesting that the CRS rodent model has utility for translational studies and novel intervention development for depression. The present study is the first to correlate multimodal MRI measures with changes in behaviour and hence, provides insight into the neurobiological changes that may underpin patient symptoms. Present findings reinforce the usefulness of the CRS model for translational studies, intervention development, and multimodal molecular and imaging studies.

6.1. Introduction

Major depressive disorder is a debilitating neuropsychiatric disease with significant morbidity and mortality. The diagnosis of depression in humans is based on persistent negative mood, clinical symptoms, and behavioural changes. However, diagnosing depression based solely on clinical features leads to suboptimal outcomes in research studies and clinical practice. Considerable effort has been focused on addressing the biological heterogeneity of depression with biomarkers, including the use of magnetic resonance imaging (MRI) techniques. For example, the cingulate cortex, a critical node of the default mode network (DMN), is one of the most extensively investigated brain regions in the context of mood disorders in MRI studies because of its role in the modulation of emotional behaviour (Drevets et al., 2008; Davey et al., 2012; Rolls et al., 2018). Resting-state functional MRI (rs-fMRI) studies of depression demonstrate functional connectivity changes in the DMN, along with other resting-state networks (RSNs) such as the salience network and the interoceptive network which are involved in processing emotions and sensory stimuli and regulating the internal state (Paulus and Stein, 2010; Mulders et al., 2015). These alterations in functional connectivity within RSNs are associated with neurometabolite (e.g., glutamine, Gln; glutamate, Glu; γ -aminobutyric acid, GABA) imbalances in depression, measured non-invasively using proton magnetic resonance spectroscopy (^1H -MRS) (Lener et al., 2017). Additionally, human MRI studies reproducibly detect reduced hippocampal volumes in patients with depression compared to age-matched healthy controls (Videbech and Ravnkilde, 2004).

Although significant progress has been made in understanding the mechanisms underpinning major depressive disorder, the causality of neuroimaging findings is difficult to infer. For example, the state vs trait nature of human imaging findings are often uncertain and difficult to study (e.g., Sheline, 2011; Brown et al., 2014). In contrast, temporal relationships between biological findings and depression-like behaviours can be studied in animal models. Moreover, MRI-based techniques can be used to investigate the same biological changes in humans and animals, allowing direct comparison of validated outcome measures. Furthermore, combining repeated behavioural and MRI measures within the same animals allows the exploration of correlation between those measures. Therefore, animal models are an indispensable tool for studying aetiology, progress and treatment of depression.

Chronic restraint stress (CRS) in Sprague Dawley rats has been shown to elicit behavioural, gene expression, protein, brain functional connectivity, and hippocampal volume changes similar to those in patients with depression. However, no study to date has examined the association between multimodal MRI measures and behavioural changes within the same animals in the CRS model of depression (Lee et al., 2009; Henckens et al., 2015; Wang et al., 2017b). This model involves restraining animals' movements for at least two hours a day for several days (Wang et al., 2017b); the continuous and predictable stress is designed to mimic everyday human stress, such as daily repetition of a stressful job and familial stresses. Our study aimed to bring previous MRI findings in CRS animals together and investigate the relationship between neurobiological and behavioural changes in the CRS rat model by performing

multimodal MRI (rs-fMRI, ¹H-MRS, and structural MRI) and behavioural tests on the same young adult male rats before and after induction of the model.

6.2. Materials and Methods

6.2.1. Ethics statement

Experimental procedures were approved by the UWA Animal Ethics Committee (RA/3/100/1640) and conducted in accordance with the National Health and Medical Research Council Australian code for the care and use of animals for scientific purposes. All investigators were trained in animal handling by the UWA Programme in Animal Welfare, Ethics, and Science (PAWES) and had valid Permission to Use Animals (PUA) licenses.

6.2.2. Animals

Young adult male Sprague Dawley rats (n = 33; 150-200 g; 6-7 weeks old) from the local Animal Resources Centre were housed in pairs under temperature-controlled conditions on a 12-hour light-dark cycle. Food and water were freely provided, except during the chronic restraint stress (CRS) procedure and fasting before the sucrose preference test. All rats acclimatized to their new environment for one week following their arrival. Behavioural tests and MRI scans were carried out at baseline and after the final restraint procedure. A control group of (n = 8) animals underwent all procedures except CRS.

6.2.3. Chronic restraint stress procedure

The CRS procedure was carried out on a bench located on the opposite side of the large animal holding room facing the wall. Each session was carried out between 12:30 and 15:30 in an effort to avoid effects associated with the circadian rhythm. In brief,

rats were weighed and placed in a transparent tube (size of the tube depending on the weight of the animal, see Table 6.1) for 2.5 h a day for 13 consecutive days as performed on Sprague Dawley rats in previous studies (Bravo et al., 2009; Ulloa et al., 2010; Stepanichev et al., 2014). The length of each restraint was adjusted to limit limb movements using tail gates. Following CRS, rats were returned to their home cages. Healthy control animals were not restrained and remained in their home cages.

Table 6.1. Weight of animals and size of restraints.

Body weight of animal (g)	Diameter of restraint (cm)	Maximum length of restraint (cm)
< 255	5	19
255-300	5	23
> 300	6	21

6.2.4. Behavioural tests

Elevated plus-maze (EPM) and forced swim tests (FST) were used to confirm increased anxiety-related behaviours and learned-helplessness induced by the CRS paradigm in rats as previously described in several preclinical studies (Suvrathan et al., 2010; Ulloa et al., 2010; Chiba et al., 2012; Bogdanova et al., 2013). Behavioural tests were carried out over a period of 3 days (Figure 6.1). On the first day, the animals were subjected to EPM test (Walf and Frye, 2007). After EPM, the animals were habituated to single housing and 1% sucrose solution as described below and deprived of food and water overnight. The next day, the sucrose preference test (SPT) (Willner et al., 1987) was carried out and on the third day, the animals underwent the FST (Slattery and Cryan, 2012). All behavioural testing occurred between 08:30 and 11:00. The full behavioural dataset can be obtained from the corresponding author upon request.



Figure 6.1. Experimental timeline. The experiment consisted of an initial one-week period of habituation upon arrival of the animals, after which the rats underwent elevated plus-maze (EPM) test (Day 1). Following EPM, animals were habituated to single housing and sucrose solution for 8 h and deprived of food and water overnight (Day 1-2). Sucrose preference test (SPT) was carried out the next day (Day 2), followed by a pre-swim test. Forced swim test (FST) was carried out on Day 3 and MRI on Day 4. The animals then underwent chronic restraint stress for 2.5 h daily for 13 consecutive days. The day after the end of CRS, animals underwent behavioural tests (Day 18-20) and MRI (Day 21) in the same order without a pre-swim test.

6.2.4.1. Elevated plus maze

EPM was carried out as detailed in Walf and Frye (2007). The apparatus consisted of two open arms (without walls or railing) and two closed arms, crossed in the middle perpendicularly to each other, and a centre area (10 cm x 10 cm). Each arm was 50 cm long and 10 cm wide and the enclosed arms had 40 cm high walls. Each arm of the maze was attached to sturdy legs, such that it was elevated 60 cm off the floor. The maze was placed in a way to ensure similar levels of illumination on both open and closed arms. One animal was tested at a time and after each trial, all arms and the centre area were wiped with 70% ethanol to remove olfactory cues. The animal was placed in the centre of the maze facing the same open arm, away from the experimenter. The animal was allowed to move freely in the maze for 5 min and the whole procedure was video recorded from approximately 120 cm above the platform using a GoPro HERO7. The experimenters stayed in the room during the procedure, but unnecessary movements and noise were minimised.

EPM data was analysed manually by researchers blinded to experimental group and timepoint. The number of entries and time spent in closed and open arms were measured. Additionally, the number and duration of rearing and grooming were also measured to investigate anxiety-related behaviours (Walf and Frye, 2007). The number of entries and time spent in the centre of the maze and behaviours such as head shaking, head dips and stretching were not considered. One animal fell off the open arm during baseline testing and was re-placed onto the maze to continue the whole 5 min testing but the data was excluded from the analyses (Walf and Frye, 2007).

6.2.4.2. Sucrose preference test

Immediately following EPM, animals were habituated to single housing and to sucrose solution (Figure 6.1). Animals were placed in individual cages with *ad libitum* access to food pellets and two 600 ml bottles, one bottle containing fresh 1% sucrose solution (D-(+)-Sucrose, AnalaR NORMAPUR® analytical reagent, VWR International BVBA, Leuven, Belgium) and the other containing tap water. The animals were trained to this condition for 8 h. Rats were given a free choice between the two bottles and the position of the bottles was switched 4 h after the start of single housing to prevent side preference in drinking behaviour. Overnight food and water deprivation was applied at the end of the 8 h habituation for up to 16 h.

The next day, SPT was performed according to a previous study with some modifications (Willner et al., 1987). Water and sucrose solution bottles were weighed, labelled and placed in corresponding cages. The position of the bottles was switched 30 min after the start of the SPT. 30 min later, the bottles were removed and re-weighed, and the animals were re-housed in their original cages. Sucrose preference

was calculated as a percentage of the total amount of liquid ingested (sucrose preference = sucrose consumption (g) / [sucrose consumption (g) + water consumption (g)]).

6.2.4.3. Forced swim test

FST was carried out as detailed in Slattery and Cryan (2012). Briefly, 20 L white opaque plastic buckets (41 cm high, 28 cm wide) were filled up to a depth of 30 cm with water at 23-25 °C. At this depth, the rats could not touch the bottom of the bucket with their tails or hind limbs. Up to four buckets were used at a time and the buckets were emptied, cleaned and refilled between animals. At baseline, 24 h before the FST session (on SPT day), rats were exposed to a pre-swim test for 10 min by placing them in the water-filled buckets (Slattery and Cryan, 2012). The next day, and at the end of the restraint period rats underwent 6 min of FST (Figure 6.1) and the procedure was video recorded from approximately 50 cm above the buckets using a GoPro HERO7.

FST data was analysed manually by researchers blinded to experimental group and timepoint using a time-sampling technique (Slattery and Cryan, 2012). The first 5 min of the video recording was split into 5-s intervals and the predominant behaviour in each 5-s period was rated. The following escape behaviours were scored: 1) swimming, with horizontal movements throughout the bucket including crossing into another quadrant and diving; 2) climbing, with upward movements of the forepaws along the side of bucket; 3) immobility, with minimal movements necessary to keep their head above water; and 4) latency, defined as the time taken to exhibit the first immobility behaviour. Grooming, head shaking and number of fecal boli were not considered. Trials during which the animals managed to escape more than once or were floating

horizontally for the duration of the test (with most of their body being completely dry at the end) were excluded from the analyses.

6.2.5. MRI data acquisition

6.2.5.1. Animal preparation

MRI data was acquired the day after the FST. Due to the well-documented effect of anaesthesia on RSNs, a combined medetomidine-isoflurane anaesthetic protocol was chosen because it produces similar RSN connectivity as in the awake condition (Paasonen et al., 2018), maintains strong inter-cortical and cortical-subcortical connectivity (Grandjean et al., 2014; Bukhari et al., 2017a) and provides stable sedation for over four hours and reproducible data from repeated fMRI experiments on the same animal one week apart (Lu et al., 2012). The rat was pre-anaesthetised using isoflurane (Isothesia™, Henry Schein Animal Health, QLD, Australia) in an induction chamber (4% isoflurane in medical air, 2 L/min). Once fully anaesthetised, the animal was transferred to a heated imaging cradle and anaesthesia was maintained with a nose cone (2% isoflurane in medical air, 1 L/min). Body temperature and respiratory rate were monitored using a PC-SAM Small Animal Monitor (SA Instruments Inc., 1030 System). An MR-compatible computer feedback heating blanket was used for maintaining animal body temperature at 37°C (± 0.5°C). A 25G butterfly catheter (SV*25BLK, Terumo Australia Pty Ltd, Macquarie Park, NSW, Australia) was implanted subcutaneously in the left flank of the animal to deliver a 0.05-0.1 mg/kg bolus injection and continuous infusion of medetomidine (1 mg/mL, Ilium Medetomidine Injection, Troy Laboratories Pty. Limited, NSW, Australia) at 0.15 mg/kg/h using a single syringe infusion pump (Legato 100 Syringe Pump, KD Scientific Inc., Holliston, USA). Once the animal's breathing rate dropped to 50 breaths/min,

isoflurane was gradually reduced to 0.5-0.75%. These anaesthetic doses were empirically determined to ensure the respiratory rate of the animals was between 50-80 breaths/min. rs-fMRI scans were started only after the isoflurane concentration had been reduced for at least 15 min and the physiology of the animal was stable during that time. After the MRI procedure, medetomidine was antagonized by an injection of 0.1 mg/kg atipamezole (5.0 mg/mL, Ilium Atipamezole Injection, Troy Laboratories Pty. Limited, NSW, Australia) using a 29G insulin syringe (BD Ultra-Fine Insulin Syringe, Becton Dickinson Pty Ltd, Macquarie University Research Park North Ryde, NSW, Australia).

6.2.5.2. MRI acquisition parameters

All MR images were acquired with a Bruker Biospec 94/30 small animal MRI system operating at 9.4 T (400 MHz, H-1), with an Avance III HD console, BGA-12SHP imaging gradients, a 72 mm (inner diameter) volume transmit coil and a rat brain surface quadrature receive coil using the imaging protocol as detailed in Seewoo et al. (2018b, 2019c). The acquisition protocol included the following sequences: 1) multi-slice 2D RARE (rapid acquisition with relaxation enhancement) sequence for three T2-weighted anatomical scans (TR = 2500 ms, TE = 33 ms, matrix = 280 x 280, pixel size = 0.1 x 0.1 mm², 21 coronal and axial slices, 20 sagittal slices, thickness = 1 mm); 2) single-shot gradient-echo echoplanar imaging (TR = 1500 ms, TE = 11 ms, matrix = 94 x 70, pixel size = 0.3 x 0.3 mm², 21 coronal slices, thickness = 1 mm, flip angle = 90°, 300 volumes, automatic ghost correction order = 1, receiver bandwidth = 300 kHz) for resting-state; and 3) point-resolved spectroscopy (PRESS) sequence with one 90° and two 180° pulses and water suppression for ¹H-MRS (TE = 16 ms, TR = 2500 ms) with 64 averages with a 3.5 x 2 x 6 mm³ voxel placed over the left sensorimotor cortex (Figure 6.2). The

sensorimotor cortex was chosen because: 1) it is a key brain region involved in psychomotor retardation ((Zarrinpar et al., 2006; Pineda, 2008), an important but poorly understood clinical feature of depression (Buyukdura et al., 2011; Ilamkar, 2014); 2) brain stimulation has been reported to decrease the severity of psychomotor retardation in patients with depression (Buyukdura et al., 2011) and increase Glu and Gln levels in the sensorimotor cortex of healthy Sprague Dawley rats (Seewoo et al., 2019c); 3) rostral regions such as the sensorimotor cortex have higher SNR when using a surface coil (Xu et al., 2013b); and 4) larger voxel sizes can be used without white matter contamination, leading to higher SNR and greater reliability and reproducibility of measured metabolite concentrations. ^1H -MRS data was acquired from the left cortex only in order to facilitate comparisons with human depression studies, which mostly examine neurometabolite changes in the left hemisphere (Moriguchi et al., 2019).

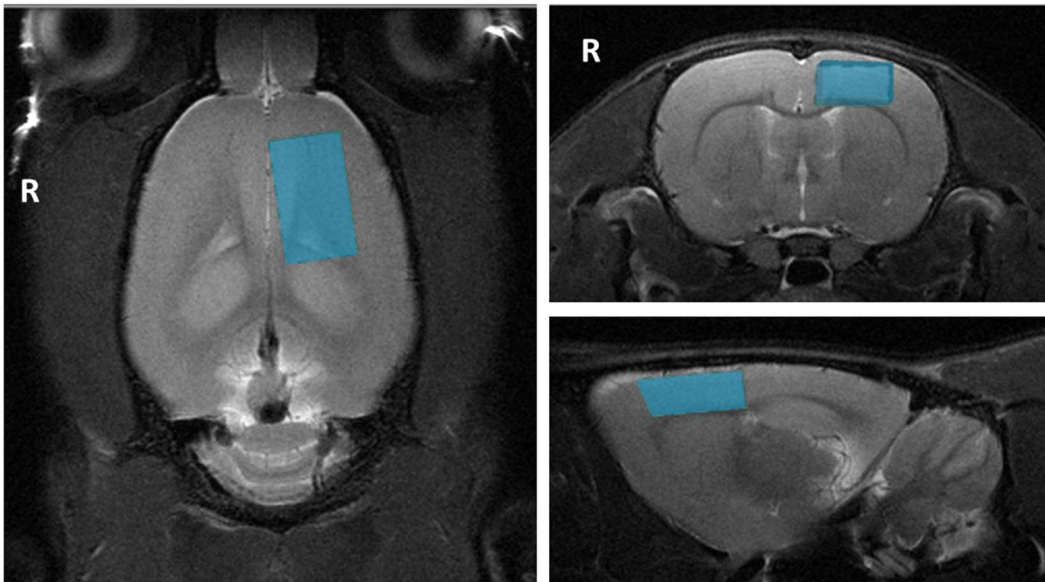


Figure 6.2. Voxel position for proton magnetic resonance spectroscopy. The figure shows the position of the voxel of interest (size of 3.5 mm × 2 mm × 6 mm) on the left sensorimotor cortex on T2-weighted images for proton magnetic resonance spectroscopy. R denotes right hemisphere.

6.2.6. Analysis steps

6.2.6.1. Behavioural data

EPM and FST videos were scored blind by two trained observers to establish the most reliable measures. Based on their low inter-individual scorer variability (< 12%), exploration (into and within closed and open arms separately), grooming and rearing for EPM, and swimming and climbing (separately and combined as “total activity”), immobility, and latency to first immobility behaviour for FST were selected for statistical analysis. Sucrose preference (%) was calculated as sucrose consumption (g)/[sucrose consumption (g) + water consumption (g)].

6.2.6.2. Rs-fMRI data

To maximise the use of collected data, rs-fMRI data and T2-weighted images collected using the same acquisition and anaesthesia protocols from a previous study (Seewoo et al., 2019c) in adult (6–8 weeks old, 150–250 g) male Sprague Dawley rats were also included in the analyses for the baseline timepoint (Table 6.2). These animals did not undergo any behavioural testing or intervention before the acquisition of MRI data. All rs-fMRI data was pre-processed and analysed in the same way. Pre-processing of data included: 1) export into DICOM format from ParaVision 6.0.1 (Bidgood Jr et al., 1997); 2) conversion into NifTI using the dcm2nii converter (64-bit Linux version 5 May 2016) (Rorden et al., 2007); 3) reorienting the brain into left-anterior-superior (LAS) axes (radiological view); and 4) skull-stripping using the qimask utility from QUIT (QUantitative Imaging Tools) (Wood, 2018). The voxel sizes were then upscaled by a factor of 10 (Tambalo et al., 2015).

All further pre-processing and analyses were performed using FSL v5.0.10 (Functional MRI of the Brain (FMRIB) Software Library) (Jenkinson et al., 2012) using the methods

described in Seewoo et al. (2021a). Single-session independent component analysis (ICA) as implemented in FSL/MELODIC (Multivariate Exploratory Linear Decomposition into Independent Components) (Beckmann et al., 2005) was used to de-noise the data (detailed in Seewoo et al., 2018b). The de-noised rs-fMRI images were then co-registered to their respective T2-weighted coronal images using six-parameter rigid body registration using FSL/FLIRT (Linear Image Registration Tool) (Jenkinson and Smith, 2001; Jenkinson et al., 2002) and normalised to a Sprague-Dawley brain atlas (Papp et al., 2014; Kjonigsen et al., 2015; Sergejeva et al., 2015) with nine degrees of freedom ‘traditional’ registration. The atlas was first down-sampled by a factor of eight to better match the voxel size of the 4D functional data. All subsequent analyses were conducted in the atlas standard space.

Multi-subject temporal concatenation group-ICA and FSL dual regression analysis were used to determine group differences (baseline, $n = 33$; restraint, $n = 15$), controlling for family-wise error (FWE) and using a threshold-free cluster enhanced (TFCE) technique to control for multiple comparisons. The resulting statistical maps were thresholded to $p < 0.05$.

To investigate the correlation between strong depression-like behaviours on functional connectivity, dual regression was also carried out using a subset of animals in the restraint group. FST measures (immobility, swimming and climbing scores and latency time) were extracted for the 15 animals scanned following restraint and sorted in order of greatest change in each FST measure. Animals were scored according to their position on the list (1 to 15). Nine of 15 animals had consistently high scores and were

used in the analysis as they exhibited the greatest change in overall behavioural outcomes in FST.

For seed-based analysis, the atlas mask for the cingulate cortex was transformed to each individual animal's functional space. The region of interest (ROI) masks (within the individual functional space) were used to extract the timecourse from the ICA de-noised data. The timecourses were used in a first-level FSL/FEAT (FMRI Expert Analysis Tool Version 6.00) analysis to generate a whole-brain correlation map. Higher-level analysis was carried out using OLS (ordinary least squares) simple mixed-effects (Beckmann et al., 2003; Woolrich et al., 2004; Woolrich, 2008) in atlas space (baseline, $n = 33$; restraint, $n = 15$). Z (Gaussianised T/F) statistic images were thresholded non-parametrically using clusters determined by $z > 2$ and a (corrected) cluster significance threshold of $p = 0.05$ (Worsley, 2001a).

6.2.6.3. ^1H -MRS

^1H -MRS data were analysed in LCModel ("Linear Combination of Model spectra" version 6.3-1L) (Provencher, 2001) using a set of simulated basis set provided by the software vendor. For data quality control, the linewidth (full width at half-maximum, FWHM) for each scan was calculated for the N-acetylaspartate+N-acetyl-aspartyl-glutamate (NAA + NAAG) resonance at 2.01 ppm and the intensity of this resonance relative to the residual intensity was obtained (signal-to-noise ratio, SNR). Mean (\pm SE) FWHM and SNR were 10.6 (\pm 0.4) Hz and 12.1 (\pm 0.4) respectively for the baseline group ($n = 17$), and 14.6 (\pm 0.8) Hz and 9.8 (\pm 0.3) respectively for the restraint group ($n = 17$). Individual metabolite concentrations were computed using the unsuppressed reference water signal for each individual scan. Cramér-Rao lower bound (CRLB) values

were calculated by LCModel and reported as percentage standard deviation of each metabolite, as a measure of the reliability of the metabolite estimates.

The metabolites of interest were GABA (baseline CRLB: $12.7\% \pm 0.4$, restraint CRLB: $14.5\% \pm 0.6$) and Glu (baseline CRLB: $3.4\% \pm 0.1$, restraint CRLB: $3.9\% \pm 0.1$), the major neurotransmitters in the brain, as well as Gln (baseline CRLB: $9.7\% \pm 0.5$, restraint CRLB: $11.4\% \pm 0.3$), a neurotransmitter precursor, and combined glutamate-glutamine (Glx; baseline CRLB: $3.6\% \pm 0.1$, restraint CRLB: $4.2\% \pm 0.1$). To accurately extract the dominating metabolic changes observed before and after CRS, and to reduce systemic variations among studied animals, a relative quantification method, using an internal spectral reference was used. All ^1H -MRS results presented here are expressed as a ratio to tCr (total creatine = Cr + PCr; baseline CRLB: $2.94\% \pm 0.06$, restraint CRLB: $3.12\% \pm 0.08$) spectral intensity, the simultaneously acquired internal reference peak (Block et al., 2009; Walter et al., 2009; Xu et al., 2013a).

6.2.6.4. Hippocampal volume

The three T2-weighted anatomical (coronal, sagittal and axial) data were pre-processed as above and then registered to the high-resolution atlas (no downsampling). Atlas masks for bilateral hippocampus and whole-brain were used to automatically extract their respective volumes from the three T2-weighted anatomical images (coronal, sagittal and axial). Hippocampal and whole-brain volumes from the three planes were averaged for each animal scan session. Spearman's rank correlation method ($n = 74$) in RStudio 3.5.2 was used to determine the correlation of whole-brain volumes with the weight of animals at baseline because the volumes of the whole brain and several brain regions are known to increase with age in rats until they are

two months old (Mengler et al., 2014). Hippocampal volume was normalised to the whole-brain volume (% whole brain volume) to adjust for differences in head size (Welniak–Kaminska et al., 2019).

6.2.6.5. Statistical analyses

For estimation based on confidence intervals (CIs), we directly introduced the raw data in <https://www.estimationstats.com/> and downloaded the results and graphs. The paired differences for the comparisons are shown with Cumming estimation plots (Ho et al., 2019). The raw data are plotted on the upper axes. Each mean difference is plotted on the lower axes as a bootstrap sampling distribution and the 95% CIs are indicated by the ends of the vertical error bars. 5000 bootstrap samples were taken; the confidence interval is bias-corrected and accelerated. To measure the effect size, we used unbiased Cohen's d (also known as standardised mean difference). Paired median difference was used to measure the effect size of open arm entries and time spent within the open arms during the EPM test because many animals did not enter the open arms and the data is not normally distributed. The p -values reported are the likelihoods of observing the effect sizes, if the null hypothesis of zero difference is true. For each permutation p -value, 5000 reshuffles of the control and test labels were performed.

All comparisons were paired except for the rs-fMRI data (see explanation in Table 6.2). Statistically significant voxels from the rs-fMRI data analyses were used as a mask to extract the functional connectivity of each individual animal at each timepoint (current cohort only) from the GLM "parameter estimate" images from stage 2 of dual regression and from the contrast of parameter estimates image from first-level FEAT

for seed-based analysis. These values were used to run unpaired estimation statistics as described above. Summary measurements (mean \pm SD) are shown as gapped lines for each group. These functional connectivity measures were also used in the correlation analyses below.

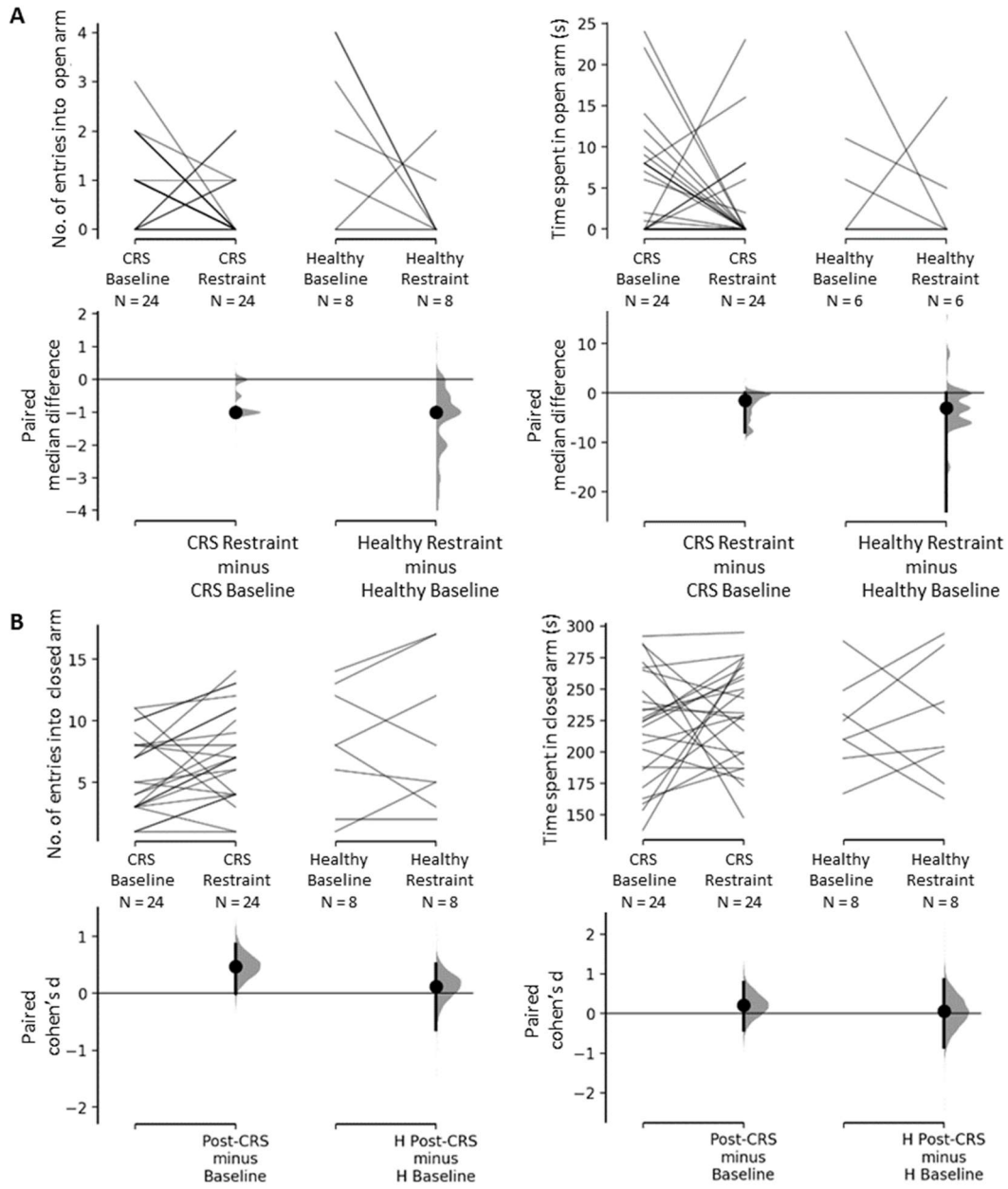
Data from the current cohort of animals which underwent imaging at both timepoints were used to correlate MRI measures to the behavioural measures. Spearman correlations (RStudio 3.5.2) between the following parameters were computed using data from both groups and timepoints: latency to first immobility behaviour from FST data; connectivity (parameter estimates) of the salience network (ICA), interoceptive network (ICA) and cingulate cortex (seed-based) from the rs-fMRI data; Glx ratio from $^1\text{H-MRS}$ data; and hippocampal volume (see Table 6.2). Pearson's correlation method ($n = 23$) in RStudio 3.5.2 was used to determine correlation between baseline percentage hippocampal volume of the CRS group and post-restraint latency to first immobility behaviour during FST.

6.3. Results

6.3.1. Increase in anxiety and depression-like behaviours

In the elevated plus-maze (EPM) test, there was a significant decrease in the number of entries into the open arms of the maze (baseline: 0.88 ± 0.18 , $n = 24$; restraint: 0.32 ± 0.13 , $n = 24$; $\text{Median}_{\text{diff}} = -1.0$, $p = 0.0^{\text{aa}}$) and a significant increase in the number of entries in the closed arms of the maze (baseline: 5.63 ± 0.66 , $n = 24$; restraint: 7.20 ± 0.74 , $n = 24$; Cohen's $d = 0.212$, $p = 0.0282^{\text{ae}}$) following chronic restraint stress (CRS). Note that there is considerable uncertainty about the magnitude of the effect of the restraint procedure on closed arms entries, with the CI stretching down toward

negligible effects (95% CI[-0.0122, 0.856]; Figure 6.3B). There were no significant differences for time spent exploring the open arms or the closed arms (Figure 6.3A-B^{ac,ag}). There was also a significant decrease in the number of times the animals demonstrated grooming behaviours (baseline: 4.63 ± 0.64 , $n = 24$; restraint: 2.28 ± 0.31 , $n = 24$; Cohen's $d = -0.921$, $p = 0.001$ ^{ai}; Figure 6.3C) and the total time spent grooming (baseline: 24.70 ± 3.93 s, $n = 23$; restraint: 14.48 ± 3.30 s, $n = 23$; Cohen's $d = -0.642$, $p = 0.0016$ ^{ak}; Figure 6.3C). However, the number of times rats exhibited rearing behaviours remained similar between the two timepoints, as did total time spent rearing (Figure 6.3D, Table 6.2^{am,ao}). Healthy control animals which did not undergo the CRS procedure did not show any changes in any of the EPM measures between the two timepoints (Figure 6.3; Table 6.2^{aa-ap}).



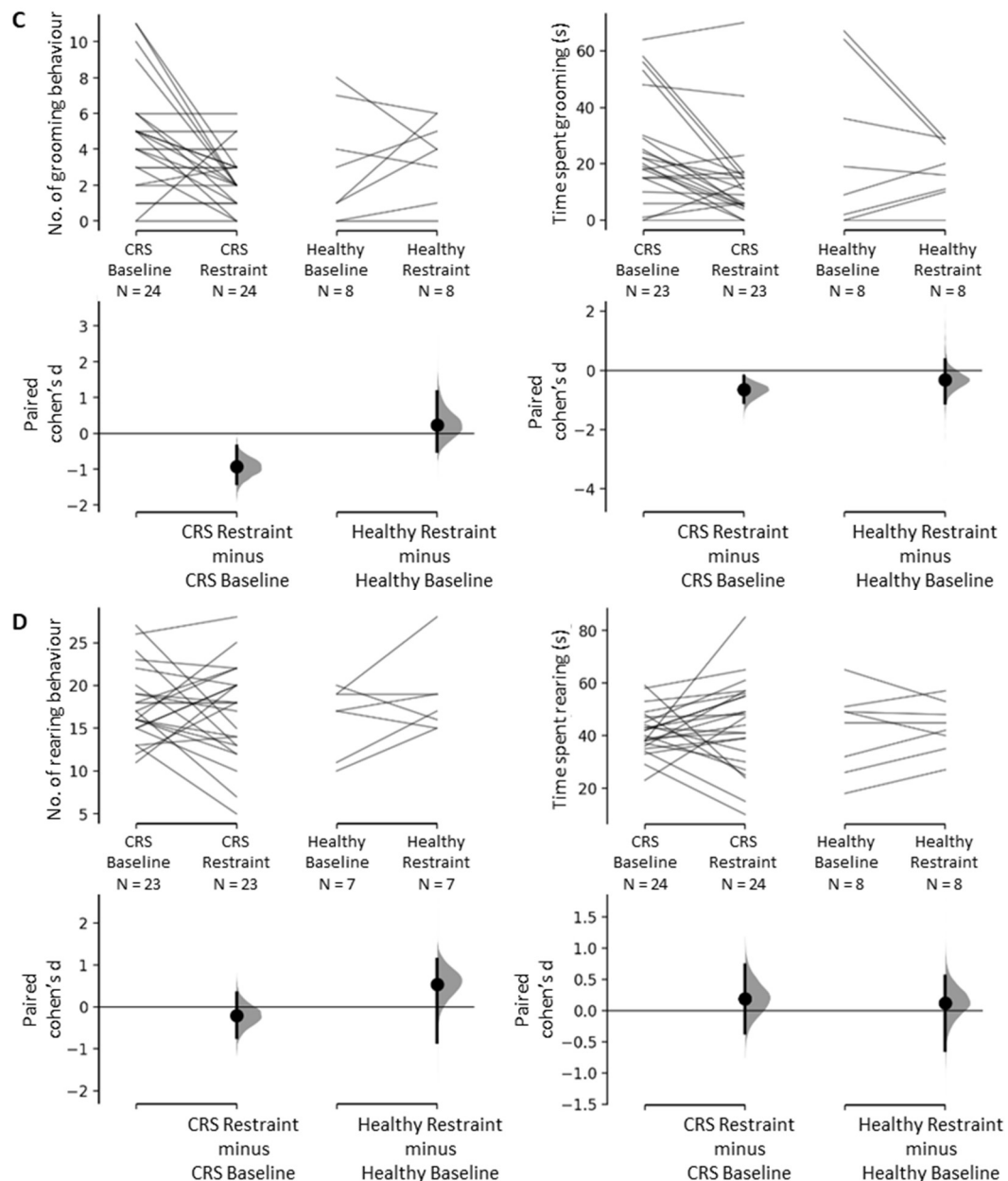


Figure 6.3. Effect of chronic restraint stress on exploration in open (A) and closed (B) arms and on stress-response behaviours (C-D) displayed during elevated plus maze test. Exploration (open and closed arm entries and time spent) and stress-related behaviours (grooming and rearing) were measured for 5 min. A shows total number of entries and time spent in open arms. The paired median differences for 2 comparisons are shown in the Cumming estimation plots. B shows total number of entries and time spent in closed arms, C shows number of grooming behaviours and time spent grooming, and D shows number of rearing behaviours and time spent rearing. The Cohen's d for 2 comparisons are shown in the Cumming estimation plots. The raw data is plotted on the upper axes; each paired set of observations is connected by a line. On the lower axes, each paired difference is plotted as a bootstrap sampling distribution. Mean differences are depicted as dots; 95% confidence intervals are indicated by the ends of the vertical error bars.

There was no average change observed in the sucrose preference test (SPT) data for both animals which underwent 13 days of restraint (baseline: 0.63 ± 0.03 , $n = 25$; restraint: 0.69 ± 0.04 , $n = 25$; 95% CI[-0.294, 0.889]; Cohen's $d = 0.289$; $p = 0.312^{aq}$) and healthy control animals (baseline: 0.81 ± 0.03 , $n = 5$; restraint: 0.78 ± 0.07 , $n = 5$; 95% CI[-1.52, 0.831]; Cohen's $d = -0.191$, $p = 0.807^{ar}$). Note that the confidence intervals are large and therefore, moderate effects in either direction cannot be ruled out.

For the forced swim test (FST), animals in both groups had similar scores for immobility and climbing behaviours at baseline, displaying total active behaviours (climbing plus swimming) for approximately 72% of the time (Figure 6.4A, Table 6.2). After restraint, total activity decreased significantly compared to baseline (baseline: 42 ± 2 , $n = 19$; restraint: 37 ± 1 , $n = 19$; Cohen's $d = -0.62$, $p = 0.0414^{as}$; Figure 6.4A). When scores for both active behaviours were split, the decrease in climbing behaviours following restraint was statistically significant (baseline: 16 ± 2 , $n = 19$; restraint: 11 ± 1 , $n = 19$; Cohen's $d = -0.696$, $p = 0.021^{aw}$), but not for swimming (baseline: 26 ± 2 , $n = 19$; restraint: 26 ± 2 , $n = 19$; Cohen's $d = 0.0269$, $p = 0.896^{au}$; Figure 6.4B). Additionally, immobility increased (baseline: 18 ± 2 , $n = 19$; restraint: 23 ± 1 , $n = 19$; Cohen's $d = 0.611$, $p = 0.0438^{av}$) and latency to first immobility behaviour decreased (baseline: 119 ± 9 s, $n = 19$; restraint: 71 ± 7 s, $n = 19$; Cohen's $d = -1.34$, $p = 0.0006^{ba}$; Figure 6.4C). Healthy control animals which did not undergo the CRS procedure did not show changes in any of the FST measures between the two timepoints (Figure 6.4; Table 6.2^{as-bb}).

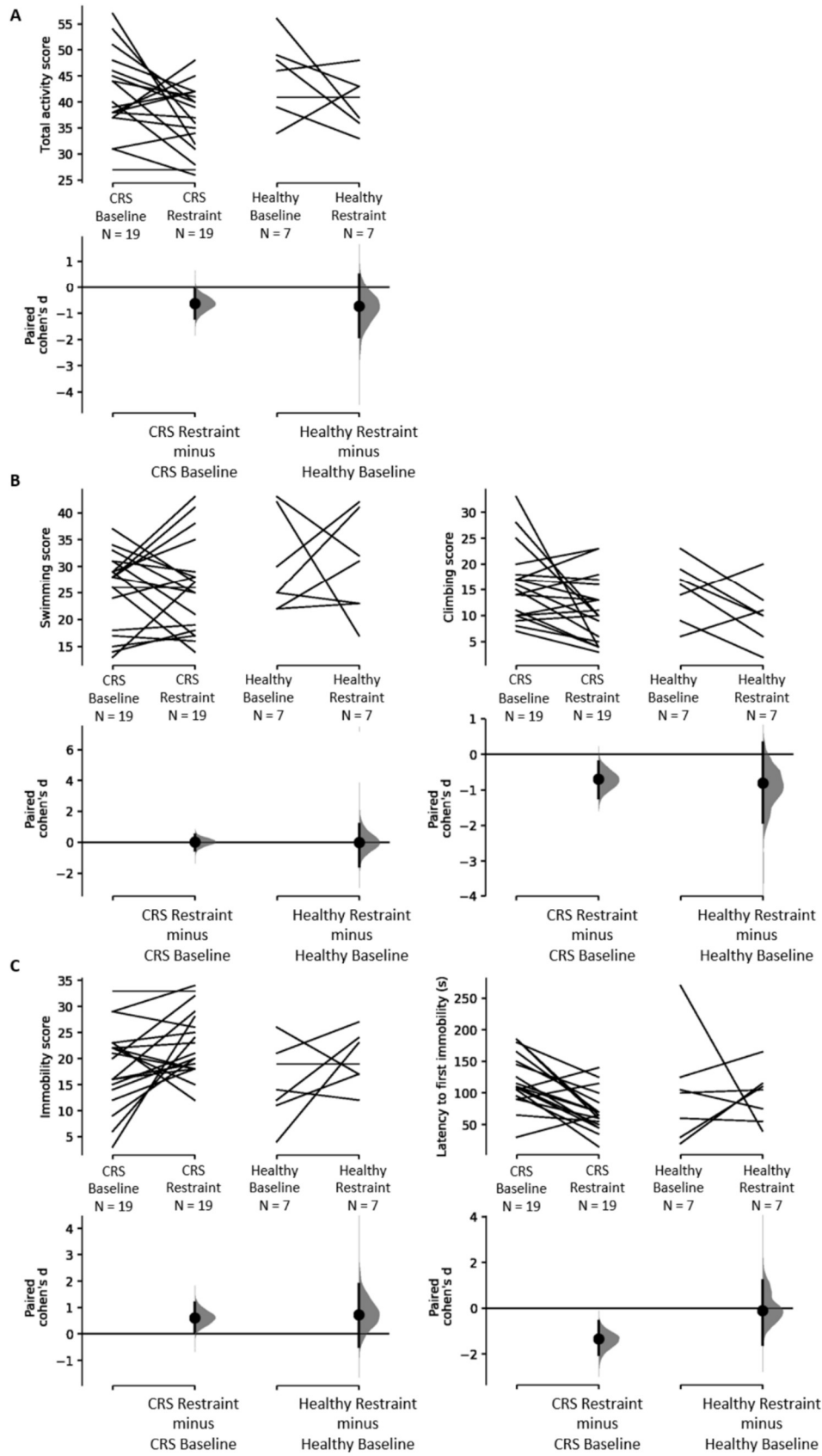


Figure 6.4. Effect of chronic restraint stress on behaviours displayed during forced swim test. Active behaviours (climbing and swimming) and immobility were measured for 5

min. A shows a decrease in active behaviours following 13 days of chronic restraint stress and no change in the healthy control group. B shows no change in swimming scores in both groups and decrease in climbing in the CRS group only. C shows an increase in immobility and a decrease in time to first immobility behaviour (known as latency time) following 13 days of chronic restraint stress and no change in the healthy control group. The Cohen's d for 2 comparisons are shown in the Cumming estimation plots. The raw data is plotted on the upper axes; each paired set of observations is connected by a line. On the lower axes, each paired mean difference is plotted as a bootstrap sampling distribution. Mean differences are depicted as dots; 95% confidence intervals are indicated by the ends of the vertical error bars.

Table 6.2. Statistical table indicating the results of all analyses. Each analysis includes a letter indicator linking the test in the table to the analysis in the text. The link to the corresponding figure, if any, is indicated under "Fig.". The estimation statistics, critical value, degrees of freedom and exact p values are listed for each test under "Statistics" and the confidence intervals of the tests and mean \pm SE are under "Power".

No	Fig	Description*	Statistics	Power
Elevated Plus Maze Test				
aa	3A	Open arm #	CRS group (n = 24/timepoint)	Paired median difference = -1.0 $p = 0.0$ baseline = 0.88 ± 0.18 restraint = 0.32 ± 0.13
ab			Healthy group (n = 8/timepoint)	Paired median difference = -1.0 $p = 0.246$ baseline = 1.75 ± 0.62 restraint = 0.38 ± 0.26
ac	3A	Open arm time	CRS group (n = 24/timepoint)	Paired median difference = -1.5 $p = 0.15$ baseline = 5.79 ± 1.43 s restraint = 2.52 ± 1.15 s
ad			Healthy group (n = 6/timepoint)	Paired median difference = -3.0 $p = 0.38$ baseline = 6.83 ± 3.89 s restraint = 2.63 ± 2.01 s
ae	3B	Closed arm #	CRS group (n = 24/timepoint)	Paired Cohen's $d = 0.462$ $p = 0.0282$ baseline = 5.63 ± 0.66 restraint = 7.20 ± 0.74

af			Healthy group (n = 8/timepoint)	Paired Cohen's $d = 0.114$ $p = 0.639$	-0.647, 0.51 baseline = 8.00 ± 1.72 restraint = 8.63 ± 2.13
ag			CRS group (n = 24/timepoint)	Paired Cohen's $d = 0.212$ $p = 0.47$	-0.415, 0.777 baseline = 220.83 ± 9.06 s restraint = 230.60 ± 7.81 s
ah		Closed arm time	Healthy group (n = 8/timepoint)	Paired Cohen's $d = 0.056$ $p = 0.888$	-0.848, 0.851 baseline = 221.75 ± 12.82 s restraint = 224.13 ± 16.89 s
ai		#	CRS group (n = 24/timepoint)	Paired Cohen's $d = -0.921$ $p = 0.001$	-1.41, -0.357 baseline = 4.63 ± 0.64 restraint = 2.28 ± 0.31
aj			Healthy group (n = 8/timepoint)	Paired Cohen's $d = 0.232$ $p = 0.464$	-0.511, 1.17 baseline = 3.00 ± 1.10 restraint = 3.63 ± 0.78
ak	3C	Grooming time	CRS group (n = 23/timepoint)	Paired Cohen's $d = -0.642$ $p = 0.0016$	-1.09, -0.185 baseline = 24.70 ± 3.93 s restraint = 14.48 ± 3.30 s
al			Healthy group (n = 8/timepoint)	Paired Cohen's $d = -0.326$ $p = 0.411$	-1.11, 0.352 baseline = 24.63 ± 9.89 s restraint = 17.75 ± 3.70 s
am		Rearing #	CRS group (n = 23/timepoint)	Paired Cohen's $d = -0.2$ $p = 0.422$	-0.732, 0.327 baseline = 17.79 ± 0.86 restraint = 16.92 ± 1.14
an	3D		Healthy group (n = 7/timepoint)	Paired Cohen's $d = 0.533$ $p = 0.19$	-0.852, 1.13 baseline = 16.14 ± 1.52 restraint = 17.38 ± 1.82
ao		Rearing time	CRS group (n = 24/timepoint)	Paired Cohen's $d = 0.187$	-0.364, 0.73 baseline = 41.38 ± 1.72 s

				$p = 0.501$	restraint = 44.36 ± 3.36 s
ap			Healthy group (n = 8/timepoint)	Paired Cohen's $d = 0.117$ $p = 0.618$	-0.639, 0.552 baseline = 41.88 ± 5.43 s restraint = 43.38 ± 3.42 s
Sucrose Preference Test					
aq			CRS group (n = 25/timepoint)	Paired Cohen's $d = 0.289$ $p = 0.312$	-0.294, 0.889 baseline = 0.63 ± 0.03 restraint = 0.69 ± 0.04
ar			Healthy group (n = 5/timepoint)	Paired Cohen's $d = -0.191$ $p = 0.807$	-1.52, 0.831 baseline = 0.81 ± 0.03 restraint = 0.78 ± 0.07
Forced Swim Test					
as	4A	Total activity	CRS group (n = 19/timepoint)	Paired Cohen's $d = -0.62$ $p = 0.0414$	-1.19, -0.0902 baseline = 42 ± 2 restraint = 37 ± 1
at			Healthy group (n = 8/timepoint)	Paired Cohen's $d = -0.726$ $p = 0.22$	-1.91, 0.489 baseline = 45 ± 3 restraint = 40 ± 2
au	4B	Swimming	CRS group (n = 19/timepoint)	Paired Cohen's $d = 0.0269$ $p = 0.896$	-0.526, 0.489 baseline = 26 ± 2 restraint = 26 ± 2
av			Healthy group (n = 8/timepoint)	Paired Cohen's $d = 0.0$ $p = 0.969$	-1.54, 1.17 baseline = 30 ± 3 restraint = 30 ± 4
aw		Climbing	CRS group (n = 19/timepoint)	Paired Cohen's $d = -0.696$ $p = 0.021$	-1.22, -0.202 baseline = 16 ± 2 restraint = 11 ± 1
ax			Healthy group (n = 8/timepoint)	Paired Cohen's $d = -0.8$ $p = 0.12$	-1.92, 0.327 baseline = 15 ± 2 restraint = 10 ± 2

ay	4C	Immobility	CRS group (n = 19/timepoint)	Paired Cohen's $d = 0.611$ $p = 0.0438$	0.0902, 1.19 baseline = 18 ± 2 restraint = 23 ± 1
az			Healthy group (n = 8/timepoint)	Paired Cohen's $d = 0.726$ $p = 0.22$	0.0902, 1.19 baseline = 15 ± 3 restraint = 20 ± 2
ba		Latency	CRS group (n = 19/timepoint)	Paired Cohen's $d = -1.34$ $p = 0.0006$	-2.03, -0.578 baseline = 119 ± 9 s restraint = 71 ± 7 s
bb			Healthy group (n = 8/timepoint)	Paired Cohen's $d = -0.0967$ $p = 0.92$	-1.59, 1.21 baseline = 101 ± 32 restraint = 95 ± 16
Resting-state functional MRI					
bc	5A & 5B ICA/dual regression	n	CRS group with all restraint data (baseline: n = 11 from current cohort and n = 22 from Seewoo et al., 2019; restraint: n = 15)	Dual regression $p < 0.05$	
bd			CRS group with restraint data based on FST findings (baseline: n = 11 from current cohort and n = 22 from Seewoo et al., 2019; restraint: n = 9)	Dual regression $p < 0.05$	
be			5C	Saliency network CRS group (baseline: n = 9 from current cohort; restraint: n = 15)	Unpaired Cohen's $d = -2.33$ $p = 0.0$

bf			Saliency network Healthy group (baseline: n = 5 from current cohort; restraint: n = 8)	Unpaired Cohen's $d = -$ 0.208 $p = 0.718$	-1.68, 0.93 baseline = 29 ± 5 restraint = 27 ± 4
bg			Interoceptive network CRS group (baseline: n = 9 from current cohort; restraint: n = 15)	Unpaired Cohen's $d = -$ 1.38 $p = 0.0032$	-2.13, -0.574 baseline = 39 ± 5 restraint = 23 ± 2
bh		5D	Interoceptive network Healthy group (baseline: n = 5 from current cohort; restraint: n = 8)	Unpaired Cohen's $d = -$ 0.539 $p = 0.374$	-1.47, 0.685 baseline = 27 ± 2 restraint = 22 ± 4
bi	6A		CRS group with all restraint data (baseline: n = 11 from current cohort and n = 22 from Seewoo et al., 2019; restraint: n = 15)	Higher-level FEAT $p < 0.05, z > 2$	
bj		seed- based analysis	CRS group (baseline: n = 9 from current cohort; restraint: n = 15)	Unpaired Cohen's $d =$ 1.51 $p = 0.0018$	0.712, 2.18 baseline = 0.13 ± 0.02 restraint = 0.29 ± 0.03
bk		6B	Healthy group (baseline: n = 5 from current cohort; restraint: n = 8)	Unpaired Cohen's $d =$ 0.752 $p = 0.214$	-0.318, 1.74 baseline = 0.15 ± 0.03 restraint = 0.24 ± 0.05
Proton Magnetic Resonance Spectroscopy					

bl	7C	Glutamine (Gln)	CRS group (n = 17/timepoint)	Paired Cohen's $d = -0.538$ $p = 0.027$	-1.19, -0.0217 baseline: 0.53 ± 0.01 restraint: 0.50 ± 0.01
bm			Healthy group (n = 8/timepoint)	Paired Cohen's $d = 0.743$ $p = 0.174$	-0.127, 1.95 baseline = 0.50 ± 0.02 restraint = 0.54 ± 0.02
bn	7D	Glutamate (Glu)	CRS group (n = 17/timepoint)	Paired Cohen's $d = -0.711$ $p = 0.0706$	-1.46, 0.134 baseline: 1.41 ± 0.02 restraint: 1.35 ± 0.02
bo			Healthy group (n = 6/timepoint)	Paired Cohen's $d = -1.1$ $p = 0.121$	-2.15, -0.122 baseline = 1.48 ± 0.04 restraint = 1.37 ± 0.04
bp	7E	Gln + Glu (Glx)	CRS group (n = 17/timepoint)	Paired Cohen's $d = -0.84$ $p = 0.0186$	-1.49, -0.115 baseline: 1.94 ± 0.02 restraint: 1.85 ± 0.03
bq			Healthy group (n = 7/timepoint)	Paired Cohen's $d = -0.41$ $p = 0.529$	-1.83, 1.12 baseline = 1.97 ± 0.04 restraint = 1.92 ± 0.05
br		GABA	CRS group (n = 16/timepoint)	Paired Cohen's $d = -0.137$ $p = 0.74$	-0.959, 0.632 baseline: 0.35 ± 0.01 restraint: 0.34 ± 0.01
bs			Healthy group (n = 8/timepoint)	Paired Cohen's $d = -0.558$ $p = 0.378$	-1.82, 0.926 baseline = 0.37 ± 0.02 restraint = 0.34 ± 0.02
bt		Gln/Glu	CRS group (n = 17/timepoint)	Paired Cohen's $d = -0.171$ $p = 0.552$	-0.767, 0.275 baseline = 0.38 ± 0.01 restraint = 0.37 ± 0.01
bu			Healthy group (n = 6/timepoint)	Paired Cohen's $d = 1.15$ $p = 0.0632$	0.45, 2.51 baseline = 0.35 ± 0.02 restraint = 0.41 ± 0.02
Animal weight and whole-brain volume					

bv	8A	Spearman's rank correlation rho because baseline weights were not normally distributed (n = 33 from current cohort, n = 41 from Seewoo et al., 2019 and unpublished data)	S = 28632 $p = 7.909e-08$ r = 0.58	Mean whole brain volume to weight ratio = $6.64 \pm 0.16 \text{ mm}^3/\text{g}$
Hippocampal volume				
bw	8B	CRS group (n = 18/timepoint)	Paired Cohen's $d = -0.811$ $p = 0.0032$	-1.33, -0.318 baseline: 5.88 ± 0.01 restraint: 5.85 ± 0.01
bx		Healthy group (n = 8/timepoint)	Paired Cohen's $d = -0.409$ $p = 0.327$	-1.64, 0.467 baseline = 5.87 ± 0.01 restraint = 5.85 ± 0.02
Correlations				
by	9A	Latency and salience network functional connectivity (not normal; Spearman's rank correlation rho; n = 35)	R = 0.180 S = 5853.7 $p = 0.3004$ $p_{\text{adj}} = 0.4440$	
bz	9B	Latency and interoceptive network functional connectivity (not normal; Spearman's rank correlation rho; n = 35)	R = 0.312 S = 4909.9 $p = 0.0678$ $p_{\text{adj}} = 0.3627$	
ca	9C	Salience and interoceptive network functional connectivity (not normal; Spearman's rank correlation rho; n = 37)	R = 0.595 S = 3414 $p = 0.0001$ $p_{\text{adj}} = 0.0017$	
cb	9D	Latency and cingulate cortex functional connectivity (not normal; Spearman's rank correlation rho; n = 35)	R = -0.484 S = 10597 $p = 0.0032$ $p_{\text{adj}} = 0.0320$	

cc	9E	Cingulate cortex and salience network functional connectivity (not normal; Spearman's rank correlation rho; n = 37)	R = - 0.560 S = 13158 $p = 0.0004$ $p_{adj} = 0.0044$	
cd	9F	Cingulate cortex and interoceptive network functional connectivity (not normal; Spearman's rank correlation rho; n = 37)	R = - 0.402 S = 11828 $p = 0.0142$ $p_{adj} = 0.1137$	
ce	9G	Latency and Glx/tCr (latency not normal; Spearman's rank correlation rho; n = 51)	R = 0.180 S = 18116 $p = 0.2055$ $p_{adj} = 0.4440$	
cf	9H	Latency and hippocampal volume (latency not normal; Spearman's rank correlation rho; n = 52)	R = 0.262 S = 17285 $p = 0.0605$ $p_{adj} = 0.3627$	
cg	9I	Post-restraint latency and baseline hippocampal volume of CRS group (normal; Pearson's product-moment correlation; n = 23)	R = 0.311 $t_{(21)} = 1.50$ $p = 0.1480$ $p_{adj} = 0.4440$	-0.116, 0.641
ch	9J	Hippocampal volume and salience network functional connectivity (salience network functional connectivity not normal; Spearman's rank correlation rho; n = 36)	R = 0.341 S = 5124 $p = 0.0427$ $p_{adj} = 0.2990$	
ci	9K	Hippocampal volume and interoceptive network functional connectivity (interoceptive network functional connectivity)	R = 0.299 S = 5444 $p = 0.0764$ $p_{adj} = 0.3627$	

		not normal; Spearman's rank correlation rho; n = 36)		
cj	9L	Hippocampal volume and cingulate cortex functional connectivity (cingulate cortex functional connectivity not normal; Spearman's rank correlation rho; n = 36)	R = - 0.431 S = 11122 $p = 0.0091$ $p_{adj} = 0.0822$	

**Number of animals are different between groups and among tests because: (i) one animal fell off the open arm during baseline EPM testing and baseline and post-restraint EPM data from this animal was excluded from the analyses, (ii) FST trials during which the animals managed to escape more than once or were floating horizontally for the duration of the test (with most of their body being completely dry at the end) were excluded from the analyses, (iii) sessions during which the CRLB of a metabolite of interest was greater than 20% in the $^1\text{H-MRS}$ data were excluded from the analyses, (iv) not all animals were imaged at baseline and following restraint due to limited access to the MRI instrument and time taken to scan each animal (~1.5 hours per animal), and (v) animals with variable physiology (e.g., rapidly increasing/decreasing breathing rates) during rs-fMRI scans were excluded from the analyses.*

6.3.2. Changes in resting-state functional connectivity

The interoceptive (Becerra et al., 2011; Seewoo et al., 2019c) and salience (Bajic et al., 2016; Seewoo et al., 2019c) networks were identified from baseline rs-fMRI data and used in dual regression analysis for detecting functional connectivity differences induced by CRS (Figure 6.5). Dual regression analysis revealed a large decrease in connectivity of the bilateral somatosensory cortex to the salience network (baseline: 36 ± 3 , $n = 9$; restraint: 19 ± 1 , $n = 15$; unpaired Cohen's $d = -2.33$, $p = 0.0^{bc,be}$; Figure 6.5A & 6.5C) and of the right somatosensory cortex to the interoceptive network (baseline: 39 ± 5 , $n = 9$; restraint: 23 ± 2 , $n = 15$; unpaired Cohen's $d = -1.38$, $p = 0.0032^{bc,bg}$; Figure 6.5B & 6.5D). As a supplementary analysis, dual regression was carried out using a subset of the restraint group, which consisted of the nine animals exhibiting the greatest change in FST behavioural outcomes. A greater number of significant voxels with $p < 0.05^{bd}$ (both networks) and lower p-values for changes in the

salience network were obtained in the same brain regions (Figure 6.5A-B; Table 6.3).

Additionally, dual regression detected a significant decrease in connectivity of the right motor cortex and bilateral insular cortex to the salience network (Figure 6.5A).

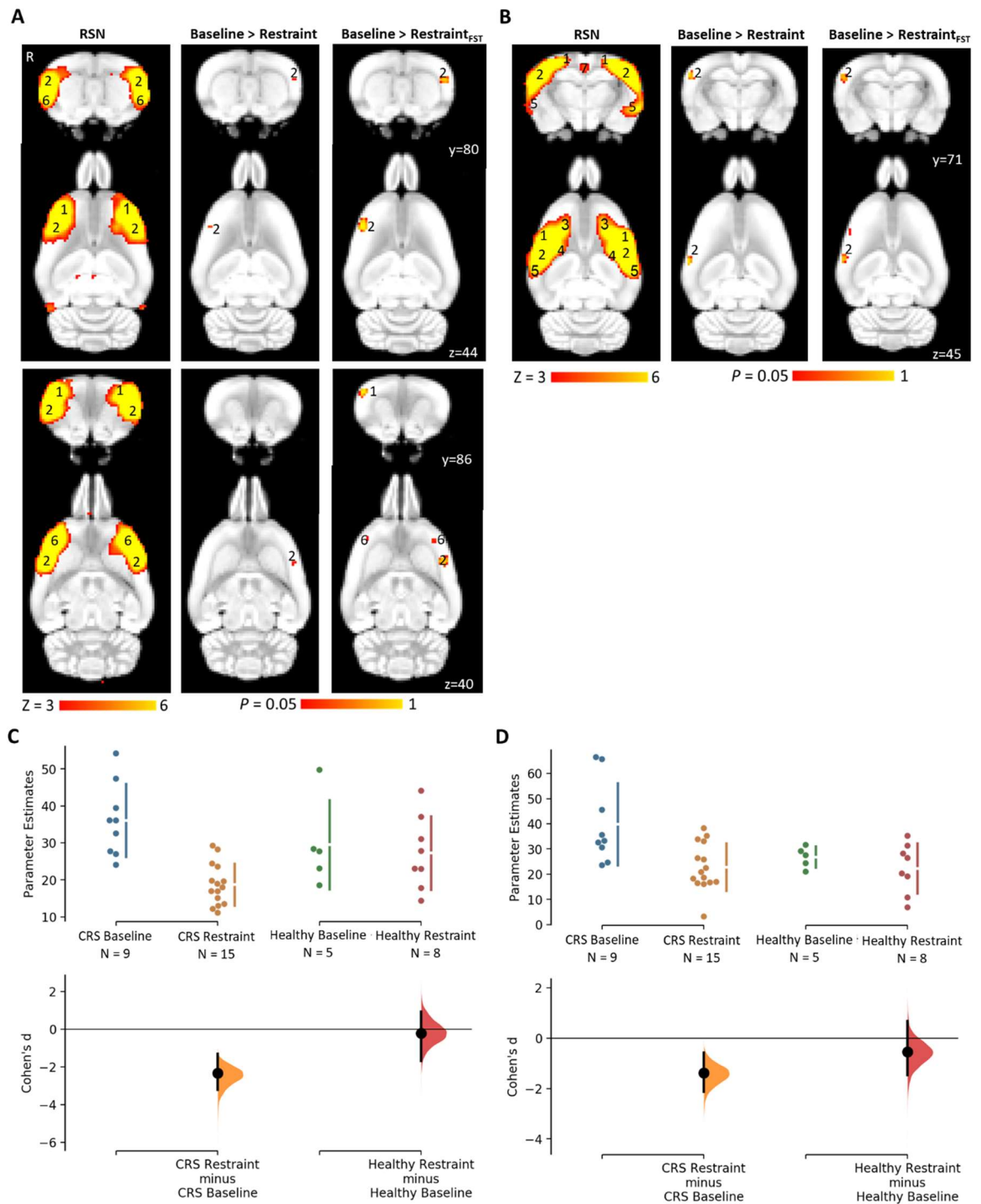


Figure 6.5. Decreased functional connectivity within the salience and interoceptive networks following chronic restraint stress as detected by dual regression (A & B)

and corresponding Cumming estimation plots (C & D). The figure illustrates coronal and corresponding axial slices of spatial statistical colour-coded maps overlaid on the rat brain atlas (down-sampled by a factor of eight). A and B show two RSNs (A, salience network and B, interoceptive network) identified in the baseline rs-fMRI scans of 6-7-week-old male Sprague Dawley rats under isoflurane-medetomidine anaesthesia. The RSN maps are represented as z-scores ($n = 33$, thresholded at $z > 3$), with a higher z-score (yellow) representing a greater correlation between the time course of that voxel and the mean time course of the component. The changes in the functional connectivity within the two RSNs following 13 days of chronic restraint stress are represented as p-values (thresholded at $p < 0.05$; baseline, $n = 33$; restraint, $n = 15$; restraint based on FST result, $n = 9$). R denotes right hemisphere. Significant clusters include various brain regions: 1, motor cortex; 2, somatosensory cortex; 3, frontal association cortex; 4, striatum/caudate putamen; 5, auditory cortex; 6, insular cortex; 7, retrosplenial cortex. The Cohen's d for 2 comparisons are shown in the Cumming estimation plots below the associated statistical map (C & D). The raw data is plotted on the upper axes; each mean difference is plotted on the lower axes as a bootstrap sampling distribution. Mean differences are depicted as dots; 95% confidence intervals are indicated by the ends of the vertical error bars.

Table 6.3. Summary of changes in functional connectivity within the interoceptive and salience networks when using all rs-fMRI data from post-restraint timepoint vs using a subset of animals showing greatest behavioural changes in forced swim test (FST).

RSN	Contrast	Minimum p-value	Total number of significant voxels
Interoceptive network	Baseline > Restraint	0.005	32
	Baseline > Restraint _{FST}	0.012	60
Salience network	Baseline > Restraint	0.029	11
	Baseline > Restraint _{FST}	0.002	127

When rs-fMRI data of all animals were analysed using a seed-based analysis, a significantly greater functional connectivity of several brain regions to the cingulate cortex was detected in the restraint group (baseline: 0.13 ± 0.02 , $n = 9$; restraint: 0.29 ± 0.03 , $n = 15$; unpaired Cohen's $d = 1.51$, $p = 0.0018^{bj}$; Figure 6.6B). Specifically, hyperconnectivity was detected in the right retrosplenial cortex, visual cortex and inferior colliculus and in the bilateral thalamus, superior colliculus, dentate gyrus and Cornu Ammonis 3 (CA3) (Figure 6.6A^{bi}). Healthy control animals which did not undergo

the CRS procedure did not show any change in functional connectivity between the two timepoints (Figure 6.5C, 6.5D & 6.6B; Table 6.2^{bf,bh,bk}).

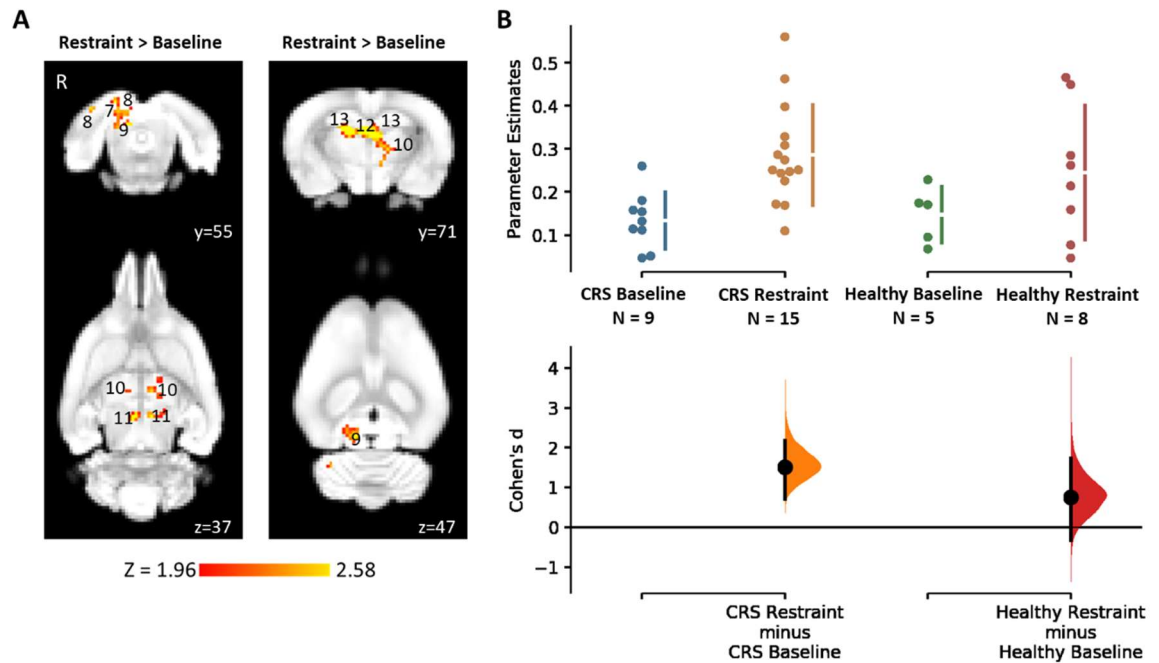
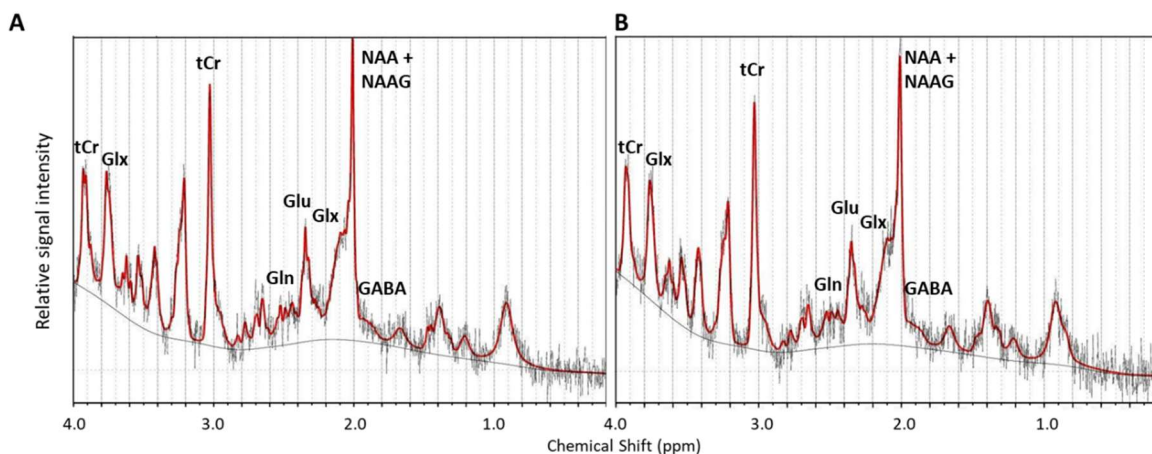


Figure 6.6. Increased functional connectivity to the cingulate cortex following chronic restraint stress as detected by seed based analysis (A) and corresponding Cumming estimation plots (B). The figure illustrates coronal and corresponding axial slices of spatial statistical colour-coded maps overlaid on the rat brain atlas (down-sampled by a factor of eight). A shows changes in the functional connectivity of the cingulate cortex between baseline and following 13 days of chronic restraint stress as spatial colour-coded Z (Gaussianised T/F) statistic images corrected for multiple comparisons at cluster level (thresholded at $p < 0.05$; baseline, $n = 33$; restraint, $n = 15$). R denotes right hemisphere. Significant clusters include various brain regions: 8, visual cortex; 9, inferior colliculus; 10, thalamus; 11, superior colliculus; 12, dentate gyrus; 13, Cornu Ammonis 3 (CA3). The Cohen's d for 2 comparisons are shown in the Cumming estimation plots below the associated statistical map (B). The raw data is plotted on the upper axes; each mean difference is plotted on the lower axes as a bootstrap sampling distribution. Mean differences are depicted as dots; 95% confidence intervals are indicated by the ends of the vertical error bars.

6.3.3. Changes in neurometabolite levels as detected by ¹H-MRS

The concentrations of the neurotransmitters GABA and Glu, the neurotransmitter precursor Gln, and combined glutamate-glutamine (Glx) were measured before and after CRS and were computed relative to tCr. Following restraint, rats had lower levels of Gln (baseline: 0.53 ± 0.01 , $n = 17$; restraint: 0.50 ± 0.01 , $n = 17$; Cohen's $d = -0.538$, $p = 0.027^{\text{bl}}$), Glu (baseline: 1.41 ± 0.02 , $n = 17$; restraint: 1.35 ± 0.02 , $n = 17$; Cohen's $d = -$

0.711, $p = 0.071^{bn}$) and Glx (baseline: 1.94 ± 0.02 , $n = 17$; restraint: 1.85 ± 0.03 , $n = 17$; Cohen's $d = -0.84$, $p = 0.0186^{bp}$) in the sensorimotor cortex (Figure 6.7C-E). Note that there is considerable uncertainty about the magnitude of the effect of the restraint procedure on Glu levels, with the CI stretching up toward negligible effects (95% CI[-1.46, 0.134]; Figure 6.7D). There was no change in GABA/tCr (baseline: 0.35 ± 0.01 , $n = 16$; restraint: 0.34 ± 0.01 , $n = 16^{br}$) and Gln/Glu (baseline: 0.38 ± 0.01 , $n = 17$; restraint: 0.37 ± 0.01 , $n = 17^{bt}$). Healthy control animals which did not undergo the CRS procedure did not show any change in neurometabolite levels between the two timepoints (Fig 7C-E; Table 6.2^{bl-bu}).



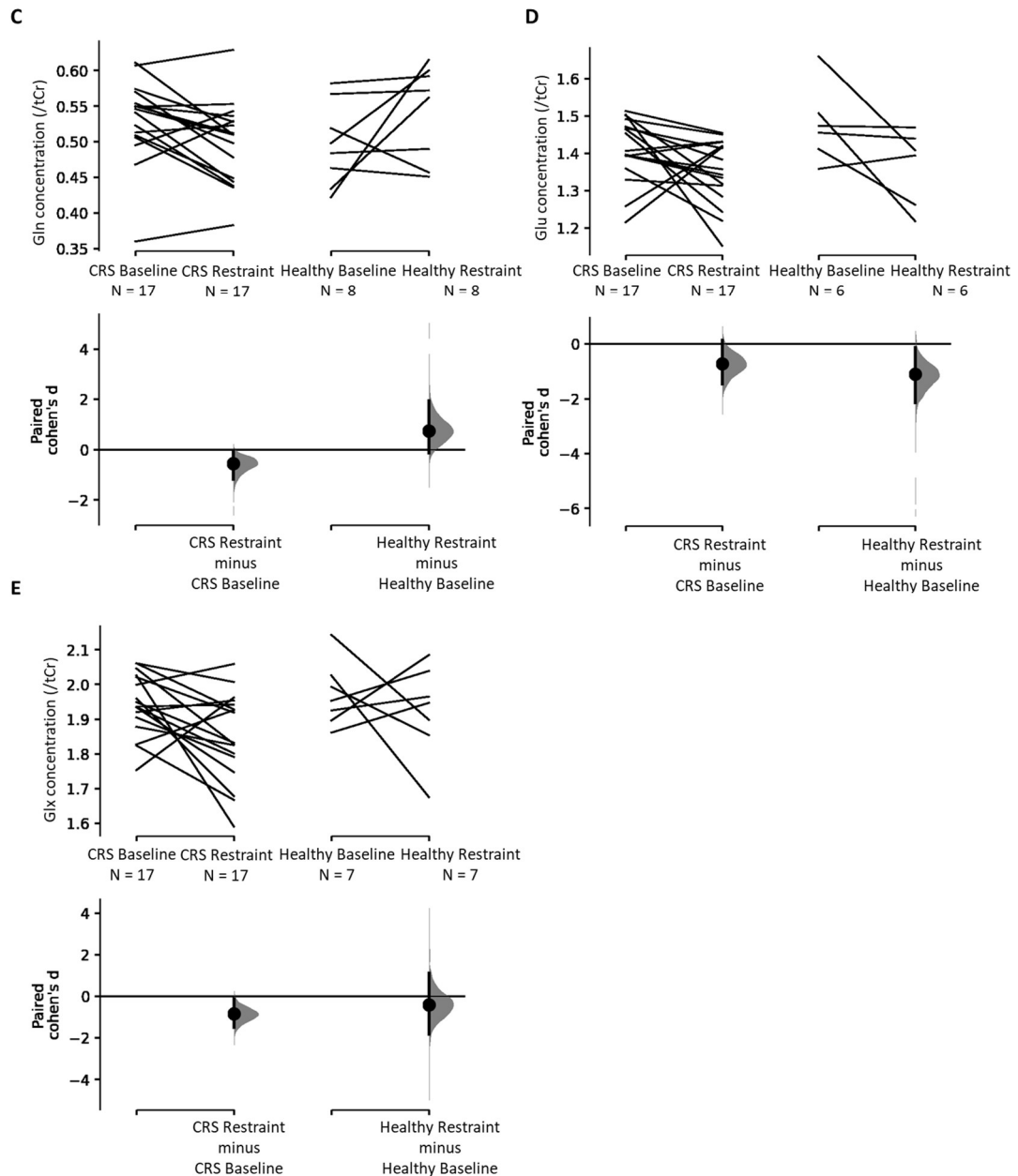


Figure 6.7. Representative spectra obtained from LCModel for proton magnetic resonance spectroscopy data at baseline (A) and restraint timepoints (B) for the CRS group and effect of restraint on glutamine (C), glutamate (D) and combined glutamine and glutamate (E). The figure shows spectra from a representative animal at baseline (A) and after 13 days of chronic restraint stress (B) depicting longitudinally reproducible peaks of various metabolites quantified using the LCModel. C-E are Cumming estimation plots showing paired Cohen's d for 2 comparisons each. The raw data is plotted on the upper axes; each paired set of observations is connected by a line. On the lower axes, each paired mean difference is plotted as a bootstrap sampling distribution. Mean differences are depicted as dots; 95% confidence intervals are indicated by the ends of the vertical error bars.

6.3.4. Change in hippocampal volume

Spearman's rank correlation method revealed a significant correlation of whole-brain volumes with the weight of the animals at baseline ($S = 28632$, $R = 0.58$, $p = 7.909e^{-8bv}$; Figure 6.8A), with the mean whole-brain volume to body weight ratio of the Sprague Dawley rats being $6.64 \pm 0.16 \text{ mm}^3/\text{g}$. Percentage hippocampal volume decreased following CRS (baseline: 5.88 ± 0.01 , $n = 18$; restraint: 5.85 ± 0.01 , $n = 18$; Cohen's $d = -0.811$; $p = 0.003^{bw}$; Figure 6.8B) but did not change significantly in healthy controls (baseline: 5.87 ± 0.01 , $n = 8$; restraint: 5.85 ± 0.02 , $n = 8^{bx}$; Figure 6.8B).

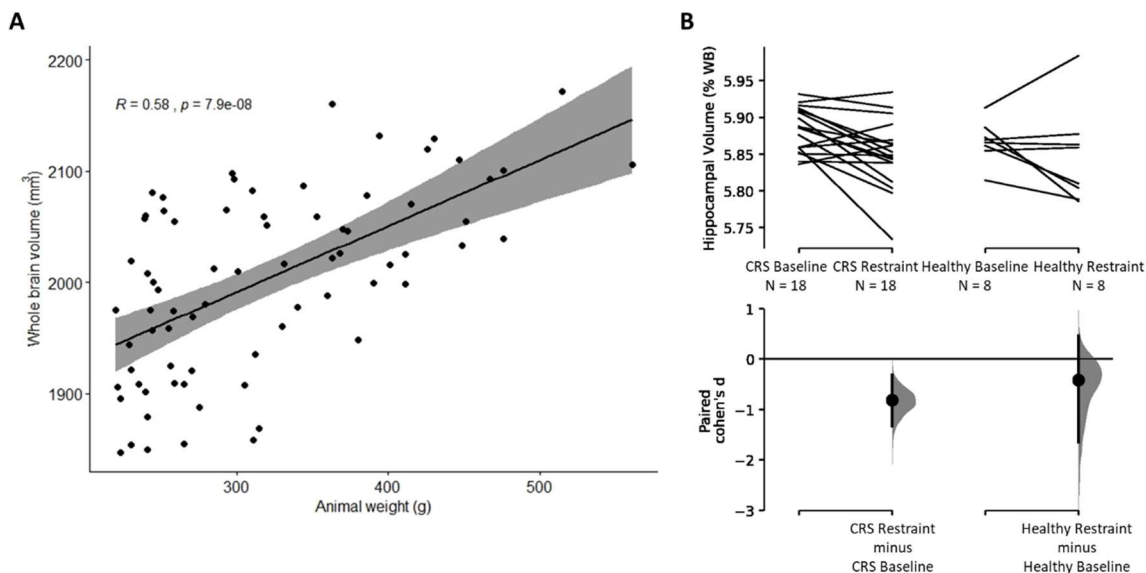


Figure 6.8. Correlation between weight of animals and whole-brain volume at baseline (A) and percentage hippocampal volume before and after chronic restraint stress (B). A shows whole-brain volumes (mm³) plotted against the animal's weight at baseline ($n = 74$). Correlation was determined using Spearman's rank correlation method. In B, hippocampal volumes were calculated as a percentage of whole-brain volume. B shows decrease in percentage hippocampal volume following 13 days of chronic restraint stress and no change in the healthy control group. The Cohen's d for 2 comparisons are shown in the Cumming estimation plots. The raw data is plotted on the upper axes; each paired set of observations is connected by a line. On the lower axes, each paired mean difference is plotted as a bootstrap sampling distribution. Mean differences are depicted as dots; 95% confidence intervals are indicated by the ends of the vertical error bars.

6.3.5. Correlations

Spearman's rank correlation test using data from both groups and timepoints revealed significant correlations between latency to first immobility behaviour and several MRI measures as well as between different MRI measures (Table 6.2^{by-cj}; Figure 6.9).

However, only the correlation and of the salience network connectivity with the interoceptive network and cingulate cortex connectivity and of the cingulate cortex connectivity with latency to first immobility behaviour survived multiple comparison correction. A Pearson's correlation test revealed no significant correlation between baseline percentage hippocampal volume of the CRS group and post-restraint latency to first immobility behaviour during FST ($R = 0.311$, $t_{(21)} = 1.50$, $p = 0.148^{cg}$; Figure 6.9I).

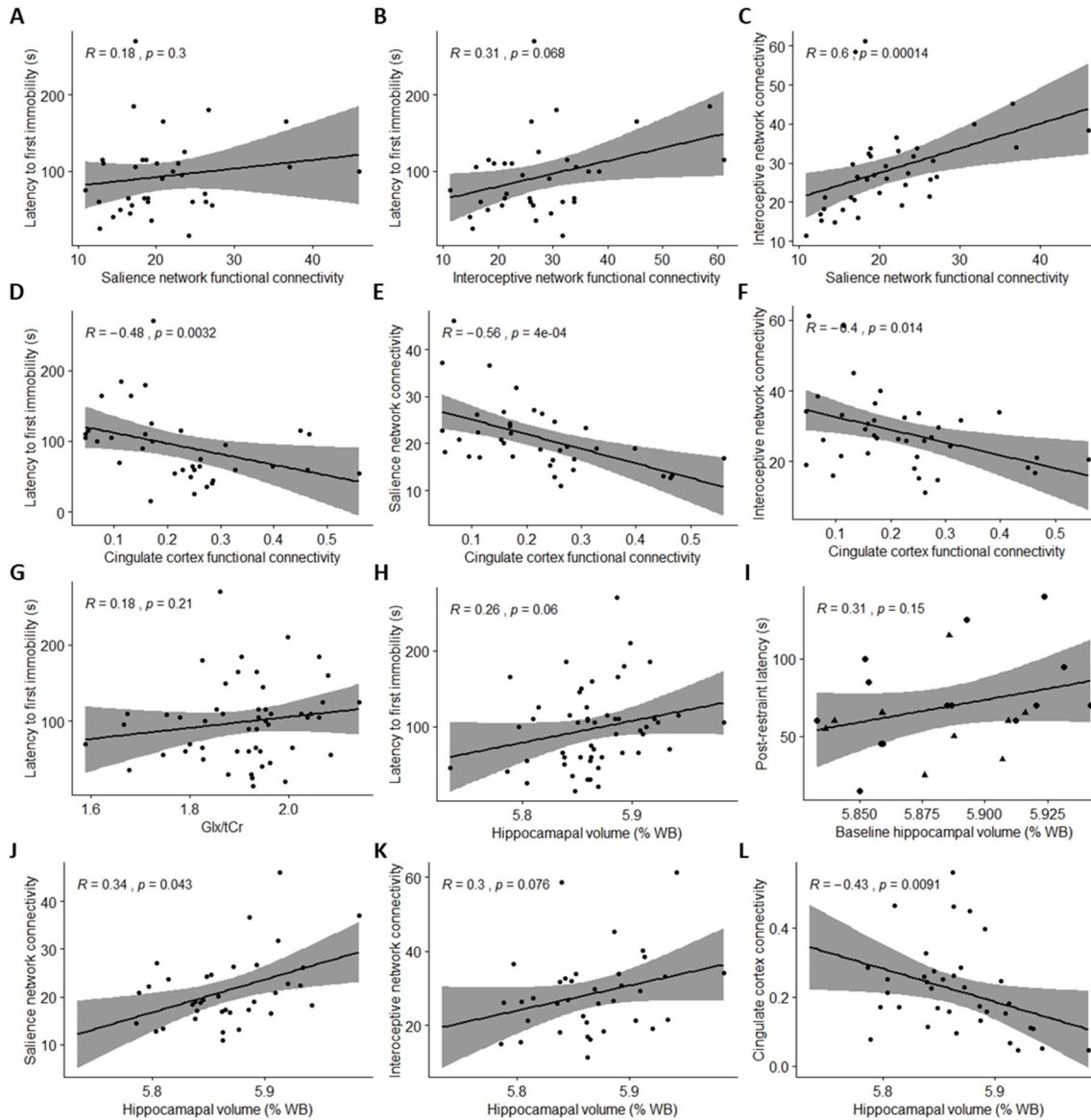


Figure 6.9. Correlations between behavioural tests and MRI measures. In A-G, comparisons of the following parameters from both CRS and healthy control groups at both timepoints were made by Spearman correlations: latency time from forced swim test data; connectivity (average parameter estimates) of the saliency network, interoceptive network and cingulate cortex from the rs-fMRI data; and Glx/tCr ratio from ^1H -MRS data (no multiple comparison correction). In H-L, hippocampal volumes were calculated as a percentage of whole-brain volume and compared to latency time from FST data (H, I), and functional brain connectivity (J-L) (no multiple comparison correction). In I, Pearson correlation was performed between baseline percentage hippocampal volume of CRS group and post-restraint latency to first immobility behaviour during forced swim test of the same animals (baseline, $n = 23$; restraint, $n = 23$). Data points with triangular shape represent the nine animals which were used for FST-based ICA/dual regression analysis.

6.4. Discussion

Animal models are an indispensable tool for studying aetiology, progress and treatment of depression in a controlled environment. However, there remains controversy regarding the validity of using rodent models of human neuropsychiatric disorders. Prior work in rodents investigating anxiety and depression-like behaviours (Suvrathan et al., 2010; Ulloa et al., 2010; Chiba et al., 2012; Bogdanova et al., 2013), peripheral biomarkers, functional connectivity of the brain (Henckens et al., 2015) and hippocampal volume (Lee et al., 2009; Alemu et al., 2019) supports the validity of the CRS paradigm as a depression model (Wang et al., 2017b). However, our study is the first to correlate MRI measures of functional, chemical and structural changes in the brain with abnormal behaviour in the CRS model. We note that most of the correlation measures did not survive multiple comparison corrections and should therefore be interpreted with caution. Nevertheless, similarities between our data and the MRI outcomes in humans suggest that the CRS model may be a useful component of translational studies aimed at developing and refining novel treatments for depression in humans.

6.4.1. Aberrant resting-state functional connectivity following chronic restraint stress

One of the most consistent pathophysiologies of depression that has emerged from rs-fMRI studies is the abnormal regulation of the cortico-limbic mood regulating circuits. The human salience and interoceptive networks play an important role in being aware of, and orienting and responding to, biologically relevant stimuli (Harshaw, 2015), while the DMN is implicated in rumination, self-referential functions, and episodic memory retrieval (Lu et al., 2012). Because these distributed neuronal networks

encompassing cortical and limbic brain regions normally regulate aspects of emotional behaviour, the dysregulation of functional connectivity within these networks is known to be associated with depression (Wang et al., 2012; Helm et al., 2018).

ICA and dual regression analysis of our rodent rs-fMRI data detected decreased functional connectivity of the bilateral somatosensory cortex to the salience network, and of the right somatosensory cortex to the interoceptive network following CRS, and the reductions in connectivity within the two RSNs were strongly correlated to each other. This is in accordance with previous studies reporting altered functional connectivity in both the salience and interoceptive networks in humans with depression compared to healthy individuals (Manoliu et al., 2014; Harshaw, 2015). For example, Yin et al. (2018) observed decreased functional connectivity of insular cortex to somatosensory and motor cortices in patients with bipolar disorder in the period of depression.

The decrease in functional connectivity within the salience and interoceptive networks is known to be associated with negative response biases in patients with depression and correlated to their severity of symptoms (Manoliu et al., 2014; Harshaw, 2015). In animals, immobility and latency to first immobility behaviour in FST are believed to reflect a failure to persist in escape-directed behaviour after stress and have been suggested to represent “behavioural despair” (Slattery and Cryan, 2012). These measures are consistently used as a preclinical screen for antidepressants and antidepressants that are effective in humans are found to decrease immobility in rats in FST (Cryan et al., 2005). However, salience and interoceptive network connectivity were not correlated with latency to first immobility behaviour during FST in our rats.

When a subset of animals showing the greatest depression-like behaviours in the FST was used in dual regression analysis, a decrease in connectivity of the right motor cortex and bilateral insular and somatosensory cortices to the salience network was also detected. Therefore, despite being a smaller group, the use of a subset of animals selected based on their FST performance resulted in increased sensitivity of the dual regression tool in detecting between-timepoint differences, showing some correlation between functional connectivity and behaviour. CRS may induce abnormal behavioural responses in animals as a result of insular dysfunction within the salience network leading to an abnormal switching between the DMN and the central executive network (Manoliu et al., 2014).

The DMN plays an important role in the pathophysiology of depression (Sheline et al., 2009; Zhu et al., 2012). One critical element of the DMN is the cingulate cortex, which has increased connectivity with other limbic areas in patients with depression (Greicius et al., 2007; Sheline et al., 2009; Davey et al., 2012; Fang et al., 2012; Rolls et al., 2018). The results of the current study are consistent with these data; we detected hyperconnectivity of the cingulate cortex to the right retrosplenial cortex, visual cortex, inferior colliculus, bilateral thalamus, superior colliculus and hippocampus following CRS. Additionally, cingulate cortex connectivity was very strongly correlated with behavioural despair (latency in FST) in our rats. Cingulate cortex connectivity plays a significant role in clinical symptoms (Walter et al., 2009), with higher functional connectivity leading to dysfunctional emotion, internal inspection, and endocrine regulation (Fang et al., 2012). For example, increased functional connectivity between the thalamus and the cingulate cortex may result from increased emotional

processing, at the cost of executive functions (Greicius et al., 2007). However, our behavioural tests did not specifically address executive functioning in rats, and this could be addressed in future studies using appropriate cognitive tests.

Our rs-fMRI findings differ from a previous animal study using a shorter CRS protocol (2 h/day for 10 days), which did not find any significant changes in the RSNs despite using the same ICA/dual regression approach of rs-fMRI data analysis performed here (Henckens et al., 2015). Moreover, when comparing 'overall connectivity strength', connectivity was increased in somatosensory and visual networks, which was not observed in our experiments. The shorter duration of the restraint stress, as well as intrinsic differences between the rs-fMRI data analysis methods used to detect changes in connectivity, and the effect of an isoflurane-only anaesthetic protocol on RSNs (Paasonen et al., 2018) used in the previous study (Henckens et al., 2015) could be the cause of these inconsistencies.

Comparison of the hyperconnectivity observed here to findings in other animal models used to investigate depression and anxiety is interesting. Brain activation in cortical and hippocampal regions in mice following chronic social defeat stress is observed in manganese-enhanced magnetic resonance imaging (Laine et al., 2017). Additionally, aberrant hippocampal, thalamic and cortical connectivity is reported in other rodent models using different data acquisition and/or analysis methods. For example, in the chronic unpredictable stress rat model, rs-fMRI studies found increased functional connectivity of the hippocampus to several brain regions (Magalhães et al., 2019), increased functional connectivity between atrophied brain regions such as the hippocampus, striatum and cingulate, motor and somatosensory cortices (Magalhães

et al., 2018) and increased regional homogeneity (coherence of intraregional spontaneous low-frequency activity) in the hippocampus, thalamus and visual cortex as well as a decreased regional homogeneity in the motor cortex (Li et al., 2018). Electrophysiology studies have also reported long-lasting inhibition of long-term potentiation in the thalamo-cortical circuitry (Zheng et al., 2012) and in the hippocampal–cortical circuitry (Cerqueira et al., 2007) in chronic unpredictable stress models while hippocampal–cortical circuitry inhibition was also reported in acute platform stress rat models (Rocher et al., 2004). These different animal models reflect specific aspects of depression and therefore, they may be useful for understanding the heterogeneity of human depression.

6.4.2. Decrease in glutamate and glutamine levels following chronic restraint stress

Several preclinical and clinical studies have proposed that altered glutamatergic neurotransmission plays a pivotal role in the pathogenesis of mood disorders (Sanacora et al., 2012; Marrocco et al., 2014; Moriguchi et al., 2019). Accordingly, another major finding of the present study was the significant decreases in Gln, Glu and Glx in the left sensorimotor cortex following CRS. Human ¹H-MRS studies have reproducibly reported a reduced concentration in Glu, Gln and/or Glx in several brain regions including the anterior cingulate cortex (Mirza et al., 2004; Luykx et al., 2012) and the prefrontal cortex (Hasler et al., 2007b; Portella et al., 2011). Similarly, other ¹H-MRS studies of animal models of depression such as the chronic mild stress and the chronic social isolation models have reported decreases in these neurometabolites in the prefrontal cortex (Hemanth Kumar et al., 2012) and hippocampus (Hemanth Kumar et al., 2012; Shao et al., 2015).

The majority of the measured neurometabolites are intracellular, with a small portion reflecting synaptic Glu, therefore to infer changes in glutamatergic neurotransmission from ^1H -MRS studies is difficult (Sanacora et al., 2012). Nevertheless, a change in Glu-related neurometabolite concentration may reflect a change in Glu–Gln cycling or overall Glu metabolism (Yildiz-Yesiloglu and Ankerst, 2006). The foremost metabolic pathway of Glu is the synthesis of Gln in glial cells from Glu, the transport of Gln to nerve cell terminals, the conversion of Gln into the neurotransmitter Glu, the release of Glu and the final re-uptake of Glu by the glia (Pfleiderer et al., 2003). Since the measured neurometabolites largely represent the intracellular pool contained in glutamatergic neurons and glia, a decrease in Glu, Gln and Glx may reflect an impairment of the neuron–astrocyte integrity, energy metabolism, glial cell dysfunction or a loss of glial cells, particularly astrocytes (Yildiz-Yesiloglu and Ankerst, 2006; Lee et al., 2013b).

The shortage in these neurometabolites might be due to a reduction in the number of astrocytes which in turn alters neuronal activity and therefore may contribute to depression-like behaviours, as previously shown in an L- α amino adipic acid (L-AAA) infusion mouse model (Lee et al., 2013b). However, there was also no correlation between Glx levels and depression-like behaviours post-CRS in the present study. This is surprising because a relatively recent meta-analysis on Glx concentrations in depression found that decrease in Glx in patients with depression was positively associated with depression severity (Arnone et al., 2015). While the functional connectivity within the DMN increased post-CRS in our animals, there were also no changes in Gln/Glu ratio in either the CRS or healthy control groups, suggesting the

absence of change in glutamatergic activity and therefore, the absence of Glu-related excitotoxicity in the cortex of our animals.

6.4.3. Decrease in hippocampal volume

There are several convergent lines of evidence from both preclinical and clinical studies that implicate the hippocampus in the pathogenesis of depression (Campbell and Macqueen, 2004). The hippocampus is a key brain region within the limbic system and plays a determinant role in emotional regulation. As mentioned above, the hippocampus is one of several regions, including the prefrontal cortex, the cingulate cortex, and the thalamus that have been identified to be part of the DMN showing abnormally higher functional connectivity in patients with depression compared to healthy individuals (Sheline et al., 2009). Additionally, the hippocampus is known to be a highly stress-sensitive structure as increased levels of glucocorticoids in stressful situations are known to disrupt hippocampal neurogenesis, which may lead to hippocampal atrophy (Dranovsky and Hen, 2006). A reduction in hippocampal volume has been consistently associated with depression in humans (McKinnon et al., 2009). However, the stage at which hippocampal atrophy begins in human depression is unclear and so is the direction of causality.

There are two main hypotheses regarding how depression is associated with hippocampal atrophy. Firstly, hippocampal volume reduction, probably as a result of early life adversity, poverty and stress, might predispose people to depression. This hypothesis seems consistent with smaller hippocampal volumes already present in first depressive episodes (Cole et al., 2011) and in young children (Barch et al., 2019) and adolescents (Rao et al., 2010) with depression. The second hypothesis, known as the

neurotoxicity hypothesis, suggests that cumulative exposure to disrupted emotion regulation, stress reactivity, glucocorticoids and antidepressant medications as a result of depression increases neuronal susceptibility to insults and therefore leads to hippocampal deficits (Sheline, 2011). This hypothesis is consistent with hippocampal atrophy being more pronounced among individuals with recurrent episodes and in chronic depression (McKinnon et al., 2009; Cheng et al., 2010; Brown et al., 2014).

The longitudinal nature of the present study precludes the first hypothesis in CRS animals. While hippocampal volume was weakly correlated with latency overall, there was no correlation between baseline hippocampal volume and post-CRS latency. This shows that baseline hippocampal volume did not predict severity of symptoms in this CRS model. Therefore, this study supports the neurotoxicity hypothesis and further suggests that the reduction in hippocampal volume might happen at a very early stage in depression, i.e., within only three weeks in this animal model. Additionally, hippocampal volume was correlated to functional connectivity of the salience network, interoceptive network and cingulate cortex, which suggests the presence of a common pathway for the mechanism of depression.

6.4.4. Study limitations

Our study has four main limitations. Firstly, only young adult male rats were used in this study, even though CRS has been shown to successfully induce depression-like behaviours in freely cycling adolescent female rats (Hibicke et al., 2017b; Hibicke et al., 2017a). Future studies could expand the applicability of present results by investigating brain changes following CRS in female rats and in older rats. Secondly, the SPT did not detect anhedonia in our animals following restraint, despite anhedonia being a well-

documented effect of CRS (e.g., Chiba et al., 2012; Ampuero et al., 2015b; Liu et al., 2016). Use of non-acidified water and longer habituation and/or test times as performed in these studies may be required. Thirdly, MRI data was acquired under anaesthesia, which could potentially alter the blood-oxygen-level-dependent (BOLD) signal detection. However, functional connectivity patterns of animals anaesthetised using a combination of low-dose isoflurane and medetomidine have good correspondence with those of awake rats (Paasonen et al., 2018) with strong inter-cortical and cortical-subcortical functional connectivity (Grandjean et al., 2014; Bukhari et al., 2017a) and are reproducible (Lu et al., 2012). Moreover, ^1H -MRS data was acquired only in the left sensorimotor cortex. Future studies can investigate neurometabolite changes in bilateral sensorimotor cortex as well as in other brain regions such as the basal ganglia, hippocampus, anterior cingulate cortex, and occipital cortex, which are extensively investigated in ^1H -MRS studies of human depression. Neurometabolite and structural changes could be confirmed using invasive methods following CRS. Finally, the pharmacological or interventional validity of the present neuroimaging findings is unknown. Future work should examine the utility of these findings as preclinical target engagement biomarkers with pharmacological and neuromodulatory interventions. If this proves to be the case, this animal model has potential utility for high throughput dose-finding studies of neurotherapeutics and novel interventions.

6.5. Conclusion

The present study is the first to demonstrate significant changes in functional connectivity, neurometabolite levels, and hippocampal volume in the same young

adult male rats post-CRS and the correlation of these measures with changes in behaviour provide insight into the neurobiological changes that may underpin patient symptoms. Cumulative exposure to stress might increase neuronal and astrocytic death leading to hippocampal atrophy and a shortage in glutamate and glutamine, which in turn alters neuronal activity and therefore contribute to learned helplessness. Overall, the substantial concordance of the present findings with the literature of human depression presents a unique opportunity for the integration of behavioural, cellular and molecular changes detected in this depression model with changes in MRI measures of brain function, chemistry and structure that may be translated to future studies of the human disorder, especially when testing the effects of new drug treatments or therapies.

Chapter 7

Depression model: Long-term effects of repeated 10 Hz LI-rTMS on chronic restraint stress model of depression

1. Published as: Seewoo, B., Feindel, K., Etherington, S., Hennessy, L., Croarkin, P., Rodger, J., 2019. M85. Validation of the chronic restraint stress model of depression in rats and investigation of standard vs accelerated rTMS treatment. *Neuropsychopharmacology*. 44:122–123. doi: 10.1038/s41386-019-0545-y (Appendix H)
2. Published as: Seewoo, B.J., Hennessy, L.A., Jaeschke-Angi, L.A., Mackie, L.A., Etherington, S.J., Dunlop, S.A., Croarkin, P.E. & Rodger, J., 2021. A preclinical study of standard versus accelerated transcranial magnetic stimulation for depression in adolescents. *Journal of Child and Adolescent Psychopharmacology*, in press. doi: 10.1089/cap.2021.0100 (Appendix I)
3. Under review: Hennessy, L.A.*, Seewoo, B.J.*, Jaeschke-Angi, L.A., Mackie, L.A., Etherington, S.J., Dunlop, S.A., Croarkin, P.E. & Rodger, J., 2022. Accelerated low-intensity repetitive Transcranial Magnetic Stimulation corrects functional connectivity and prevents anxiety response following chronic restraint stress.

The findings from Chapter 6 set the stage for investigating the effects of repeated LI-rTMS on the chronic restraint stress (CRS) model of depression. Since we have shown in Chapter 5 that 1 Hz stimulation has milder effects than 10 Hz, only 10 Hz LI-rTMS was used in this chapter to investigate its effects in more detail in the depression model. Currently approved rTMS protocols for the treatment of MDD involve daily (weekday) stimulation, using 10 Hz or iTBS frequencies, for 4-6 weeks (Horvath et al., 2010). Recently, accelerated treatment protocols (multiple daily stimulation sessions for 1-2 weeks) have been explored, with the goal of reducing the time and cost burdens on patients and clinicians (Loo et al., 2007; Holtzheimer et al., 2010; George et al., 2014; McGirr et al., 2015; Fitzgerald et al., 2018; Modirrousta et al., 2018). However, the design of accelerated protocols varies widely between studies (Sonmez et al., 2019), reducing statistical power. As a result, to date there is no clear evidence

of a biological benefit of accelerated over standard protocols (Fitzgerald et al., 2018; Modirrousta et al., 2018).

We first performed a pilot study comparing the effects of the standard 10 Hz protocol (1 stimulation session/weekday) and an accelerated 10 Hz LI-rTMS protocol (3 stimulation sessions/weekday). In the standard LI-rTMS group, animals receiving active treatment did not show any significant differences in behaviours compared to animals receiving sham treatment. This may be due to the small sample ($n = 5/\text{group}$).

However, in the accelerated LI-rTMS group, significant improvement in anxiety and depression-like behaviours were detected compared to sham treatment ($n = 5/\text{group}$).

Specifically, animals receiving active treatment showed less stretching during the elevated plus maze test and less immobility, greater latency to first immobility behaviour, and increased climbing behaviours during the forced swim test.

Because the accelerated protocol out-performed the standard protocol, only accelerated LI-rTMS was delivered in the main CRS experiments. However, therapeutic effects were not detected on the MRI and behavioural measures in our extended longitudinal study which used slightly older animals. In addition, differences in the outcomes following CRS in our experiments compared to previous studies suggest that the response to CRS and potentially rTMS may depend on the age of the animals.

Overall, our results suggest that there may be some benefit of accelerated LI-rTMS in rescuing anxiety-like behaviours induced following CRS in young adult male rats. Our findings highlight that it will be important to take into account the developmental state of the brain when designing interventions for paediatric neuromodulation.

7.1. Introduction

Repetitive transcranial magnetic stimulation (rTMS) is a non-invasive brain stimulation technique that is FDA approved as a therapy for treatment-resistant major depressive disorder (MDD) (Horvath et al., 2010). Currently approved rTMS protocols for the treatment of MDD involve daily (weekday) stimulation sessions, using 10 Hz or iTBS frequencies, for 4-6 weeks (Horvath et al., 2010). Recently, accelerated treatment protocols (multiple daily stimulation sessions for 1-2 weeks) have been explored, with the goal of reducing the time and cost burdens on patients and clinicians (Loo et al., 2007; Holtzheimer et al., 2010; George et al., 2014; McGirr et al., 2015; Fitzgerald et al., 2018; Modirrousta et al., 2018). However, the design of accelerated protocols varies widely between studies (Sonmez et al., 2019) reducing statistical power; to date there is no clear evidence of a biological benefit of accelerated over standard protocols (Fitzgerald et al., 2018; Modirrousta et al., 2018). Further investigation is required to understand the brain-based mechanisms of rTMS to harness its therapeutic effects in MDD.

Refining rTMS protocols via the use of animal models is a useful approach to developing evidence-based treatment protocols. Recent work has examined the effectiveness of different rTMS intensities in rodent models, showing that low intensities (10-50 mT; 1-5% of rodent motor threshold) have significant behavioural and neurological effects (Makowiecki et al., 2014; Tang et al., 2016a; Poh et al., 2018; Tang et al., 2018). In a mouse model of depression 10 Hz rTMS delivered at an intensity of 50 mT reduced psychomotor agitation and increased cortical and hippocampal BDNF and hippocampal neurogenesis levels (Heath et al., 2018). In addition, MRI

studies in healthy rats demonstrate that 10 Hz rTMS at 13 mT has long lasting effects on resting state networks and neurochemistry (Seewoo et al., 2019c). Low-intensity stimulation also has benefits in human studies (Huang and Rothwell, 2004; Huang et al., 2005; Boggio et al., 2010), and offers advantages over high intensity by reducing side effects (Wassermann, 1998; Rossi et al., 2009) and equipment cost.

Here we build on the previous body of research by studying the neurobiological effects of an accelerated stimulation protocol using low-intensity (13 mT) rTMS in a rat model of depression. Chronic restraint in rats has previously been shown to induce functional, anatomical and chemical changes in the brain that model the changes observed in human patients with MDD, including hypoconnectivity within the salience and interoceptive networks, hyperconnectivity of several brain regions to the cingulate cortex, decreased hippocampal volume, and decreased sensorimotor glutamate and glutamine levels (Seewoo et al., 2020a). In this study, we first determined that in the short term, the accelerated protocol was more effective in mediating behavioural change than the standard once-per-day protocol. We then used an extended longitudinal study design to monitor the effects of accelerated rTMS on the brain and behavioural changes that occur following chronic restraint stress, during the treatment period and up to 2 weeks after the cessation of treatment.

7.2. Materials and Methods

7.2.1. Animals

Rats were sourced from the Animal Resources Centre located in Canning Vale, Western Australia. Cohorts of 30 (pilot study; 1 excluded) and 56 (main study; one excluded) male Sprague Dawley rats were used, which were aged 5-6 weeks on arrival. Although

all animals were ordered within the same age range, weights between the two cohorts were significantly different ($t = 5.6630$, $df = 82$; $p < 0.0001$) with rats in the pilot study ($242.79 \text{ g} \pm 14.18$) being significantly smaller than rats in the main study (293.87 ± 47.35). Rats were habituated to the animal care facility for one week prior to commencing the experiments. All animals were group-housed with two rats per cage, and kept in a temperature-controlled, standard 12h light/dark cycle environment. All animals were given food and water *ad libitum*, with the exception of during the Chronic Restraint Stress and Sucrose Preference Test Pre-test fasting procedures.

7.2.2. Study Overview

The experimental protocol was approved by the University of Western Australia Animal Ethics Committee (RA/3/100/1640) and was in accordance with the Western Australia Animal Welfare Act (2002) and the National Health and Medical Research Council's *Australian Code for the Care and Use of Animals for Scientific Purposes (8th Edition, 2013)*. All researchers held valid Permission to Use Animals (PUA) licenses and were trained and competent in all relevant procedures.

In the pilot study, our objective was to compare the short-term efficacy of standard and accelerated rTMS protocols in alleviating depression-like behaviours. The duration of treatment in this pilot study was half of the conventional duration for each type of treatment (2 weeks for standard and 1 week for accelerated) and was chosen to provide a rapid insight into the relative efficacy of standard and accelerated protocols. Animals were randomly assigned to one of six groups ($n = 5$ per group): standard active treatment, standard sham treatment, accelerated treatment, accelerated sham treatment, no treatment (depression-induced control group), or healthy controls (no

interventions). With the exception of animals in the healthy control group, all animals underwent chronic restraint stress for 2.5 hours per day for 13 days. Following CRS, animals in the standard treatment groups received 1 session of active or sham stimulation per day, for 5 consecutive days per week, for 2 weeks. Animals in the accelerated treatment groups received 3 sessions of active or sham stimulation per day (spaced 1 hour apart), for 5 consecutive days per week, for 1 week. Each stimulation session consisted of 10 min of 10 Hz low-intensity stimulation, in line with previous animal studies (Seewoo et al., 2019c). Behavioural tests were conducted at baseline, post CRS and after mid treatment.

In the main study, we investigated more thoroughly the effects of the accelerated protocol, which provided the best outcome in the pilot study. Animals were randomly assigned to one of four groups: accelerated active treatment (n = 20 per group), accelerated sham treatment (n = 20 per group), no treatment (depression-induced control group; n = 16 per group), or healthy controls (no interventions; n = 3 per group). With the exception of animals in the healthy control group, all animals underwent chronic restraint stress for 2.5 hours per day for 13 days. Following CRS, animals received 3 sessions of active or sham stimulation per day (spaced 1 hour apart), for 5 consecutive days per week, for 2 weeks. Each stimulation session consisted of 10 min of 10 Hz low-intensity stimulation, in line with the pilot study and previous animal studies. To quantify the behavioural and brain-related changes, a series of behavioural tests and Magnetic Resonance Imaging (MRI) procedures were conducted at baseline, after the chronic restraint stress period, midway through

treatment, post-treatment, and at one-week and two-week follow-up time points (Figure 7.1).

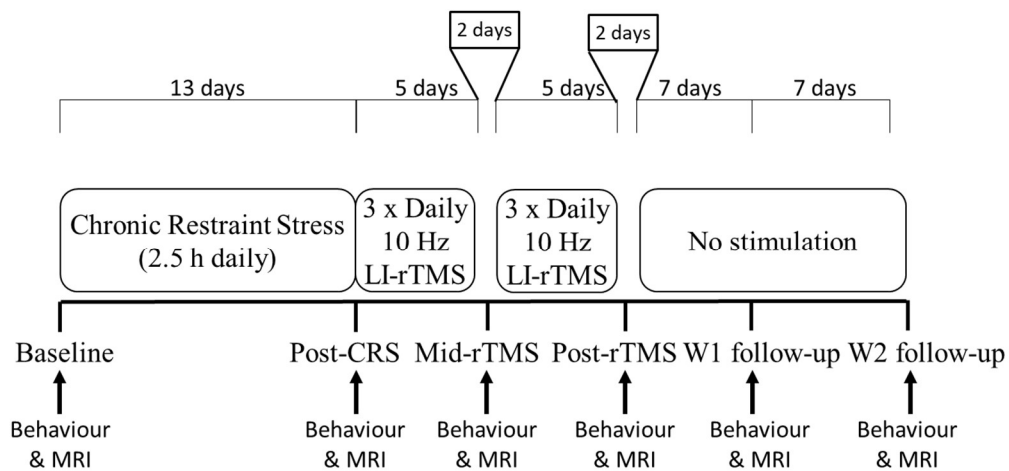


Figure 7.2. Experimental timeline and study design. Behavioural tests and MRI were conducted over a consecutive 4-day period at each timepoint.

7.2.3. Chronic restraint stress

Depression-like behaviours were induced in the rats using a Chronic Restraint Stress (CRS) model (Ulloa et al., 2010), as validated in Seewoo et al. (2020a). This involved placing the rats in individual transparent acrylic tubes for 2.5 hours each day, for 13 consecutive days.

7.2.4. Repetitive Transcranial Magnetic Stimulation

After one week of habituation, stimulation was delivered at 10 Hz using a custom-built round coil (8mm inner diameter x 16.2mm outer diameter x 10mm height; 460 turns of 0.25mm diameter copper wire; 6.1 Ω resistance). The coil was connected to a pulse generator and produced a magnetic field intensity of 24 mT at the coil surface and 13 mT at the surface of the cortex (Grehl et al., 2015; Seewoo et al., 2018b). Sham stimulation was delivered with the pulse generator switched off to act as a handling control. Animals were placed on the investigator's lap, with the coil held against the top-left side of the animal's head for the duration of the treatment session. The coil

was placed between the left eye and ear to target the left prefrontal cortex to reflect clinical protocols used for human patients. Each treatment session was conducted during the afternoon, commencing between 12:00-13:30. Stimulation protocols for standard and accelerated LI-rTMS groups are described in “study overview”.

7.2.5. Behavioural testing

7.2.5.1. Elevated Plus Maze

Animals first underwent the Elevated Plus Maze (EPM) test (see Walf and Frye (2007) for full protocol) to assess the presence of anxiety-related behaviours. Animals were placed in the centre of a plus-shaped maze, facing an open arm, and allowed to explore the maze for 5 minutes.

7.2.5.2. Sucrose Preference Test

The Sucrose Preference test was conducted following the EPM, but yielded unreliable results as previously reported (Seewoo et al., 2020a). Protocol is described in supplementary information.

7.2.5.3. Forced Swim Test

The Forced Swim Test (FST) was conducted last in the sequence of behavioural tests and followed the protocol by Slattery and Cryan (2012), to evaluate learned-helplessness. Animals were individually placed in white, opaque 20L buckets (height = 41cm, diameter = 28cm) filled with water to depth of 30cm. Water temperature was regulated to 23-25°C. Animals swam freely for 6 minutes, after which they were removed from the buckets, dried with a towel, and returned to their home cages. Prior to the first test, animals were exposed to the test conditions in a pre-test (Slattery and Cryan, 2012), where they were placed in water for 10 minutes.

7.2.5.4. Analysis

For the EPM and FST, behaviour was recorded using a GoPro Hero7 (GoPro, Inc.) camera and the footage analysed offline (full 5 minutes for the EPM, the first 5 minutes for the FST) by a trained experimenter blind to condition and time point. For the EPM, exploration was determined through the number of exits and time spent in the open and closed arms. Number of occurrences and time spent exhibiting rearing and grooming behaviours were also measured to quantify stress responses. In the event that an animal fell off the maze, it was quickly placed back on the maze (in the starting position) to resume the test (therefore retaining full exposure to the test) but the session was excluded from the analyses. For the FST, the video was split into 5 second segments. Each segment was analysed to determine the predominant behaviour. Behaviours were classified as either climbing, swimming, or immobility behaviours. Latency to the first segment with predominant immobility was also determined.

7.2.6. Magnetic Resonance Imaging

7.2.6.1. Anaesthesia

Magnetic resonance imaging (MRI) was used to characterise the functional, chemical and structural changes occurring in the brain. Imaging sessions were conducted in the two days following the Forced Swim Test. Animals were placed in an induction box containing 4% Isoflurane in medical air, then transferred to the MRI machine as described previously (Seewoo et al., 2020a). Isoflurane was slowly reduced to 2% and 0.05 mg/kg bolus dose and continuous 0.15 mg/kg/hr infusion of medetomidine were delivered subcutaneously. The concentration of isoflurane was gradually decreased to 0.5-0.75% for resting-state functional MRI (rs-fMRI) data collection. At the conclusion

of the imaging session, animals were returned to their home cage and a 0.15mg/kg subcutaneous injection of atipamezole was administered as a medetomidine reversal agent.

7.2.6.2. MRI protocol

Images were acquired using a 9.4 T (400MHz; H-1) Bruker Biospec 94/30 US/R pre-clinical MRI machine (Bruker BioSpin GmbH, Germany). A BGA-12SHP imaging gradient system and Avance III console were operated using ParaVision 6.0.1 software. A 72mm-diameter (pilot) and 86mm-diameter (main study) volume transmit coil, and rat brain surface quadrature receiver head coil were also used. To acquire the scans, we followed a previous imaging protocol, as detailed in (Seewoo et al., 2018b; Seewoo et al., 2020a). First, an anatomical localiser scan was obtained, followed by a multi-slice 2D rapid acquisition with relaxation enhancement (RARE) sequence for three T2-weighted anatomical scans (21 coronal slices, 21 axial slices, 20 sagittal slices, 1mm thickness; TE = 33ms, TR = 2500ms; 280 x 280 matrix; 0.1 x 0.1mm² pixel size). For 1H-magnetic resonance spectroscopy, a point resolved spectroscopy (PRESS) sequence consisting of a 90° pulse followed by two 180° pulses and water suppression was obtained (64 averages; TE = 16ms, TR = 2500ms), using a single voxel (3.5 x 2 x 6mm³) placed over the left sensorimotor cortex (for consistency with locations chosen in human studies; as discussed in (Seewoo et al., 2020a)). For the rs-fMRI, single-shot gradient echo planar imaging was acquired (21 coronal slices, 1mm thickness; TE = 11ms, TR = 1500ms; 94 x 70 matrix; 0.3 x 0.3mm² pixel size; 90° flip angle; 300 volumes; first order automatic ghost correction; 300kHz receiver bandwidth).

7.2.6.3. Data Analysis

All MRI data was processed and analysed as previously described in Seewoo et al. (2020a).

All rs-fMRI data was pre-processed and analysed using FSL v5.0.10 (Functional MRI of the Brain (FMRIB) Software Library) (Jenkinson et al., 2012) and following the data analysis pipeline detailed in Seewoo et al. (2021a). Multi-subject temporal concatenation group-ICA and FSL dual regression analysis was conducted (see supplementary information), followed by seed-based analysis using the atlas mask for the cingulate cortex. Higher-level analysis was carried out using OLS (ordinary least squares) simple mixed-effects (Beckmann et al., 2003; Woolrich et al., 2004; Woolrich, 2008) in atlas space. Z (Gaussianised T/F) statistic images were thresholded non-parametrically using clusters determined by $z > 2$ and a (corrected) cluster significance threshold of $p = 0.05$ (Worsley, 2001a).

To assess hippocampal volume, the three T2-weighted anatomical (coronal, sagittal and axial) data were pre-processed as above and then registered to the high-resolution atlas (no downsampling). Atlas masks for bilateral hippocampus (including cornu ammonis and dentate gyrus) and whole-brain (grey matter, white matter and cerebrospinal fluid) were transformed to each individual animal's anatomical space. The 'fslstats' command was used to extract bilateral hippocampal volumes and whole-brain volumes from each of the three planes. Hippocampal and whole-brain volumes from the three planes were averaged for each animal scan session. Hippocampal volume was normalised to whole brain volume to adjust for differences in head size, as

previously described by Welniak–Kaminska et al. (2019). All hippocampal volume results presented here are expressed as a percentage of whole-brain volume.

¹H-MRS data were analysed in LCModel (“Linear Combination of Model spectra” version 6.3-1L) (Provencher, 2001) using a simulated basis set provided by the software vendor. Individual metabolite concentrations were computed using the unsuppressed reference water signal for each individual scan. Cramér-Rao lower bound (CRLB) values were calculated by LCModel and reported as percent standard deviation of each metabolite, as a measure of the reliability of the metabolite estimates. The metabolites of interest were γ -aminobutyric acid (GABA), glutamate (Glu), glutamine (Gln), and combined glutamate-glutamine (Glx). All ¹H-MRS results are expressed as a ratio to tCr (total creatine = Cr + PCr) spectral intensity, the simultaneously acquired internal reference peak (Block et al., 2009; Walter et al., 2009; Xu et al., 2013a).

Statistical Analysis

Statistical analysis was conducted using SPSS (v. 21, IBM Corporation, Armonk, New York, USA), RStudio (v. 4.0.2), RStudio Team, Boston, Massachusetts, USA), and DABEST (via <https://estimationstats.com>), with figures created and directly downloaded from <https://estimationstats.com>.

Paired student’s t-tests and Wilcoxon signed ranks tests (for non-parametric data) were used to assess the effect of the chronic restraint stress model on all behavioural measures and MRI outcomes compared to baseline. Mixed model analysis of variance (ANOVA) was used to test the effect of treatment group and timepoint for both behavioural tests and change in functional connectivity, hippocampal volume, and

metabolite levels. Visual inspection of QQ plots was used to assess normality. All variables met the assumption of normal distribution except the following behavioural measures: open arm exit count, time spent in open arms, time spent grooming, and climbing count. These variables were then log transformed to meet normality. Follow-up Tukey's HSD and Games-Howell *post hoc* tests were used to account for multiple comparisons.

Estimation statistics based on confidence intervals (CI) and 5000 bootstrap samples were conducted to further assess the data over time within each treatment group. *P* values represent the likelihood of observing the effect sizes, with Cohen's *d* used to measure effect size (with the exception of the behavioural test multi-paired plots, which instead used the paired median difference due to a large number of animals recording zero counts and thus a non-normal distribution).

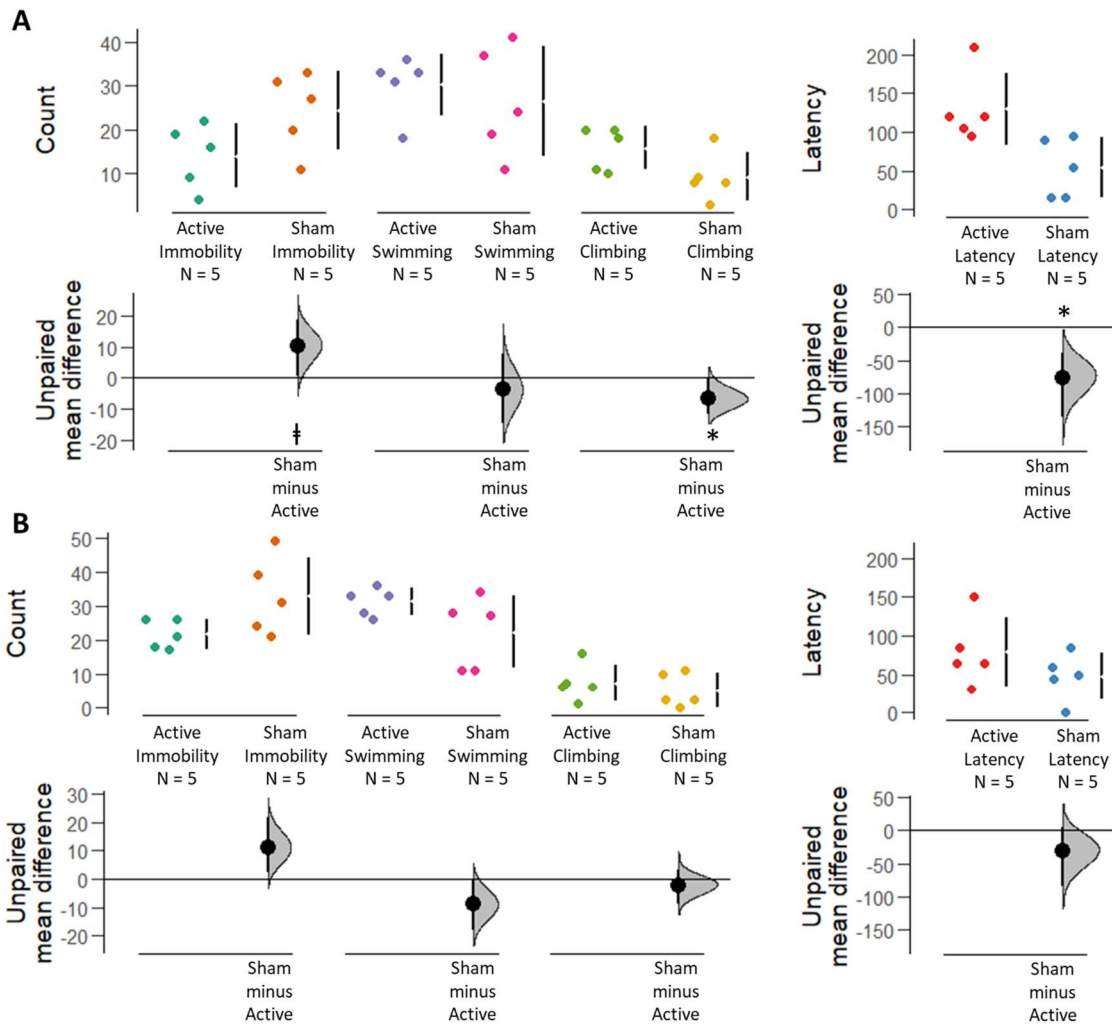
All measurements are presented as mean \pm SEM unless otherwise specified, and the level for statistical significance was set at $p < .05$.

7.3. Results

7.3.1. Short-term Pilot Study: Standard vs Accelerated Treatment

A pilot test was conducted, comparing the short-term efficacy of a standard once-daily protocol of rTMS treatment delivery versus an accelerated three times daily timeline (Figure 7.2). Behaviour was assessed at the end of treatment using a Mann-Whitney *U* test. In the Forced Swim Test, the group receiving active stimulation following the accelerated (3-times daily) protocol had a significantly longer latency until the first immobility count ($M = 130.00$, $SD = 45.96$) compared to the sham group ($M = 54.00$, $SD = 38.79$; $p = .011$), and a significantly higher total climbing count in the active group (M

= 15.80, $SD = 4.92$) compared to sham ($M = 9.20, SD = 5.45; p = .035$). Additionally, the active group showed a trend towards less immobility ($p = .076$). In the Elevated Plus Maze, there were no significant differences between active and sham groups, however there was a trend for more grooming in the active group ($p = .059$). Unlike the accelerated treatment, the standard (once-daily) protocol found no significant differences ($p > .05$) between the active and sham groups for any of the behaviours in the FST and EPM.



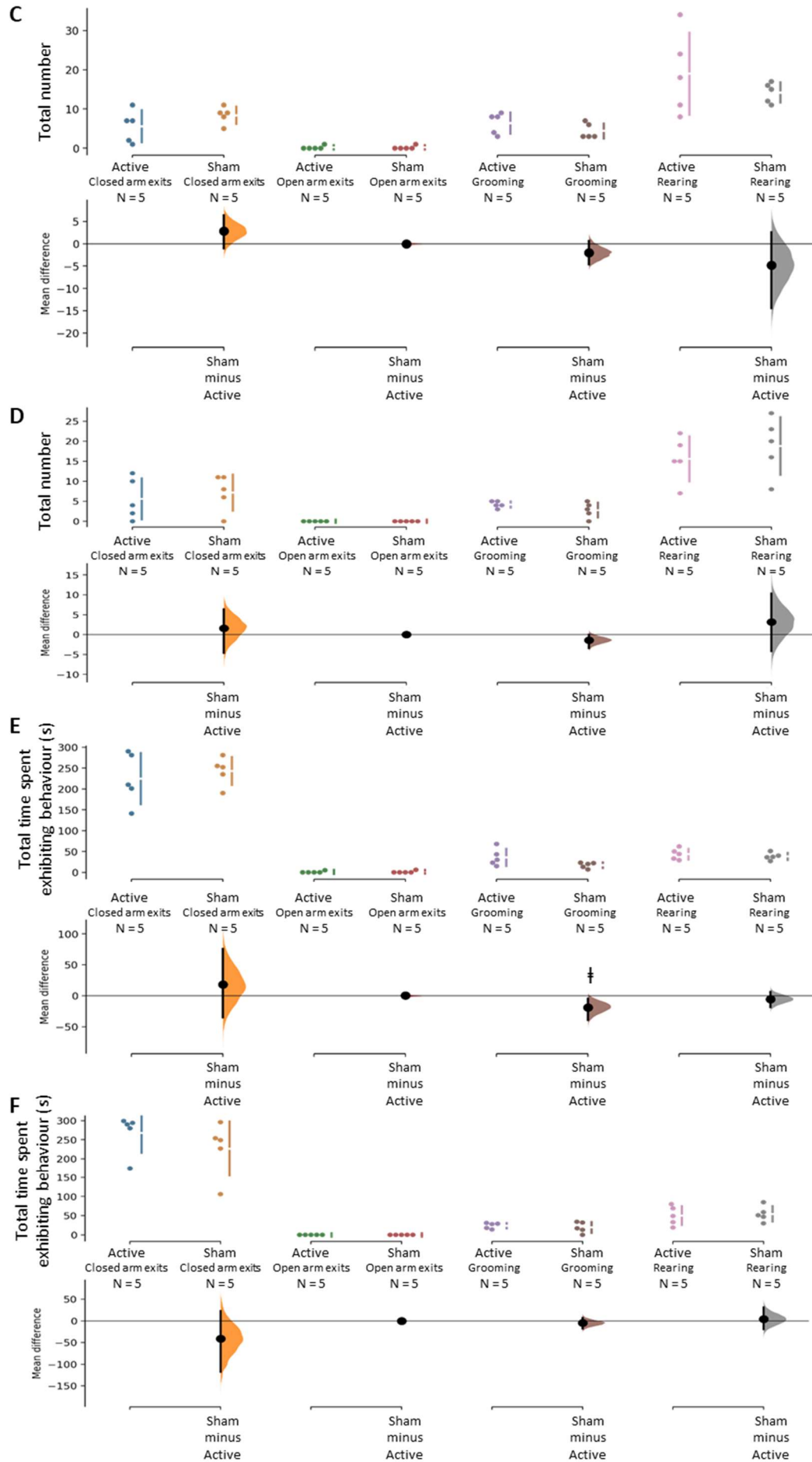


Figure 7.2. Comparisons of depression and anxiety-related behaviours during forced swim test (A-B) and elevated plus maze test (C-F) between active and sham groups of the accelerated (A, C, E) and standard (B, D, F) LI-TMS protocols. The figure shows total count of behaviours and total time taken to exhibit the first immobility count (seconds) following the accelerated protocol (B) and standard protocol (B) during the forced swim test, and total count of behaviours and total time spent (seconds) exhibiting behaviours following the accelerated protocol (C and E, respectively) and standard protocol (D and F, respectively) during the elevated plus maze test. Raw data are plotted on the top section of the estimation plot, with unpaired mean difference for the comparisons on the bottom. The bootstrap sampled distributions are shown via bolded vertical lines, with the centre circle indicating the average mean difference, and non-bolded ends representing error bars for the 95% CIs. † $p < 0.1$, * $p < 0.05$

These results indicate that there was a significant decrease in learned helplessness and a trend towards a decrease in anxiety-related behaviour during the treatment period following the accelerated (3-times daily) protocol. However, there were no significant differences between groups following the standard (once-daily) treatment protocol. We therefore chose to continue with a full longitudinal study using the accelerated treatment protocol.

7.3.2. Main Study – extended longitudinal study of accelerated LI-rTMS following chronic restraint stress

7.3.2.1. Baseline vs Post-CRS

We first compared brain and behaviour changes in rats at baseline and immediately following CRS to confirm that our intervention had induced changes associated with depression and anxiety-like conditions as previously published (Suvrathan et al., 2010; Chiba et al., 2012; Seewoo et al., 2020a). Assessment of rs-fMRI data using seed-based analysis identified a reduction in functional connectivity between the cingulate cortex and a range of regions following CRS ($t_{47} = 8.1116$, $p < .001$; Figure 7.3). However, in contrast to our previous findings, the percentage of total hippocampal volume did not change immediately following CRS compared to baseline levels (Baseline: $M = 5.865\%$, $SE = 0.005$; Post-CRS: $M = 5.873\%$, $SE = 0.008$; $p = .356$). In addition, individual left or

right hippocampal volumes did not change post-CRS timepoints (left $M = 2.903 \%$, $SE = 0.004$, $p = 0.247$; right $M = 2.971 \%$, $SE = 0.004$; $n = 49$; $p = .630$). There were also no significant changes in any measured neurometabolite levels following CRS ($p > .05$) (not shown; see supplementary material information).

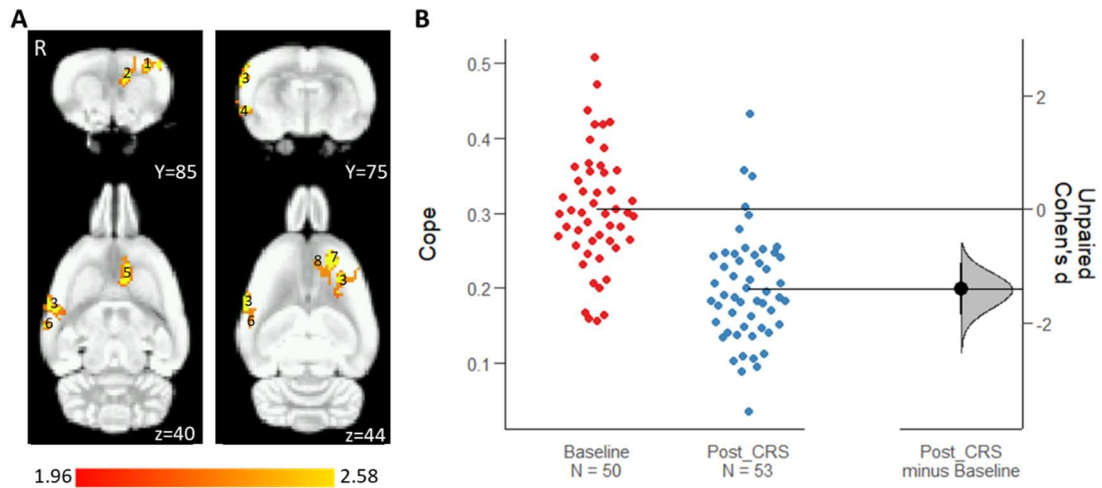


Figure 7.3. Comparisons of functional connectivity to the cingulate cortex between baseline and post-CRS timepoints assessed via seed based analysis (A) and Cumming estimation plot (B). A. Seed based analysis using cingulate cortex seed. The figure displays coronal and axial slices of spatial statistical colour-coded maps overlaid on the rodent brain atlas, with resting-state networks represented as z scores ($1.96 < z < 2.58$) corrected for multiple comparisons at cluster level (thresholded at $p < 0.05$). The numbers on the right refer to the slice position on the atlas. R denotes right hemisphere. Significant differences were found in: 1, motor cortex; 2, cingulate cortex; 3, somatosensory cortex; 4, insular cortex; 5, infralimbic cortex; 6, auditory cortex; 7, frontal association cortex; and 8, prelimbic cortex. B. Average COPE extracted from individual animals' functional connectivity to the cingulate cortex is plotted on the left of the estimation plot, with unpaired Cohen's d for the two comparisons on the right. The bootstrap sampled distribution is shown via bolded vertical lines, with the centre circle indicating the mean difference, and non-bolded ends representing error bars for the 95% CIs.

Behavioural changes following CRS confirmed that anxiety and depression-like behaviours had been successfully induced (Seewoo et al., 2020a). In the Elevated Plus Maze, there was a significant increase in the number of exits out of both the closed arms (Baseline $M = 6.82$, $SE = 0.59$; Post-CRS $M = 9.33$, $SE = 0.48$; $n = 52$; $Z = -3.375$, $p = .001$) and open arms (Baseline $M = 0.63$, $SE = 0.18$; Post-CRS $M = 1.04$, $SE = 0.19$; $n = 51$; $Z = -1.698$, $p = .089$) following CRS (Figure 7.4). There was also a significant decrease in the total amount of time spent in the closed arms (Baseline $M = 220.37$, SE

= 4.88; Post-CRS $M = 193.21$, $SE = 6.96$; $n = 52$; $t_{51} = 3.771$, $p < .001$), and a significant increase in total time spent in the open arms (Baseline $M = 3.72$, $SE = 1.50$; Post-CRS $M = 9.64$, $SE = 2.18$; $n = 50$; $Z = -2.562$, $p = .010$). Additionally, there was an increase in number of times the animals exhibited grooming behaviours (Baseline $M = 2.59$, $SE = 0.29$; Post-CRS $M = 3.59$, $SE = 0.33$; $n = 51$; $Z = -2.148$, $p = .032$). However, there were no significant changes in total time spent grooming, number of times demonstrating rearing behaviour, or total time spent rearing. In the Forced Swim Test, there was a significant decrease in swimming compared to baseline levels (Baseline $M = 31.64$, $SE = 2.16$; Post-CRS $M = 24.81$, $SE = 2.12$; $n = 36$; $t_{35} = 3.142$, $p = .003$; Figure 7.4). There was also an increase in immobility and a reduced latency to the first immobility score, although these differences were not significant. There were no significant differences found for climbing behaviour.

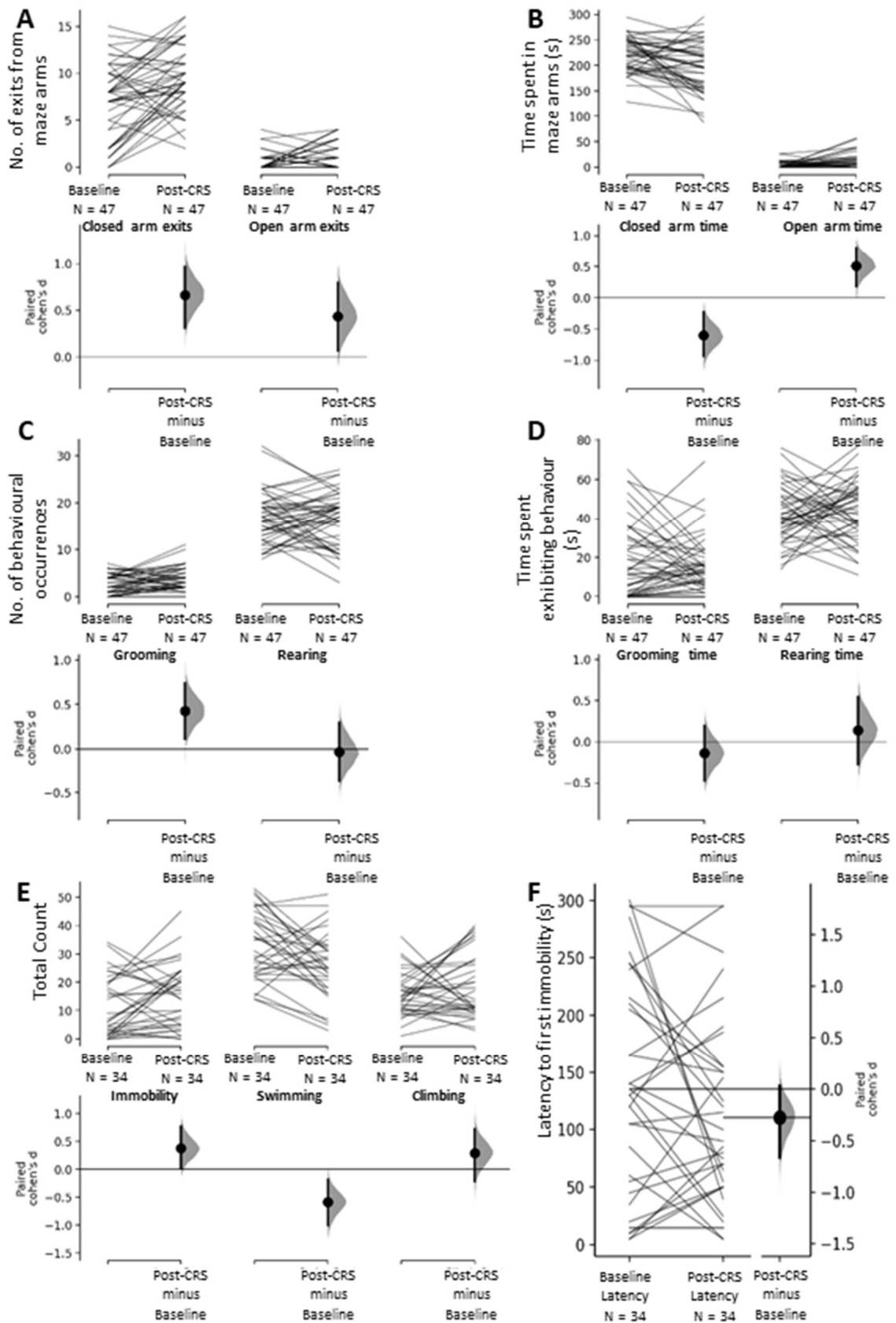


Figure 7.4. Comparisons of depression-related behaviours at baseline and post-CRS timepoints from the Elevated Plus Maze (A-B) and Forced Swim Test (C-E). A. Total number of exits into closed and open arms (i.e., exploration behaviour). B. Total time spent (sec) in closed and open arms (i.e., exploration behaviour). C. Total number of times and total

time spent exhibiting anxiety-related behaviours (grooming and rearing behaviours). D. Total count of immobility, swimming, and climbing behaviours. E. Time taken to exhibit the first immobility count. Raw data is plotted on the top segment of the estimation plots, with paired data points connected via a line. Paired Cohen's d for the two comparisons are shown in the bottom segment* of the Cumming estimation plots (*NB: right side in E). Bootstrap sampled distributions are shown via bolded vertical lines, with the centre circle indicating the mean difference, and non-bolded ends representing error bars for the 95% CIs.

7.3.2.2. rTMS Treatment and long-term outcomes

Having confirmed that CRS had induced brain and behavioural changes associated with depression and particularly anxiety-like symptoms, we then allocated animals to one of three groups and delivered accelerated rTMS treatment, accelerated sham treatment, or no intervention for 2 weeks. MRI and behavioural outcome measures were monitored weekly during, and for 2 weeks following treatment.

7.3.2.2.1. Resting-state fMRI

Using seed-based analysis of fMRI data, the mixed model ANOVA found a significant main effect of timepoint on functional connectivity to the cingulate cortex ($F_{5,254.765} = 13.0303$, $p < .001$), but no main effect of treatment or interaction between the two variables suggesting that brain connectivity changed over time in all rats, but this was not affected by accelerated LI-rTMS (Figure 7.5).

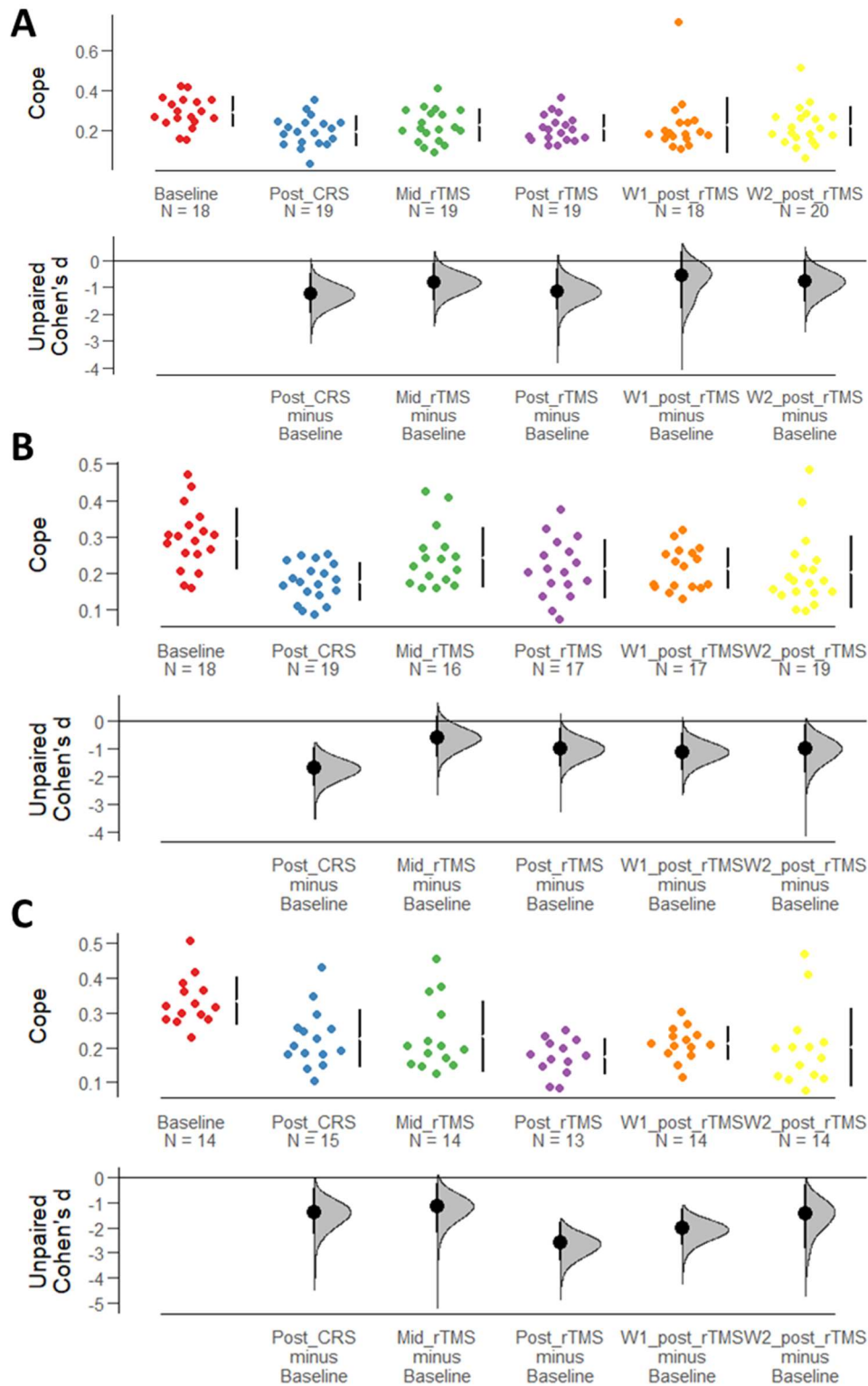


Figure 7.5. Comparisons of functional connectivity to the cingulate cortex across all timepoints for active treatment (A), sham treatment (B) and depression control (C) conditions. Data is displayed as a Cumming estimation plot. Raw data is plotted on the top section of the estimation plot, with unpaired Cohen's d for the comparisons to baseline on the bottom. The bootstrap sampled distribution is shown via bolded vertical lines, with the centre circle indicating the mean difference, and non-bolded ends representing error bars for the 95% CIs.

7.3.2.2.2. Hippocampal volume

The mixed model ANOVA found a significant main effect of timepoint on total hippocampal volume ($F_{5,260.518} = 3.5139, p = .004$), but no main effect of group or interaction between the two variables. Similarly, when left and right hippocampal volumes were analysed separately, the mixed model ANOVA found a significant main effect of timepoint for both left ($F_{5,260.973} = 2.4694, p = .033$) and right hippocampal volumes ($F_{5,260.51} = 3.4140, p = .005$), but no main effect of group or interaction between the two variables. These data suggest that hippocampal volume slightly increased over time following CRS, and that this was not affected by accelerated LI-rTMS (Figure 7.6).

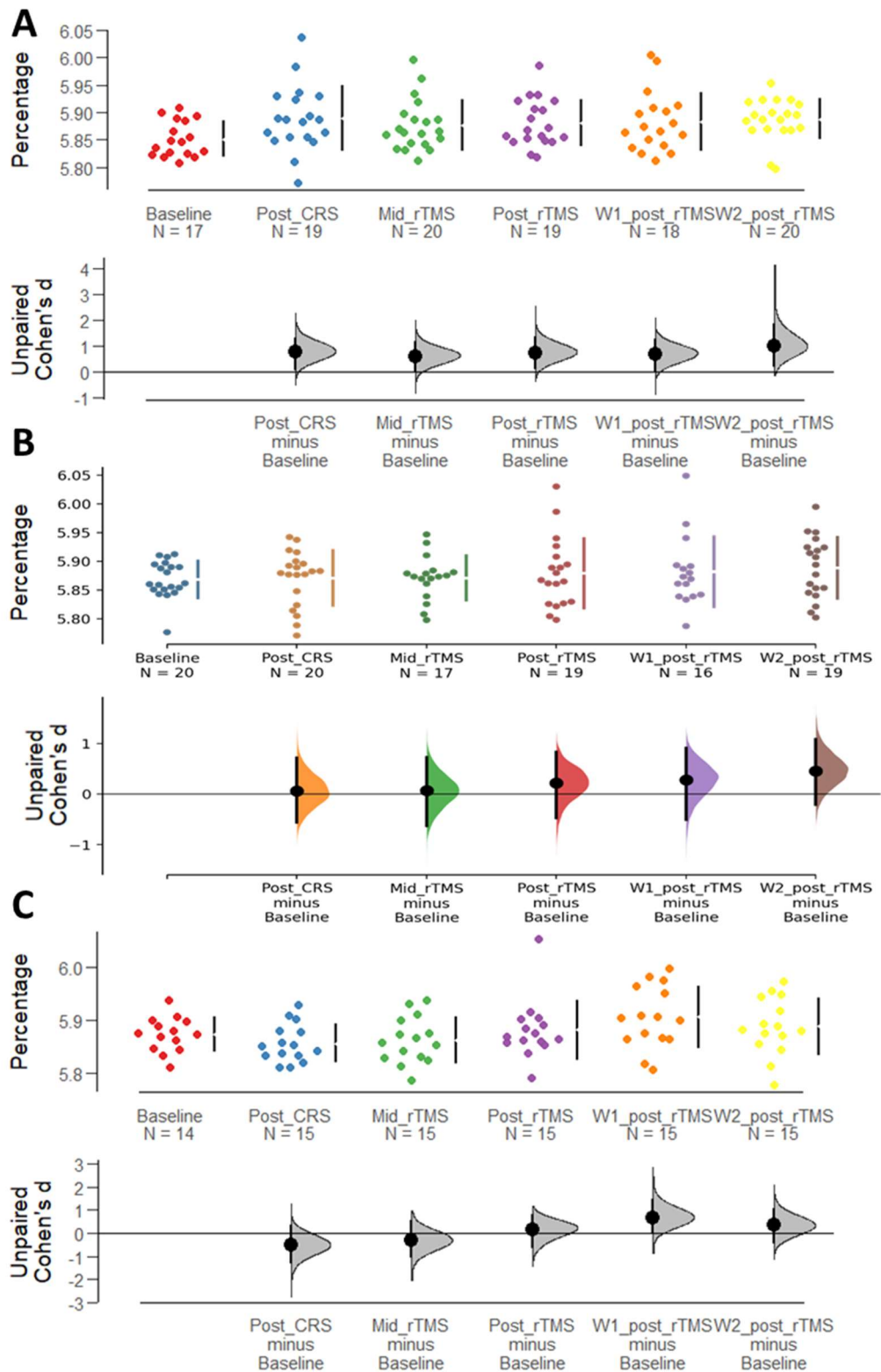
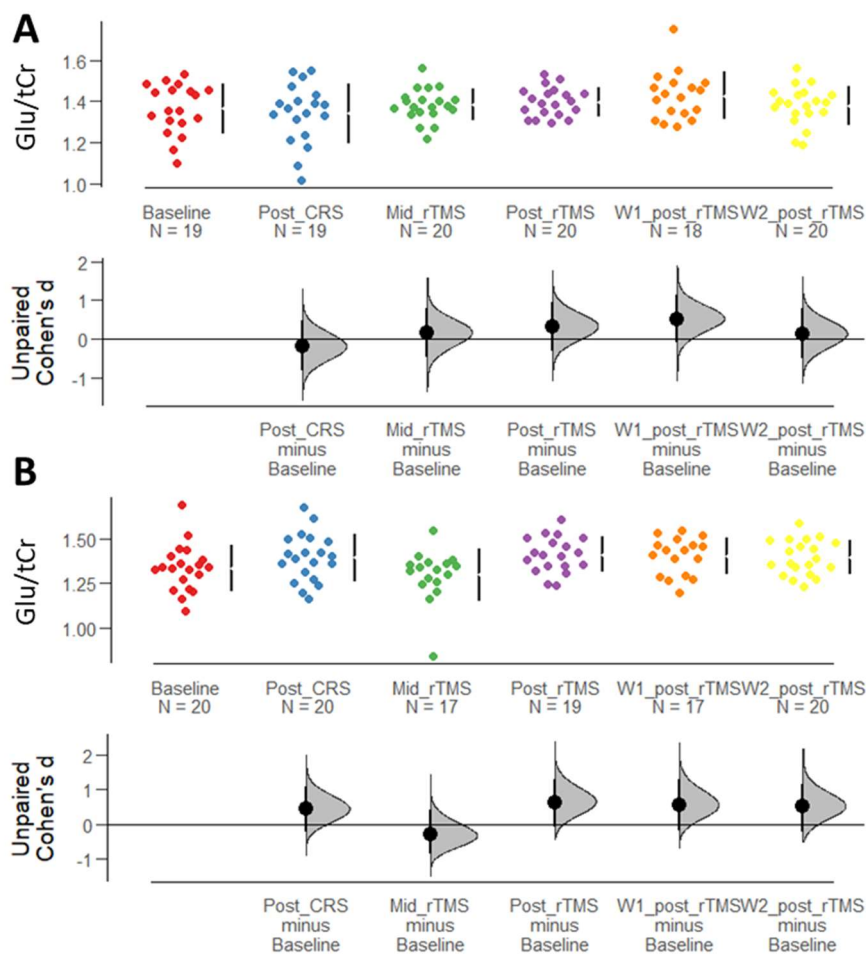


Figure 7.6. Comparisons of total hippocampal volume across all timepoints for active treatment (A), sham treatment (B) and depression control (C) conditions. Data is displayed as a Cumming estimation plot. Raw data is plotted on the top section of the estimation plot, with unpaired Cohen's *d* for the comparisons to baseline on the bottom. The bootstrap sampled distribution is shown via bolded vertical lines, with the centre circle indicating the mean difference, and non-bolded ends representing error bars for the 95% CIs.

7.3.2.2.3. ¹H Magnetic Resonance Spectroscopy

The levels of γ -aminobutyric acid (GABA), glutamate (Glu), glutamine (Gln) and combined glutamate-glutamine (Glx) were measured in the sensorimotor cortex across all timepoints and determined as concentrations relative to tCr. A mixed model ANOVA was used to compare the levels across all conditions and timepoints. There was a significant main effect of timepoint on the levels of Glu ($F_{5,264.98} = 3.2163, p = .008$), but not for GABA, Gln, or Glx ($p > .05$). There was no main effect of group or significant interaction found for any of these recorded metabolites. The data suggest that there were small fluctuations in glutamate over time, that were not affected by accelerated LI-rTMS (Figure 7.7).



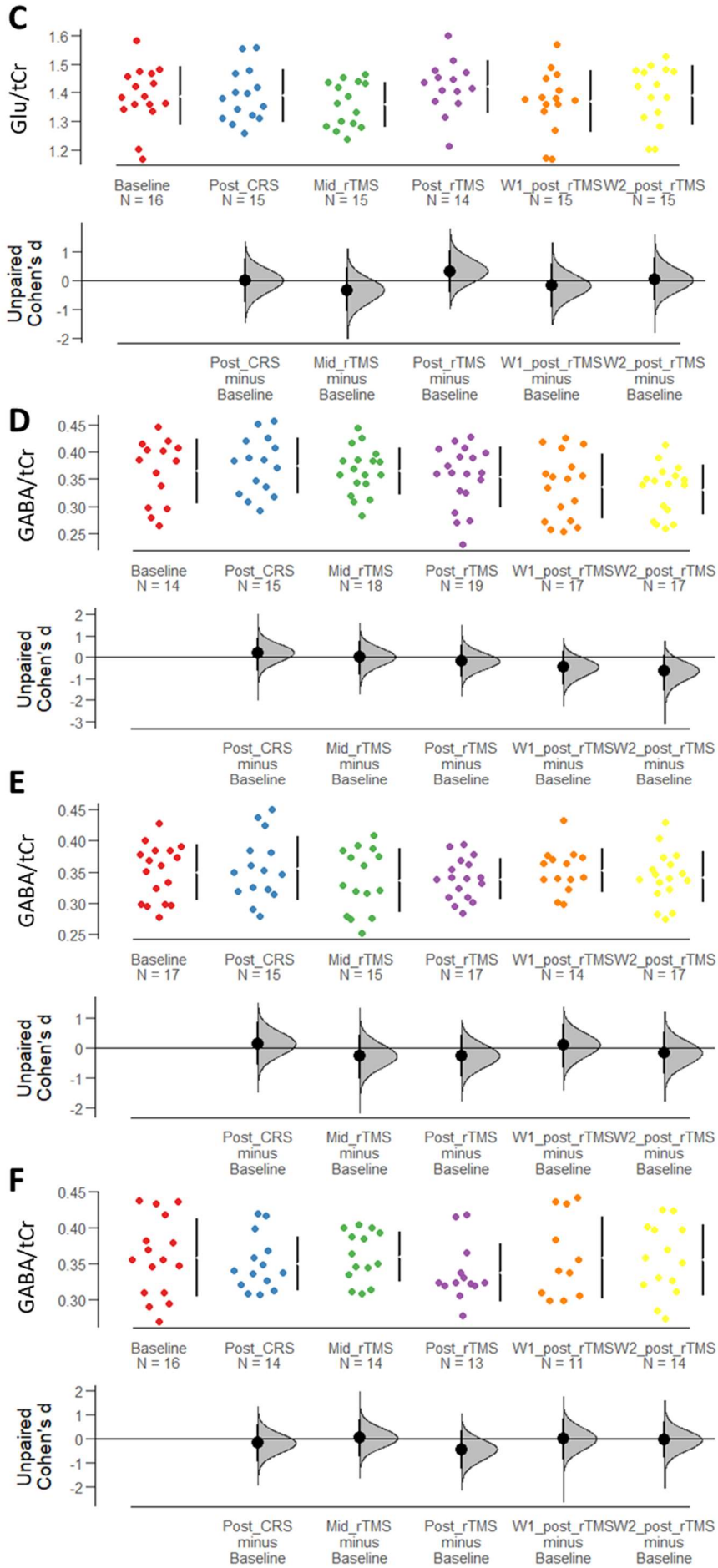


Figure 7.7. Concentration levels across all timepoints for Glutamate (Glu) (A-C) and GABA (D-F). Levels of Glutamate are shown within active (A), sham (B) and depression control (C) conditions. Levels of GABA are shown within active (D), sham (E) and depression control (F) conditions. Data is displayed as a Cumming estimation plot. Raw data is plotted on the top section of the estimation plot, with unpaired Cohen's d for the comparisons to baseline on the bottom. The bootstrap sampled distribution is shown via bolded vertical lines, with the centre circle indicating the mean difference, and non-bolded ends representing error bars for the 95% CIs.

7.3.2.2.4. Behaviour

Consistent with the results from MRI, there was no clear effect of LI-rTMS on behaviour following CRS. In the Elevated Plus Maze, the mixed model ANOVA found a significant interaction between treatment group and timepoint for total time spent grooming ($F_{10,115} = 1.99, p = .041$), but with no significant simple main effects. There were no interactions found for the other variables, however a main effect of timepoint was found for total time spent in closed and open arms, total exits from closed and open arms, and total count of grooming behaviours (Figure 7.8). No variables showed an effect of treatment on behaviour in the EPM.

For the Forced Swim Test, there was a significant interaction between treatment group and timepoint for swimming ($F_{7.20,112.94} = 2.18, p = .039$), with a significant simple main effect of timepoint ($F_{3.64, 112.94} = 3.33, p = .016$), but no significant simple main effect of treatment group. However, there were no significant interactions or main effects found for the other variables (Figure 7.8).

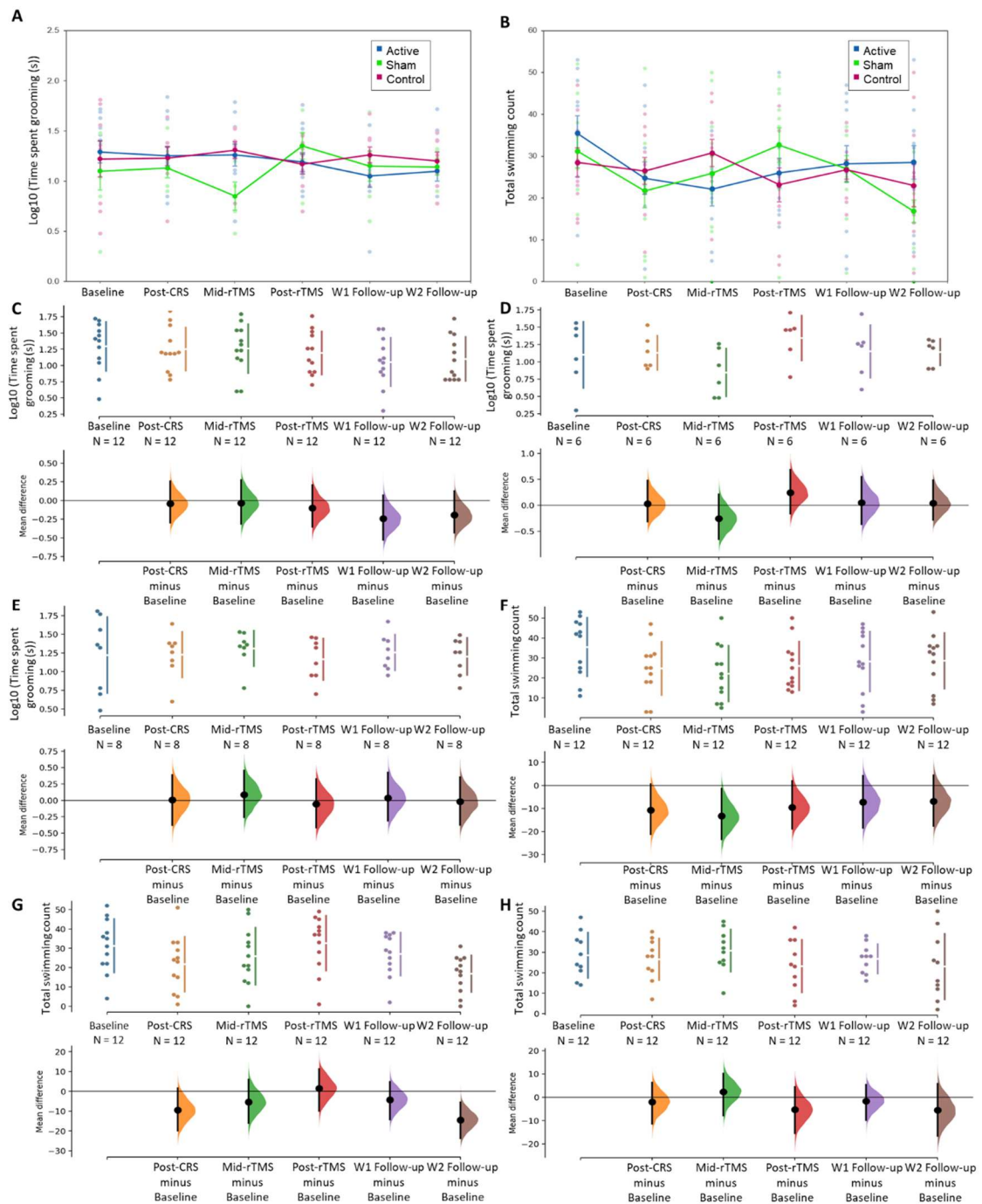


Figure 7.8. Behaviours with significant interactions from the Elevated Plus Maze (A-D) and Forced Swim Test (E-H) displayed across all timepoints. Total time spent exhibiting grooming behaviour (A-D) shown across all conditions (A), and individually for active (B), sham (C) and depression control (D) conditions. Total count of swimming (E-H) shown across all conditions (E), and individually for active (F), sham (G) and depression control (H) conditions. Data is displayed as a line graph (A, E) and Cumming estimation plots (B-D, F-H). Raw data is plotted on the top section of the estimation plot, with unpaired Cohen's *d* for the two comparisons on the bottom. The bootstrap sampled distribution is shown via bolded vertical lines, with the centre circle indicating the mean difference, and non-bolded ends representing error bars for the 95% CIs.

7.4. Discussion

rTMS is an established and valuable tool for treating patients with major depressive disorder. However, there is scope for improvement in the delivery and outcomes through optimisation and tailoring of treatment parameters. Building on our previous work studying LI-rTMS effects in healthy adult rats, our aim in the present study was to evaluate standard vs accelerated LI-rTMS protocols on brain and behavioural outcomes in a rat model of depression. However, although the accelerated protocol out-performed the standard protocol in our pilot study, therapeutic effects were not detected in our extended longitudinal study which used slightly older animals. In addition, differences in the outcomes following CRS in our experiments compared to previous studies suggest that the response to CRS and potentially rTMS may depend on the age of the animals. Overall, our results suggest that there may be some benefit of accelerated LI-rTMS in rescuing anxiety-like behaviours induced following CRS in young adolescent male rats (pilot study). However, these benefits were not observed in animals that were slightly older by roughly 50g (~ 1 week; main study). Our findings highlight that it will be important to take into account the developmental state of the brain when designing interventions for pediatric neuromodulation.

7.4.1. Decreased functional connectivity and behavioural response following Chronic Restraint Stress

Abnormal functional connectivity is a common characteristic of depression and anxiety in human patients (Kim et al., 2011; Hilbert et al., 2014; Kaiser et al., 2015; Mulders et al., 2015), with the cingulate cortex generally showing increased functional connectivity with regions in the limbic system, resulting in deficits in moderating and regulating the processing of emotion in mood disorders (Greicius et al., 2007; Davey et

al., 2012; Connolly et al., 2013; Mulders et al., 2015; Rolls et al., 2018). Similarly, following chronic restraint stress in rodents, we and others have previously demonstrated decreased functional connectivity within the salience and interoceptive networks, and hyperconnectivity of multiple regions to the cingulate cortex (Seewoo et al., 2020a). However, in the current study, we instead identified a decrease in connectivity between the cingulate cortex and several brain regions.

The most likely explanation is that here we used animals that were 1-2 weeks younger than those used in our previous study (Brust et al., 2015). Younger animals were expressly used in the present study to allow them to fit in the MRI imaging cradle at the latest timepoint imaged. However, behavioural responses to stress are known to vary non-linearly across developmental periods in rodents: although novelty exploration in the EPM generally decreases with age, adolescent animals are less anxious and more explorative than both juvenile and young-adult animals (Macrì et al., 2002). Furthermore, the impact of a stressor on EPM behaviours is stronger in adolescent mice compared to young adult mice (Stone and Quartermain, 1997). Overall, behavioural responses can vary greatly in immature rodents (Brust et al., 2015), and this is likely to explain the difference in outcomes following CRS between our previous and current studies.

An interesting finding in our experiments is that the changes induced by CRS are more compatible with changes related to anxiety, and less suggestive of depression-like behaviours. Whilst hypoconnectivity of regions to the cingulate cortex is not generally reported in depression studies, a decrease in connectivity between various regions has previously been seen in human patients with trauma and/or anxiety (Hahn et al., 2011;

Kennis et al., 2015; Chang and Yu, 2018; Chen et al., 2018). The lack of change in hippocampal volume and metabolite concentrations further support that the animals in this study might have developed phenotypes that were higher in anxiety and stress, than in depression.

The presence of an anxious phenotype was further supported by the results of behavioural tests. In addition to an increase in inactive behaviours and a reduction in active behaviours in the Forced Swim Test, suggesting an increase in learned-helplessness, animals unexpectedly showed an increase in locomotor activity in the EPM, potentially reflecting heightened agitation and hyperactivity. An increase in anxiety and agitation is also consistent with other translational animal models of depression, such as olfactory bulbectomy in mice (Masini et al., 2004; Wang et al., 2007; Heath et al., 2018), and with clinical symptoms of depression in human patients (Angst et al., 2009; Iwanami et al., 2015; Serra et al., 2019). However, psychomotor agitation is also a common symptom of anxiety disorders, particularly when comorbidities of anxiety and mood disorders are present (Zbozinek et al., 2012; Kaiser et al., 2021). Taken together with the decreased connectivity suggested by rs-MRI, the behavioural outcomes reported here suggest that CRS in young rats causes an anxiety-like phenotype.

7.4.2. Accelerated LI-rTMS did not affect connectivity, hippocampal volume, metabolites or behaviour

We did not observe any changes in our brain or behavioural measures following accelerated LI-rTMS in the main study. This was surprising given the results from our pilot study suggesting that just one week of accelerated rTMS rescued the effects of CRS. We cannot rule out that the pilot study produced false positive result due to a

relatively small sample size ($n = 5$ per group), or that the reduced statistical power due to multiple timepoints in the main study resulted in a false negative, despite the larger group size of $n=12$. Interestingly, where previous studies have shown large behavioural changes following sham stimulation attributed to handling effects (Neely et al., 2018; Rittweger et al., 2021), the current study observed only mild fluctuations that did not reach significance.

An alternative explanation is that the pilot cohort was roughly 1 week younger compared to the main cohort due to availability of animals from the supplier, and thus may have responded differently to LI-rTMS. Further supporting a confounding effect of age in our experiments, we found that the phenotype induced in the main cohort showed features that were more related to anxiety than to depression, and the efficacy of rTMS in treating anxiety is not established. A further concern is that significant brain growth continues to occur until approximately 9 weeks of age (Bandeira et al., 2009), with certain regions still developing up to 11 weeks of age (Fu et al., 2013). The continuing maturation of the brain likely underpins the significant effect of timepoint observed across almost all of the measures in our study, and raises the possibility that conflicting impacts of CRS, rTMS and concurrent age-related brain maturation changes might have masked changes. It will be important to further examine the effect of rTMS protocols using older animals in order to assess the effects in animals after cerebral and behavioural development is complete.

It is also possible that LI-rTMS was applied at an intensity that was too low to have an effect. In a previous study directly comparing stimulation intensities, only the medium intensity (50mT – roughly twice as strong as the current LI-rTMS) and high intensity (1

T) protocols caused behavioural changes, while LI-rTMS at 10 mT had no effect (Heath et al., 2018). Nonetheless, it is well established that intensities lower than 20 mT alter brain structure and function in healthy rats, in non-psychiatric mouse models of disease and in drosophila (Rodger et al., 2012; Makowiecki et al., 2014; Poh et al., 2018; Sherrard et al., 2018; Dufor et al., 2019; Seewoo et al., 2019c). However, these studies have mostly targeted brain regions that are superficially located such as cortex and cerebellum (Makowiecki et al., 2014; Dufor et al., 2019; Poh et al., 2019) and higher intensities may be necessary to stimulate the cortex strongly enough to modify downstream interconnected brain regions sufficiently to influence mood. rTMS in clinical studies involving psychomotor deficits have all used high intensity (> 1 T) (Baeken et al., 2010a; Hoepfner et al., 2010). It will be important to determine the intensity that is required to induce relevant change in depression as this will allow insight into the mechanisms that are involved in treating neuropsychiatric disorders.

7.4.3. Conclusion

Overall, our study suggests that accelerated 10 Hz low-intensity rTMS is not an effective treatment for the anxiety phenotypes induced in adolescent rats by chronic restraint, but may be more effective in younger animals. Future studies in young, mature, and aged animals are needed to develop age-specific protocols that can help increase the efficiency of translational pipelines and ensure that patients receive optimal treatment with minimal time and financial costs.

7.5. Supplementary Material

7.5.1. Full Behavioural Methods

7.5.1.1. Elevated Plus Maze

Animals first individually underwent the Elevated Plus Maze (EPM) test (Walf and Frye, 2007) to assess the presence of anxiety-related behaviours. Animals were placed on a plus-shaped platform, elevated 60cm above the ground, with all four arms equally sized (50cm x 10cm). The platform comprised two perpendicular open arms (consisting of just the platform – i.e., no barriers), two closed arms (enclosed due to the presence of 40cm tall barriers around the three sides of the arm), and a shared centre area (10cm x 10cm). Animals were placed in the centre of the maze, facing an open arm, and able to explore the maze undisturbed for 5 minutes total. There was equal illumination across the maze, and minimal noise inside the experiment room so as to not disrupt or startle the animals and affect their behaviour. The maze was also cleaned with 70% ethanol after each test, to sanitise the maze and remove any lingering olfactory remnants from the previous animal. The test was monitored and recorded using a GoPro Hero7 (GoPro, Inc.) camera suspended approximately 120cm above the maze, after which the video recordings were used to conduct the analyses. In the event that an animal fell off the maze, animals were quickly placed back on the maze (in the starting position) to resume the test (therefore retaining full exposure to the test) but were excluded from the analyses.

7.5.1.2. Sucrose Preference Test

The Sucrose Preference Test (SPT) was conducted as two modified versions of previous protocols (Willner et al., 1987), to assess the animals' preference for consuming sucrose solution versus water as a behavioural assessment of anhedonia, one of the

symptoms of clinical depression. To habituate the animals to sucrose solution, 48 hours prior to the first preference test, the two 600mL water bottles in the animals' home cages were replaced with two 600mL bottles containing 1% sucrose solution. The rats still had access to *ad libitum* food and water during this time. Twenty-four hours prior to the first test, one bottle of sucrose solution was then replaced with a water-only bottle. The position of the bottles in the cage was swapped after 12 hours, to prevent the development of a left-right bias when the animals search for the sucrose bottle. Prior to each Sucrose Preference Test, the animals were single-housed upon completion of the EPM. Two versions of the test were then implemented.

The first group of animals (n = 35) were single-housed with *ad libitum* food and water. Sixteen hours before the test (at approximately 17:00 on the day of the EPM), animals then underwent overnight fasting of both food and water to prepare for the test. Immediately before the test (at approximately 09:00), one bottle of water and one bottle of 1% sucrose solution were weighed and placed in each of the cages. The left-right position of the bottles in the cage were swapped after 30 minutes. One hour after the start of the test, the bottles were removed and reweighed, and the animals were returned to their home cages (with food and water again provided *ad libitum*).

The second group of animals (n = 21) were single-housed with one bottle of 1% sucrose solution and one bottle of water (and *ad libitum* food) for habituation to the upcoming test. At approximately 17:00 (following the EPM), the bottles were weighed and placed back into the cages to begin the test. The test duration was 24 hours, with bottle position swapped approximately half-way through the test. At the conclusion of

the test, bottles were again removed and reweighed, and the animals returned to their home cages.

Using the recorded weights of the sucrose solution and water bottles before and after test, sucrose preference was calculated as a percentage, using the following formula: Sucrose preference = [sucrose consumption (g)] / [sucrose consumption (g) + water consumption (g)]. The mean percentage of sucrose preference for each time point was then examined. Upon analysis of the results, it was found that there were no significant changes between baseline and post-CRS timepoints, and thus the assessment did not adequately reflect anhedonic behaviour and was thus excluded from the main study.

7.5.1.3. Forced Swim Test

The Forced Swim Test (FST) was conducted according to the protocol by Slattery and Cryan (2012), to evaluate learned-helplessness. Twenty-four hours before the animals underwent the baseline Forced Swim Test, a pre-test was conducted to expose the animal to the test conditions prior to data collection. Animals were individually placed in white, opaque 20L buckets (height = 41cm, diameter = 28cm) filled with water to depth of 30cm. The depth ensured that the rats were not supporting themselves on the base of the bucket using their hind limbs or tails. Water temperature was regulated to 23-25°C. Animals swam freely for 10 minutes, after which they were removed from the buckets, dried with a towel, and returned to their home cages. Four animals were tested at the same time (one animal per bucket), with equal illumination across the testing area, and minimal noise inside the experiment room. The buckets were emptied, rinsed, and cleaned with 70% ethanol after each test. The Forced Swim

Test then followed the same procedure as the pre-test, but with a duration of only 6 minutes total. The test was conducted on the day following each Sucrose Preference Test. The test was monitored and recorded using a GoPro Hero7 camera suspended on a tripod approximately 50cm above the test area, and the recordings were used to later conduct the analyses.

7.5.2. Summary tables for pilot study

Supplementary Table 7.1. Mean and standard error (SE) for each measured behaviour in the Forced Swim Test and Elevated Plus Maze for each group at the mid-treatment timepoint in the pilot study.

		Active	Sham	Depression Control	Healthy Control
		Mean (SE)	Mean (SE)	Mean (SE)	Mean (SE)
Accelerated	Immobility	14.00 (7.38)	24.40 (8.99)	31.00 (6.06)	16.80 (11.84)
	Swimming	30.20 (7.05)	26.40 (12.48)	17.50 (5.69)	34.00 (14.53)
	Climbing	15.80 (4.92)	9.20 (5.45)	11.50 (4.51)	9.20 (7.98)
	Latency	130.00 (45.96)	54.00 (38.79)	62.50 (40.52)	111.00 (59.41)
Standard	Immobility	21.60 (4.28)	32.80 (11.41)	32.00 (8.25)	18.00 (12.90)
	Swimming	31.20 (4.09)	22.20 (10.57)	22.50 (7.33)	34.60 (15.11)
	Climbing	7.20 (5.45)	5.00 (5.10)	5.50 (4.65)	7.40 (8.65)
	Latency	79.00 (44.36)	48.00 (30.94)	32.50 (9.57)	112.00 (87.15)
Accelerated	Closed exits	5.60 (4.10)	8.40 (2.19)	11.50 (3.32)	7.60 (7.06)
	Closed time	224.60 (61.68)	242.60 (33.69)	198.00 (53.40)	227.80 (56.42)
	Open exits	0.20 (0.45)	0.20 (0.45)	0.50 (1.00)	0.60 (0.89)
	Open time	1.00 (2.24)	1.20 (2.68)	4.50 (9.00)	2.40 (3.91)
	Grooming no	6.40 (2.70)	4.40 (1.95)	0.00 (0.00)	2.00 (1.87)

	Grooming time	35.80 (20.73)	17.00 (6.82)	0.00 (0.00)	12.60 (15.95)
	Rearing no	19.00 (10.44)	14.20 (2.59)	20.25 (4.99)	18.40 (7.50)
	Rearing time	43.60 (13.28)	38.20 (8.64)	53.00 (11.40)	53.20 (19.23)
Standard	Closed exits	5.60 (5.18)	7.20 (4.55)	7.50 (4.04)	11.60 (5.18)
	Closed time	267.60 (52.23)	226.40 (71.79)	206.75 (46.33)	204.80 (47.60)
	Open exits	0.00 (0.00)	0.00 (0.00)	0.25 (0.50)	1.40 (1.95)
	Open time	0.00 (0.00)	0.00 (0.00)	1.00 (2.00)	9.00 (12.73)
	Grooming no	4.20 (0.84)	2.80 (1.92)	0.5 (1.00)	1.80 (1.48)
	Grooming time	24.00 (7.52)	19.20 (14.10)	1.5 (3.00)	11.20 (11.71)
	Rearing no	15.60 (5.64)	18.80 (7.26)	12.25 (4.79)	19.80 (6.69)
	Rearing time	50.00 (25.06)	54.40 (20.12)	32.50 (11.21)	48.60 (16.56)

Supplementary Table 7.2. Statistical results for the Mann-Whitney U test comparing the active and sham animals for both treatment protocols (accelerated and standard) at the mid-treatment timepoint in the pilot study. Each measured behaviour in the Forced Swim Test and Elevated Plus Maze is shown.

		Mann-Whitney U	Permutation <i>p</i> value	Mean difference	95% CI
Accelerated	Immobility	$U = 4.00, Z = -1.78, p = .076$.062	10.4	(0.4, 18.8)
	Swimming	$U = 12.00, Z = -0.11, p = .917$.552	-3.8	(-14.4, 7.8)
	Climbing	$U = 2.50, Z = -2.11, p = .035$.039	-6.6	(-11.4, 0.0)
	Latency	$U = 0.50, Z = -2.53, p = .011$	< .001	-76.0	(-134.0, -37.0)
Standard	Immobility	$U = 4.50, Z = -1.68, p = .093$.053	11.2	(2.4, 21.6)
	Swimming	$U = 6.50, Z = -1.27, p = .206$.130	-9.0	(-18.4, -0.8)

	Climbing	$U = 10.00, Z = -0.53, p = .599$.446	-2.2	(-8.8, 3.2)
	Latency	$U = 6.50, Z = -1.26, p = .207$.214	-31.0	(-84.0, 4.0)
Accelerated	Closed exits	$U = 6.50, Z = -1.27, p = .206$.183	2.8	(-1.0, 6.4)
	Closed time	$U = 11.50, Z = -0.21, p = .834$.591	18.0	(-35.4, 75.6)
	Open exits	$U = 12.50, Z = 0.00, p = 1.000$.447	0.0	(-0.6, 0.2)
	Open time	$U = 12.00, Z = -0.15, p = .881$.447	0.2	(-3.0, 2.6)
	Grooming no	$U = 5.50, Z = -1.51, p = .130$.167	-2.0	(-4.6, 0.6)
	Grooming time	$U = 3.50, Z = -1.89, p = .059$.047	-18.8	(-39.6, -4.6)
	Rearing no	$U = 9.50, Z = -0.63, p = .530$.350	-4.8	(-14.4, 2.6)
	Rearing time	$U = 10.00, Z = -0.52, p = .602$.443	-5.4	(-18.4, 6.4)
Standard	Closed exits	$U = 10.50, Z = -0.42, p = .674$.554	1.6	(-4.6, 6.4)
	Closed time	$U = 7.00, Z = -1.15, p = .251$.386	-41.2	(-118.0, 23.4)
	Open exits	$U = 12.50, Z = 0.00, p = 1.000$.000	0.0	(0.0, 0.0)
	Open time	$U = 12.50, Z = 0.00, p = 1.000$.000	0.0	(0.0, 0.0)
	Grooming no	$U = 6.50, Z = -1.29, p = .197$.095	-1.4	(-3.4, 0.0)
	Grooming time	$U = 11.00, Z = -0.31, p = .754$.564	-4.8	(-18.0, 7.2)
	Rearing no	$U = 7.00, Z = -1.15, p = .249$.422	3.2	(-4.2, 10.4)
	Rearing time	$U = 11.00, Z = -0.31, p = .754$.769	4.4	(-19.6, 30.8)

7.5.2. Summary tables and figures for main study

Supplementary Table 7.3. Statistical results for the comparison of Baseline and Post-CRS timepoints for all behavioural and MRI measures in the main study.

		Baseline	Post-CRS	Parametric? (Y/N)	T / Z value	df	P value	CI	N
		Mean (SE)	Mean (SE)						
FST	Immobility	11.40 (1.75)	15.00 (1.92)	N	- 1.822	-	.068	-	35
	Swimming	31.64 (2.16)	24.81 (2.12)	Y	3.142	35	.003	(2.42, 11.25)	36
	Climbing	15.17 (1.34)	18.20 (1.88)	N	- 1.305	-	.192	-	35
	Latency	127.16 (16.07)	103.92 (13.46)	N	- 1.274	-	.203	-	37
EPM	Closed exits	6.89 (0.59)	9.33 (0.48)	N	- 3.375	-	.001	-	52
	Closed time	220.37 (4.88)	193.21 (6.96)	Y	3.771	51	.000	(12.70, 41.61)	52
	Open exits	0.63 (0.18)	1.04 (0.19)	N	- 1.698	-	.089	-	51
	Open time	3.72 (1.50)	9.64 (2.18)	N	- 2.562	-	.010	-	50
	Grooming no	2.59 (0.29)	3.59 (0.33)	N	- 2.148	-	.032	-	51
	Grooming time	17.45 (2.61)	15.53 (1.98)	N	- 0.317	-	.751	-	49
	Rearing no	16.63 (0.78)	16.04 (0.79)	N	- 0.588	-	.557	-	52
	Rearing time	41.25 (2.05)	42.62 (2.12)	Y	- 0.483	50	.631	(-7.08, 4.34)	51
fMRI	Seed-based analysis	0.30 (0.01)	0.19 (0.01)	Y	8.112	47	< .001	(0.08, 0.13)	48
Hippocampal volume	Bilateral	5.87 (0.01)	5.87 (0.01)	Y	- 0.931	48	.356	(-0.03, 0.01)	49
	Left	2.90 (0.003)	2.90 (0.004)	Y	- 1.171	48	.247	(-0.01, 0.004)	49
	Right	2.97 (0.003)	2.97 (0.004)	Y	- 0.485	48	.630	(-0.01, 0.01)	49
MRS	Glu	1.37 (0.02)	1.38 (0.02)	Y	0.208	55	.836	(-0.04, 0.04)	56
	Gln	0.51 (0.01)	0.51 (0.01)	N	816.5	-	.883	-	56
	Glx	1.88 (0.02)	1.88 (0.02)	Y	0.165	55	.870	(-0.05, 0.06)	56

	GABA	0.36 (0.01)	0.36 (0.01)	Y	- 0.339	39	.737	(-0.03, 0.02)	40
--	------	----------------	----------------	---	------------	----	------	------------------	----

Supplementary Table 7.4. Mean and standard deviation (SD) for each measured behavioural and MRI outcome at all timepoints in the main study.

		Baseline	Post-CRS	Mid-rTMS	Post-rTMS	Wk1 Follow up	Wk2 Follow up
		Mean (SD)	Mean (SD)	Mean (SD)	Mean (SD)	Mean (SD)	Mean (SD)
Active group							
FST	Immobility	9.00 (8.53)	14.17 (10.44)	16.25 (11.23)	15.50 (11.16)	17.25 (13.47)	16.17 (13.97)
	Swimming	35.50 (14.61)	24.75 (13.38)	22.17 (13.91)	26.00 (12.16)	28.25 (15.03)	28.58 (13.93)
	Climbing	1.22 (0.19)	1.25 (0.24)	1.30 (0.21)	1.24 (0.21)	1.12 (0.24)	1.25 (0.23)
	Latency	123.33 (106.88)	79.16 (57.08)	108.33 (63.90)	90.83 (45.87)	107.50 (90.74)	117.50 (96.50)
EPM	Closed exits	7.87 (4.87)	9.73 (3.71)	7.80 (3.86)	7.00 (4.12)	10.33 (3.24)	10.67 (4.06)
	Closed time	232.73 (35.54)	185.67 (51.73)	171.07 (54.23)	203.00 (69.85)	146.93 (66.86)	157.13 (59.76)
	Open exits	0.50 (1.09)	1.29 (1.44)	1.07 (1.59)	1.00 (1.84)	2.93 (3.25)	2.21 (2.58)
	Open time	4.07 (8.58)	11.27 (15.88)	12.13 (17.63)	8.60 (13.12)	32.20 (34.51)	15.60 (16.79)
	Grooming no	3.53 (1.77)	4.00 (3.07)	3.67 (2.29)	3.67 (2.35)	3.60 (2.29)	2.93 (2.28)
	Grooming time	1.29 (0.38)	1.25 (0.33)	1.26 (0.38)	1.19 (0.33)	1.05 (0.37)	1.10 (0.31)
	Rearing no	17.27 (7.07)	16.53 (5.36)	16.07 (5.32)	13.47 (5.04)	16.67 (6.71)	17.47 (5.96)
	Rearing time	39.93 (16.39)	44.14 (13.28)	43.00 (16.46)	37.79 (9.76)	41.07 (16.26)	42.29 (13.96)
fMRI	Seed-based analysis	0.29 (0.08)	0.20 (0.07)	0.23 (0.08)	0.21 (0.07)	0.23 (0.14)	0.22 (0.10)
Hippocampal volume	Bilateral	5.85 (0.03)	5.89 (0.06)	5.88 (0.05)	5.88 (0.04)	5.88 (0.05)	5.89 (0.04)
	Left	2.89 (0.02)	2.91 (0.03)	2.91 (0.03)	2.91 (0.02)	2.90 (0.03)	2.91 (0.03)
	Right	2.96 (0.02)	2.98 (0.03)	2.97 (0.02)	2.97 (0.03)	2.98 (0.03)	2.98 (0.02)
MRS	Glu	1.37 (0.12)	1.34 (0.15)	1.38 (0.08)	1.40 (0.07)	1.43 (0.12)	1.38 (0.10)
	GABA	0.36 (0.06)	0.37 (0.05)	0.36 (0.04)	0.35 (0.06)	0.34 (0.06)	0.33 (0.05)
Sham group							

FST	Immobility	10.18 (9.71)	16.09 (15.31)	13.09 (11.97)	11.91 (9.82)	10.73 (8.70)	14.55 (15.94)
	Swimming	31.25 (13.86)	21.75 (14.19)	25.92 (14.76)	32.67 (14.24)	27.00 (11.09)	16.83 (9.47)
	Climbing	0.98 (0.49)	1.19 (0.28)	1.21 (0.19)	1.10 (0.15)	1.24 (0.21)	1.36 (0.21)
	Latency	136.15 (93.03)	135.77 (108.91)	140.38 (88.52)	134.62 (100.84)	130.00 (81.52)	133.46 (93.79)
EPM	Closed exits	6.88 (3.79)	8.19 (3.51)	7.94 (4.37)	8.38 (4.11)	10.25 (4.75)	10.38 (4.05)
	Closed time	216.44 (37.73)	198.38 (62.87)	215.94 (37.94)	197.94 (70.92)	139.94 (69.77)	161.44 (69.88)
	Open exits	0.83 (1.85)	0.92 (1.38)	0.67 (1.15)	0.92 (1.62)	2.92 (3.15)	2.25 (3.31)
	Open time	2.89 (8.67)	13.22 (20.64)	6.33 (10.02)	2.78 (5.78)	15.11 (22.61)	8.11 (13.66)
	Grooming no	1.79 (1.81)	3.29 (1.86)	1.86 (1.35)	4.00 (2.69)	1.71 (2.02)	2.43 (1.55)
	Grooming time	1.10 (0.48)	1.13 (0.25)	0.84 (0.35)	1.34 (0.32)	1.15 (0.38)	1.14 (0.19)
	Rearing no	15.87 (3.66)	12.33 (5.38)	15.60 (6.05)	14.40 (4.90)	18.73 (6.23)	15.80 (5.07)
	Rearing time	40.73 (11.41)	36.93 (16.10)	48.13 (21.94)	42.93 (16.04)	44.80 (13.15)	36.33 (12.43)
fMRI	Seed-based analysis	0.29 (0.09)	0.18 (0.05)	0.24 (0.08)	0.21 (0.08)	0.21 (0.06)	0.20 (0.10)
Hippocampal volume	Bilateral	5.87 (0.03)	5.87 (0.05)	5.87 (0.04)	5.88 (0.06)	5.88 (0.06)	5.89 (0.05)
	Left	2.90 (0.02)	2.90 (0.02)	2.90 (0.02)	2.90 (0.03)	2.90 (0.03)	2.91 (0.03)
	Right	2.97 (0.02)	2.97 (0.03)	2.97 (0.02)	2.97 (0.03)	2.98 (0.04)	2.98 (0.03)
MRS	Glu	1.34 (0.13)	1.39 (0.13)	1.30 (0.15)	1.41 (0.10)	1.40 (0.11)	1.39 (0.10)
	GABA	0.35 (0.04)	0.36 (0.05)	0.34 (0.05)	0.34 (0.03)	0.35 (0.03)	0.34 (0.04)
Depression control group							
FST	Immobility	17.10 (12.29)	14.90 (8.35)	15.30 (9.87)	22.30 (8.95)	19.40 (9.61)	24.20 (14.12)
	Swimming	28.50 (11.04)	26.50 (10.17)	30.80 (10.32)	23.20 (12.87)	26.80 (7.18)	23.00 (16.01)
	Climbing	1.06 (0.08)	1.11 (0.42)	1.11 (0.22)	1.09 (0.39)	1.02 (0.28)	1.03 (0.27)
	Latency	103.50 (102.17)	82.50 (60.66)	79.50 (58.90)	128.50 (94.05)	104.50 (88.99)	74.00 (59.39)
EPM	Closed exits	6.85 (3.40)	10.62 (3.15)	9.85 (3.08)	9.92 (3.09)	10.38 (3.18)	10.77 (2.59)

	Closed time	208.31 (32.11)	194.31 (44.11)	190.08 (38.32)	184.08 (39.50)	164.77 (35.53)	142.31 (69.88)
	Open exits	0.77 (1.36)	1.23 (1.42)	0.54 (0.88)	0.77 (1.24)	1.31 (2.06)	1.77 (2.28)
	Open time	5.33 (8.62)	10.33 (15.77)	5.83 (7.93)	5.58 (11.17)	6.42 (11.70)	10.17 (16.10)
	Grooming no	2.31 (2.29)	3.08 (2.29)	4.00 (2.35)	3.31 (1.55)	3.23 (2.13)	2.62 (2.14)
	Grooming time	1.23 (0.51)	1.23 (0.31)	1.31 (0.24)	1.17 (0.28)	1.26 (0.24)	1.20 (0.25)
	Rearing no	17.08 (5.89)	19.23 (4.15)	17.77 (4.80)	17.54 (4.94)	19.92 (6.18)	17.08 (5.91)
	Rearing time	44.08 (15.77)	46.46 (12.70)	50.15 (17.17)	50.62 (17.87)	48.85 (16.28)	42.38 (17.56)
fMRI	Seed-based analysis	0.33 (0.07)	0.23 (0.08)	0.23 (0.10)	0.17 (0.05)	0.21 (0.05)	0.20 (0.11)
Hippocampal volume	Bilateral	5.87 (0.03)	5.86 (0.04)	5.86 (0.04)	5.88 (0.06)	5.91 (0.06)	5.89 (0.05)
	Left	2.90 (0.02)	2.89 (0.02)	2.90 (0.02)	2.91 (0.03)	2.92 (0.03)	2.91 (0.03)
	Right	2.97 (0.02)	2.96 (0.03)	2.96 (0.03)	2.97 (0.03)	2.99 (0.03)	2.98 (0.03)
MRS	Glu	1.39 (0.10)	1.39 (0.09)	1.36 (0.08)	1.42 (0.09)	1.37 (0.11)	1.39 (0.10)
	GABA	0.36 (0.05)	0.35 (0.04)	0.36 (0.04)	0.34 (0.04)	0.36 (0.06)	0.36 (0.05)

Supplementary Table 7.5. Statistical results for the mixed-model ANOVA interactions and main effects comparing the active, sham and control animals at all timepoints in the main study. All behavioural and MRI measures are shown.

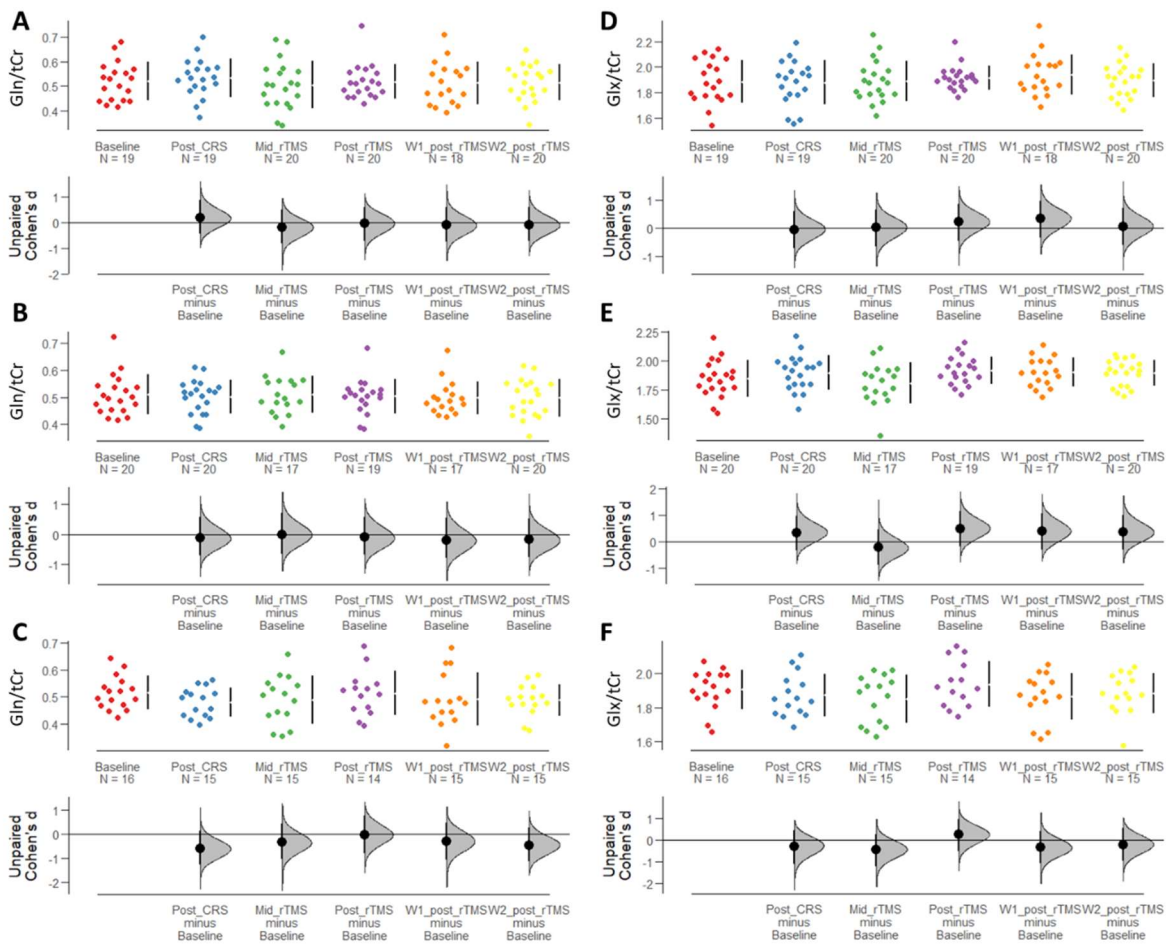
		Interaction Group * Time			Main Effect - Timepoint			Main Effect - Group			N
		F value (df)	P value	Partial Eta ²	F value (df)	P value	Partial Eta ²	F value (df)	P value	Partial Eta ²	
FST	Immobility	1.17 (10, 150)	.313	.073	1.94 (5, 150)	.091	.061	1.37 (2, 30)	.270	.084	3 3
	Swimming	2.18 (7.2, 112.94)	.039	.123	3.33 (3.64, 112.94)	.016	.097	0.094 (2, 31)	.911	.006	3 4
	Climbing	1.61 (6.77, 91.35)	.145	.017	1.33 (3.38, 91.35)	.267	.047	1.93 (2, 27)	.165	.125	3 0

	Latency	0.967 (10, 160)	.474	.057	0.697 (5, 160)	.627	.021	1.07 (2, 32)	.356	.063	3 5
EPM	Closed exits	0.965 (10, 205)	.475	.045	7.10 (5, 205)	.000	.148	0.71 (2, 41)	.499	.033	4 4
	Closed time	1.50 (10, 205)	.140	.068	16.26 (5, 205)	.000	.284	0.18 (2, 41)	.835	.009	4 4
	Open exits	.754 (5.68, 102.25)	.601	.040	7.56 (2.84, 102.25)	.000	.174	0.41 (2, 36)	.670	.022	3 9
	Open time	1.89 (7.25, 119.60)	.074	.103	4.65 (3.62, 119.60)	.002	.124	1.59 (2, 33)	.220	.088	3 6
	Grooming no	1.86 (10, 195)	.052	.087	3.00 (5, 195)	.012	.071	1.72 (2, 39)	.192	.081	4 2
	Grooming time	1.99 (10, 115)	.041	.147	0.59 (5, 115)	.705	.025	0.33 (2, 23)	.720	.028	2 6
	Rearing no	1.40 (9.57, 191.34)	.185	.065	2.27 (4.78, 191.34)	.052	.054	2.08 (2, 40)	.138	.094	4 3
	Rearing time	0.82 (8.88, 173.24)	.594	.041	1.45 (4.44, 173.24)	.214	.036	1.43 (2, 39)	.251	.068	4 2
fMRI	SBA	0.92 (10, 254.76)	.517	0.03	13.03 (5, 254.77)	< .001	0.02	0.16 (2, 55.28)	.851	0.00581	5 5
HIPV	Bilateral	1.26 (10, 260.58)	.252	0.05	3.51 (5, 260.52)	.004	0.06	0.001 (2, 55.87)	.999	0.000018 4	5 6
	Left	1.18 (10, 261.04)	.307	0.04	2.47 (5, 260.97)	.033	0.05	0.03 (2, 55.87)	.972	0.00101	5 6
	Right	1.05 (10, 260.58)	.399	0.04	3.41 (5, 260.51)	.005	0.06	0.01 (2, 55.80)	.991	0.000339	5 6
MRS	Glu	1.64 (10, 264.96)	.095	0.06	3.22 (5, 264.98)	.008	0.06	0.27 (2, 54.86)	.766	0.00966	5 6
	GABA	1.01 (10, 235.69)	.439	0.04	1.16 (5, 235.69)	.328	0.02	0.80 (2, 235.69)	.456	0.03	5 6

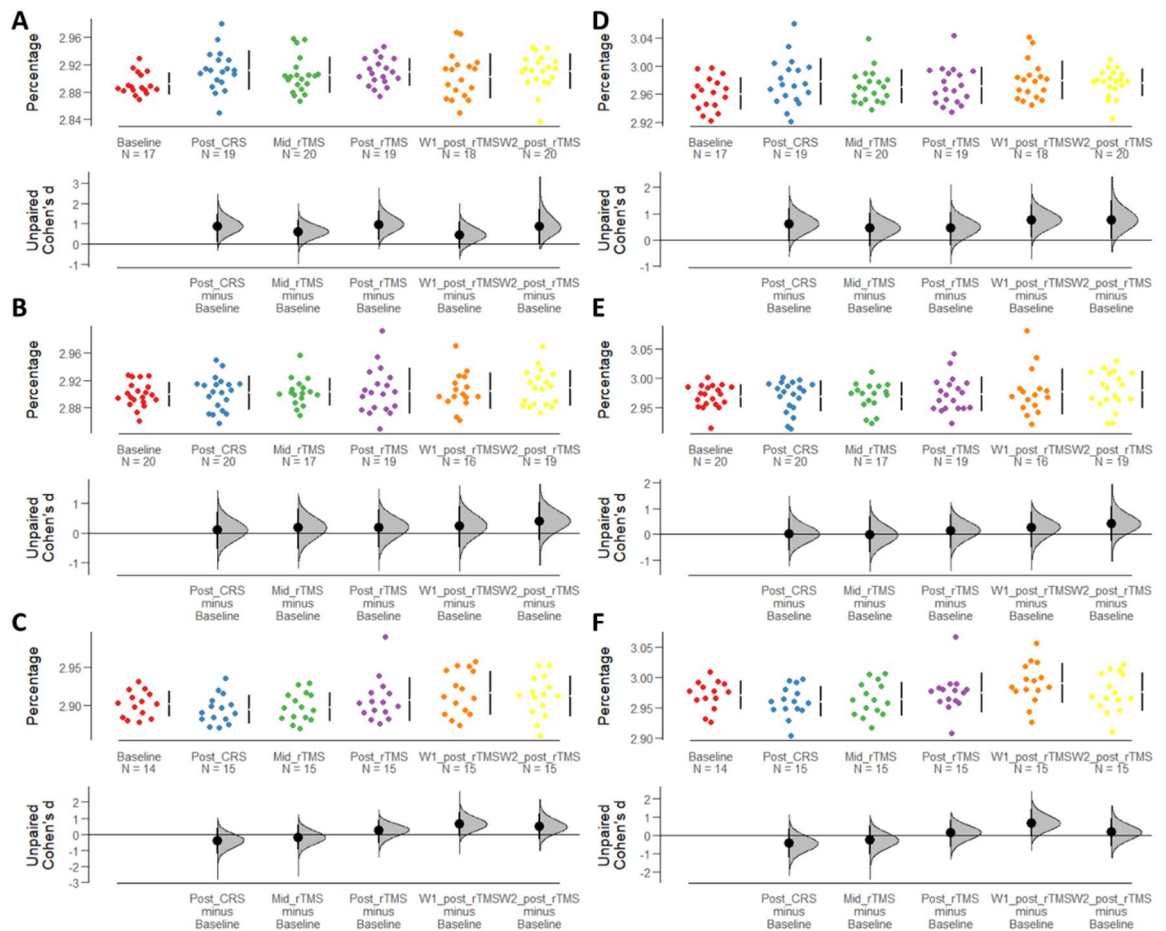
		235.54)						52.31)			
	Gln	0.38 (10, 266.03)	.953	0,01	0.40 (5, 266.04)	.849	0.0074 6	1.45 (2, 54.92)	.243	0.05	5 6
	Glx	0.75 (10, 265.84)	.681	0.03	1.90 (5, 265.85)	.095	0.03	0.55 (2, 55.22)	.578	0.02	5 6

Supplementary Table 7.6. Comparisons of effect sizes (partial eta-squared and Cohen's r) for all comparisons in the pilot study and main study. Yellow cells indicate small effect size, blue cells indicate medium effect size, and green cells indicate large effect size.

		Main study (ANOVA)			Pilot study (Mann-Whitney U)			
Effect Size		Partial Eta ²			Partial Eta ²		Cohen's <i>r</i>	
Comparison		Interaction	Main effect (Timepoint)	Main effect (Group)	Accelerated Active vs Sham	Standard Active vs Sham	Accelerated Active vs Sham	Standard Active vs Sham
FST	Immobility	.073	.061	.084	.350	.231	.563	.532
	Swimming	.123	.097	.006	.001	.094	.035	.402
	Climbing	.017	.047	.125	.494	.122	.668	.168
	Latency	.057	.021	.063	.711	.155	.801	.399
EPM	Closed exits	.045	.148	.033	.178	.020	.402	.133
	Closed time	.068	.284	.009	.005	.147	.066	.364
	Open exits	.040	.174	.022	.000	.000	.000	.000
	Open time	.103	.124	.088	.002	.000	.047	.000
	Grooming no	.087	.071	.081	.255	.185	.478	.408
	Grooming time	.147	.025	.028	.395	.011	.598	.098
	Rearing no	.065	.054	.094	.044	.147	.199	.364
	Rearing time	.041	.036	.068	.030	.011	.165	.098
fMRI	SBA	.03	0.02	.006	NA	NA	NA	NA
Hipp Vol	Bilateral	.05	.06	< .001	NA	NA	NA	NA
	Left	.04	.05	.001	NA	NA	NA	NA
	Right	.04	.06	< .001	NA	NA	NA	NA
MRS	Glu	.06	.06	.010	NA	NA	NA	NA
	GABA	.04	.02	.03	NA	NA	NA	NA
	Gln	.01	.007	.05	NA	NA	NA	NA
	Glx	.03	.03	.02	NA	NA	NA	NA



Supplementary Figure 7.1. Comparisons of glutamine (Gln) (A-C) and combined glutamine-glutamate (Glx) (D-F) levels across all timepoints. Levels of Gln are shown within active (A), sham (B) and depression control (C) conditions. Levels of Glx are shown within active (D), sham (E) and depression control (F) conditions. Data is displayed as a Cumming estimation plot. Raw data is plotted on the top section of the estimation plot, with unpaired Cohen's d for the comparisons to baseline on the bottom. The bootstrap sampled distribution is shown via bolded vertical lines, with the centre circle indicating the mean difference, and non-bolded ends representing error bars for the 95% CIs.



Supplementary Figure 7.2. Comparisons of left (A-C) and right (D-F) hippocampal volume (as a percentage of whole brain volume) across all timepoints. Percentage left hippocampal volumes are shown within active (A), sham (B) and depression control (C) conditions. Percentage right hippocampal volumes are shown within active (D), sham (E) and depression control (F) conditions. Data is displayed as a Cumming estimation plot. Raw data is plotted on the top section of the estimation plot, with unpaired Cohen's *d* for the comparisons to baseline on the bottom. The bootstrap sampled distribution is shown via bolded vertical lines, with the centre circle indicating the mean difference, and non-bolded ends representing error bars for the 95% CIs.

7.5.3. Resting-state fMRI: Independent component analysis methods and results

In addition to examining fMRI data via seed-based analysis, multi-subject temporal concatenation group-ICA and FSL dual regression analysis were conducted (see Seewoo et al. (2021a) for full analysis details). Single-session independent component analysis (ICA) as implemented in FSL/MELODIC (Multivariate Exploratory Linear Decomposition into Independent Components) (Beckmann et al., 2005) was used to

de-noise the data (detailed in Seewoo et al., 2018b). The de-noised rs-fMRI images were then co-registered to their respective T2-weighted coronal images using six-parameter rigid body registration using FSL/FLIRT (Linear Image Registration Tool) (Jenkinson and Smith, 2001; Jenkinson et al., 2002) and normalised to a Sprague-Dawley brain atlas (Papp et al., 2014; Kjonigsen et al., 2015; Sergejeva et al., 2015) with nine degrees of freedom ‘traditional’ registration. The atlas was first down-sampled by a factor of eight to better match the voxel size of the 4D functional data. All subsequent analyses were conducted in the atlas standard space.

Multi-subject temporal concatenation group-ICA and FSL dual regression analysis were used to determine group/timepoint differences, controlling for family-wise error (FWE) and using a threshold-free cluster enhanced (TFCE) technique to control for multiple comparisons. The resulting statistical maps were thresholded to $p < 0.05$. Anatomical locations on the statistical maps showing significant differences were then labelled using a rat brain atlas (Paxinos and Watson, 1998). Based on Seewoo et al. (2021a), the following components were assessed: 1) Interoceptive network (IC0); 2) Salience network (IC2); 3) Default Mode Network (IC3).

Independent components analysis of the resting-state fMRI data identified no changes between baseline and post-CRS for any component, though a mixed model ANOVA identified an interaction between treatment group and condition ($F_{8,701.57} = 2.96$, $p = .003$), with significant main effects of timepoint ($F_{4,701.59} = 15.15$, $p < .001$) and component ($F_{2,696.88} = 91.18$, $p < .001$). There was no main effect of treatment group found. Post hoc analyses of changes within treatment groups found an increase in connectivity at the mid-treatment timepoint for IC2 (Mid-treatment vs Post-treatment

$p = 0.033$; Mid-treatment vs Wk 1 $p = 0.014$; $n = 20$) in animals receiving active treatment, a decrease in connectivity for IC0 at the first post-treatment follow-up (Mid-treatment vs Wk 1 $p = 0.007$; $n = 20$), and IC2 (Mid-treatment vs Wk 1 $p = 0.014$; Mid-treatment vs Wk 2 $p = 0.003$; $n = 20$) and IC3 (Mid-treatment vs Wk 1 $p = 0.031$; Mid-treatment vs Wk 2 $p = 0.006$; $n = 20$) at the first and second follow-up for the sham group, and a decrease for IC0 (Mid-treatment vs Post-treatment $p = 0.039$; Mid-treatment vs Wk 1 $p = 0.016$; Post-CRS vs Post-treatment $p = 0.041$; Post-CRS vs Wk 1 $p = 0.039$; $n = 20$) and IC3 post-treatment which then corrected in the two weeks following for the depression control group (Post-CRS vs Mid-treatment $p = 0.017$; Post-CRS vs Post-treatment $p = 0.007$; Post-CRS vs Wk 1 $p = 0.044$; Post-CRS vs Wk 2 $p = 0.019$; $n = 15$).

Supplementary Table 7.7. Statistical results for the Wilcoxon signed-rank test comparing the rs-fMRI ICA results at baseline and post-CRS in the main study.

		Baseline	Post-CRS	V value	P value	N
		Mean (SE)	Mean (SE)			
fMRI - ICA	IC0	23.6 (1.3)	23.0 (1.3)	643	.579	48
	IC2	20.2 (0.9)	20.1 (1.0)	583	.964	48
	IC3	16.5 (0.6)	16.1 (0.6)	645	.566	48

Supplementary Table 7.8. Mean Z scores and standard deviations (SD) for the rs-fMRI ICA results in each group at baseline and post-CRS in the main study.

		Baseline	Post-CRS	Mid-rTMS	Post-rTMS	Wk1 Follow up	Wk2 Follow up
		Mean (SD)	Mean (SD)	Mean (SD)	Mean (SD)	Mean (SD)	Mean (SD)
Active group	IC0	20.76 (7.29)	23.34 (7.46)	25.61 (11.67)	20.72 (8.95)	20.78 (8.38)	23.42 (9.48)
	IC2	17.92 (5.09)	20.85 (6.15)	22.87 (8.06)	18.39 (5.46)	17.85 (5.82)	20.51 (6.40)

	IC3	14.71 (3.44)	15.22 (3.97)	15.68 (2.93)	15.03 (5.02)	14.81 (5.44)	16.07 (4.33)
Sham group	IC0	26.65 (11.01)	22.54 (10.00)	23.85 (5.73)	24.46 (11.34)	20.12 (6.88)	19.45 (7.01)
	IC2	22.89 (7.46)	19.97 (8.43)	23.12 (5.96)	21.45 (8.55)	18.70 (6.49)	18.34 (5.96)
	IC3	17.41 (4.41)	16.69 (4.51)	17.98 (2.32)	16.00 (4.20)	15.24 (3.01)	14.93 (4.26)
Depression Control Group	IC0	23.37 (7.55)	23.15 (8.85)	20.74 (5.56)	15.48 (2.46)	16.71 (3.29)	19.93 (9.43)
	IC2	19.30 (5.22)	19.17 (5.73)	19.00 (4.75)	15.52 (2.63)	16.72 (6.31)	16.93 (5.91)
	IC3	18.02 (4.60)	16.96 (3.43)	14.50 (3.23)	13.02 (1.92)	14.19 (3.39)	13.66 (3.60)

Supplementary Table 7.9. Statistical results for the mixed-model ANOVA interactions and main effects for the rs-fMRI ICA results all timepoints in the main study.

	F value (df)	P value
Interaction: Time*Group*IC	0.34 (16,696.88)	.993
Interaction: Time*Group	2.96 (8,701.57)	.003
Interaction: Time*IC	0.46 (8,696.88)	.881
Interaction: Group*IC	1.13 (4,696.88)	.339
Main Effect: Timepoint	15.15 (4,701.59)	< .001
Main Effect: Group	1.71 (2,53.89)	.190
Main Effect: IC	91.18 (2,696.88)	< .001

Chapter 8

Changes in the white matter of young male Sprague Dawley rats following chronic restraint stress and following low-intensity rTMS: a diffusion MRI study

Published as: Seewoo, B.J., Feindel, K.W., Won, Y., Joos, A.C., Figliomeni, A., Hennessy, L.A. & Rodger, J., 2021. White matter changes following chronic restraint stress and neuromodulation: a diffusion magnetic resonance imaging study in young male rats. *Biological Psychiatry Global Open Science*, in press. doi: 10.1016/j.bpsgos.2021.08.006 (Appendix J)

Abnormal brain white matter connectivity and integrity have been described in depression. However, few studies have used diffusion MRI (dMRI) to investigate the longitudinal impact of repeated rTMS delivery on the white matter. In addition to rs-fMRI, MRS and anatomical data being acquired, dMRI data was also acquired during the experiments described in Chapters 5-7. dMRI measures the diffusion of water, which is largely restricted to the direction of fibre tracts, to enable *in vivo* investigations of white matter tissue microstructure. In this chapter, we used dMRI to investigate white matter changes following LI-rTMS in healthy rats and in the CRS rat model of depression. Specifically, we investigated: (1) the longitudinal effects of 10 Hz and 1 Hz stimulation delivered for 10 min daily for 15 days in healthy animals (Chapter 5); (2) the effect of CRS (Chapter 6); and (3) the effect of an accelerated protocol of 10 Hz LI-rTMS (10 min three times daily, five days/week for two weeks) in animals post-restraint (Chapter 7). In healthy animals, 10 Hz and 1 Hz stimulation induced similar changes in diffusion and kurtosis fractional anisotropy, although changes induced by 10 Hz stimulation were detected earlier than those following 1Hz stimulation. Additionally, 10 Hz stimulation increased axial and mean kurtosis within the external capsule, suggesting that the two protocols may act via different underlying

mechanisms. Brain-maturation-related changes in white matter such as increased corpus callosum, fimbria, and external and internal capsule fibre cross-section were compromised in CRS animals compared to healthy controls and were rescued by 10 Hz LI-rTMS. Immunohistochemistry revealed increased myelination within the corpus callosum in LI-rTMS-treated CRS animals compared to those which received sham or no stimulation. Overall, decreased WM connectivity and integrity in the CRS model corroborate findings in patients experiencing depression with high anxiety, and the observed LI-rTMS-induced effects on WM structure suggest that LI-rTMS might rescue abnormal white matter by increasing myelination.

8.1. Introduction

Depression is a heterogeneous disorder affected by subject-related variables such as sex, age, diet, and genetic background (Ridding and Ziemann, 2010), and up to one-third of adults are treatment-resistant. Repetitive transcranial magnetic stimulation (rTMS) has been used clinically for treatment-resistant depression for over a decade (O'Reardon et al., 2007), but its underlying mechanisms are still unclear. While translational animal models of depression do not replicate the full complexity of human mood disorders, they can provide homogeneous endophenotypes of depression that facilitate the investigation of causal effects (e.g., genetic and environmental factors), as well as the efficacy of treatments such as rTMS (Krishnan and Nestler, 2011). The chronic restraint stress (CRS) depression model in Sprague-Dawley rats has been validated in several pharmacological and MRI studies. Following CRS, animals exhibit changes resembling those found in human depression, including altered behaviour (Suvrathan et al., 2010; Seewoo et al., 2020a), gene expression (Hunter et al., 2016) and protein levels (Ampuero et al., 2015a), as well as dysfunctional connectivity (Henckens et al., 2015), reduced glutamate and glutamine levels (Seewoo et al., 2020a), and hippocampal atrophy (Vyas et al., 2002; Alemu et al., 2019; Seewoo et al., 2020a).

One of the least understood aspects of depression in patients is related to the microstructural changes often present in the white matter. Diffusion MRI (dMRI) measures the diffusion of water and enables *in vivo* investigation of tissue microstructure and macro organization of fibre bundles. Water diffusion has been shown to be increased in patients with depression (Ota et al., 2015; Kamiya et al.,

2018) and in other animal models of depression (Hemanth Kumar et al., 2014; Zalsman et al., 2017) using several dMRI measures including mean diffusivity, a global measure of water diffusion, and radial kurtosis, a measure of diffusion restriction perpendicular to axonal direction. These different measures that can be derived from dMRI data are known to provide complementary and partly overlapping information by reflecting changes in white matter integrity, specifically with respect to cell density, size, and membrane permeability. Myelin content, known to decrease in depression (Lehmann et al., 2017; Sacchet and Gotlib, 2017), is a key factor that drives the changes in dMRI measures and this has been demonstrated in mice with demyelination (Falangola et al., 2014; Guglielmetti et al., 2016).

The authors previously acquired multimodal MRI data following low-intensity rTMS (LI-rTMS) in healthy rats (rs-fMRI and MRS data published: Seewoo et al., 2019c) and following CRS (rs-fMRI, MRS and hippocampal volume data published: Seewoo et al., 2020a). In the current study, we analyzed the dMRI data acquired in these experiments to investigate changes in the white matter of healthy rats following LI-rTMS and CRS. We also report diffusion changes and myelin changes in the white matter in the CRS model following LI-rTMS treatment.

8.2. Materials and Methods

8.2.1. Animals

Experimental procedures were approved by the UWA Animal Ethics Committee (RA/3/100/1430 and RA/3/100/1640). Young adult male Sprague-Dawley rats (5-8 weeks old, 150-250g) from the Animal Resources Centre (Canning Vale, Western Australia) were maintained in a temperature-controlled animal care facility on a 12-

hour light-dark cycle with food and water *ad libitum*. The CRS procedure was carried out for 2.5 h/day for 13 consecutive days as described previously (Seewoo et al., 2020a). Animals receiving LI-rTMS were habituated to handling and the coil as described previously (Rodger et al., 2012; Makowiecki et al., 2014). LI-rTMS was delivered using a custom-built round coil (Supplementary Methods) at an intensity of approximately 13 mT at the surface of the cortex (Seewoo et al., 2018b). During the sham procedure, the coil was disconnected.

Healthy animals from Seewoo et al. (2019c) did not undergo the CRS procedure but received 10 min LI-rTMS at 10Hz (n = 9; CRS⁻/10Hz⁺) or 1Hz (n = 9; CRS⁻/1Hz⁺) to the right brain hemisphere once daily for 15 days (Figure 8.1A). For the CRS experiments (unpublished data and data from Seewoo et al., 2020a), animals were randomly assigned to one of the following groups: 1) CRS⁺/10Hz⁺ animals (n = 22) underwent CRS and received accelerated 10Hz LI-rTMS (10 min three times daily, one hour apart, five days/week for two weeks) to the left hemisphere; 2) CRS⁺/0Hz⁺ (n = 21) animals underwent CRS and sham LI-rTMS; 3) CRS⁺/0Hz⁻ (n = 19) restraint control animals underwent CRS but did not receive any stimulation; and 4) CRS⁻/0Hz⁻ (n = 8) healthy control animals did not undergo CRS or stimulation (Figure 8.1B). Since we have previously shown that 1Hz stimulation has milder effects than 10Hz (Seewoo et al., 2019c), only 10Hz LI-rTMS was used for the next experiments to investigate its effects in more detail in the depression model. Additionally, a pilot study comparing the effects of the accelerated 10Hz LI-rTMS protocol (3 stimulation sessions/day) and the standard 10Hz protocol (1 stimulation session/day) showed significant improvement in

depression-like behaviours in animals receiving accelerated LI-rTMS only (Seewoo et al., 2019a). Therefore, only accelerated LI-rTMS was delivered in the CRS experiments.

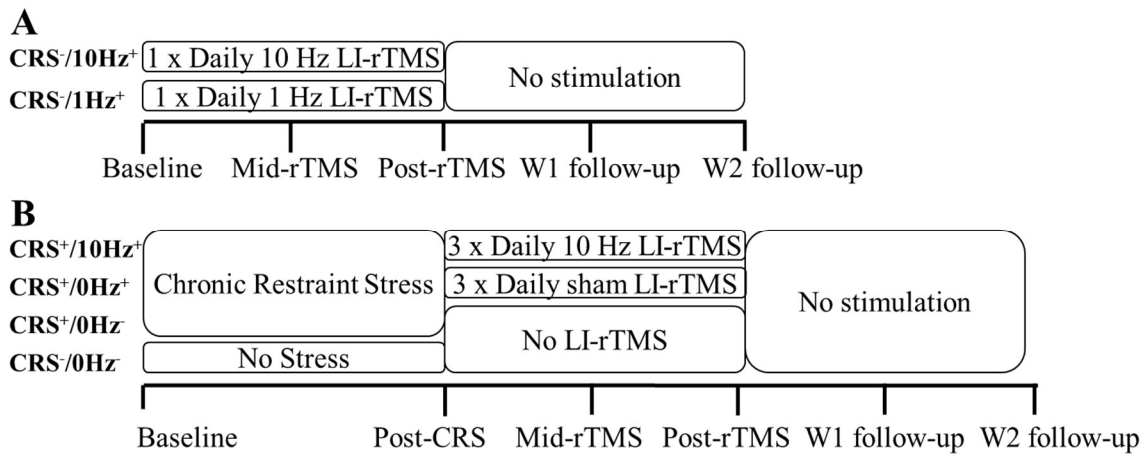


Figure 8.1. Timeline of an experiment. A shows the timeline for the Seewoo et al. (2019) study, which consisted of two weeks of daily 10 min stimulation at 10 Hz (10 pulses/s, total of 6000 pulses) or 1 Hz (1 pulse/s, total of 600 pulses) delivered to healthy animals. B shows the timeline for the CRS model experiments, which consisted of 4 groups of animals. CRS⁺/10Hz⁺, CRS⁺/0Hz⁺, and CRS⁺/0Hz⁻ groups were all subjected to the CRS procedure but CRS⁺/10Hz⁺ animals received accelerated 10 Hz LI-rTMS (10 pulses/s, total of 6000 pulses delivered three times daily, one hour apart, five days a week for two weeks), CRS⁺/0Hz⁺ animals received a sham version of the stimulation protocol and CRS⁺/10Hz⁻ received no stimulation or extra handling. The CRS⁻/0Hz⁻ animals were not subjected to the CRS procedure and did not receive any stimulation or extra handling. The animals from both A and B had five sessions of MRI scans, each separated by at least one week and stimulation (if any) was ceased at the Post-rTMS timepoint.

8.2.2. MRI data acquisition

Anesthesia and physiological monitoring were performed as previously described (Seewoo et al., 2020a). MRI data acquisition timepoints for the CRS⁻/10Hz⁺ and CRS⁻/1Hz⁺ animals have been previously described (Seewoo et al., 2019c) (Figure 8.1A). For the CRS experiments, baseline dMRI data was acquired, followed by the CRS procedure and post-CRS dMRI (Figure 8.1B). LI-rTMS was then delivered, with weekly imaging. MRI data were also acquired seven and 14 days after stimulation cessation (W1 and W2 follow-ups).

MRI hardware and software setup has been described previously (Seewoo et al., 2019c) (Supplementary Methods). B0 shimming was completed for a region of interest covering the brain using the Bruker Mapshim routine before dMRI data acquisition using a spin-echo echo-planar imaging sequence. Five non-diffusion images were also acquired during each dMRI scan.

CRS⁻/10Hz⁺ and CRS⁻/1Hz⁺ animals were imaged with the following imaging parameters: repetition time (TR) = 2800 ms, echo time (TE) = 21.0 ms, field-of-view (FOV) = 28.2 × 21.0 mm², matrix size = 94 × 70, 21 coronal slices (scanner axial), thickness = 1 mm, in-plane resolution = 0.3 × 0.3 mm², diffusion duration (δ) = 3.5 ms and diffusion gradient separation (Δ) = 11 ms. Multi-shell dMRI data consisted of 30 diffusion gradient directions, b-values = 1000 and 2000 s/mm² and imaging time = 6 min 4 s.

For the CRS experiments, two dMRI datasets were acquired with the following imaging parameters: TR = 3000 ms, TE = 20.8 ms, FOV = 25.6 × 21.6 mm², matrix size = 64 × 54, 29 axial slices (scanner coronal), thickness = 0.4 mm, in-plane resolution = 0.4 × 0.4 mm², δ = 3.5 ms, and Δ = 12 ms. Single-shell dMRI data consisted of 81 diffusion sampling directions with b-value = 3000 s/mm² and imaging time = 8 min 36 s. Multi-shell dMRI data consisted of 30 diffusion gradient directions, b-values = 1000 and 2000 s/mm² and imaging time = 6 min 30 s.

8.2.3. dMRI data analysis

dMRI data processing was carried out using the MRtrix3 software package (Tournier et al., 2019) and included denoising (Veraart et al., 2016a; Veraart et al., 2016b; Cordero-Grande et al., 2019), removal of Gibbs ringing artifacts (Kellner et al., 2016), and B1

field inhomogeneity correction (Tustison et al., 2010). Skull-stripping was performed using the qimask utility from QUIT (QUantitative Imaging Tools) (Wood, 2018).

8.2.3.1. Tract-based spatial statistics

Multi-shell dMRI datasets were analyzed using the Tract-Based Spatial Statistics (TBSS) method (Smith et al., 2006) in the FMRIB Software Library (FSL) v6.0.3 (Jenkinson et al., 2012) and adapted for using rodent data (Supplementary Methods). First, the pre-processed datasets were converted to NifTI file format (Neuroimaging Informatics Technology Initiative, <https://nifti.nimh.nih.gov/>). Diffusion kurtosis parameter maps for fractional anisotropy (FA), mean diffusivity (MD), axial diffusivity (AD), radial diffusivity (RD), kurtosis fractional anisotropy (KFA), mean kurtosis (MK), mean kurtosis tensor (MKT), axial kurtosis (AK) and radial kurtosis (RK), as well as diffusion tensor parameter maps for FA, MD, AD, and RD, were then generated for each animal at each timepoint using the diffusional kurtosis estimator v2.6.0 (Tabesh et al., 2011). Next, the statistical parametric mapping (SPM12) toolbox (using MATLAB, version 9.10.0.1602886 (R2021a) [The MathWorks, Inc.] compiler) was used to convert the above parameter maps into a format compatible with input through the DTI-ToolKit (DTI-TK) v2.3.1 software. DTI-TK was then used to spatially normalize each dataset to a population-specific template (Zhang et al., 2007) using a tensor-based registration formulation (Zhang et al., 2006). These co-registered images were concatenated to create one single 4D image for each diffusion parameter and fed into the FSL/TBSS pipeline.

The mean of all FA images was computed and used to generate a mean FA 'skeleton' and a skeleton mask using an FA threshold of 0.26 (Harris et al., 2016). The mean FA

and mean FA skeleton mask were used to skeletonize all parameter maps which were then fed into the voxel-wise analysis using nonparametric permutation testing (FSL/randomise).

8.2.3.2. Fixel-based analysis

Single-shell dMRI data were used to generate and analyze fixel-based metrics, including the apparent fibre density (AFD), fibre cross-section (FC), and the combination of AFD and FC (FDC), using the multi-tissue fixel-based analysis (FBA) pipeline implemented in MRtrix3 as outlined previously (Raffelt et al., 2012; Raffelt et al., 2015; Raffelt et al., 2017; Wright et al., 2017). In this study, a population-based template was generated based on 50 datasets across groups and timepoints. Whole-brain tractography was performed on the template with probabilistic tracking at a cutoff of 0.2 (Tournier et al., 2010).

For track-weighted imaging analysis, whole-brain tractography was performed in native space for each rat using the same parameters outlined above and registered to the study-specific template to normalize both the length and spatial location of the streamlines. The normalized tractograms were then used to generate the average pathlength map (APM), representing the average length of tracks passing through each voxel (Pannek et al., 2011), and mean curvature map (MC), representing the average curvature of all tracks passing through each voxel.

Differences between timepoints were determined using non-parametric permutation testing over 5000 permutations (Nichols and Holmes, 2002; Smith and Nichols, 2009).

8.2.3.3 Statistical analyses

Because of the longitudinal nature of the data presented, within-group comparisons were performed to investigate changes over time. To quantify the change with and without restraint, baseline and post-restraint timepoints were compared using equal number of animals from CRS⁻/0Hz⁻ and CRS⁺/0Hz⁻ groups (n = 8). For all image analyses, all voxels in the brain were corrected using the threshold-free cluster enhancement method with family-wise error correction (Winkler et al., 2014). Statistically significant differences for maps were visualized at a Bonferroni corrected p-value of 0.006 (rTMS effects) and 0.025 (CRS effects). In addition, raw diffusion values from four regions of interest (ROI) within the corpus callosum, internal capsule, external capsule, and fimbria (manually drawn using ITK-SNAP 3.3.0 (Yushkevich et al., 2006); www.itksnap.org) were extracted and analyzed using RStudio v3.6.1. (RStudio Team, 2018). ANOVA ('lmerTest' package) was utilized to test for any significant effect of animal group or timepoint. When there was an effect of both animal group and timepoint, *post hoc* pairwise comparisons were performed with FDR correction ('emmeans' package) to determine significant differences in diffusion parameters between timepoints for each group and ROI.

8.2.4 Brain immunohistochemistry

At the end of the study, the rats were euthanized with an overdose of sodium pentobarbitone (> 160 mg/kg i.p.) and transcardially perfused with 200 ml of 4% paraformaldehyde in 0.2 M Phosphate Buffer. Brains were post-fixed in 4% paraformaldehyde solution at 4°C and transferred to 30% sucrose in PBS 48 hours before cryosectioning into 40µm coronal sections. Five brains from each of the CRS⁺/10Hz⁺, CRS⁺/0Hz⁺, and CRS⁺/0Hz⁻ groups were selected and three sections were chosen per brain for immunohistochemical staining at positions 80, 88, and 97 on our

MRI population template corresponding to Bregma -3.11 mm, -2.11 mm, -0.11 mm (Paxinos et al., 2015). Sections were processed for immunohistochemistry (Supplementary Methods) using rabbit anti-myelin basic protein polyclonal antibody (ab40390) and anti-NeuN monoclonal antibody (MAB377). Sections were imaged on a Nikon confocal C2, NI-E microscope with a 10x lens, captured using NIS Elements AR software using the same settings, and analyzed using FIJI (ImageJ 1.53c, National Institutes of Health) software by an operator blinded to conditions (Schindelin et al., 2012) (Supplementary Methods). Data were analyzed and plotted using RStudio v3.6.1. (RStudio Team, 2018). ANOVA ('lmerTest' package) was utilized to test for any significant effect of animal group or ROI. *Post hoc* Mann-Whitney two-sample rank-sum test with FDR correction ('rstatix' package) was then used to determine significant differences in MBP intensity between groups.

8.3. Results

8.3.1. White matter changes following 10 Hz and 1 Hz LI-rTMS in healthy rats

We first examined whether LI-rTMS induced any changes in white matter tracts in healthy rats. TBSS analysis of the 10 Hz and 1 Hz data revealed an increase in DKI/DTI FA for both frequencies. This increase was detectable at the W1 follow-up timepoint in the 10 Hz group but was observed only at the W2 follow-up timepoint in the 1 Hz group (Figure 8.2). In addition, only the 10 Hz group exhibited an increase in external capsule AK, internal and external capsule KFA and MK, and fimbria and external capsule MKT (Figures 8.2-8.3). ROI-based analyses showed that both groups showed an increase in internal capsule DTI/DKI FA, but only the 1 Hz group showed an increase in fimbria DTI FA (Figure 8.3). Additionally, internal capsule AD and fimbria RK increased

in the 10 Hz group only and corpus callosum RK increased in both groups

(Supplementary Figure 8.1).

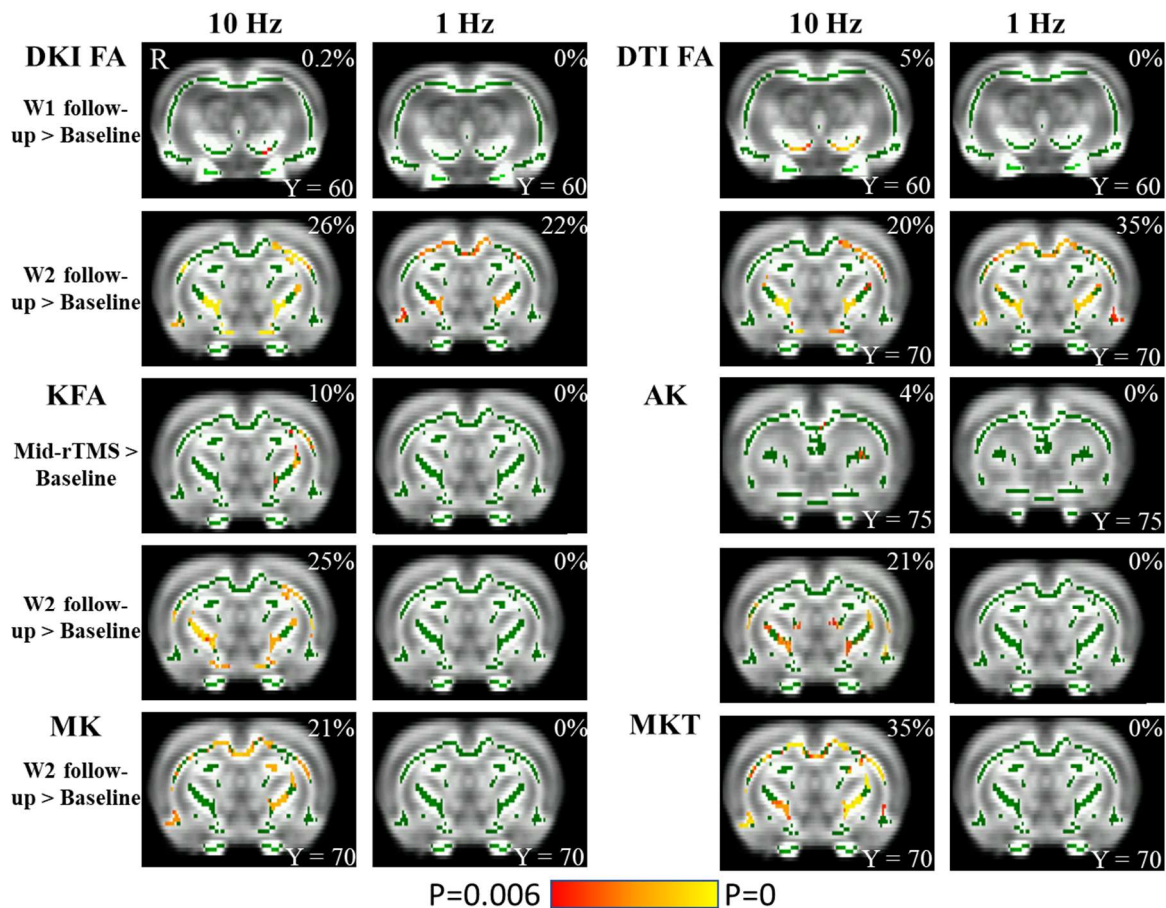


Figure 8.2. TBSS analysis shows significant changes in diffusion and kurtosis parameters following 10 Hz or 1 Hz LI-rTMS in healthy rats ($P_{\text{Bonferroni}} < 0.006$). The figure illustrates changes between baseline and four timepoints: after one (Mid-rTMS) and two weeks (Post-rTMS) of daily stimulation and one (W1 follow-up) and two weeks (W2 follow-up) post-stimulation cessation. Green represents mean FA skeleton of all animals; red denotes an increase post-stimulation. The percentage in the top right corner of the coronal slices represents the percentage of the significant voxels relative to the whole skeleton voxels for each parameter. LI-rTMS was delivered to the right side of the brain (denoted by R).

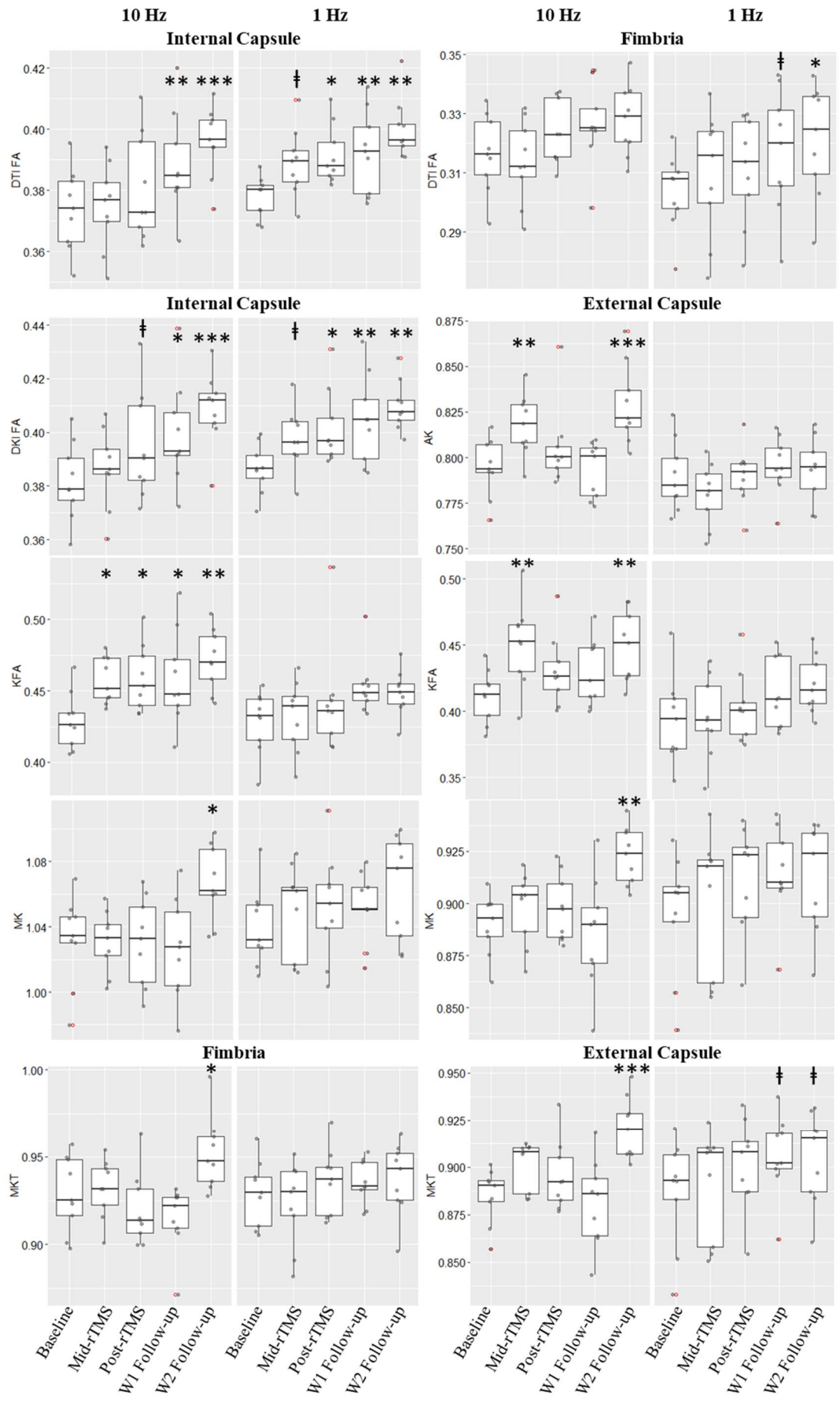


Figure 8.3. Significant changes in DTI and DKI measures within the internal and external capsules and fimbria in healthy animals receiving 10 Hz or 1 Hz LI-rTMS ($p_{FDR} < 0.006$). The boxplots illustrate changes between baseline and four timepoints: after one (Mid-rTMS) and two weeks (Post-rTMS) of daily stimulation and one (W1 follow-up) and two weeks (W2 follow-up) post-stimulation cessation. † $p_{FDR} < 0.1$, * $p_{FDR} < 0.05$, ** $p_{FDR} < 0.01$, *** $p_{FDR} < 0.001$.

8.3.2. Rat model of depression: white matter changes following CRS

Having demonstrated that LI-rTMS altered white matter tracts in healthy animals, to examine the effects of LI-rTMS in a disease model was pertinent. rTMS is an FDA-approved treatment of depression and therefore, a rat model of depression (chronic restraint stress) was chosen. We first report CRS-induced white matter changes in restrained animals compared to healthy unrestrained animals.

Changes in white matter diffusion and kurtosis were observed in both restrained and unrestrained groups, likely reflecting brain maturation. DTI AD, DTI/DKI RD, and DTI/DKI MD decreased significantly from baseline at the post-restraint timepoint, while DKI AD decreased in healthy animals only, and AK and DTI FA increased in restrained animals only (Figure 8.4A). ROI-based analyses showed that both groups exhibited a significant decrease in external capsule DTI RD and increase in external capsule DTI FA, while internal capsule DTI FA increased in restrained animals only and fimbria RK increased in healthy animals only (Figure 8.5A).

Following restraint, animals exhibited smaller and delayed brain maturation-related changes in white matter fibre cross-section and morphology compared to unrestrained animals. Unrestrained animals showed a greater increase in internal capsule FC and FDC and corpus callosum and fimbria FDC compared to restrained animals (Figure 8.4B). Additionally, there was a significant increase in AFD, APM, and MC in unrestrained animals only. ROI-based analyses showed a significant increase in internal

capsule FC and corpus callosum and fimbria FDC in both groups. Only the unrestrained animals exhibited a significant increase in corpus callosum, fimbria and external capsule FC, internal capsule FDC and external capsule and fimbria APM (Figure 8.5B).

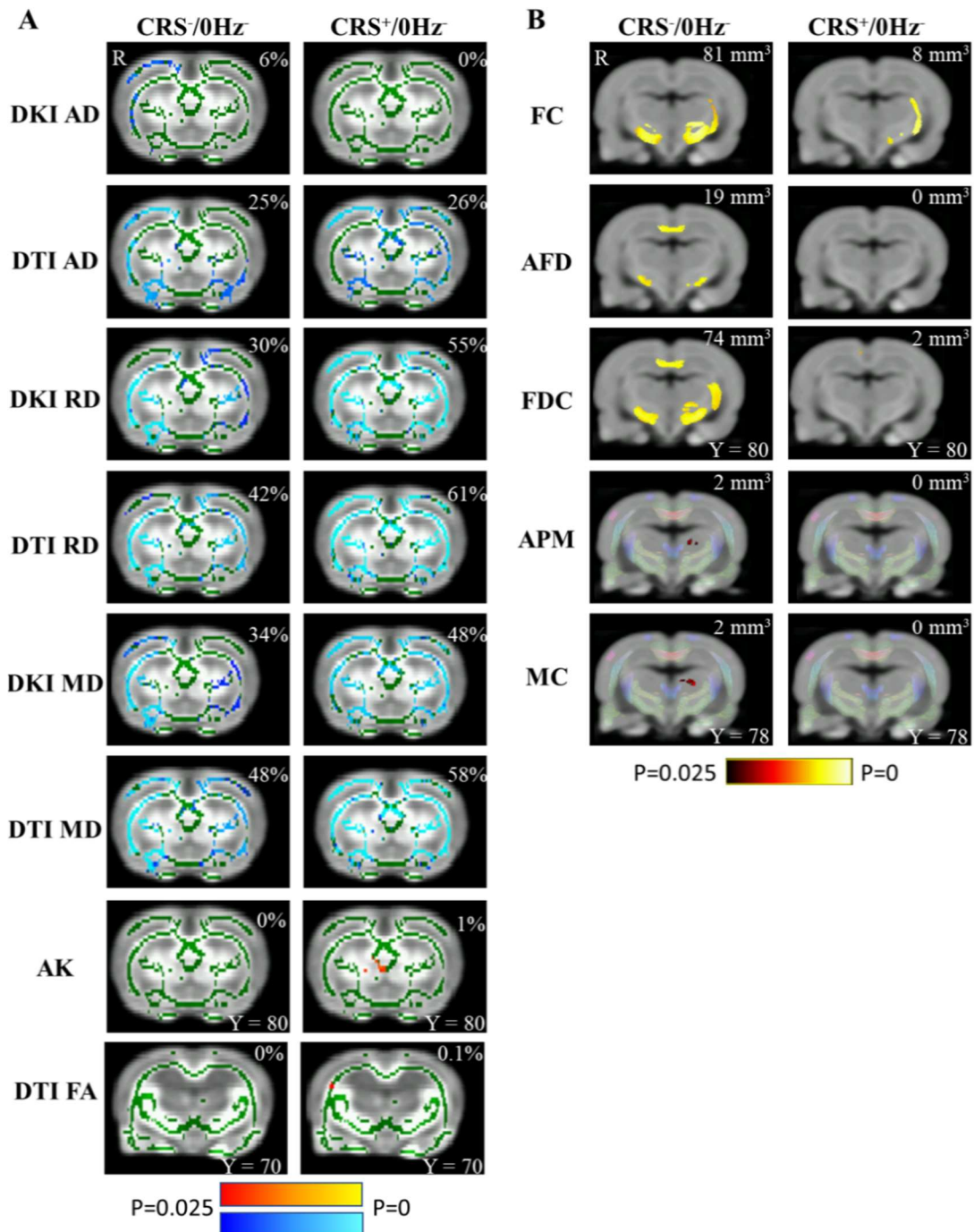
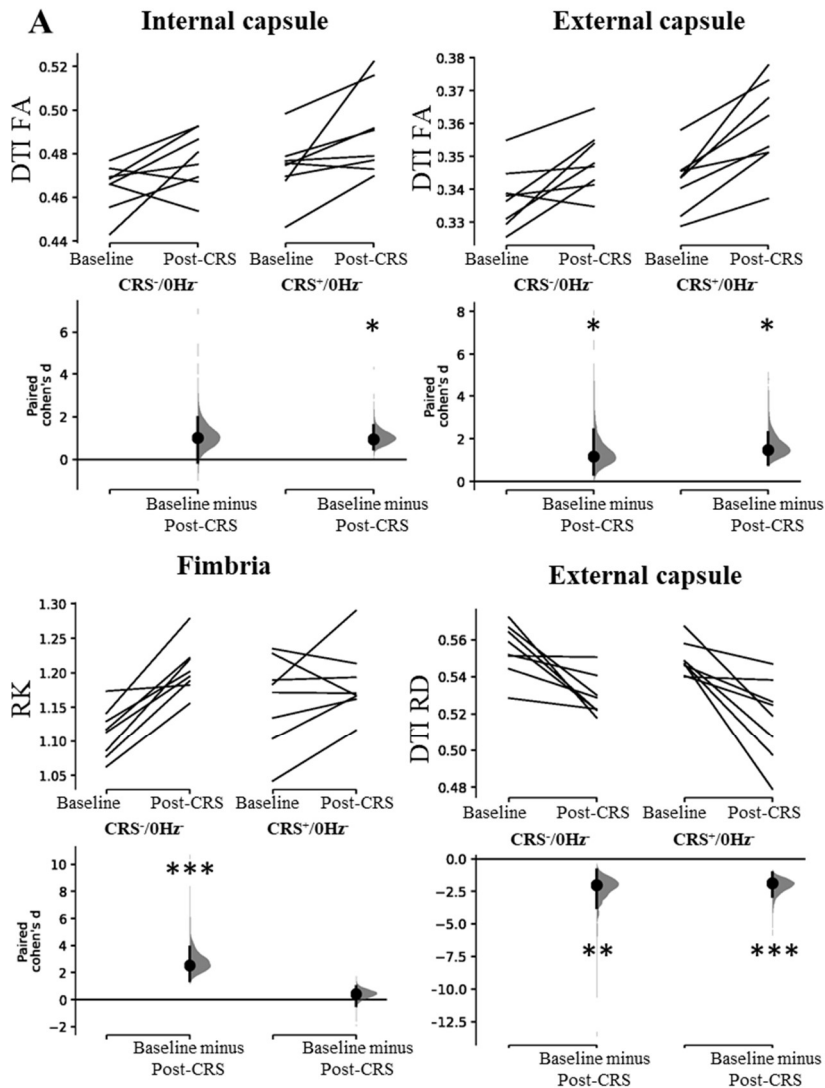
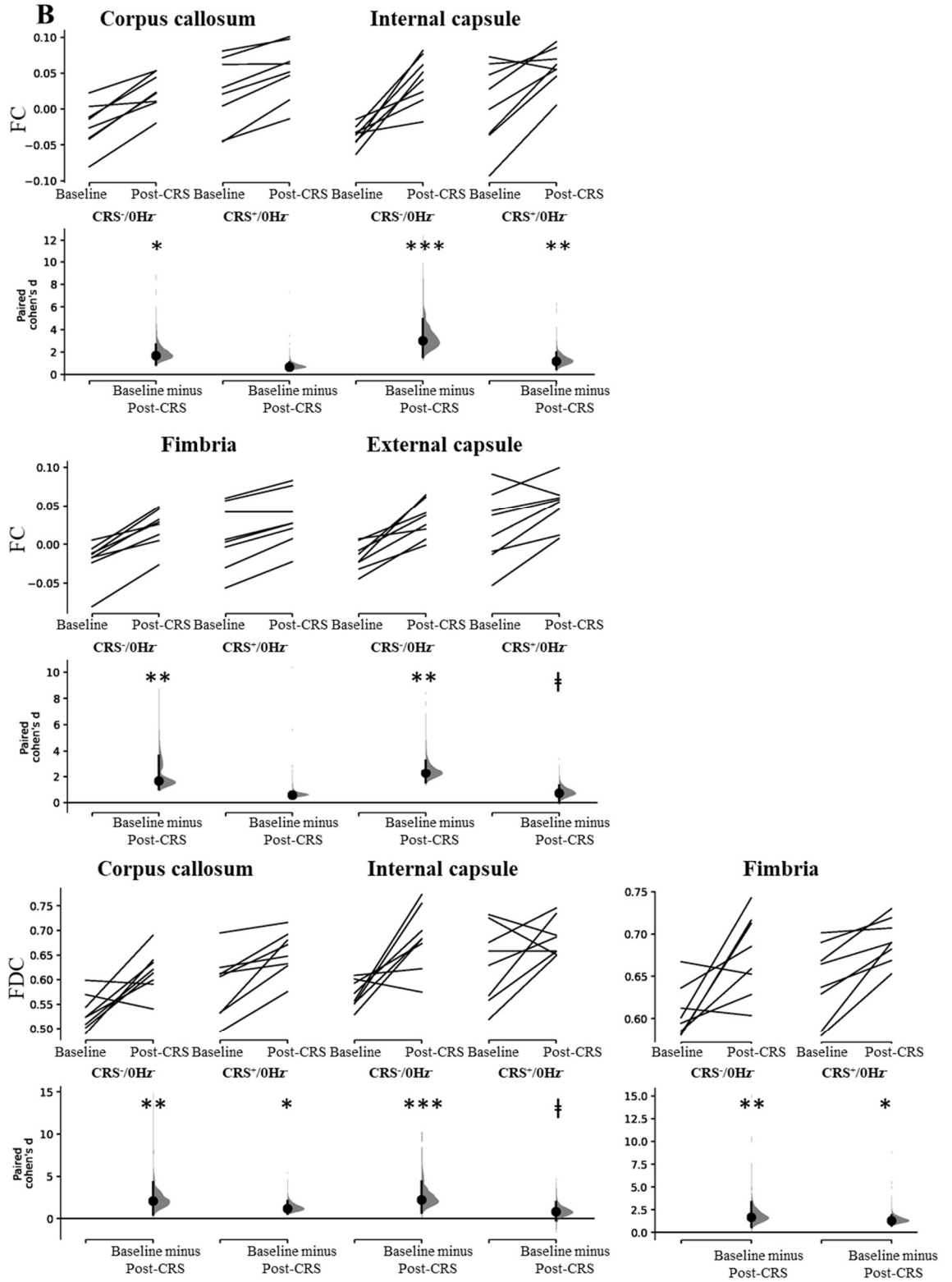


Figure 8.4. Chronic restraint stress (CRS) results in significant changes in the white matter ($P_{\text{Bonferroni}} < 0.025$). A shows results from TBSS analysis. Green represents the mean FA skeleton of all animals; red denotes an increase and blue represents a reduction post-restraint. The percentage on the top right corner of each coronal slice represents the percentage of the significant voxels relative to the whole skeleton voxels for each parameter. B

shows results from the fixel-based analysis and track-weighted imaging. Rats that underwent CRS (CRS+/0Hz) had a smaller increase in fibre cross-section (FC), apparent fibre density (AFD), combination of AFD and FC (FDC), average pathlength mapping (APM), and mean curvature (MC). Statistically significant fixels are overlaid on the population template. The whole-brain template tractogram is also overlaid on the population template for APM and MC. The number at the top right corner of each coronal slice represents the volume of significant voxels. The right side of the brain is denoted by R.





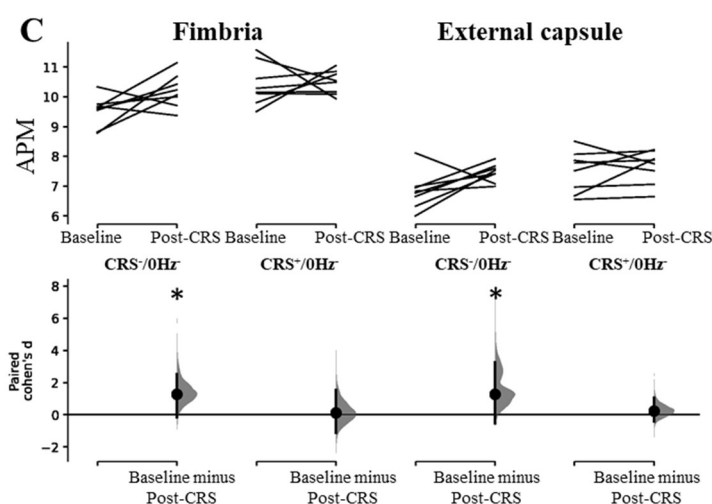


Figure 8.5. Chronic restraint stress (CRS) results in significant changes in (A) DTI measures and (B) fibre cross-section (FC), combination of apparent fibre density and FC (FDC), and (C) average pathlength mapping (APM) within white matter regions. The Cohen's d for two comparisons are shown in the Cumming estimation plots. The raw data is plotted on the upper axes; each paired set of observations is connected by a line. On the lower axes, each paired mean difference is plotted as a bootstrap sampling distribution. Mean differences are depicted as dots; 95% confidence intervals are indicated by the ends of the vertical error bars. † $p_{FDR} < 0.1$, * $p_{FDR} < 0.05$, ** $p_{FDR} < 0.01$, *** $p_{FDR} < 0.001$

8.3.3. Rat model of depression and treatment: white matter changes following CRS and accelerated 10 Hz LI-rTMS

8.3.3.1 dMRI

Having identified changes in white matter that were induced by CRS, we then determined whether these changes could be rescued using LI-rTMS. Similar to changes reported following CRS, there was a significant increase in DTI FA and FC when comparing post-restraint and W2 follow-up timepoints in all groups (Figure 8.6), suggesting ongoing brain maturation. LI-rTMS and control groups showed similar amount of change in DTI/DKI FA overall, but only the control group showed changes within the corpus callosum (Figure 8.7). DKI/DTI RD decreased over time in the corpus callosum in the sham and control groups but decreased over time in the fimbria in the LI-rTMS group (Figure 8.7). While FC increased with time in all groups, there was a greater increase in FC in the internal capsule and fimbria of the LI-rTMS group

compared to sham and control groups, suggesting a significant effect of LI-rTMS in normalizing the white matter changes observed post-restraint (Figure 8.6B). ROI-based analyses showed similar changes in FC and FDC in all groups (Supplementary Figure 8.2).

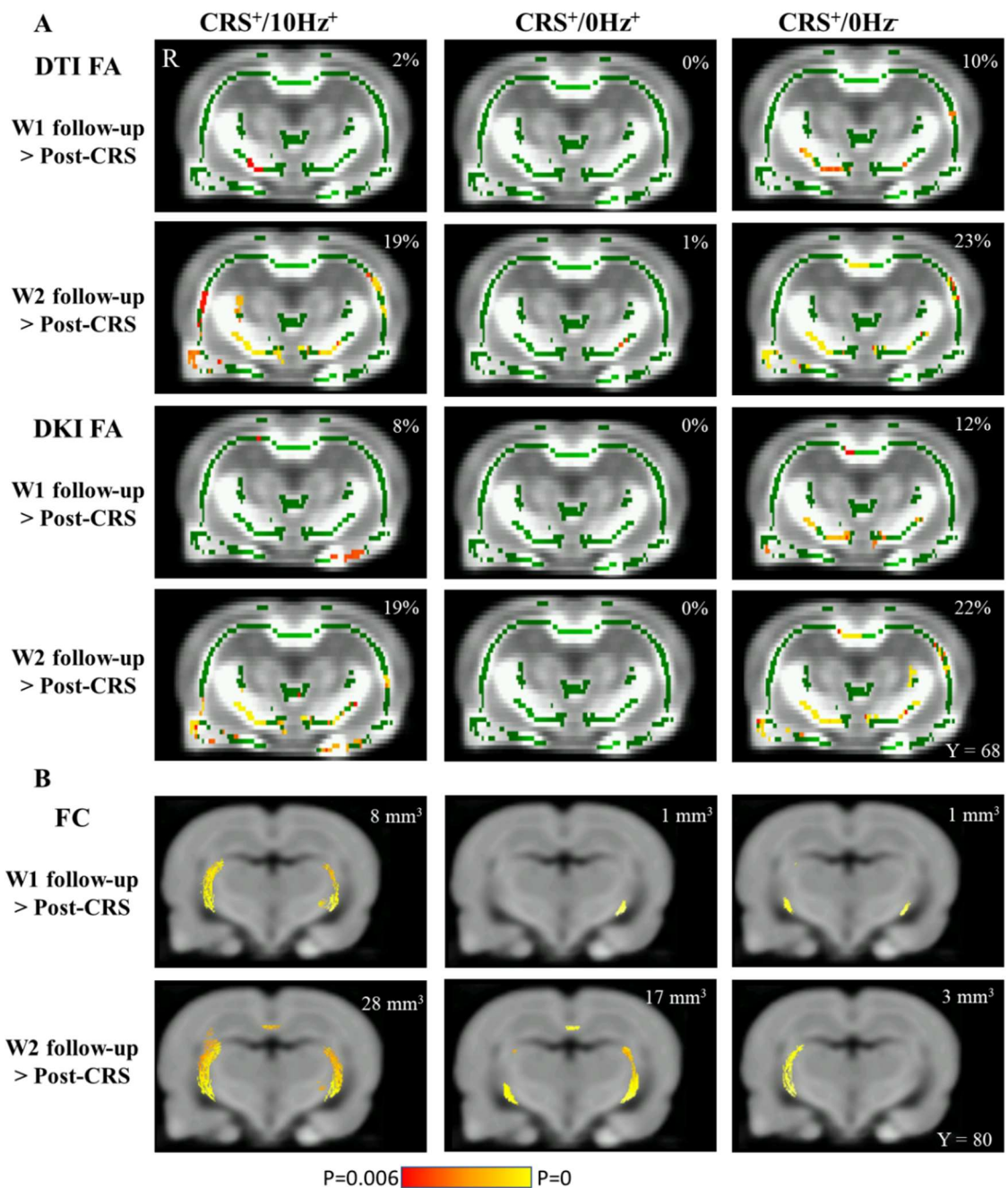
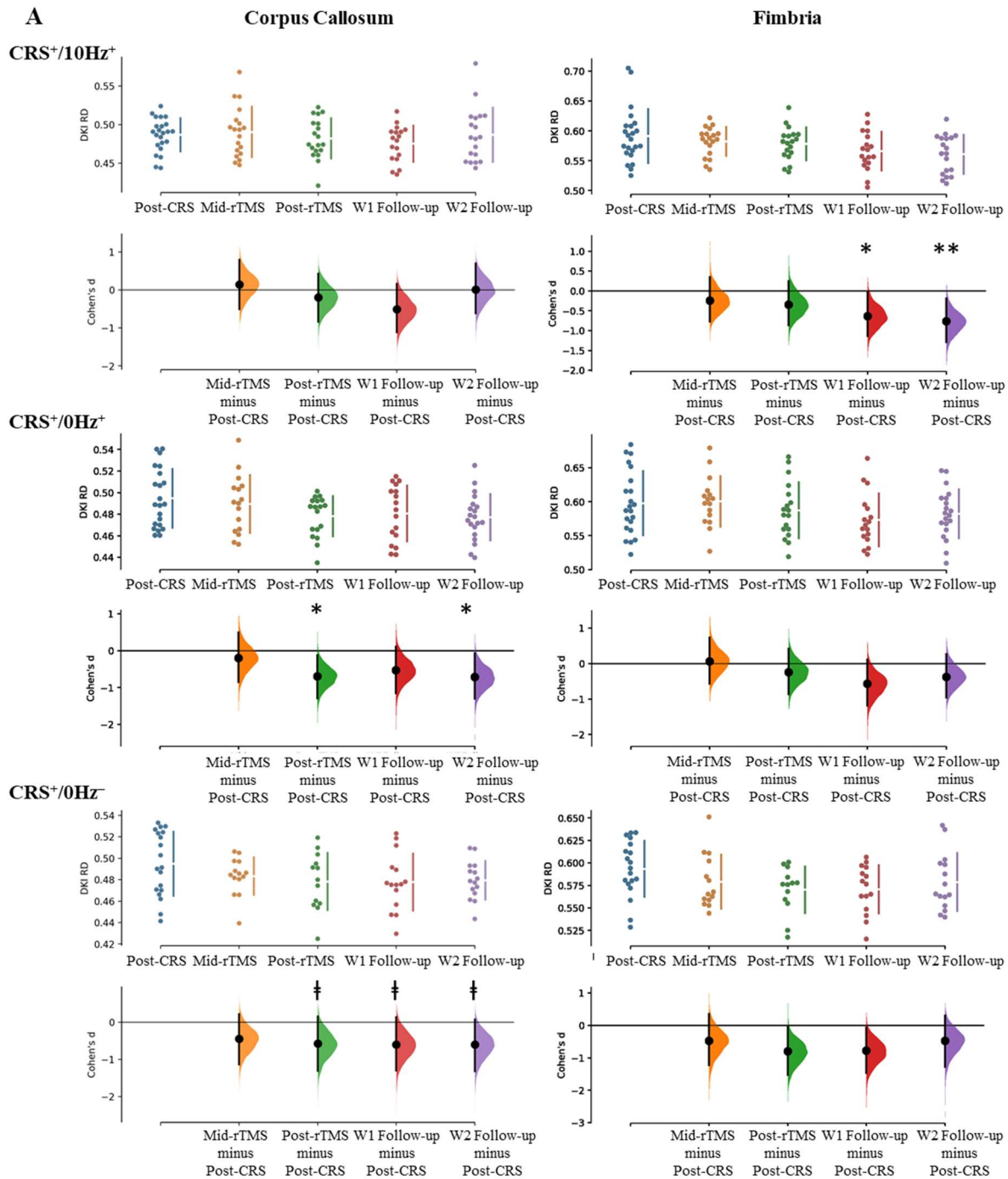


Figure 8.6. Increase in (A) DTI/DKI FA and (B) fibre cross-section following restraint in animals receiving active (CRS⁺/10Hz⁺), sham (CRS⁺/0Hz⁺), and no stimulation (CRS⁺/0Hz). A shows results from TBSS analysis. Green represents the mean FA skeleton of all animals; red denotes an increase post-restraint. The percentage on the top right corner of

each coronal slice represents the percentage of the significant voxels relative to the whole skeleton voxels for each parameter. B shows results from the fixel-based. Statistically significant fixels are overlaid on the population template. The number at the top right corner of each coronal slice represents the volume of significant voxels. The right side of the brain is denoted by R. LI-rTMS was delivered to the left side of the brain. All voxels were thresholded at a minimum Bonferroni-corrected p-value of 0.006.



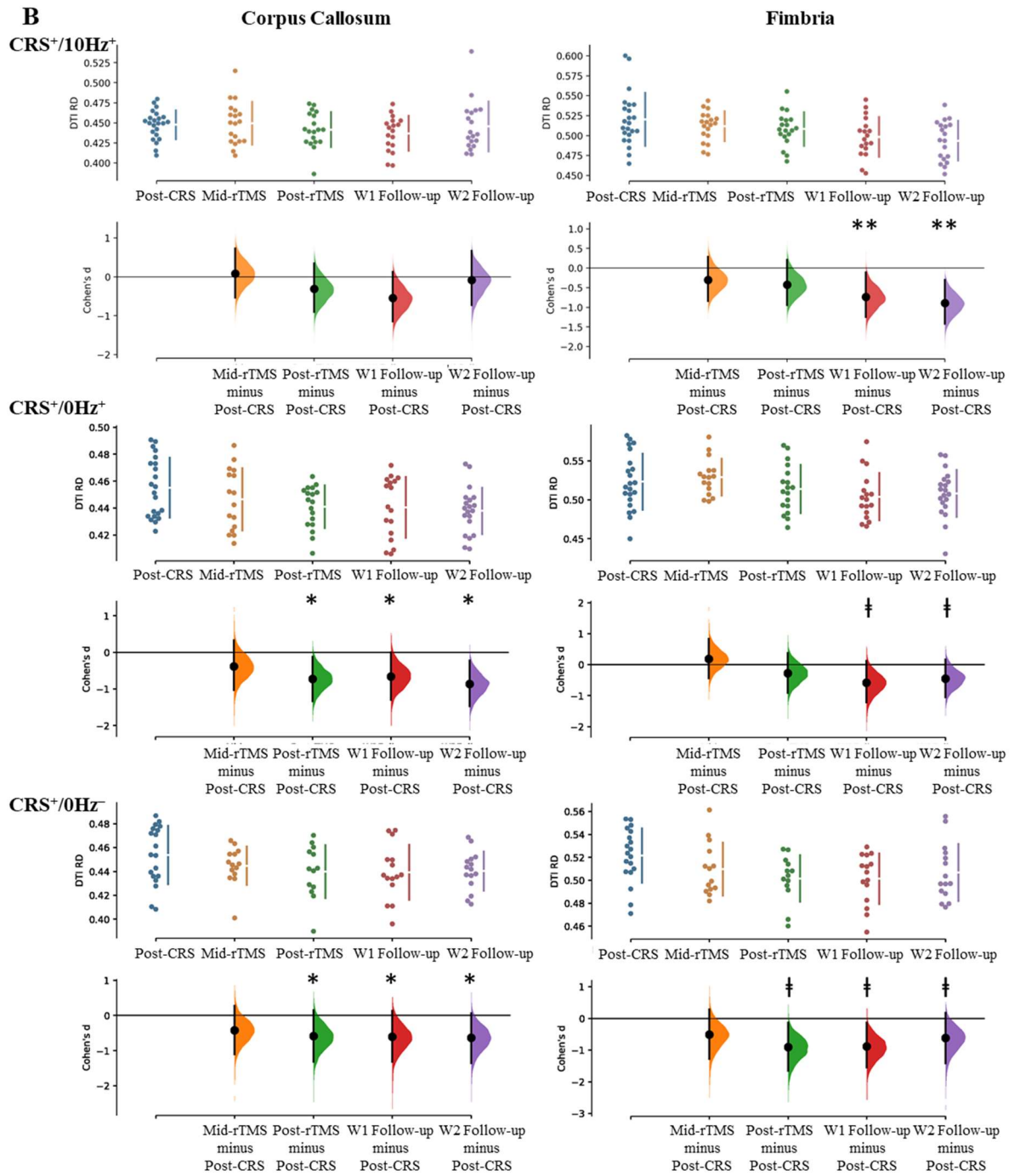


Figure 8.7. Significant changes in (A) DKI RD and (B) DTI RD within the corpus callosum and fimbria in animals receiving active (CRS⁺/10Hz⁺), sham (CRS⁺/0Hz⁺), and no stimulation (CRS⁺/0Hz⁻). The Cohen's d for 4 comparisons against the shared control Post-CRS are shown in the above Cumming estimation plot. The raw data is plotted on the upper axes. On the lower axes, mean differences are plotted as bootstrap sampling distributions. Each mean difference is depicted as a dot. Each 95% confidence interval is indicated by the ends of the vertical error bars. †p_{FDR} < 0.1, *p_{FDR} < 0.05, **p_{FDR} < 0.01.

8.3.3.2 Immunohistochemistry

Given that we found a decrease in DTI and DKI RD post-rTMS, and that changes in RD are related to myelination, we measured the relative immunodensity of the MBP fluorescent signal in the left, centre, and right regions of the corpus callosum in the CRS⁺/10Hz⁺, CRS⁺/0Hz⁺, and CRS⁺/0Hz⁻ groups (Figure 8.8A). A near-significant difference was detected between groups (ANOVA, $F_{[2,12]} = 3.710$; $p = 0.056$). Given the small sample size ($n = 5$ /group), a *post hoc* Mann-Whitney two-sample rank-sum test was performed. CRS⁺/10Hz⁺ animals showed greater MBP immunodensity than CRS⁺/0Hz⁺ animals or CRS⁺/0Hz⁻ animals at each ROI (Figure 8.8B). This difference was greater in the left hemisphere which received LI-rTMS (Table 8.1), supporting the FBA findings that LI-rTMS rescued the delayed myelination caused by CRS.

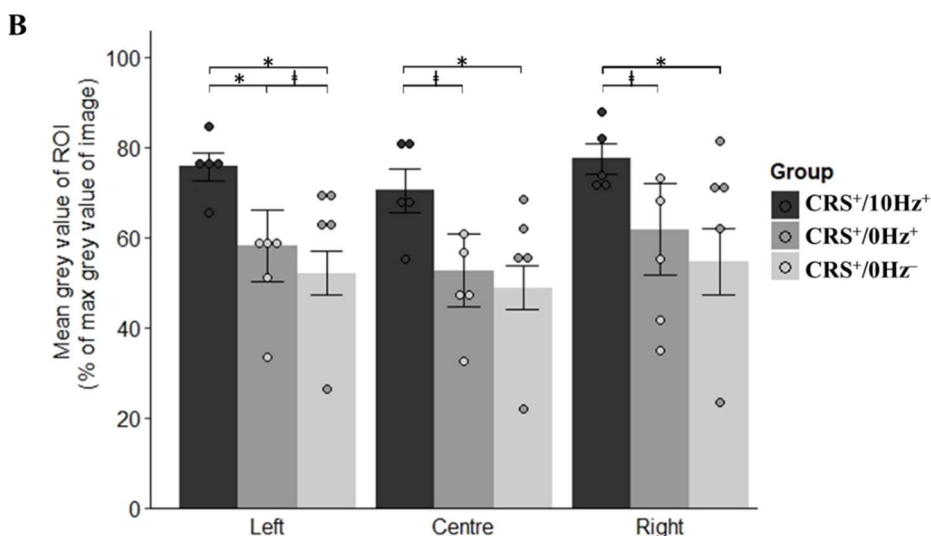
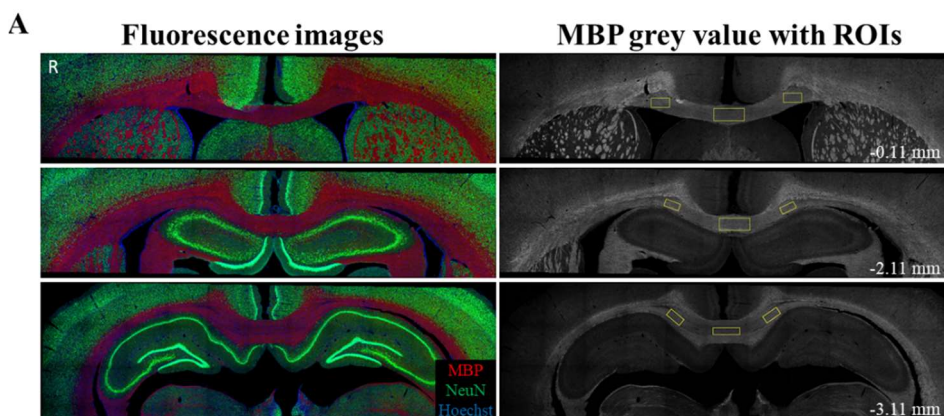


Figure 8.8. Myelin Basic Protein (MBP) immunostaining in CRS animals receiving active (CRS⁺/10Hz⁺), sham (CRS⁺/0Hz⁺), and no stimulation (CRS⁺/0Hz⁻). A shows representative images of the three sections selected from each brain for immunostaining. Left: original fluorescent signal of MBP staining (red), NeuN (green), and Hoechst signal (blue). Right: grey-scale images of MBP fluorescent signal (white) with left, centre and right ROIs overlaid (yellow) from which immunodensity was measured. LI-rTMS was delivered to the left side of the brain. R represents the right side of the brain. B shows mean \pm SEM of the mean grey value of the left, centre, and right ROIs measured as the percentage of the maximum grey value of the image. Comparisons were made by Mann-Whitney two-sample rank-sum test with FDR correction. LI-rTMS was delivered to the left side of the brain. †p < 0.1, *p < 0.05.

Table 8.1. Statistical table indicating the results of MBP analyses.

ROI	CRS ⁺ /10Hz ⁺ > CRS ⁺ /0Hz ⁺	CRS ⁺ /10Hz ⁺ > CRS ⁺ /0Hz ⁻	CRS ⁺ /0Hz ⁺ > CRS ⁺ /0Hz ⁻
Left	p _{FDR} = 0.024 * Effect size = 0.694	p _{FDR} = 0.012 * Effect size = 0.826	p _{FDR} = 0.075 † Effect size = 0.495
Centre	p _{FDR} = 0.071 † Effect size = 0.561	p _{FDR} = 0.048 * Effect size = 0.694	p _{FDR} = 0.21 Effect size = 0.297
Right	p _{FDR} = 0.071 † Effect size = 0.561	p _{FDR} = 0.024 * Effect size = 0.760	p _{FDR} = 0.274 Effect size = 0.231

8.4. Discussion

To our knowledge, the current study is the first to employ dMRI to track whole-brain white matter changes in healthy and CRS animals over time and following multiple sessions of LI-rTMS. While caution is needed when linking diffusion measures to microstructural correlates, based on the current literature, our dMRI and histological findings suggest that the restorative effects of LI-rTMS on the white matter are at least in part due to an increase in myelination.

8.4.1 High-frequency LI-rTMS induces greater and faster changes in the white matter of healthy rats than low-frequency LI-rTMS

In the present study, we observed extensive white matter changes in healthy Sprague-Dawley rats following 10 Hz and 1 Hz LI-rTMS using both DKI and conventional DTI. The increase in anisotropy observed following 10 Hz stimulation likely stems from the

increased axial (parallel) diffusivity observed within the internal capsule, which in turn may result from an increase in packing density of fibre bundles and axons, axonal diameter increase, changes in neurofibrils, and/or increased complexity of extracellular matrix (Wu and Cheung, 2010). Increased diffusion restriction perpendicular to axonal direction (RK) in the corpus callosum of both groups likely reflects increased myelination and/or number of axons (Wu and Cheung, 2010). Interestingly, RK is thought to be more influenced by cellular membranes and myelin sheaths, whereas AK (parallel to axonal direction) is considered to be primarily affected by intracellular structures. Although interpreting DKI metrics in terms of tissue microstructure is challenging, a significantly higher AK in the 10 Hz could be considered consistent with higher neurite density and increased microstructural complexity along the axial direction of white matter fibres. It will be interesting to determine whether the frequency-specific changes in white matter observed here are linked to the frequency-specific effects that have been reported on neuronal excitability, functional connectivity, neurometabolite changes, *inter alia* (Pell et al., 2011; Arnone et al., 2015; Tang et al., 2015; Seewoo et al., 2018a).

There are a few dMRI reports on the effect of rTMS on water diffusion in healthy subjects, but only the effects of a single rTMS session were assessed and results were inconclusive. One study reported no changes following high- or low-frequency rTMS (Niehaus et al., 2000), in contrast with other 1 Hz stimulation studies finding a brief (5 min) restriction in diffusion within the stimulated region compared to the contralateral region (Mottaghy et al., 2003) and changes lasting up to 20 minutes were also reported in remote non-stimulated regions (Abe et al., 2014). One explanation for the

longer-lasting effects observed in the present study is that two weeks of daily repeated rTMS reinforced the changes in diffusion, inducing a long-lasting (cumulative) effect on white matter organization and structural integrity within the whole brain (Muller-Dahlhaus and Vlachos, 2013).

8.4.2 Compromised brain maturation-related changes following CRS

Local fibre density, fibre cross-section, average pathlength and mean curvature increased from baseline in healthy control animals which may suggest changes in fibre morphology, an overall increase in number of axons, and/or total intra-axonal volume within fibre bundles within the corpus callosum, fimbria and internal and external capsules (Raffelt et al., 2017). These results concur with the work of Mengler et al. (2014), who reported progressive increases in cortical thickness and volume of several brain regions in healthy rats up until two months of age. Moreover, like in the present study, they found a decrease in AD, RD, and MD during the first 6 months of cerebral development (Mengler et al., 2014). Our DTI/DKI measures confirm these findings and further show an increase in fimbria RK, which likely reflects increased myelination leading to more diffusion restriction radially (Wu and Cheung, 2010). Overall, our results confirm and extend previous studies of ongoing brain maturation-related changes in young adult rats.

Interestingly, animals subjected to restraint stress exhibited less of these brain maturation-related changes, with the greatest impact on changes related to fibre morphology (AFD, APM, and MC). However, the DTI and DKI results are less clear-cut. Microstructural disruption in white matter, axonal degeneration, and demyelination in depression are generally believed to produce higher RD and MD and lower FA in both

patients with depression (Ota et al., 2015; Chen et al., 2016; Tymofiyeva et al., 2017; van Velzen et al., 2020) and animal models of depression (McIntosh et al., 2017; Nagy et al., 2020), such as the Wistar–Kyoto strain genetic model (Zalsman et al., 2017) and chronic unpredicted mild stress model (Hemanth Kumar et al., 2014). Keeping in mind that relating DTI and DKI measures to tissue microstructure is difficult, our observation of higher FA values being driven by a decrease in RD and MD contradicts the above-mentioned studies. Nevertheless, the heterogeneity of symptoms of depression may lead to these differential microstructural alterations (Blood et al., 2010; human: Wang et al., 2013; animal: Khan et al., 2016; Zhao et al., 2016). For example, increased FA and decreased RD can be associated with high levels of anxiety in human depression (Blood et al., 2010; Shizukuishi et al., 2013; Coloigner et al., 2019). Similarly, different animal model strains are prone to variation in behavioural and physiological adaptations to repeated stress and therefore exhibit different changes in dMRI (Magalhães et al., 2017). Overall, while the exact pathological processes occurring in patients with depression and CRS animals are still unknown, increased AK and decreased MD and RD strongly suggest that water diffusion is more restricted and white matter structure is altered by CRS.

8.4.3 Accelerated 10 Hz LI-rTMS rescued brain maturation-related changes

Given that we have shown changes in white matter linked to ongoing brain maturation in our young rats, dissecting changes related to brain-maturation, CRS and LI-rTMS is difficult. For example, an increase in FA has consistently been reported in patients with depression following repeated high-frequency rTMS (Kozel et al., 2011; Peng et al., 2012) and electroconvulsive therapy (Nobuhara et al., 2004; Lyden et al., 2014). In

contrast, in the present study, FA increased over time in all three CRS groups, suggesting there was no effect of LI-rTMS on FA. However, we cannot rule out that changes in FA due to LI-rTMS were masked by ongoing maturation.

Nonetheless, some measures were specific to LI-rTMS, and these were consistent with an increase in myelination. Myelination has been positively correlated to fibre cross-section in previous animal studies combining dMRI and immunohistochemistry (Malhotra et al., 2019) and in human dMRI studies of demyelinating diseases (Gajamange et al., 2018; Storelli et al., 2020). We observed a greater increase in fibre cross-section in the active group, consistent with their higher level of MBP in the corpus callosum compared to sham and depression control groups. The combination of an increase in fibre cross-section and myelination in the corpus callosum (Nuñez et al., 2000) reflects normal cerebral development in rats and these changes typically continue well into adulthood (3-6 months) but were impaired in sham and depression control animals. That exposure to early life stress alters white matter development in humans, non-human primates, and rodents is well established (Islam and Kaffman, 2021). In addition, abnormal myelination has been reported in human patients with depression, and animal models of depression and anxiety-like behaviours (Liu et al., 2012; Sacchet and Gotlib, 2017). Therefore, our results suggest that LI-rTMS may rescue brain-maturation and/or CRS-related changes, potentially via increased survival of oligodendrocytes and/or increased myelin production (Cullen et al., 2019).

Because neuronal activity is a major regulator of oligodendrocyte biology during development and in adulthood (Barres and Raff, 1993; Cullen et al., 2019), brain stimulation is a compelling therapeutic approach to promote myelin repair. Low-

intensity magnetic stimulation as used in the present study has been shown to increase survival of newly generated oligodendrocytes in mice (Cullen et al., 2019), which may underpin the increased myelination observed in our experiments. Interestingly, low-intensity magnetic stimulation does not trigger action potentials (Grehl et al., 2015; Tang et al., 2016b), but has been shown to increase excitability of pyramidal neurons in cortical slices (Tang et al., 2016a) and alter conduction velocity of axons in the corpus callosum (Cullen et al., 2021). These changes to intrinsic neuronal properties may alter the probability of neuronal firing, leading to the increased myelination described in both studies. It is possible that higher intensities of rTMS, such as those used in clinical settings, might have the same outcomes. For example, direct electrical stimulation to the corticospinal tract at supra-threshold intensities has been shown to result in proliferation and differentiation of oligodendrocyte progenitor cells (Li et al., 2010). Although both stimulation protocols would ultimately increase myelination, that they likely do so via different mechanisms is interesting to note.

8.4.4 Study limitations and future directions

Our study has two main limitations. Firstly, dMRI cannot directly measure microstructural changes, which need to be confirmed using invasive methods in animal studies. For example, retrograde tract-tracing data together with immunohistochemistry of gliosis status can further verify dMRI changes. Secondly, older adult rats that have completed cerebral development (6 months or older) can be used to exclude brain-maturation-related changes seen in the present study. Nonetheless, combining the use of DKI and conventional DTI along with fixel-based white matter tractography improved the detection of changes induced by CRS and LI-rTMS and provided more directionally specific and complementary information

compared to using these approaches individually. These findings suggest that multiple diffusion and kurtosis parameters should be used in conjunction with AFD and track-weighted imaging measures to assist in further advancing our understanding of depression disease progression and rTMS treatment.

8.4.5 Conclusion

In conclusion, this study found evidence of delayed brain maturation-related changes in restrained animals, but these were partly rescued by LI-rTMS. Importantly, by integrating dMRI and immunohistochemistry, our results raise the possibility that LI-rTMS and potentially rTMS may exert therapeutic effects by rescuing abnormal myelination, in addition to their well-characterized effects on neuronal plasticity (Tang et al., 2015), providing new insight into their mechanism of action and potential therapeutic applications.

8.5. Supplementary Methods

8.5.1. LI-rTMS procedure

Animals receiving active or sham LI-rTMS were habituated to handling and to the LI-rTMS coil during the habituation period. The animals were allowed to roam freely on the experimenter and during the period of stimulation, they remained relatively still without restraint. LI-rTMS was delivered using a custom-built round coil (described in detail in Grehl et al., 2015; Seewoo et al., 2018b). The coil was held by the experimenter on one hemisphere of the rat brain (between the eye and the ear) above the animal's head less than 1 mm from the skull. The magnetic field of the coil has been described in (Seewoo et al., 2018b). The monophasic pulse generated an intensity of approximately 13 mT at the surface of the cortex, which is below motor

threshold (Grehl et al., 2015; Seewoo et al., 2018b). The estimated intensity of induced electric field at the level of the cortex is less than 10 mV/mm, which is much less than the 28 mV/mm estimated to be the minimum intensity required to produce an action potential in pyramidal neurons (Radman et al., 2009; Madore et al., 2021).

Healthy animals from Seewoo et al. (2019c) received 10 min LI-rTMS at 10 Hz (10 pulses per second, total of 6000 pulses) or 1 Hz (1 pulse per second, total of 600 pulses) to the right brain hemisphere once daily for 15 days. For the CRS experiments, animals received accelerated 10 Hz LI-rTMS (10 pulses per second, total of 6000 pulses over a period of 10 min, repeated three times daily, one hour apart, five days/week for two weeks) to the left hemisphere. The hemisphere that was stimulated in Seewoo et al. (2019c) was chosen arbitrarily (but kept consistent across animals) because only healthy animals were used, and the aim of the experiments was to describe ipsilateral and contralateral changes post LI-rTMS. However, the left hemisphere was chosen for the CRS experiments because 10 Hz rTMS is normally applied to the left dorsolateral prefrontal cortex in depression in humans. We note that in human studies using a figure-of-8 coil, there is strong evidence that current flow in the anterior-posterior direction causes different effects from current flowing in the posterior-anterior direction (Stephani et al., 2016; Hannah and Rothwell, 2017). However, circular coils as used in the present study induce a clockwise flow of current in the left hemisphere, and an anticlockwise flow of current in the right hemisphere and to our knowledge, there is no evidence showing directional effects using a circular coil.

Animal preparation for MRI

The rat was pre-anaesthetised in an induction chamber (4% isoflurane in medical air, 2 L/min). Once fully anaesthetised, the animal was transferred to a heated imaging cradle and anaesthesia was maintained with a nose cone (2% isoflurane in medical air, 1 L/min). Body temperature and respiratory rate were monitored using a PC-SAM Small Animal Monitor (SA Instruments Inc., 1030 System). An MR-compatible computer feedback heating blanket was used for maintaining animal body temperature at 37°C (\pm 0.5°C). A 25G butterfly catheter was implanted subcutaneously in the left flank of the animal to deliver a 0.05-0.1 mg/kg bolus injection and continuous infusion of medetomidine at 0.15 mg/kg/h using an infusion pump. Once the animal's breathing rate dropped to 50 breaths/min, isoflurane was gradually reduced to 0.5-0.75%. These anaesthetic doses were empirically determined to ensure the respiratory rate of the animals was between 50-80 breaths/min; we refer readers to our recent study on the pharmacokinetics of medetomidine for guidance on establishing a standardized anaesthetic protocol (Kint et al., 2020). After the MRI procedure, medetomidine was antagonized by an injection of atipamezole (0.1 mg/kg).

8.5.2. MRI data acquisition

For the CRS/10Hz⁺ and CRS/1Hz⁺ animals, dMRI data was acquired at baseline and following seven (Mid-rTMS) and 14 days (Post-rTMS) of daily stimulation (Figure 8.1A). Another two imaging sessions were performed seven and 20 days after stimulation was ceased for the 10 Hz group, and seven and 14 days after stimulation was ceased for the 1 Hz group (W1 and W2 follow-ups). The only difference between the imaging timeline of the two groups was the timing of the Week 2 follow-up imaging session (20 days after stimulation cessation for the 10 Hz group and 14 days after stimulation

cessation in the 1 Hz group) due to MRI hardware failure that delayed scanning of the 10 Hz group (Seewoo et al., 2019c). For the CRS experiments, baseline dMRI data was acquired, followed by the CRS procedure and post-CRS dMRI data acquisition (Figure 8.1B). LI-rTMS was then delivered for five days a week for two weeks, with weekly imaging (Mid-rTMS and Post-rTMS). Another two imaging sessions were performed seven and 14 days after stimulation was ceased (W1 and W2 follow-ups).

All MR images were acquired with a Bruker Biospec 94/30 small animal MRI system operating at 9.4 T (400 MHz, H-1), with an Avance III HD console, BGA-12SHP imaging gradients, a 86 mm (inner diameter) volume transmit coil and a rat brain surface quadrature receive coil. Following a tri-plane scan to determine the position of the rat brain, high-resolution T2-weighted coronal, axial and sagittal images were acquired using a multi-slice 2D RARE (rapid acquisition with relaxation enhancement) sequence with fat suppression from 21 x 1-mm-thick interlaced slices (20 slices for sagittal) with slice gap of 0.05 mm and: field-of-view = 28.0 mm x 28.0 mm; matrix size = 280 x 280; 0.1 mm x 0.1 mm in-plane pixel size; repetition time (TR) = 2500 ms; echo time (TE) = 33 ms; RARE factor = 8; echo spacing = 11 ms; number of averages (NA) = 2; number of dummy scans (DS) = 2; flip angle (α) = 90°; receiver bandwidth (BW) = 34722.2 Hz; and scan time = 2 min 55 s. Prior to acquiring the dMRI data, B0 shimming was completed for a region of interest covering the brain using the Bruker Mapshim routine. dMRI datasets were acquired during each scanning session using a spin-echo echo-planar imaging sequence. Five non-diffusion images were also acquired during each dMRI scan.

8.5.3. dMRI data analysis

8.5.3.1. Tract-based spatial statistics (TBSS)

FA is often related to tissue directionality and organisation and used as a measure of white matter 'integrity'. In the same way that the anisotropy of the diffusion tensor is described by the scalar FA, KFA reflects the anisotropy of the kurtosis tensor. Unlike other DKI measures, however, KFA depends solely on the kurtosis tensor and not on the diffusion tensor (Hansen and Jespersen, 2016). MD is a global measure of water diffusion which is related to cell density, size, and parenchyma permeability; RD is a measure of the diffusion perpendicular to the principal direction which reflects axonal integrity; and AD is the diffusion in the main direction of the white matter fibres which reflects myelin integrity. In DKI, MK is a dimensionless parameter that reflects the average degree of diffusion restriction, while AK and RK measure the kurtoses along the directions parallel and perpendicular to the principal diffusion direction, respectively. The directionally averaged MK tends to be less sensitive to changes when there are opposite trends of diffusivity and kurtosis changes in axial and radial directions (Wu and Cheung, 2010). An increase in MKT has been associated with increased complexity of extracellular matrix, potentially as a result of more non-Gaussian diffusion with increased density of neurites (Khan et al., 2016).

Following the generation of diffusion tensor and kurtosis parameter maps, the statistical parametric mapping (SPM12) toolbox built using the MATLAB compiler was used to generate diffusion tensor coordinates that enabled the generation of tensor image files for each dataset, a format compatible for input through the DTI-ToolKit (DTI-TK) software package to spatially normalise each dataset to a population-specific template (Zhang et al., 2007). DTI-TK is a non-parametric, diffeomorphic deformable

image registration software that incrementally estimates its displacement field using a tensor-based registration formulation (Zhang et al., 2006). The combined displacement field generated was then used to co-register each parameter map to the final population template. These co-registered images were concatenated to create one single 4D image for each diffusion parameter and fed into the FSL/TBSS pipeline.

The mean of all FA images was computed and used to generate a mean FA 'skeleton', which represents all tracts that are common in all images. A skeleton mask was then generated using an FA threshold of 0.26 (Harris et al., 2016). The mean FA and mean FA skeleton mask were used to skeletonise all parameter maps which were then fed into the voxel-wise group analysis using nonparametric permutation testing (FSL/randomise) with the threshold-free cluster enhancement (TFCE) option (Winkler et al., 2014). Statistically significant differences for maps were visualised at a family-wise error-corrected p-value of 0.05.

8.5.3.2. Fixel-based analysis (FBA)

For single-shell dMRI data, we employed the multi-tissue fixel-based analysis (FBA) pipeline implemented in MRtrix3 (Raffelt et al., 2017), where the fixel refers to individual fibre bundle elements in each voxel (Raffelt et al., 2012). Tissue response functions for the white matter and CSF were estimated for each dataset in MRtrix3 (Dhollander et al., 2019) and a unique set of average tissue response functions computed. The datasets were upsampled by a factor of 2 because this has been suggested to increase anatomical contrast and improve downstream template building, registration, tractography and statistics (Raffelt et al., 2012). The group average response functions were then used to obtain the fibre orientation distribution

(FOD) estimation from the upsampled images using multi-tissue constrained spherical deconvolution (Tournier et al., 2004; Jeurissen et al., 2014). Following bias field correction and global intensity normalisation of the multi-tissue compartment parameters, a population-based FOD template was generated based on $n = 50$ data across groups and timepoints with a maximum harmonic degree (l_{max}) = 4, because noise in higher harmonic orders can result in decreased registration accuracy (Raffelt et al., 2011). Individual FOD images computed with $l_{max} = 8$ were co-registered to the study-specific unbiased FOD template space. Fixel-based metrics, including the apparent fibre density (AFD), fibre cross-section (FC), and the combination of AFD and FC, called FDC, were derived from co-registered FOD maps and the correspondence maps (Raffelt et al., 2017). Whole-brain tractography was performed on the FOD template using the iFOD2 tractography algorithm with probabilistic tracking at a cutoff of 0.2, minimum length of 0.5 mm, maximum length of 25 mm, angle of 22.5 degrees, and 20 million streamlines (Tournier et al., 2010), followed by the spherical deconvolution informed filtering of tractograms (SIFT) method (Smith et al., 2013) to reduce tractography reconstruction biases and reduce the streamlines to 2 million. Statistical differences between timepoints were analysed at each fixel using connectivity-based fixel enhancement (CFE) with standard parameters ($C = 0.5$, $H = 3$, and $E = 2$) using the general linear model (Raffelt et al., 2015). Family-wise error (FWE)-corrected p-values were then assigned to each fixel using non-parametric permutation testing over 5000 permutations (Nichols and Holmes, 2002). To visualize all p-values less than 0.05, we thresholded the fixels using “mrview” at 0.95.

For track-weighted imaging (TWI) analysis, whole-brain tractography was also performed in native space for each rat using the same parameters outlined above and registered to the study-specific FOD template to normalise both the length and spatial location of the streamlines. The normalised tractograms were then used to generate the average pathlength map (APM), representing the average length of tracks passing through each voxel (Pannek et al., 2011) and mean curvature map (MC), representing the average curvature of all tracks passing through each voxel. Differences between timepoints were determined using non-parametric permutation testing over 5000 permutations and TFCE (Smith and Nichols, 2009). As above, a FWE-corrected p-value of less than 0.05 was considered significant.

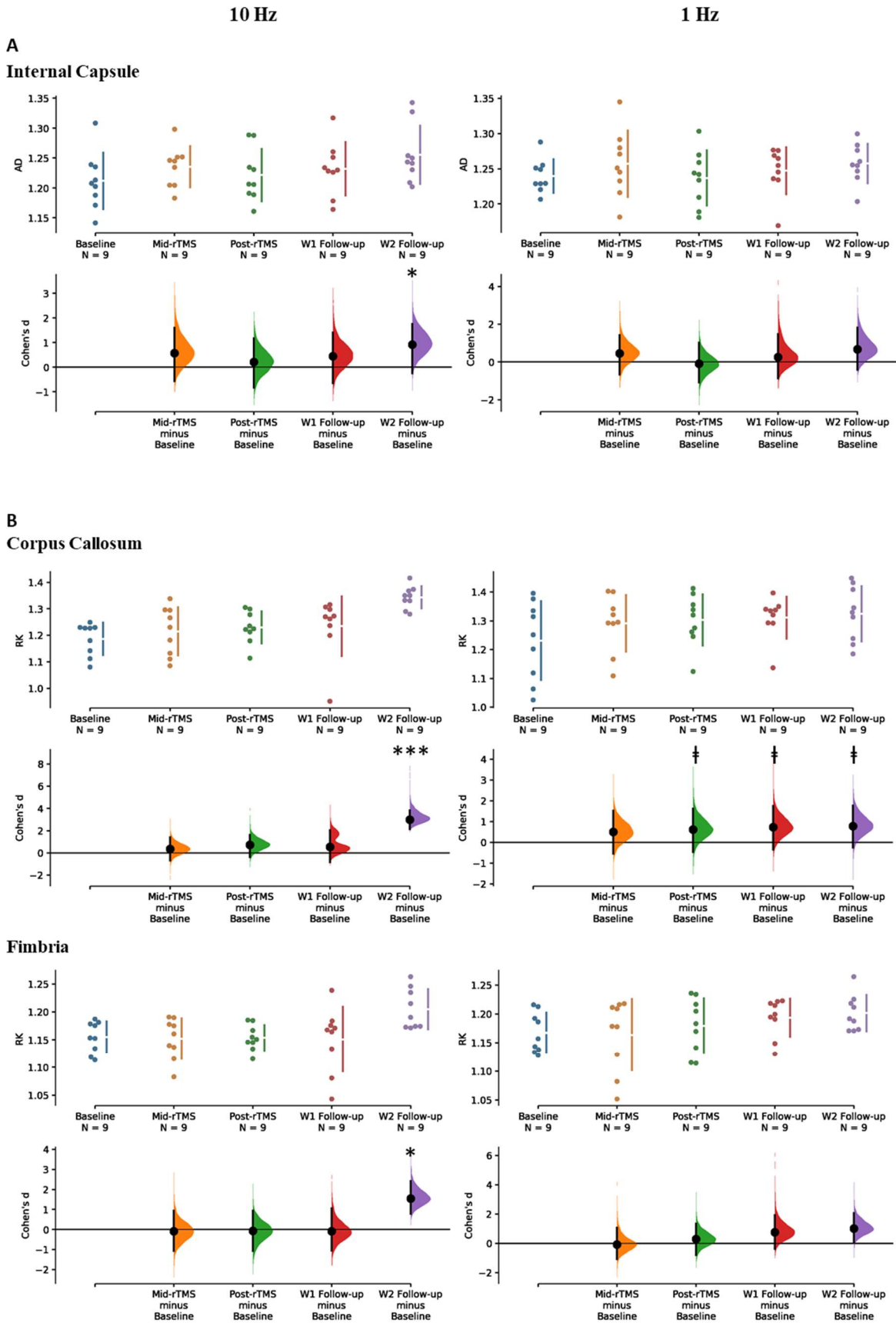
8.5.2. Brain immunohistochemistry

Sections were blocked and permeabilized for 1h in antibody diluent (5% normal donkey serum, 0.1% bovine serum albumin, 0.1% Triton in 0.1M PBS) before incubating in primary antibodies (1:250 rabbit anti-myelin basic protein polyclonal antibody, product code: ab40390; and 1:1000 mouse anti-NeuN monoclonal antibody, product code: MAB377) overnight at 4°C. The following day, sections were washed in PBS before incubation with donkey anti-mouse AlexaFluor 488 (1:500), donkey anti-rabbit AlexaFluor 555 (1:400), and Hoechst (1:1000) for 2h at room temperature. Sections were washed in PBS, mounted onto superfrost+ slides, and cover-slipped with Fluoromount.

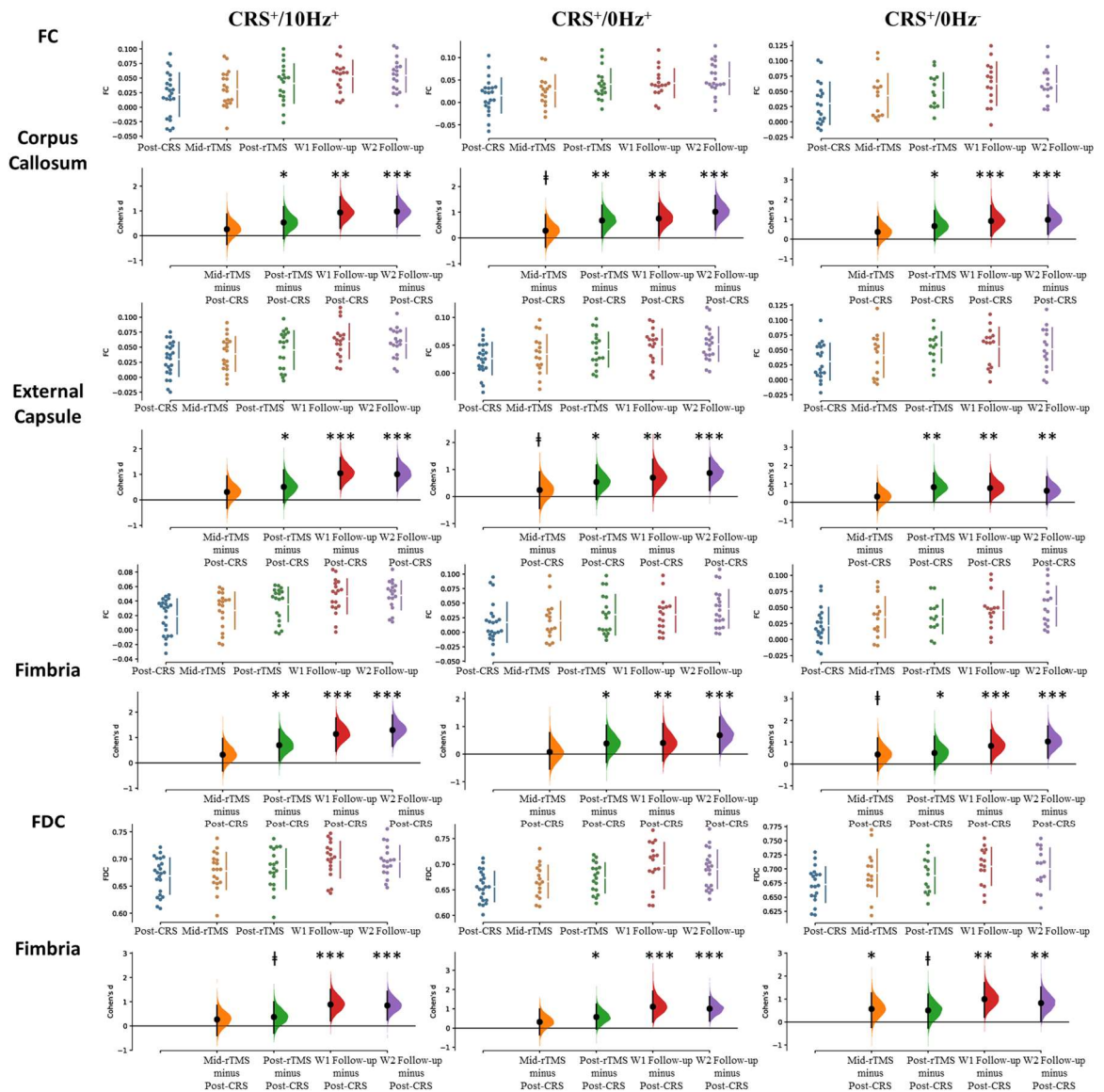
A Nikon confocal C2, NI-E microscope with a 10x lens was used for confocal imaging. Sections were imaged using three Z-stacks at 4µm thickness and images were collected and maximum projections made using NIS Elements AR software. All images were

acquired using the same settings and were analyzed by an operator blinded to conditions using FIJI (ImageJ 1.53c, National Institutes of Health) software (Schindelin et al., 2012). Myelin basic protein (MBP) signal intensity within three ROIs positioned in the left, centre and right area of the corpus callosum of each section was assessed by measuring the mean grey value (“Measure” function) as a percentage of maximum signal intensity within the section (“Find Maxima” function). Data from the three sections were averaged for each ROI and analyzed and plotted using RStudio v3.6.1. (RStudio Team, 2018).

8.6. Supplementary Figures



Supplementary Figure 8.1. Significant changes in (A) axial diffusivity (DKI AD) and (B) radial kurtosis (RK) in healthy animals receiving 10 Hz or 1 Hz LI-rTMS ($p_{FDR} < 0.006$). The Cohen's d for 4 comparisons against the shared control Baseline are shown in the above Cumming estimation plot. The raw data is plotted on the upper axes. On the lower axes, mean differences are plotted as bootstrap sampling distributions. Each mean difference is depicted as a dot. Each 95% confidence interval is indicated by the ends of the vertical error bars. † $p_{FDR} < 0.1$, * $p_{FDR} < 0.05$, ** $p_{FDR} < 0.01$, *** $p_{FDR} < 0.001$.



Supplementary Figure 8.2. Significant changes in the corpus callosum and external capsule FC and fimbria FDC in animals receiving active ($CRS^+/10Hz^+$), sham ($CRS^+/0Hz^+$), and no stimulation ($CRS^+/0Hz^-$). The Cohen's d for 4 comparisons against the shared control Post-CRS are shown in the above Cumming estimation plot. The raw data is plotted on the upper axes. On the lower axes, mean differences are plotted as bootstrap sampling distributions. Each mean difference is depicted as a dot. Each 95% confidence interval is indicated by the ends of the vertical error bars. † $p_{FDR} < 0.1$, * $p_{FDR} < 0.05$, ** $p_{FDR} < 0.01$, *** $p_{FDR} < 0.001$.

Chapter 9

Changes in the rodent gut microbiome following chronic restraint stress and low-intensity rTMS

Under review: Seewoo, B.J., Arena-Foster, Y., Hennessy, L.A., Gorecki, A.M., Anderton, R. & Rodger, J., 2021 Changes in the rodent gut microbiome following chronic restraint stress and low-intensity rTMS.

Growing evidence indicates that the community of microorganisms throughout the gastrointestinal tract, known as the gut microbiome, is associated with depression.

However, the bidirectional communication between the brain and the gut microbiome makes it difficult to separate the direct antidepressant effects of drugs on the brain from their antimicrobial effects on the gut microbiome, which in turn may reverse depression. rTMS, on the other hand, is a brain-specific treatment for depression and can therefore be used to isolate and investigate the potential top-down effects of rTMS-induced brain changes on the gut microbiome. In this chapter, we assessed gut microbiome changes longitudinally following chronic restraint stress (CRS) and 10 Hz low-intensity rTMS treatment using rat faecal samples acquired during the experiments described in Chapter 7. We also correlated these changes to MRI and behavioural data described in Chapter 7. CRS increased abundance within the Proteobacteria (Deltaproteobacteria, Desulfovibrionales) and Firmicutes (*Anaerostipes*, *Frisingococcus*), with decreases in Firmicutes family (*Acidaminococcaceae*) and genera (*Roseburia*, *Phascolarctobacterium* and *Fusicatenibacter*) persisting for up to 4 weeks post CRS. The decrease in Firmicutes was not observed in the handling control and LI-rTMS groups, suggesting that handling alone may have sustained changes in gut microbiome associated with CRS. Nonetheless, LI-rTMS was specifically associated with an increase in *Roseburia* genus that developed 2 weeks after treatment, and the

abundance of both *Roseburia* and *Fusicatenibacter* genera was significantly correlated with rTMS behavioural and MRI outcomes. In addition, LI-rTMS treated rats had a reduction in apoptosis pathways and several indicators of reduced inflammatory processes. These findings provide evidence that the brain can influence the gut microbiome in a “top-down” manner, presumably via stimulation of descending pathways, and/or indirectly via behavioural modification.

9.1. Introduction

Major depressive disorder (MDD) is a debilitating neuropsychiatric syndrome with significant morbidity and mortality due to the risk of suicide. Whilst the exact cause of depression is still largely unknown, current research suggests that mental illnesses such as MDD are caused by a complex array of genetic, neurological, hormonal, immunological, environmental, and psychological factors. These factors may be integrated via the gut-brain axis, the bidirectional communication network between the central and enteric nervous systems consisting of neural and immune pathways as well as the hypothalamic-pituitary-adrenal axis (Capuco et al., 2020; Cruz-Pereira et al., 2020). There is increasing evidence that gut-brain signalling is altered in MDD, with changes in the gut microbiome playing a key role (Kochar et al., 2018); (Barandouzi et al., 2020). However the causal relationships between the “bottom” (gut, microbiome), and the “top” (mood and brain function) of the gut-brain axis remain unclear. Understanding the influence of the brain on the microbiome in MDD may therefore facilitate improved treatment options.

Currently, most studies have investigated the bottom-up effects of the gut microbiome on brain chemistry and relevant behaviour in depression. The gut, including the composition of the microbiome, influences mood, cognition and other neurological functions (Clapp et al., 2017; Makris et al., 2021). For example, a faecal microbiota transplant from stressed animals or patients with depression to healthy animals has been shown to increase anxiety and depression-like behaviours in recipients, whereas the transplant of healthy microbiota to patients with depression conversely decreases depression symptoms (Chinna Meyyappan et al., 2020). Similarly, probiotic treatment

has been shown to reduce anxiety- and depression-related behaviours (Bravo et al., 2011) and restore brain changes related to depression and emotion processing (Bercik et al., 2010; Tillisch et al., 2013). However, the evidence for a top-down influence of the brain on the microbiome is less clear. While the brain regulates gastrointestinal motility, secretory activity and immune responses (Mayer, 2011), and psychological stress can change microbiome composition (Galley et al., 2014), a direct influence of brain signalling on the microbiome has not been definitively demonstrated.

Additionally, many antidepressant medications targeting brain function and mood are delivered orally and have antimicrobial properties (Valles-Colomer et al., 2019; Ait Chait et al., 2020), making it difficult to differentiate between potential top-down effects of neurological change on the gut, and the direct effect of oral medication on microbiome composition (Lukić et al., 2019; McGovern et al., 2019).

The use of brain-specific treatment methods can help to dissect the top-down effects of depression treatment on the gut microbiome. Non-invasive brain stimulation has exhibited potential positive effects on the gut microbiome in patients with weight disorders through subsequent improvements in weight (Artifon et al., 2020; Ferrulli et al., 2021). Here we use repetitive transcranial magnetic stimulation (rTMS), a non-invasive FDA-approved treatment for depression (O'Reardon et al., 2007) that uses electromagnetic induction to alter the excitability of the brain (George et al., 2000).

Given the evidence for perturbed gut-brain signalling in depression, we hypothesised that this brain-specific treatment for depression would allow us to isolate any potential top-down effects of the brain on the gut microbiome. Because of the variability of human subjects not only in terms of the gut microbiome but also in their response to

rTMS, here we use a well characterised chronic restraint intervention in rats to: 1) validate the effects of a chronic restraint stress model of depression on gut microbial composition and diversity in male Sprague-Dawley rats and 2) identify the effects of low-intensity rTMS treatment on the gut microbiome in this depression model.

9.2. Methods

All experimental procedures were approved by the University of Western Australia (UWA) Animal Ethics Committee (RA/3/100/1640) and conducted in accordance with the *National Health and Medical Research Council Australian code* for the care and use of animals for scientific purposes. All investigators were trained in animal handling by the UWA Programme in Animal Welfare, Ethics, and Science (PAWES) and had valid Permission to Use Animals (PUA) licenses.

9.2.1. Animals

The microbiome samples analysed here were collected from several cohorts of rats over a 2-year period. In addition to CRS and rTMS described in detail below, animals underwent behavioural testing and MRI imaging procedures to measure brain anatomy, resting-state functional MRI (rs-fMRI) and neurotransmitter levels (Magnetic Resonance Spectroscopy) (Figure 9.1). The outcomes of MRI (including rs-fMRI, hippocampal volume and neurotransmitter levels) and behavioural tests are used in the present study for correlation analysis and have been submitted for publication in full elsewhere. Summary of behavioural data are available on the Figshare repository (<https://figshare.com/>), with doi: 10.6084/m9.figshare.16866790. Full raw behavioural and MRI datasets are available on request to the corresponding author.

Young adult male Sprague-Dawley rats (5-6 weeks old, 150-200g) from the Animal Resources Centre (Perth, Western Australia) were maintained in a temperature-controlled animal care facility on a 12-hour light-dark cycle with food and water *ad libitum* (except during restraint). Animals were allowed to acclimatise to the facility for one week following their arrival. Cages contained two acidified water bottles (acidified as per safety regulations) and 500g of food pellets. To ensure the influence of diet on the gut microbiome was minimal, the diet for all animals was kept consistent and the weights of the animals were recorded weekly. Animals were randomly assigned to one of the following groups: 1) active group consisting of animals (n=12) which underwent CRS and received accelerated 10 Hz LI-rTMS (10 min three times daily, one hour apart, five days/week for two weeks) to the left hemisphere; 2) sham group consisting of (n=12) animals which underwent CRS and sham LI-rTMS; and 3) control group consisting of animals (n=7) which underwent CRS but did not receive any stimulation or extra handling during the treatment period (Figure 9.1). Animals were housed in pairs, such that those within the same group were co-housed to prevent transmission of faecal dysbiosis (Sun et al., 2013). At the end of the study, animals were euthanised by intraperitoneal overdose of pentobarbitone (Lethabarb) anaesthesia (160 mg/kg i.p.).

The CRS procedure was carried out for 2.5 h/day for 13 consecutive days as described previously (Seewoo et al., 2020a). Animals receiving LI-rTMS were habituated to handling and the coil as described previously (Rodger et al., 2012; Makowiecki et al., 2014). LI-rTMS was delivered at a frequency of 10 Hz using a custom-built round coil at an intensity of approximately 13 mT at the surface of the cortex, which is below the

rodent's motor threshold (Seewoo et al., 2018b). Stimulation was delivered following an accelerated protocol: 3 times daily at 1-hour intervals for 2 weeks (Seewoo et al., 2019a; Seewoo et al., 2021b). During the sham procedure, the coil was disconnected. Faecal pellets were collected from rats in all groups prior to CRS (baseline), after the last CRS procedure (post-CRS), at the end of the treatment period (post-rTMS) and two weeks after end of the treatment period (follow-up) (Figure 9.1).

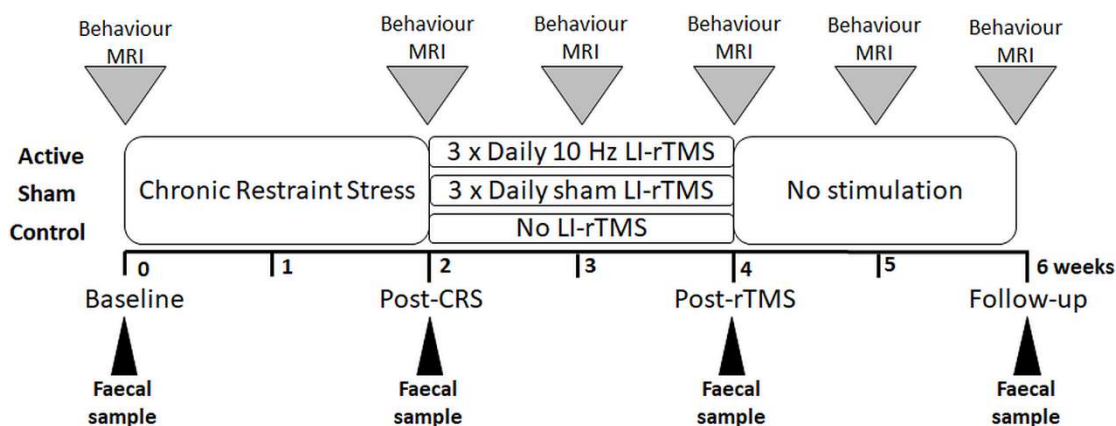


Figure 9.1. Experimental timeline. The research design consisted of an initial one-week period of habituation upon arrival of the animal. Rats then underwent chronic restraint stress for 2.5 h daily for 13 consecutive days. Animals were randomly allocated to 3 groups: active animals received 10 min of 10 Hz LI-rTMS three times daily (one hour apart, five days a week for two weeks), sham animals received a sham version of the stimulation protocol and depression control animals received no stimulation or extra handling. Faecal samples were collected at baseline (before the start of CRS), after the end of the 13 days of CRS (Post-CRS), after the end of the treatment period (Post-rTMS) and two weeks after the end of the treatment period (Follow-up).

9.2.2. Sample preparation and sequencing

Between 2 and 6 faecal pellets per animal were collected four timepoints, each separated by two weeks: baseline, post CRS, post LI-rTMS and follow up (Figure 9.1).

Pellets were collected during behavioural testing sessions when they were spontaneously and abundantly expelled in a clean and controlled environment with no additional interventions. Pellets were frozen within 10 min of production at each collection timepoint and stored separately at -80°C until the completion of the animal

cohort. Using aseptic techniques to avoid cross contamination, rat faecal pellets were subsequently weighed into microcentrifuge tubes, and a 10 g mid-section of each pellet was sent to Australian Genome Research Facility (AGRF, Australia) for DNA extraction and sequencing of the *16S rRNA* gene V3-V4 region on an Illumina MiSeq platform using the 2 × 300 bp V3 chemistry. The V3V4 primers used by AGRF were a modified 341F (5'-CCTAYGGGRBGCASCAG-3') and a modified 806R (5'-GGACTACNNGGGTAT CTAAT-3') (Yu et al., 2005). The 16S raw sequencing data is publicly available at Figshare repository (<https://figshare.com/>), with doi: 10.6084/m9.figshare.16866790.

9.2.3. 16S data processing

Raw sequencing reads were subjected to quality and adapter trimming using the `bbduk.sh` command available in the BBTools suite (version 38.87) (<https://jgi.doe.gov/data-and-tools/bbtools/>), with the following input parameters: `qtrim=r trimq=20 ktrim=r k=23 mink=11 minlen=200 hdist=1 tpe tbo`. Next, the MeFiT pipeline (version 1.0) (Parikh et al., 2016) was run with default parameters to merge trimmed overlapping paired-end reads. The summary statistics of the trimmed and merged sequence reads are available in Table S1. For filtering and clustering of merged reads into operational taxonomic units (OTUs), the MICCA software (version 1.7.2) was used (Albanese et al., 2015). In detail, merged sequences of less than 420 bp were filtered using the `micca filter` command. Then, the `micca otu` command was run to perform *de novo* greedy clustering of the sequences into OTUs using a sequence identity threshold of 97%, along with the removal of chimeric sequences and singleton OTUs. For each representative OTU sequence, taxonomic information was assigned using the Bayesian LCA-based taxonomic classification method (version 2.3-alpha) with

a minimum e-value of $1e-10$ and 100 bootstrap replications, against the NCBI 16S ribosomal RNA database (Gao et al., 2017a). A minimum confidence score of 80 was used to accept a taxonomic assignment at each level. Multiple sequence alignment of the OTU representative sequences was performed using PASTA (Mirarab et al., 2014), where the output alignment file was used for phylogenetic tree construction using FastTree (Price et al., 2010) under the GTR model with CAT approximation. The OTU table, as well as the taxonomic information, are available in Table S2.

Prior to analysing both alpha and beta diversities using the phyloseq (McMurdie and Holmes, 2013) and amplicon (<https://rdr.io/github/microbiota/amplicon>) R packages, rarefaction of the OTU table was performed at 8462 sequences per sample. For alpha diversity analysis, four indices were evaluated, including the number of observed OTUs, abundance-based coverage estimator (ACE), Shannon entropy and inverse Simpson. Comparison of alpha diversity between groups and different timepoints was performed using ANOVA with post-hoc Tukey test. For beta diversity analysis, principal coordinates analysis (PCoA) was performed at the OTU level using both weighted and unweighted UniFrac distance metrics, followed by the analysis of similarity test (ANOSIM) to test for differences in microbial communities between groups and different timepoints. Volatility analysis was performed for each group of rat subjects by comparing the Aitchison distances for OTUs between successive samples collected from the same animal over time (Bastiaanssen et al., 2021). Prediction of the microbial communities for KEGG functional pathways was performed using PICRUSt2 (version 2.3.0-b) (Douglas et al., 2020).

9.2.4. Statistical analysis

To identify significant bacterial taxa and KEGG pathways between groups and different timepoints, the analysis of composition of microbiomes (ANCOM) procedure (Lin and Peddada, 2020) was performed on unfiltered absolute abundance data, adjusted for cage and study batch effects. The p -values were adjusted using the Benjamini-Hochberg procedure at the significance level of 0.05. Significant bacterial taxa and KEGG pathways were declared by using ANCOM's W -statistic with a threshold of 0.7. All ANCOM test results are available in Table S4. For each differentially abundant taxa and KEGG pathways identified by ANCOM, further statistical testing was performed on the centered log-ratio (CLR)-transformed raw taxa and KEGG abundance values as described below.

9.2.3.1. Effect of CRS

Bacterial diversity and composition were similar between groups at baseline. Due to the small sample size, data from the baseline and post-CRS timepoints were pooled from the three groups receiving restraint to determine the effects of CRS on the gut microbiome. The difference in bacterial composition between baseline and post-CRS timepoints was examined by the Wilcoxon signed rank test ($n=29$ /timepoint).

9.2.3.2. Effect of LI-rTMS

To determine the effects of LI-rTMS on the gut microbiome, the Quade test was used to determine if there was a significant effect of timepoint (post-CRS, post-rTMS and follow-up) in each group, followed by *Post hoc* Wilcoxon signed rank test to determine paired differences between timepoints. The Benjamini-Hochberg false discovery rate (FDR) method was used to correct for multiple comparisons at the significance level of 0.05.

9.2.3.3. Correlation analysis

Magnetic resonance imaging (MRI) and behavioural data were acquired at the four timepoints using previously published methods (Seewoo et al., 2020a). Spearman correlations were performed between the microbiome data and the following MRI and behavioural measures from unpublished results: GABA and glutamate concentration (as a ratio to total creatine concentration) obtained from proton magnetic resonance spectroscopy (1H-MRS) within the sensorimotor cortex; hippocampal volume obtained from T2-weighted anatomical MRI data; cingulate cortex functional connectivity obtained from seed-based analysis of resting-state functional MRI (rs-fMRI) data; functional connectivity within the interoceptive network, salience network and default mode network obtained from independent component analysis of rs-fMRI data; number of exits from the open arms of the elevated plus maze (EPM); time spent immobile during the forced swim test (FST); time spent swimming during FST; and latency, which is the time taken to exhibit the first immobility behaviour during FST.

9.3. Results

9.3.1. Effect of CRS on the gut microbiome

CRS did not induce any changes in alpha diversity or beta diversity (Supplementary Figures 9.1-9.10). However, class-level analyses revealed a significant increase in Deltaproteobacteria post-CRS ($V=102$, $p=0.011$) which was accompanied by an increase in the corresponding Desulfovibrionales order ($V=98$, $p=0.009$; Figure 9.2). Genus-level analysis showed marked increases in both *Anaerostipes* and *Frisingicoccus* of the *Clostridia* class ($V=68$, $p<0.001$; $V=86$, $p=0.004$ respectively; Figure 9.2). There were no significant changes in any other taxa or KEGG pathways.

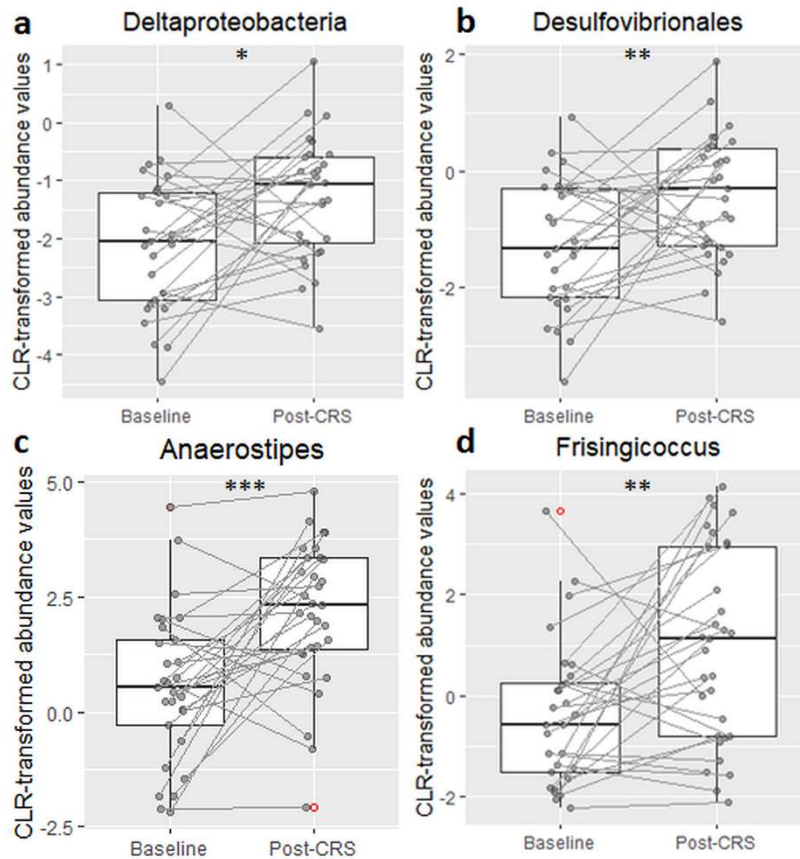


Figure 9.2. Effect of chronic restraint stress on abundance of Deltaproteobacteria class (a), and its corresponding Desulfovibrionales order (b), and Anaerostipes (c), and Frisingicoccus (d) genera of the Clostridia class. The figure shows boxplots of centered log-ratio transformed taxa abundances for taxa identified as significant in the ANCOM's W-statistic (threshold of 0.7). Between-timepoint comparisons were made by Wilcoxon signed rank test. * $p < 0.05$; ** $p < 0.01$; *** $p < 0.001$.

9.3.2. Effect of LI-rTMS on the gut microbiome

LI-rTMS did not induce any changes in alpha diversity or beta diversity (Supplementary Figures 9.1-9.10). Class-level analyses revealed a significant decrease in the Negativicutes class over time in the depression control group ($F_{(2,12)}=12.20$, $p=0.001$; $p_{FDR}=0.031$ for all; Figure 9.3). This decrease was accompanied by a significant decrease in the corresponding Acidaminococcales order ($F_{(2,12)}=12.20$, $p=0.001$; $p_{FDR}=0.047$ for all).

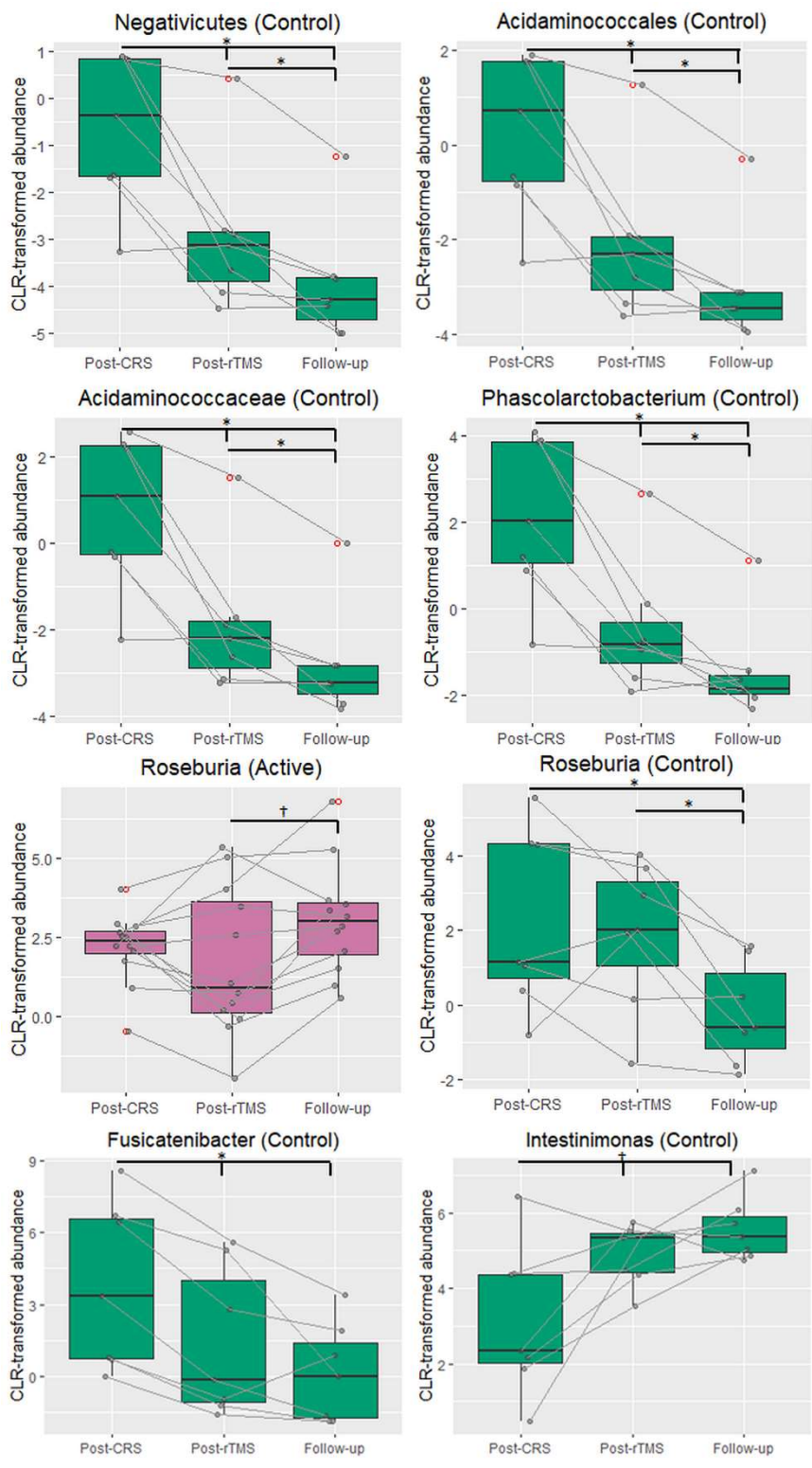


Figure 9.3. Changes in abundance of taxa between timepoints within the active, sham and depression control groups. The figure shows boxplots of centered log-ratio transformed taxa abundances for taxa identified as significant in the ANCOM's W-statistic (threshold of 0.7). Quade test was used to determine if there was a significant effect of timepoint (post-CRS, post-rTMS and follow-up) in each group. Between-timepoint comparisons were made by Post hoc Wilcoxon signed rank test with Benjamini-Hochberg FDR correction. †p < 0.1; *p < 0.05.

Within the Negativicutes class, *Acidaminococcaceae* family also significantly decreased over time in the depression control group ($F_{(2,12)}=20.37$, $p<0.001$; $p_{FDR}=0.031$ for Post-CRS vs Post-rTMS, $p_{FDR}=0.023$ for Post-CRS vs Follow-up and Post-rTMS vs Follow-up), as did the corresponding *Phascolarctobacterium* genus ($F_{(2,12)}=14.14$, $p<0.001$; $p_{FDR}=0.023$ for Post-CRS vs Post-rTMS and Follow-up, $p_{FDR}=0.031$ for Post-rTMS vs Follow-up). Additionally, there was a significant effect of timepoint for the *Roseburia* genus from the Clostridia class in the active ($F_{(2,22)}=4.569$, $p=0.022$) and depression control groups ($F_{(2,12)}=5.243$, $p=0.023$). There was a trend for an increase in *Roseburia* genus between the post-rTMS and follow-up timepoints ($p_{FDR}=0.081$) in the active group while *Roseburia* genus decreased significantly at the follow-up timepoint compared to both post-CRS and post-rTMS timepoints in the depression control group ($p_{FDR}=0.047$ for both). Furthermore, within the Clostridia class in the control group, there was a significant decrease in *Fusicatenibacter* genus from the post-CRS timepoint to the post-rTMS and follow-up timepoints ($F_{(2,12)}= 15.23$, $p<0.001$; $p_{FDR}=0.047$ for both) and a trend for an increase in *Intestinimonas* genus from the post-CRS timepoint to the post-rTMS and follow-up timepoints ($F_{(2,12)}= 7.868$, $p=0.007$; $p_{FDR}=0.07$ for both). There were several significant changes in KEGG functional pathways (Table 9.1, Figure 9.4).

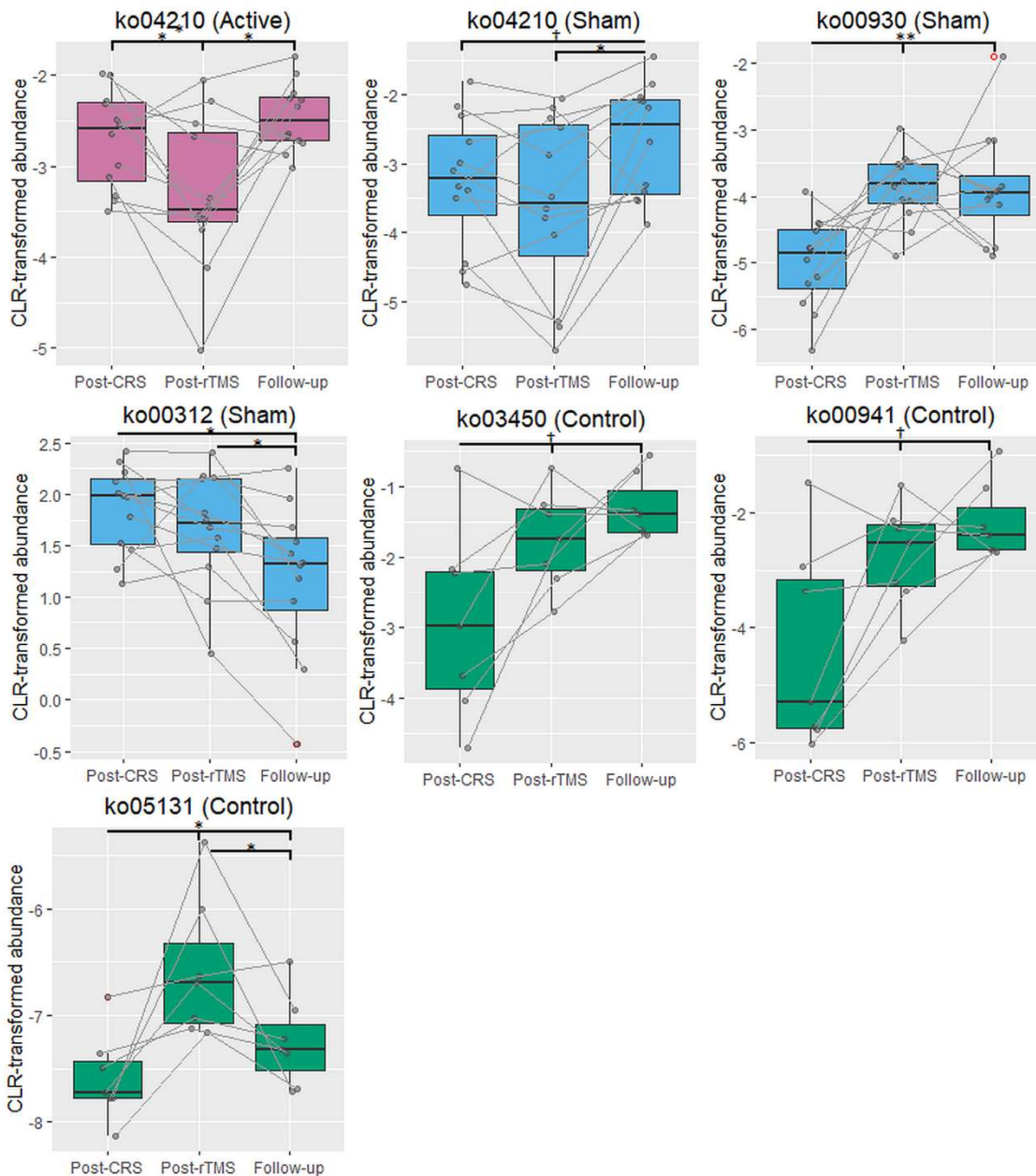


Figure 9.3. Changes in KEGG pathways between timepoints within the active, sham and depression control groups. The figure shows boxplots of centered log-ratio transformed KEGG pathway abundances for pathways identified as significant in the ANCOM's W-statistic (threshold of 0.7). Quade test was used to determine if there was a significant effect of timepoint (post-CRS, post-rTMS and follow-up) in each group. Between-timepoint comparisons were made by *Post hoc* Wilcoxon signed rank test with Benjamini-Hochberg FDR correction. † $p < 0.1$; * $p < 0.05$; ** $p < 0.01$.

Table 9.1. Summary of changes in abundance for KEGG functional pathways following chronic restraint stress (CRS) and between timepoints within the active, sham and depression control groups. Active animals received 10 min of 10 Hz LI-rTMS three times daily (one hour apart, five days a week for two weeks), sham animals received a sham version of the stimulation protocol with the coil turned off and control animals received no stimulation or extra handling.

KEGG	Functional pathway	Group	Quade test	Timepoint comparison	Mean \pm SD
ko04210	Apoptosis	Active	$F_{(2,22)} = 8.272$ $p = 0.002$	Post-CRS vs Post-rTMS $p_{FDR} = 0.031$ Post-rTMS vs Follow-up $p_{FDR} = 0.028$	Post-CRS = -2.71 ± 0.53 Post-rTMS = -3.32 ± 0.83 Follow-up = -2.46 ± 0.37
		Sham	$F_{(2,22)} = 7.286$ $p = 0.003$	Post-CRS vs Follow-up $p_{FDR} = 0.078$ Post-rTMS vs Follow-up $p_{FDR} = 0.037$	Post-CRS = -3.25 ± 0.96 Post-rTMS = -3.60 ± 1.29 Follow-up = -2.67 ± 0.82
ko00930	Caprolactam degradation	Sham	$F_{(2,22)} = 5.016$ $p = 0.016$	Post-CRS vs Post-rTMS $p_{FDR} = 0.007$ Post-CRS vs Follow-up $p_{FDR} = 0.007$	Post-CRS = -5.00 ± 0.67 Post-rTMS = -3.87 ± 0.53 Follow-up = -3.88 ± 0.84
ko00312	beta-Lactam resistance	Sham	$F_{(2,22)} = 6.790$ $p = 0.005$	Post-CRS vs Follow-up $p_{FDR} = 0.031$ Post-rTMS vs Follow-up $p_{FDR} = 0.010$	Post-CRS = 1.85 ± 0.42 Post-rTMS = 1.66 ± 0.56 Follow-up = 1.17 ± 0.74
ko03450	Non-homologous end-joining	Control	$F_{(2,12)} = 7.455$ $p = 0.008$	Post-CRS vs Post-rTMS $p_{FDR} = 0.070$ Post-CRS vs Follow-up $p_{FDR} = 0.070$	Post-CRS = -2.94 ± 1.35 Post-rTMS = -1.75 ± 0.69 Follow-up = -1.28 ± 0.45
ko00941	Flavonoid biosynthesis	Control	$F_{(2,12)} = 5.243$ $p = 0.023$	Post-CRS vs Post-rTMS $p_{FDR} = 0.070$ Post-CRS vs Follow-up $p_{FDR} = 0.070$	Post-CRS = -4.37 ± 1.77 Post-rTMS = -2.74 ± 0.91 Follow-up = -2.15 ± 0.67
ko05131	Shigellosis	Control	$F_{(2,12)} = 17.71$ $p < 0.001$	Post-CRS vs Post-rTMS $p_{FDR} = 0.023$ Post-CRS vs Follow-up $p_{FDR} = 0.023$ Post-rTMS vs Follow-up $p_{FDR} = 0.031$	Post-CRS = -7.58 ± 0.41 Post-rTMS = -6.57 ± 0.66 Follow-up = -7.25 ± 0.42

9.3.3. Correlation between the gut microbiome and brain and behavioural measures

Spearman's rank correlation test using data from all groups and timepoints revealed significant correlations of microbiome composition and KEGG pathways with several MRI and behavioural measures (Figure 9.5). However, none of these correlations survived multiple comparison correction in the active and depression control groups.

In the sham group, GABA was positively correlated to Negativicutes class ($r=0.47$, $p=0.005$, $p_{FDR}=0.037$), Acidaminococcales order ($r=0.48$, $p=0.005$, $p_{FDR}=0.037$), *Acidaminococcaceae* family ($r=0.45$, $p=0.007$, $p_{FDR}=0.047$) and *Phascolarctobacterium* genus ($r=0.46$, $p=0.006$, $p_{FDR}=0.045$). Glutamate was positively correlated to Negativicutes class ($r=0.58$, $p<0.001$, $p_{FDR}=0.005$), Acidaminococcales order ($r=0.58$, $p<0.001$, $p_{FDR}=0.004$), *Acidaminococcaceae* family ($r=0.59$, $p<0.001$, $p_{FDR}=0.004$) and *Phascolarctobacterium* genus ($r=0.60$, $p<0.001$, $p_{FDR}=0.003$), but negatively correlated to the *Intestinimonas* genus ($r=-0.46$, $p=0.005$, $p_{FDR}=0.037$) and ko03450 ($r=-0.48$, $p=0.003$, $p_{FDR}=0.033$) and ko00941 ($r=-0.49$, $p=0.003$, $p_{FDR}=0.029$) pathways. For the forced swim test, time spent immobile was positively correlated to the *Phascolarctobacterium* ($r=0.44$, $p=0.007$, $p_{FDR}=0.048$) and *Fusicatenibacter* genera ($r=0.51$, $p=0.002$, $p_{FDR}=0.020$), but negatively correlated to the *Intestinimonas* genus ($r=-0.47$, $p=0.004$, $p_{FDR}=0.037$) and ko03450 ($r=-0.56$, $p<0.001$, $p_{FDR}=0.007$) and ko00941 ($r=-0.54$, $p<0.001$, $p_{FDR}=0.010$) pathways. Latency to first immobility behaviour was positively correlated to the ko03450 pathway ($r=0.56$, $p<0.001$, $p_{FDR}=0.007$), but negatively correlated to the Negativicutes class ($r=-0.62$, $p<0.001$, $p_{FDR}=0.002$), Acidaminococcales order ($r=-0.63$, $p<0.001$, $p_{FDR}=0.002$), *Acidaminococcaceae* family ($r=-0.65$, $p<0.001$, $p_{FDR}=0.001$) and both *Phascolarctobacterium* and *Fusicatenibacter* genera ($r=-0.66$, $p<0.001$, $p_{FDR}=0.001$ for both).

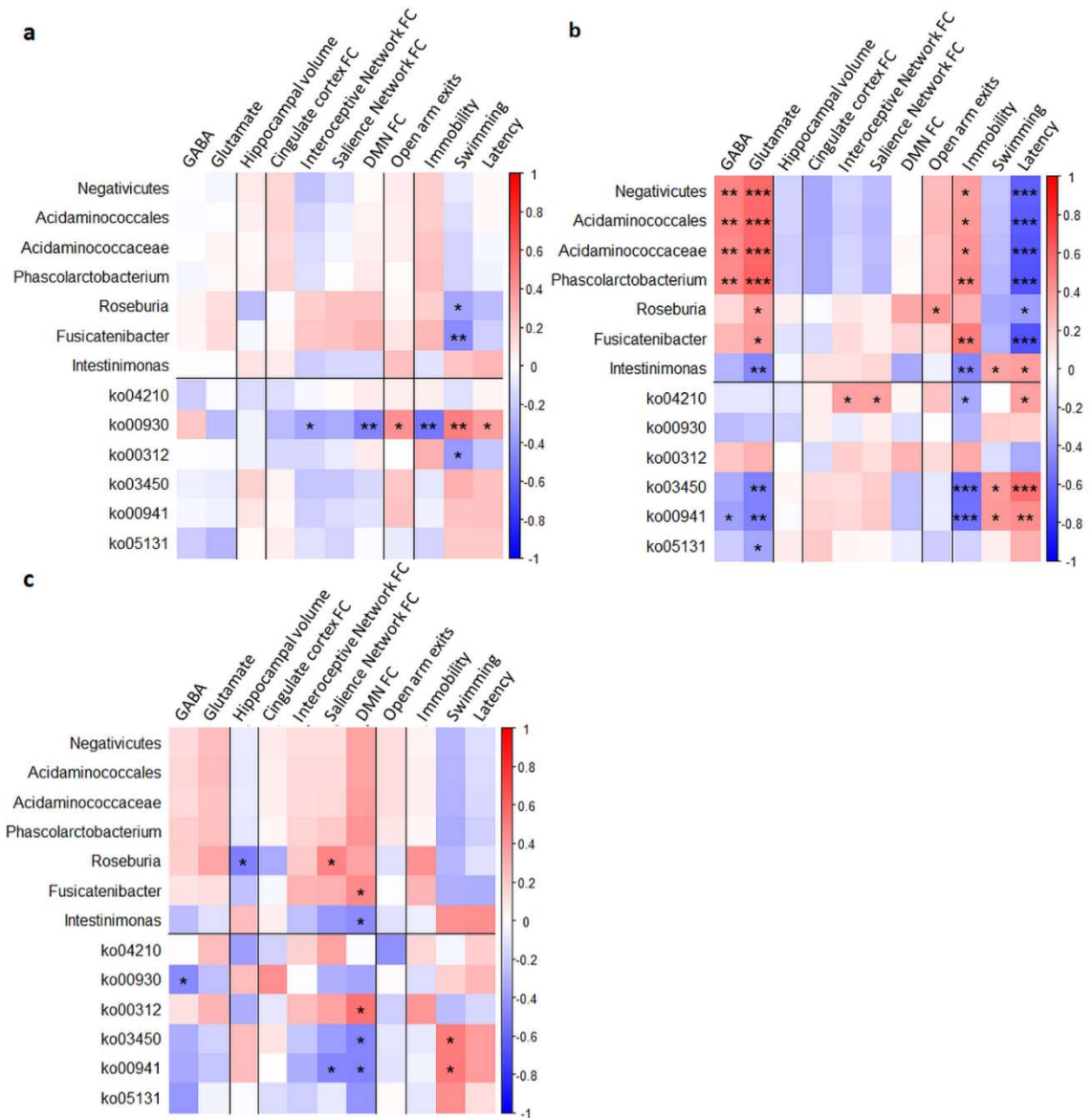


Figure 9.5. Correlations between microbiome data and MRI and behavioural measures. Centered log-ratio transformed abundances of taxa and KEGG pathways for taxa and pathways identified as significant in the ANCOM's W-statistic (threshold of 0.7) were correlated to the following parameters by Spearman correlations: GABA/tCr and Glutamate/tCr ratios from 1H-MRS data; hippocampal volume; connectivity (average z-scores) of the cingulate cortex, interoceptive network, salience network and default mode network from the rs-fMRI data; number of exits from the open arms from elevated plus maze data; and time spent immobile (Immobility) and swimming, and latency time to exhibit first immobility behaviour from forced swim test data. * $p < 0.05$, ** $p < 0.01$, *** $p < 0.001$ (no multiple comparison correction).

9.4. Discussion

There is increasing evidence that the gut-brain axis plays a key role in the aetiology and treatment of depression. Our study confirmed previously reported changes in the gut resident bacteria composition following CRS in rats and adds that handling the rats after CRS caused a significant effect on the abundance of Firmicutes phylum. Our main finding was that LI-rTMS increased the abundance of the anti-inflammatory *Roseburia* genus, which was correlated with behavioural improvement in the forced swim test. Taken together with the decrease in apoptosis pathways following LI-rTMS, as well as the correlation of caprolactam pathway with functional outcomes only in rTMS treated animals, our results suggest that LI-rTMS may have anti-inflammatory and protective effects on the gut microbiome that are associated with its therapeutic effects.

9.4.1. Diversity and volatility

Diversity of the gut microbiome is often used as an index for health, with an increase in overall diversity and species richness being a good indicator of health and a reduction or lack of diversity often signalling disease (Shreiner et al., 2015). However, there is no consensus in the literature regarding whether or how the gut microbiota richness and diversity changes in human depression and preclinical models (Barandouzi et al., 2020; Simpson et al., 2021). In the present study, neither CRS nor LI-rTMS induced changes in alpha or beta diversity parameters, or in volatility; in the literature, there is evidence for no change (Naseribafrouei et al., 2014; Zheng et al., 2016), a decrease (Kelly et al., 2016; Huang et al., 2018) and an increase in diversity (Jiang et al., 2015). This disparity is likely due to the high individual variability in gut microbiome composition together with underpowered studies and the presence of confounders such as effect of antidepressants or other oral prescription medications. The ability to control for

potential effects of diet, lifestyle and environment on the gut microbiome is an important advantage of performing animal studies, and can potentially increase the sensitivity of detecting microbiome changes that can then be validated in humans (Bear et al., 2020).

However, the timing of our study may have contributed to the lack of changes in diversity and volatility after CRS: in our studies the animals received CRS for only 2 weeks, which may not be sufficient for differences to appear. Other studies in mice performed CRS daily for 5 weeks and found more extensive changes compared to those reported here (Yang et al., 2021). rTMS treatment was also short because we applied an accelerated treatment (3x daily for 2 weeks) instead of the conventional single daily treatment for 4-6 weeks. The trend towards a reduction in volatility over time in our data suggests that more time may be required for the microbiome to change in response to environmental stressors and treatment, and our data may reflect overlapping changes due to CRS and treatment.

Despite the lack of change in overall diversity, our results identify changes in the sub-levels of two of the major phyla (Proteobacteria and Firmicutes) following CRS, similar to changes described in human patients with depression. We observed an increase in Deltaproteobacteria class of the Proteobacteria phylum, principally due to an increase in the Desulfovibrionales order. Proteobacteria have consistently been shown to be upregulated in a chronic unpredictable mild stress mouse model (Tian et al., 2019) and in patients with depression (Barandouzi et al., 2020; Cheng et al., 2020; Simpson et al., 2021), matching our findings.

9.4.2. CRS and LI-rTMS increase abundance of Firmicutes

The most significant changes in our study were in the Firmicutes which is one of the most abundant phyla in the microbiome of rats and humans and have been linked to a wide range of human health conditions including obesity and mental illness (Barandouzi et al., 2020). Several studies have shown that patients with depression have altered abundance of Firmicutes, but results remain inconsistent: both increases and decreases in the overall abundance of Firmicutes have been reported in patients with depression (Barandouzi et al., 2020; Capuco et al., 2020). Other analysis approaches such as the Firmicutes/Bacteroidetes ratio have been related to several neurological diseases and inflammatory conditions (Zhang et al., 2021), including obesity (Crovesy et al., 2020), autism spectrum disorders (Coretti et al., 2018) and inflammatory bowel diseases (Stojanov et al., 2020), with a reduced ratio associated with improvement. However more recent studies have highlighted the difficulty in associate the Firmicutes/Bacteroidetes ratio with health status, not only because of the challenges of controlling for confounders (Magne et al., 2020), but also because of the variation of this ratio across the human lifespan (Mariat et al., 2009).

Despite the lack of change in overall diversity, we observed differences between groups in abundance of specific sub-taxa. Members of the *Lachnospiraceae* family (Clostridia class: *Anaerostipes* and *Frisingicoccus* genera) significantly increased following CRS, supporting previous findings that link increased Firmicutes with pro-inflammatory processes also implicated in depression (Huang et al., 2018; Barandouzi et al., 2020). However, the changes in Firmicutes that occurred in the weeks following CRS are more difficult to interpret. The most consistent changes were detected in the control group, with downregulation of the *Lachnospiraceae* family, suggesting a

spontaneous decrease in the effects of CRS over time once the restraint intervention was stopped. However, the decreases were not observed in the active and sham groups, suggesting that handling the rats during LI-rTMS procedures had a significant impact on their microbiome, potentially sustaining the effects of CRS. While we cannot rule out that bacteria were directly transmitted from the researchers to the rats, this is unlikely because of the strict physical containment and personal protection equipment protocols in place in the animal care facility (PC2). Rather, handling has been shown to have significant effects on rodent behaviour and wellbeing, most often reducing anxiety (Schmitt and Hiemke, 1998). However, some studies have shown that handling may have different outcomes depending on the animal's experiences and environment (Pritchard et al., 2013). It is therefore possible that the handling associated with delivering active and sham LI-rTMS sustained the stress induced by CRS.

While the data suggest that the handling component of rTMS is primarily responsible for maintaining high abundance of Firmicutes genera in the weeks following CRS, an increase in *Roseburia* genus only in the rTMS group identifies a specific effect of rTMS. In contrast to other Firmicutes genera, *Roseburia* is considered a beneficial bacterium that has a positive impact on the immune system: the flagellar system of *Roseburia intestinalis* reduces intestinal inflammation by suppressing IL-17 in the host (Zhu et al., 2018), and its abundance has been reported to decrease under various disease conditions (Patterson et al., 2017; Tamanai-Shacoori et al., 2017). However, recently, a higher abundance of *Roseburia* has also previously been linked to changes in gut microbiome in mice and to cerebral hypometabolism (Sanguinetti et al., 2018). Interestingly, previous studies of the gut microbiome following brain stimulation (using

different protocols in patients with weight disorders) have shown an increase in Clostridia, the class to which *Roseburia* belongs, and these were interpreted as being anti-inflammatory and therefore beneficial (Artifon et al., 2020; Ferrulli et al., 2021), although different taxonomic sub-levels were involved compared to our study. Our study highlights that it is difficult to interpret changes in bacteria at the phyla level because taxa within the Firmicutes phylum have different functions.

9.4.3. Functional and pathway implications of microbiome changes

Although we found no changes in KEGG pathways following CRS, the characteristics of the different bacterial sub-taxa can suggest mechanisms whereby microbial changes might contribute to depression after chronic stress. Notably, genera in the Desulfovibrionales order are sulphate reducing and have been implicated in gastrointestinal inflammation through hydrogen sulphide accumulation in the gut (Dordević et al., 2021). In addition, the expression of lipopolysaccharides on the outer cell membrane of this order are thought to stimulate a host immune response through pro-inflammatory receptor stimulation and cytokine release (Hakansson and Molin, 2011). An extensive body of literature supports the association between depression and a chronic low-grade inflammatory response (Berk et al., 2013) and therefore, a higher abundance of these pro-inflammatory bacteria may play a role in development and/or maintenance of depression (Barandouzi et al., 2020; Kunugi, 2021).

Only one KEGG pathway was significantly altered following active LI-rTMS: apoptosis was decreased following treatment but returned to post-CRS levels at the 2 week follow up. Interestingly, anti-apoptotic effects of LI-rTMS have been reported in the brain: LI-rTMS has been shown to decrease genes related to apoptosis and

inflammation (Grehl et al., 2015; Clarke et al., 2021) and when delivered at higher intensities promotes survival signalling pathways after a stroke (Caglayan et al., 2019). rTMS also increases the pro-survival factors such as BDNF, not only in the brain but also peripherally in serum (Makowiecki et al., 2014; Niimi et al., 2016; Heath et al., 2018; Feng et al., 2019). Taken together, our data showing a decrease in the apoptotic pathway and an increase in the anti-inflammatory *Roseburia* genus, specifically following active LI-rTMS, suggest that this brain-specific treatment may reduce inflammation and dysbiosis in the gut. It will be important to determine in future studies whether the impact of TMS on the microbiome is due to vagal nerve activation, or if circulating factors such as cytokines and/or BDNF are involved.

9.4.4. Correlations of microbiome with behaviour and MRI

Using data collected from the same animals and published in previous studies (Seewoo et al., 2019a; Seewoo et al., 2021b), we correlated behavioural and MRI outcomes with the sub-taxa of interest identified in our current analysis. A key finding was that in the active LI-rTMS group, *Fusicatenibacter* and *Roseburia* were negatively correlated with swimming behaviour in the FST. These genera are both members of the *Lachnospiraceae* family which has been consistently negatively correlated with symptoms of depression in humans (Vacca et al., 2020). Correlation of KEGG pathways with behavioural and MRI outcomes identified only the caprolactam pathway in active LI-rTMS (Rampelli et al., 2020). The caprolactam pathway is involved in the degradation of carbon compounds found in man made products such as nylon, synthetic fibres and plasticisers. Increases in the caprolactam pathway are interesting because they have been associated with longevity in humans, and high levels of caprolactam metabolising bacteria may provide a protection against toxins in the

environment. Environmental toxins such as plastics and synthetic organic compounds have an impact on mental health (Daniel et al., 2020; Minatoya and Kishi, 2021; Schirmer et al., 2021) and our results raise the possibility that LI-rTMS may facilitate the growth of micro-organisms that can breakdown these compounds, potentially provide a protective effect.

9.4.5. Study limitations and future directions

The current study has several limitations. Firstly, we did not include a control group of rats that had no intervention (ie. Non-CRS and non-rTMS group). While this group would have been useful to track the spontaneous changes in gut microbiome over the 6 weeks of the study, our aims and statistical approach were to compare animals longitudinally over time to explore how the microbiome changes over time in individual animals in response to CRS and rTMS. This longitudinal approach is useful for understanding individual changes that are likely to occur in humans. Secondly, only male rats were utilised in this study, as the CRS model is most reliable in male Sprague Dawley rats. Given that there are strong sex differences in depression aetiology and treatment and in the gut-brain axis, future studies should expand the applicability of present results by investigating microbiome changes in female rats (Eid et al., 2019; Holingue et al., 2020). Thirdly, the rats in this study were young adults. Age has been shown to have a significant effect on the composition of the gut microbiome (Agans et al., 2011; Radjabzadeh et al., 2020). Six months or older rats that have fully completed cerebral development (Mengler et al., 2014) could be used in future studies to exclude potentially confounding effects of brain-maturation with age. Lastly, avoiding the effects of co-housing animals is difficult. While animals in the same treatment group were co-housed in the present study to avoid microbial transfer between study

groups, the fact that co-housed animals tend to have more similar microbiome could mask or exaggerate the results.

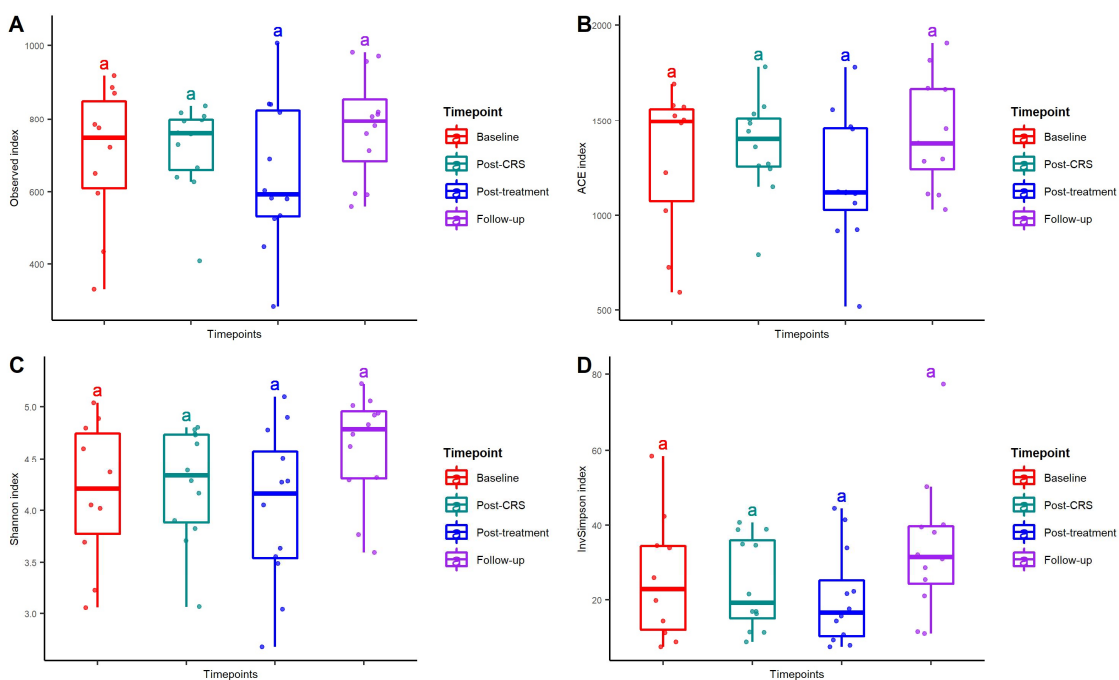
We also acknowledge the widely recognised challenges and limitations of modelling and measuring depression-like behaviour in rats: depression is diagnosed in humans based on subjective measures that are difficult to evaluate in rats. In choosing our behavioural tests, we selected tests that are considered the gold standard in the literature (EPM and FST) and test for anxiety and learned helplessness/stress responses respectively (Seewoo et al., 2020a). Although performing additional tests could potentially provide more information about the models and interventions, we believe that our design represents an acceptable trade-off that optimises the quality of the data without redundancy (Cryan and Mombereau, 2004; Shoji et al., 2016) or “over testing” that could increase stress levels and compromise outcomes.

9.4.6. Conclusion

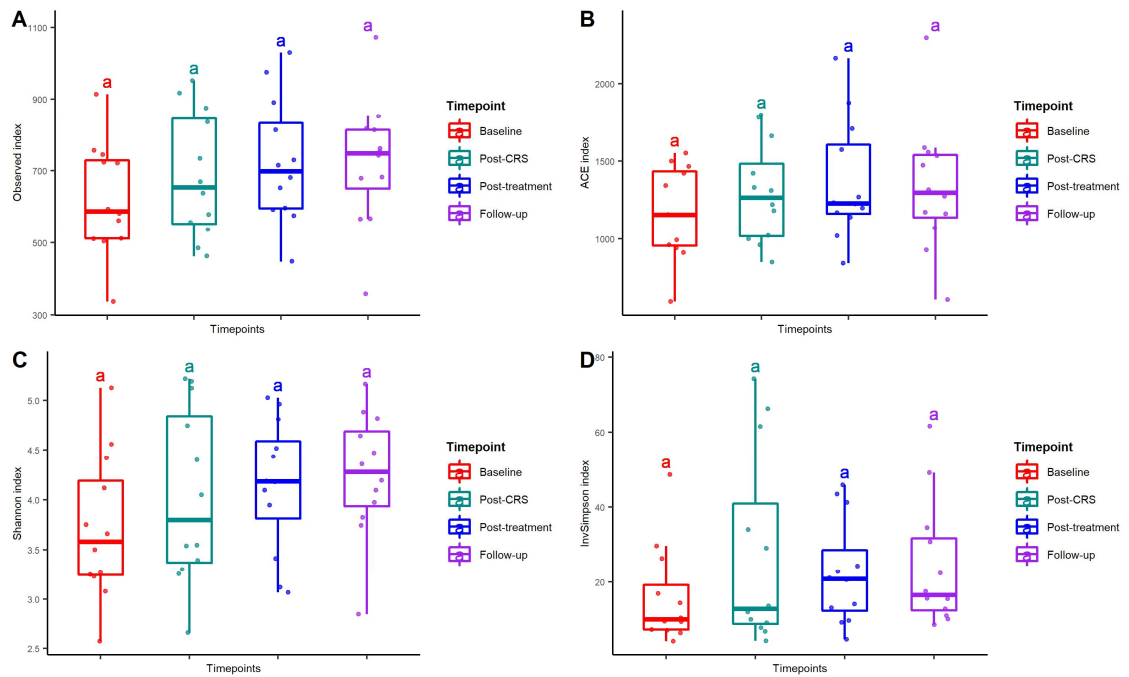
In conclusion, this study is the first of its kind to investigate the effects of CRS and LI-rTMS treatment on the gut microbiome longitudinally in male Sprague Dawley rats. Specifically, we found that chronic stress induced gut microbial dysbiosis, which was associated with high levels of anxiety and depression as well as brain changes. Our results after CRS highlight that although handling had a major impact on microbiome composition, there was evidence supporting a top-down effect of rTMS on the gut microbiome, with the main outcome being an increase in abundance of the *Roseburia* genus. The change in the microbiome was observed only in the LI-rTMS group, and not in the sham or no-handling control groups, suggesting that it was a consequence of altering brain activity with LI-rTMS. However, it remains unclear whether the increase

in *Roseburia* is a direct effect via stimulation of neural pathways that connect the brain to the gut, or whether it is an indirect effect, resulting from the behavioural (mood) improvements. Given that *Fusicatenibacter* abundance was also significantly correlated with behaviour, but was not significantly altered by rTMS at the group level, and that handling alone had a significant impact on the microbiome, it is likely that there is complex feedback between microbiome, behaviour (including stress levels) and brain function: future studies should investigate faecal transplants and vagal nerve transection interventions to further explore the interplay of the gut brain axis components with behaviour and mood.

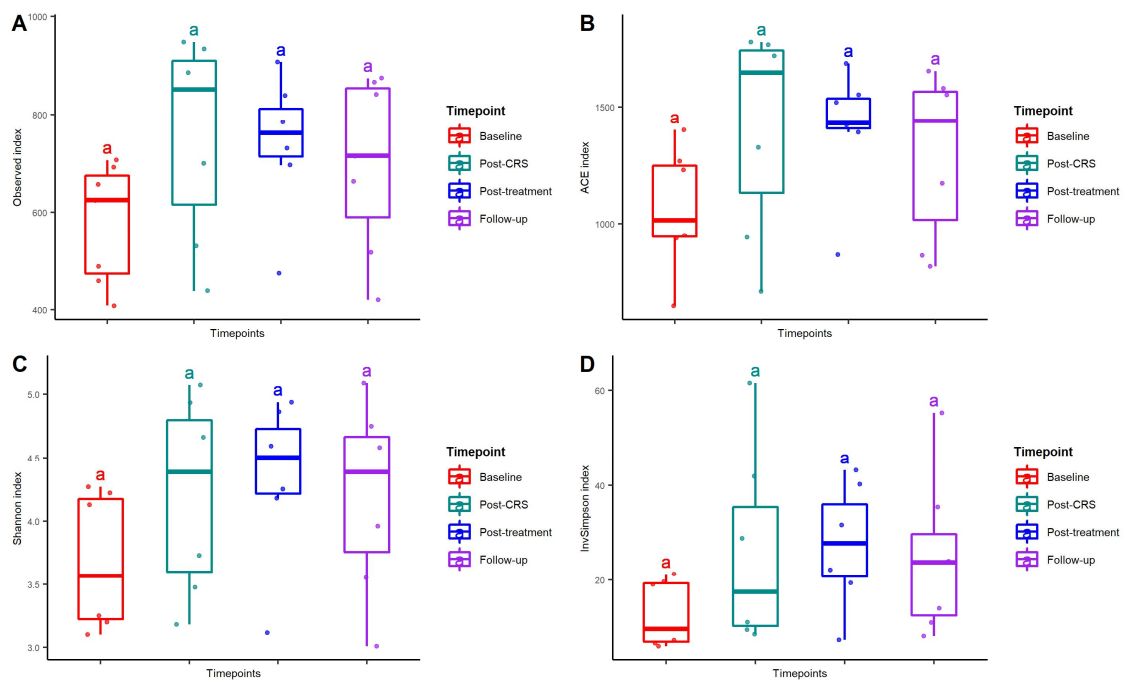
9.5. Supplementary Figures



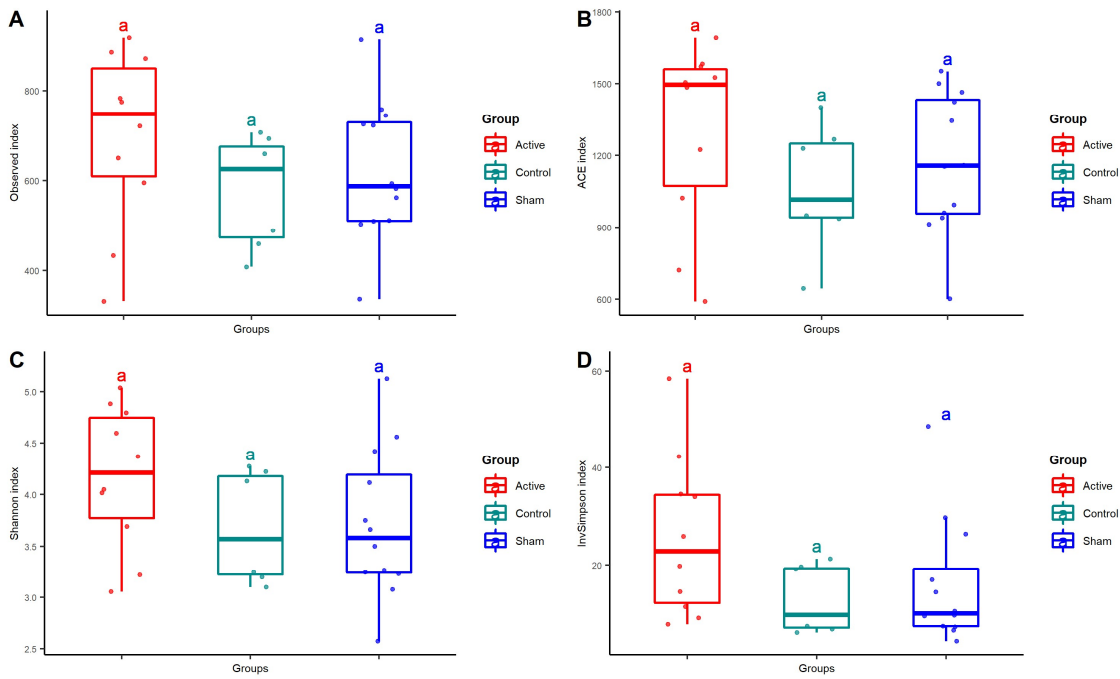
Supplementary Figure 9.1. Changes in alpha diversity between timepoints within the active group. A number of observed OTUs (observed index); B abundance-based coverage estimators (ACE) index; C Shannon entropy index; and D inverse Simpson index.



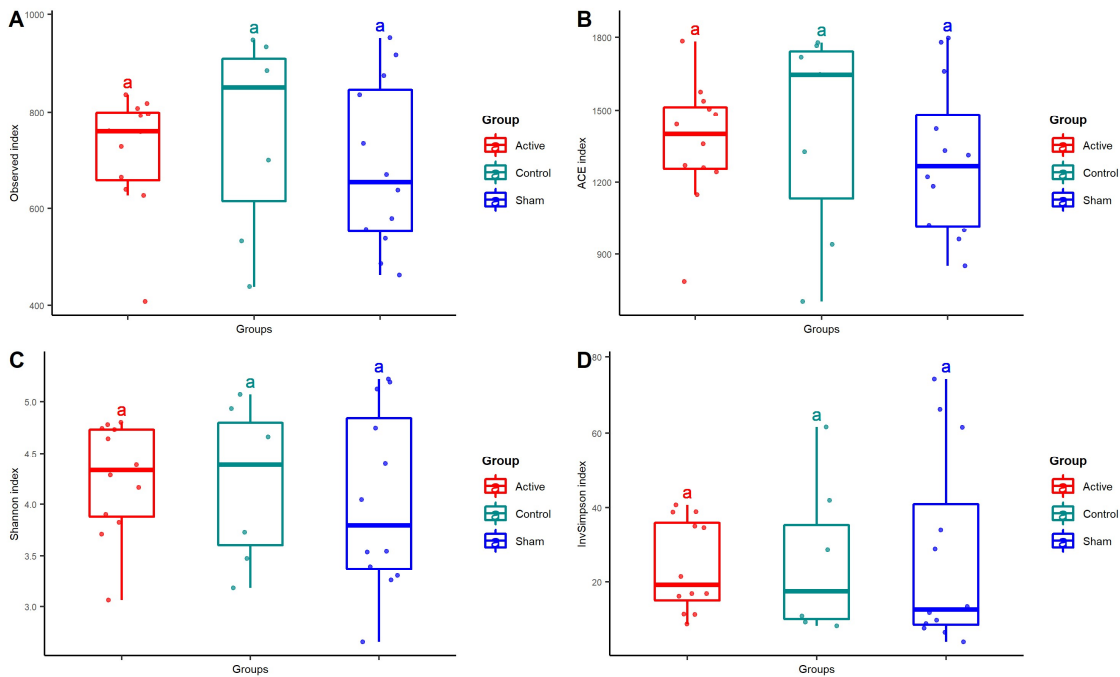
Supplementary Figure 9.2. Changes in alpha diversity between timepoints within the sham group. A number of observed OTUs (observed index); B abundance-based coverage estimators (ACE) index; C Shannon entropy index; and D inverse Simpson index.



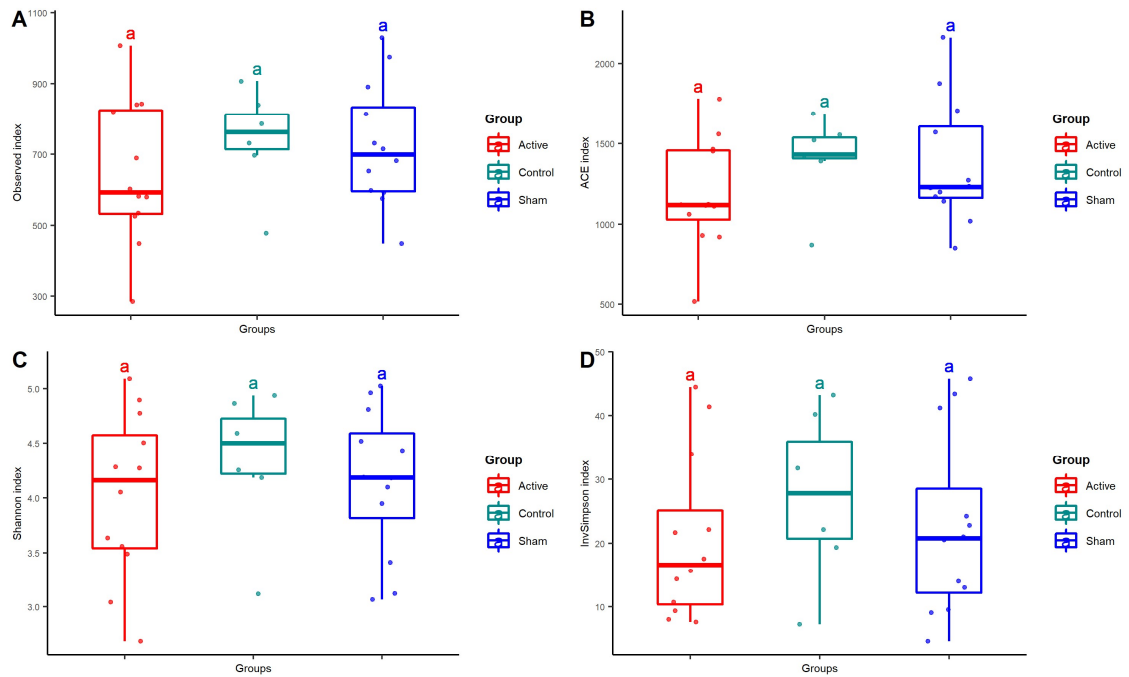
Supplementary Figure 9.3. Changes in alpha diversity between timepoints within the control group. A number of observed OTUs (observed index); B abundance-based coverage estimators (ACE) index; C Shannon entropy index; and D inverse Simpson index.



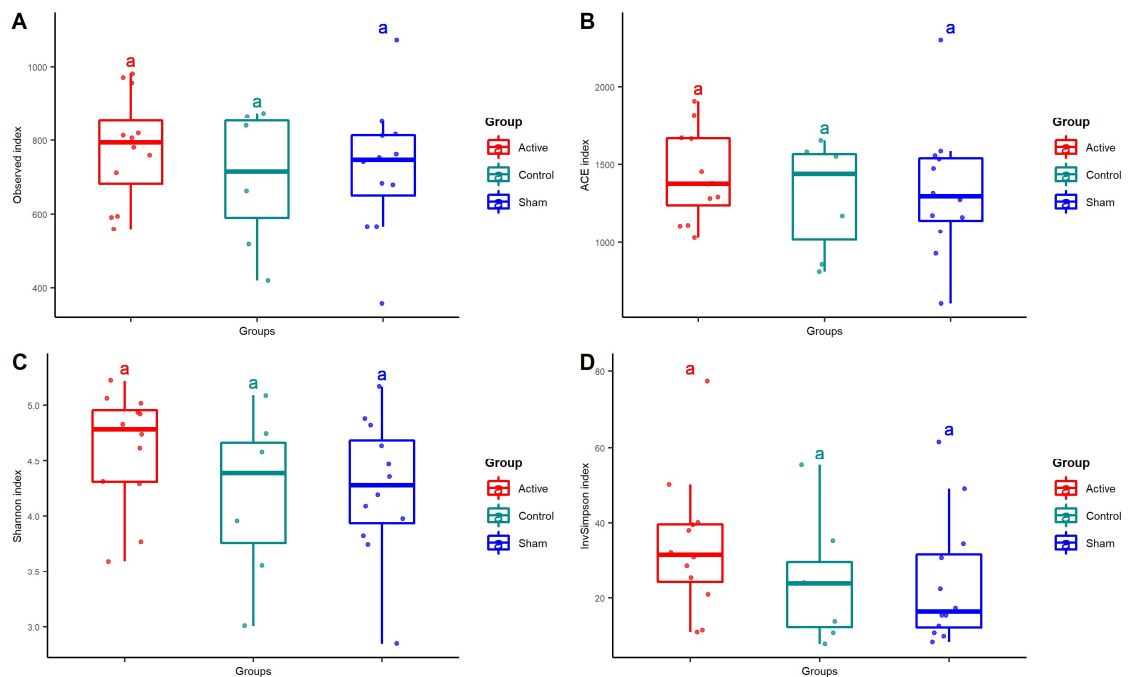
Supplementary Figure 9.4. Changes in alpha diversity between groups at the baseline timepoint. A number of observed OTUs (observed index); B abundance-based coverage estimators (ACE) index; C Shannon entropy index; and D inverse Simpson index.



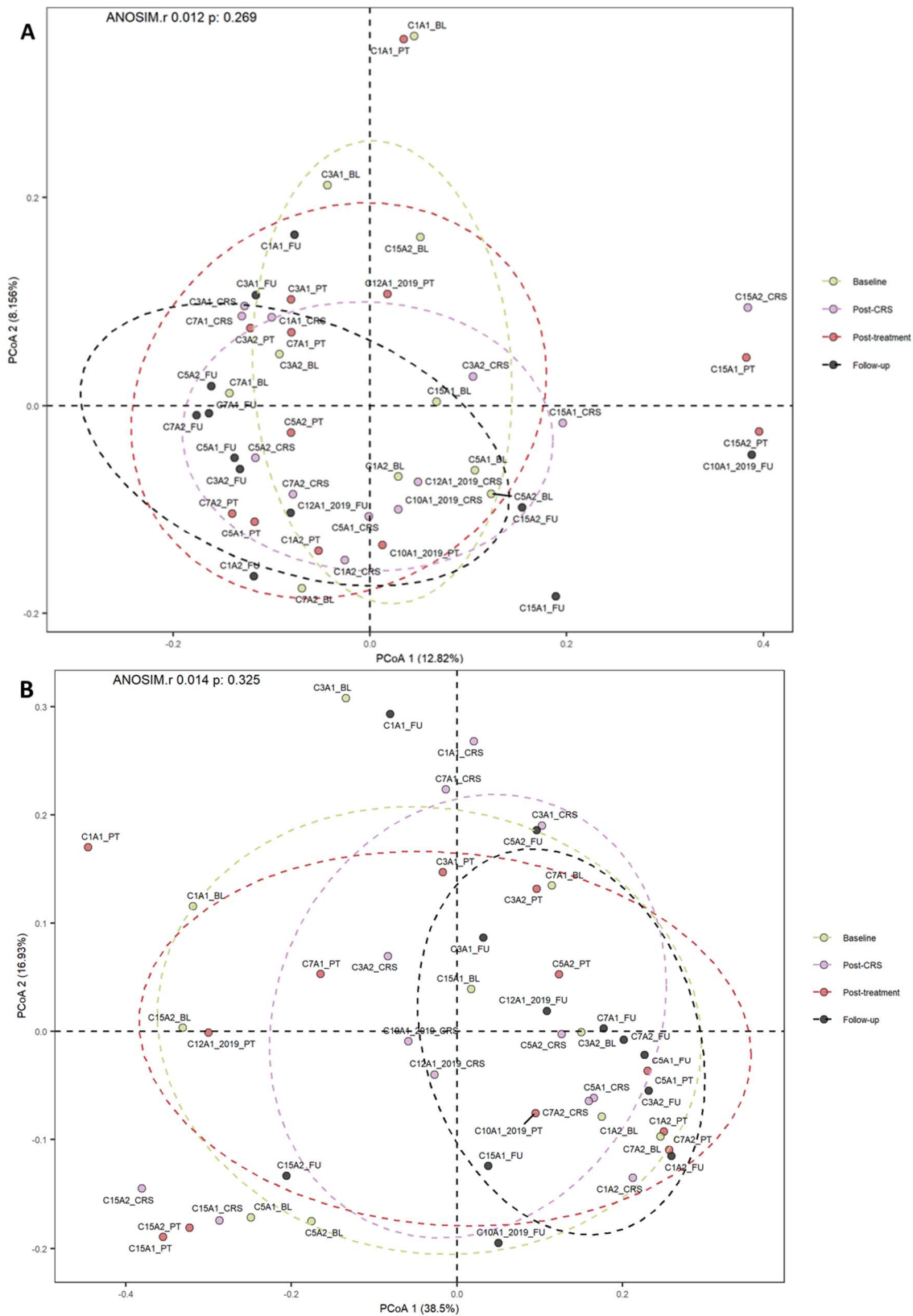
Supplementary Figure 9.5. Changes in alpha diversity between groups at the post-CRS timepoint. A number of observed OTUs (observed index); B abundance-based coverage estimators (ACE) index; C Shannon entropy index; and D inverse Simpson index.



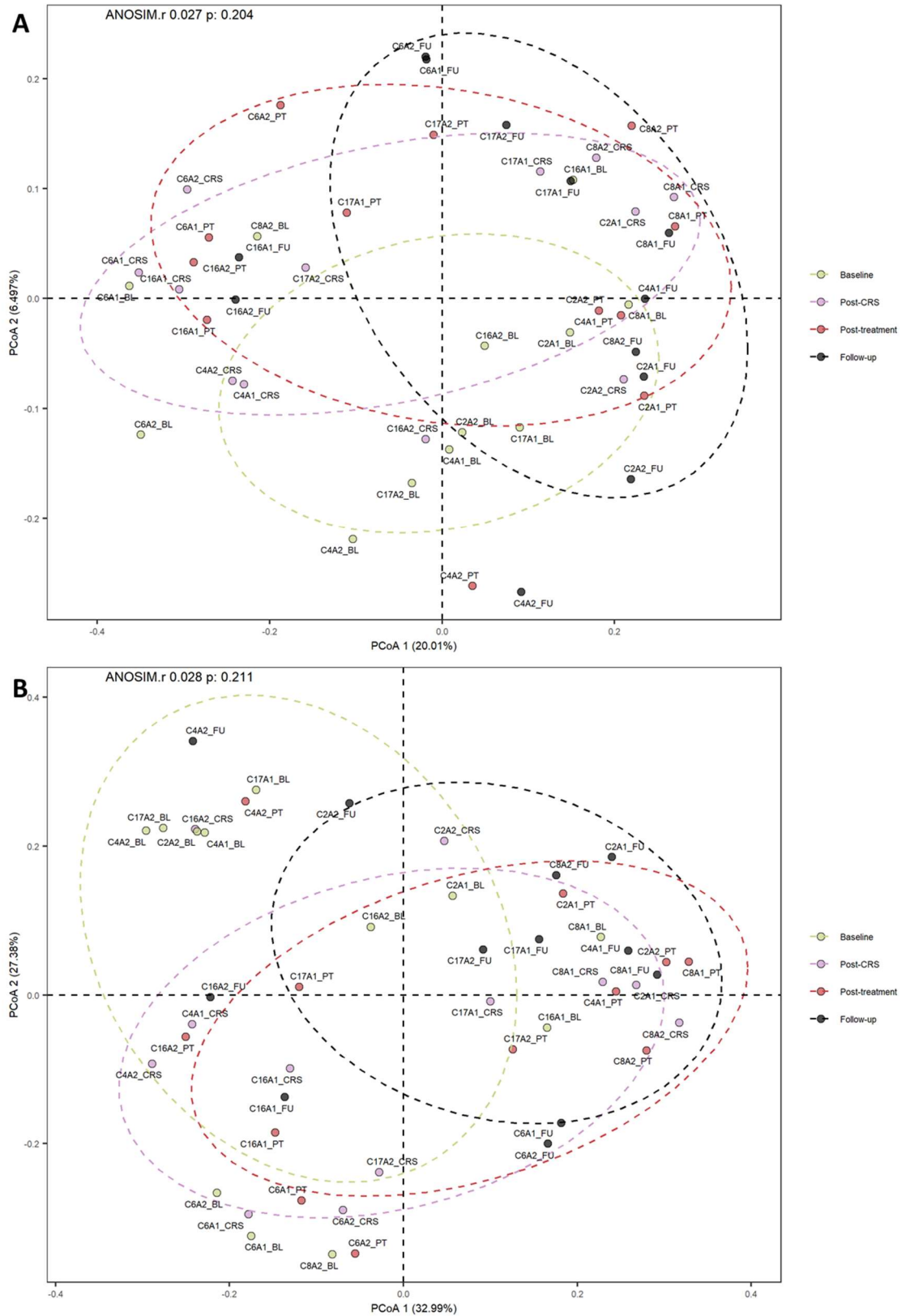
Supplementary Figure 9.6. Changes in alpha diversity between groups at the post-rTMS timepoint. A number of observed OTUs (observed index); B abundance-based coverage estimators (ACE) index; C Shannon entropy index; and D inverse Simpson index.



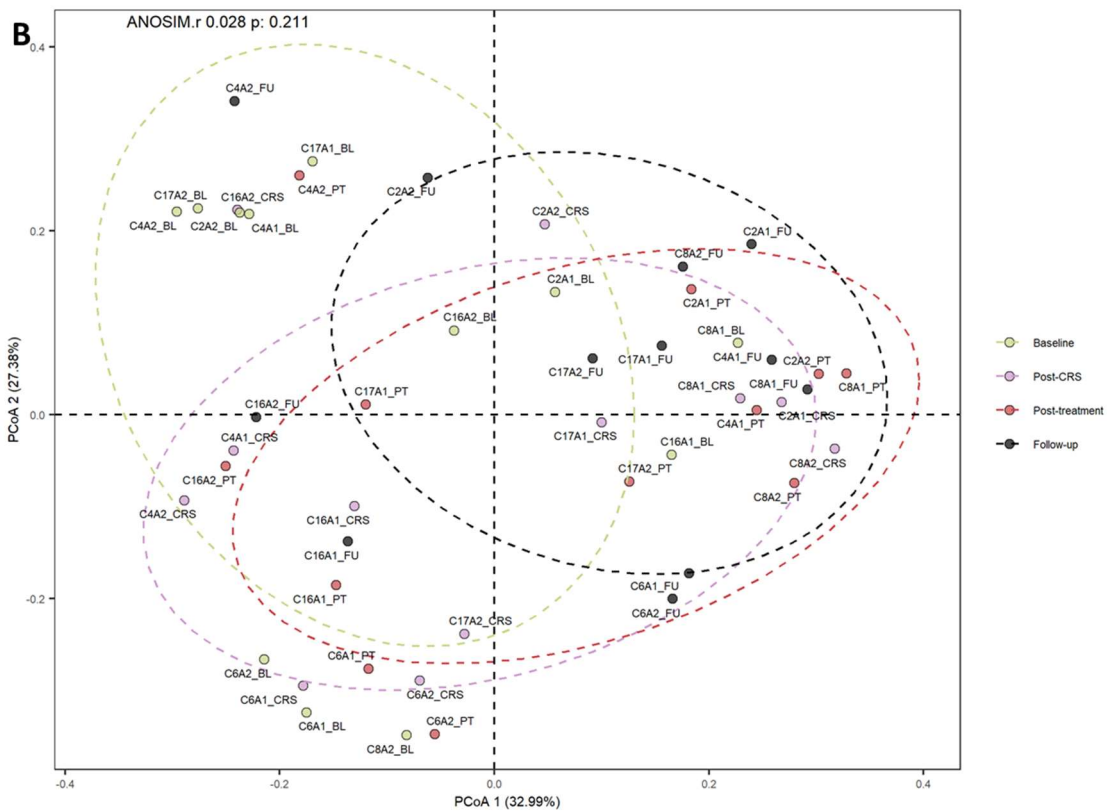
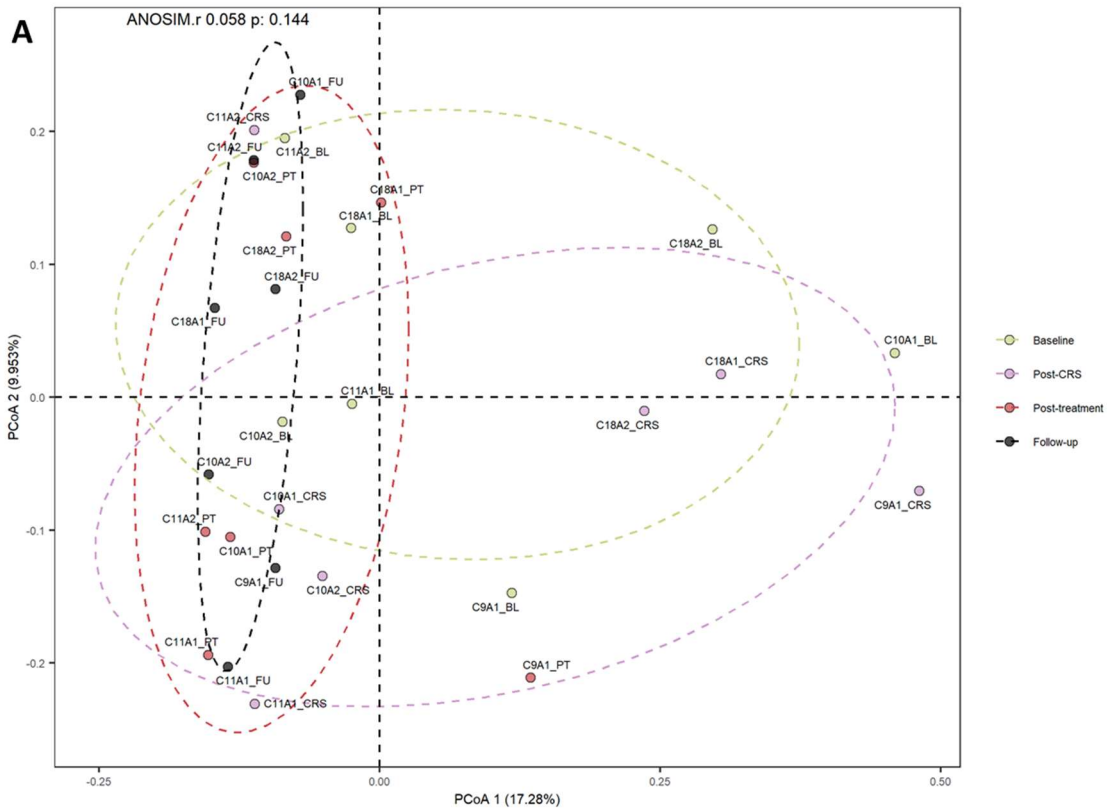
Supplementary Figure 9.7. between groups at the two weeks follow-up timepoint. A number of observed OTUs (observed index); B abundance-based coverage estimators (ACE) index; C Shannon entropy index; and D inverse Simpson index.



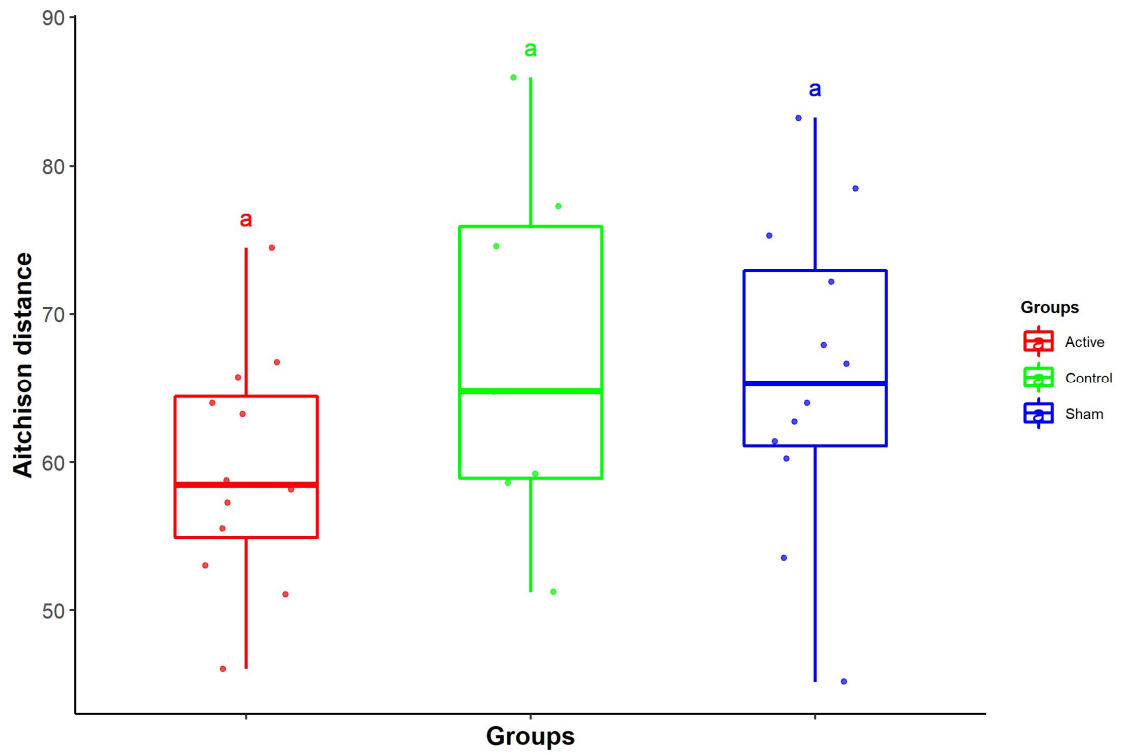
Supplementary Figure 9.8. Principal coordinates analysis based on weighted (A) and unweighted (B) UniFrac distance metrics between timepoints in the active group.



Supplementary Figure 9.9. Principal coordinates analysis based on weighted (A) and unweighted (B) UniFrac distance metrics between timepoints in the sham group.



Supplementary Figure 9.10. Principal coordinates analysis based on weighted (A) and unweighted (B) UniFrac distance metrics between timepoints in the depression control group.



Supplementary Figure 9.11. Difference in microbial volatility between the groups. The Aitchison distance of both post-CRS and post-rTMS timepoints for each animal was computed, and then the distance values between the animal groups were compared.